

Hydroconversion of cis-Decalin on Noble Metal-Containing Zeolites

Von der Fakultät Chemie der Universität Stuttgart
zur Erlangung der Würde eines
Doktors der Naturwissenschaften (Dr. rer. nat.)
genehmigte Abhandlung

von

Dominic Santi

aus Bietigheim-Bissingen

Hauptberichter: Prof. Dr.-Ing. Jens Weitkamp

Mitberichter: Prof. Dr. Cosima Stubenrauch

Tag der mündlichen Prüfung: 21.09.2012

Institut für Technische Chemie
der Universität Stuttgart
2012

Die vorliegende Arbeit entstand in der Zeit von Juni 2008 bis Dezember 2011 am Institut für Technische Chemie der Universität Stuttgart.

Mein besonderer Dank gilt Herrn Prof. Dr.-Ing. Jens Weitkamp für die Überlassung dieses faszinierenden und vielschichtigen Themas, sowie für die sehr engagierte Betreuung meiner Arbeit.

Danken möchte ich auch Herrn Prof. Dr.-Ing. Elias Klemm für die sehr guten Rahmenbedingungen am Institut für Technische Chemie.

Frau Prof. Dr. Cosima Stubenrauch danke ich für die Übernahme des Koreferats.

Ebenso danken möchte ich Herrn Dr. Vincenzo Calemma und Herrn Dr. Marco Ferrari von Eni S.p.A. für die ausgezeichnete Zusammenarbeit im Rahmen des Industrieprojekts.

Ganz besonders möchte ich meinen Kollegen Sandra Rabl, Andreas Haas und Tobias Holl für die sehr gute Zusammenarbeit im Rahmen des Projekts danken. Zusammen mit Ines Kley, Nicole Weiß, Arne Bressel und Frank Salzbauer ergaben sich viele fruchtbare und interessante Diskussionen.

Ferne danke ich Matthias Aimer, Daniel Barunovic, Harun Bilgili, Gregor Näfe, Sebastian Plebst und Daniel Pötsch, die im Rahmen von Praktika und Diplomarbeiten zu dieser Arbeit beigetragen haben.

Dank gebührt ebenfalls Heike Fingerle, Barbara Gering, Herrn Prof. Dr. Michael Hunger und Matthias Scheibe für die Durchführung verschiedener Analysen und Charakterisierungen.

Ein großer Dank gilt meinen Eltern die mich immer unterstützt haben und mir mein Studium ermöglichten. Meinen Freunden und besonders meiner Partnerin möchte ich für die Unterstützung und die Geduld während meines Studiums und vor allem während der Anfertigung dieser Arbeit danken.

Abstract

There has recently been considerable concern about polynuclear aromatic hydrocarbons in diesel fuel, as they have a variety of unfavorable properties like low cetane numbers, poor cold-flow properties, propensity of soot formation and high specific CO₂ emissions. The conversion of such polynuclear aromatic hydrocarbons into hydrogen-rich, environmentally benign blending cuts for diesel fuel continues to be among the challenges of heterogeneous catalysis. In the best case, such a conversion would lead to alkanes with the same carbon number as the polynuclear aromatic hydrocarbons. This route would comprise two steps, namely the complete hydrogenation of the aromatic rings to naphthenes followed by their selective ring opening to alkanes. While the first step is generally considered as state-of-the-art catalysis, the selective ring opening continues to be a challenge in today's catalysis research.

In this thesis, the influence of the nature of the noble metal, the structure of the zeolite catalysts and their acidic properties on the selective ring opening of cis-decalin was studied, and a catalytic system was developed which enables unprecedented selectivities and yields of open-chain decanes (OCDs). Different noble metals (ruthenium, rhenium, palladium and rhodium) supported on the faujasite Na,H-Y were investigated to identify the best suited noble metal for this reaction. As already known from literature, iridium and platinum supported on faujasites are very promising catalysts for this reaction: Maximum yields of OCDs as high as 31 and 39 %, respectively, had been described. Since none of the evaluated noble metals showed better results all subsequent experiments were conducted on catalysts containing either iridium or platinum. To investigate the influence of the zeolite structure on the selectivities and yields to OCDs, different types of 12-membered ring pore zeolites (Na,H-mordenite, K,H-L, H-SAPO-5, Na,H-EMC-2, Na,H-[Al]Beta-14 and Na,H-ZSM-5) were loaded with about 3 wt.-% of platinum or iridium and tested in the hydroconversion of decalin. To examine the influence of the Brønsted acid sites on the reaction, the strengths of the sites were varied in three different ways, namely (i) the isomorphous substitution of aluminum by boron in zeolite Beta, (ii) the variation of the molar ratio $n_{\text{Si}} / n_{\text{Al}}$, again in zeolite Beta, and (iii) the exchange of the charge-compensating cations by different alkali metals in zeolites Beta, mordenite and L. The strengths of the Brønsted acid sites were determined by FT-IR spectroscopy and pyridine as a probe molecule. The best catalyst obtained through these variations was 3.4Ir/H_{0.58}CS_{0.42}-[Al]Beta-14, leading to selectivities and yields of OCDs as high as 47 % and 43 %, respectively.

I	Table of Contents	
II	Symbols, Indices and Abbreviations	IV
1	Zusammenfassung.....	1
2	Summary.....	6
3	Introduction and Objectives	10
4	Literature Review	12
4.1	Structures and Pore Architectures of Zeolites	12
4.2	Acid Sites in Zeolites	19
4.3	Hydrodecyclization of Multi-Ring Aromatics, Naphthenoaromatics and Multi-Ring Naphthenes.....	27
4.3.1	Mechanistic Principles of the Ring-Opening Reaction.....	27
4.3.2	Hydrodecyclization on Bifunctional and Monofunctional Catalysts.....	35
4.3.3	High-Performance Ring-Opening Catalysts (HIPEROcs).....	45
5	Experimental Section.....	49
5.1	Preparation of the Catalysts	50
5.1.1	Dry-Gel Conversion.....	50
5.1.2	Starting Materials.....	50
5.1.3	Modification of the Zeolites.....	53
5.1.4	Decomposition of the Noble-Metal Complex.....	56
5.1.5	Forming of the Catalyst Powder	57
5.1.6	Reduction of the Noble Metal.....	57
5.2	Characterization of the Catalysts and Starting Materials.....	57
5.3	Conditions in the Catalytic Experiments	61
5.4	Product Analysis by Capillary Gas Chromatography.....	64
5.5	Evaluation of the Catalytic Experiments	66

6	Characterization of the Catalysts and Respective Zeolitic Supports.....	70
6.1	Chemical Composition.....	70
6.2	Physical and Structural Properties	76
6.3	Metal Dispersion	87
6.4	Acidic Properties.....	89
7	Hydrodecyclization of Decalin	96
7.1	Influence of the Noble Metal	96
7.2	Influence of the Zeolite Structure	99
7.2.1	Platinum-Containing Zeolites	99
7.2.2	Iridium-Containing Zeolites.....	104
7.3	Influence of the Strength of the Brønsted Acid Sites	110
7.3.1	Isomorphous Substitution	110
7.3.2	Variation of the Molar Ratio of Silicon to Aluminum.....	112
7.3.3	Variation of the Nature of the Charge-Compensating Cation	116
7.4	Variation of the Iridium Content.....	130
7.5	Variation of the Hydrogen Pressure.....	138
7.6	Structural and Chemical Prerequisites for HIPEROCs.....	140
8	References	142
9	Appendices	148
9.1	Retention Times	148
9.2	Derivation of the Equations for the Calculations of Conversion, Yields and Selectivities	152
9.2.1	Nomenclature	152
9.2.2	Conversion X_{Dec}	155
9.2.3	Yield Y_j	159
9.2.4	Selectivity S_j	160

9.2.5	Modified Selectivity S_j^*	161
9.3	Pyridine Concentrations Determined by FT-IR Spectroscopy	163
9.4	References	164

II Symbols, Indices and Abbreviations

Symbols

Symbol	Unit	Designation
A	$\text{m}^2 \cdot \text{kg}^{-1}$	specific surface area according to Brunauer, Emmett and Teller
A	$\text{A} \cdot \text{s}$	peak area in the chromatogram
\bar{A}	m^{-1}	integral absorption coefficient
c	$\text{mol} \cdot \text{dm}^{-3}$	concentration
C_q	Hz	quadrupole constant
CN	-	cetane number
d	m	diameter
f	-	compound-specific FID correction factor
F	-	relative fraction in ^{29}Si MAS NMR spectrum
k	-	number of aluminum or boron atoms coordinated to a silicon atom
l	m	length
$LHSV$	h^{-1}	liquid hourly space velocity
m	kg	mass
MP	K or $^{\circ}\text{C}$	melting point
n	mol	molar amount
n	-	number of carbon atoms
\dot{n}	$\text{mol} \cdot \text{s}^{-1}$	molar flux
p	Pa	pressure
p_0	Pa	vapor pressure of nitrogen in the reference cell
p_i	Pa	partial pressure

S	-	electronegativity
S	-	selectivity
S^*	-	modified selectivity
SI	-	spaciousness index
t	s	time
T	K or °C	temperature
\dot{V}	$\text{m}^3 \cdot \text{s}^{-1}$	volumetric flow rate
X	-	conversion
Y	-	yield
γ	-	stoichiometric factor
δ	-	chemical shift
ε	$\text{m} \cdot \text{mol}^{-1}$	extinction coefficient
θ	°	angle
λ	m	wavelength

Indices

amorph.	amorphous
BA	Brønsted acid site
BET	Brunauer, Emmett and Teller
cat	catalyst
Dec	decalin
deg	degassing
des	desorption
i	element in an equation
int	intermediate
j	a product or group of products in the stoichiometric equation
LA	Lewis acid site
max.	maximum
r	reaction
rel	relative
ret	retention
RT	room temperature
s	solid

Abbreviations

A	acid site
AFI	aluminophosphate five
ALPO	aluminophosphate
a.u.	arbitrary units
B	basic probe molecule
*BEA	zeolite Beta
BEC	zeolite Beta polymorph C
BET	Brunauer, Emmett and Teller
C ₉ -	hydrocarbons with less than 10 carbon atoms (hydrocracked products)
DGC	dry-gel conversion
DHP(s)	dehydrogenated product(s)
DRIFT	diffuse reflectance infrared fourier transform
EFAL	extra-framework aluminum
EMC	Elf (or Ecole Supérieure) Mulhouse Chimie
EMT	Elf (or Ecole Supérieure) Mulhouse Chimie – two
Eq.	Equation
Exp.	experimental
FAU	faujasite
FI	flow indicator
FID	flame ionization detector
FT	fourier transform
FTC	framework type code
GC	gas chromatograph(y)
GCxGC	comprehensive two-dimensional gas chromatography

GC/MS	gas chromatography / mass spectrometry
HIPEROCS	high-performance ring-opening catalysts
HPDEC	high power decoupling
ICP-OES	inductively coupled plasma - optical emission spectrometer, spectrometry
IR	infrared
ITQ	Instituto de Tecnologia Química Valencia
IUPAC	International Union of Pure and Applied Chemistry
IZA	International Zeolite Association
L	zeolite L (Linde Division, Union Carbide)
L	Lewis acid site
LCO	light cycle oil
LTL	Linde Type L
M	metal
M	Molar
Ma.	Masse(n)
MAS	magic angle spinning
MBDe	multiply branched decanes
MCM	Mobil Composition of Matter
MFC	mass flow controller
MFI	Mobile Five
MOR	mordenite
MR	membered-ring
n.a.	not applicable
n.d.	not determined
NMR	nuclear magnetic resonance

NNN(s)	next nearest neighbor(s)
NV	needle valve
OCD(s)	open-chain decane(s)
OCN(s)	open-chain nonanes(s)
PCP(s)	protonated cyclopropane(s)
PI	pressure indicator
pred.	predicted
prim.	primary
RE	rare earth
Ref.	reference
ROP(s)	ring-opening product(s)
rpm	rounds per minute
SAPO	silicoaluminophosphate
sec.	secondary
SEM	scanning electron microscope
sk-Iso(s)	skeletal isomer(s)
T	tetrahedrally coordinated atoms
TCD	thermal conductivity detector
TEAOH	tetraethylammonium hydroxide
tert.	tertiary
TGA	thermogravimetric analyzer
TMS	tetramethylsilane
TPD	temperature-programmed desorption
USY	ultrastable Y zeolite
UV	ultraviolet

V	valve
vol.	volume
wt.	weight
XRD	X-ray diffractogram, diffractometer
ZO ⁻	negatively charged zeolite framework
ZSM-5	Zeolite Socony Mobil five

Abbreviations of Hydrocarbons

B-	butyl
Bu	butane
CHx	cyclohexane
CPn	cyclopentane
DE-	diethyl
Dec	decalin
DM-	dimethyl
E-	ethyl
Hp	heptane
Hx	hexane
M-	methyl
Nap	naphthalene
No	nonane
Oc	octane
P-	propyl
Pn	pentane
Py	pyridine
Ttr	tetralin

Nomenclature of the Catalysts

The nomenclature of the herein used catalysts differs from the IUPAC (International Union of Pure and Applied Chemistry) name due to a simpler manageability. In the case of isomorphically substituted zeolites, aluminum or boron are enclosed in square brackets in front of the zeolite name, *e.g.* [B]Beta. Separated by a hyphen are the symbols of the charge-compensating cations. The subscripts after the symbol stands for the mole fraction of the respective cation. The cations are listed in the order of their equivalent fractions (product of mole fraction and charge) and separated from each other by a comma. The equivalent fraction of protons is calculated as the molar amount of aluminum minus the sum of equivalents of all metal cations. The symbol of the noble metal is separated from the cations by a slash. The number in front of the noble metal corresponds to the amount of this metal in weight percent based on the dry zeolite mass. The molar ratio of silicon to aluminum ($n_{\text{Si}} / n_{\text{Al}}$) is indicated after the zeolite name and a hyphen.

The designations of the so named zeolites turned out to be straightforward and useful in the present work. However, they also tend to be somewhat lengthy. In those cases where the full designation is not needed, a second, much shorter nomenclature is used. It contains just the name of the noble metal followed by a slash and the names of the charge compensating cations and, finally, after a hyphen the name of the zeolite.

1 Zusammenfassung

Monocyclische Aromaten in reiner Form sind wichtige Basis-Chemikalien, z. B. für die Herstellung von Polymeren. Im Gegensatz dazu sind polycyclische Aromaten höchst unerwünscht. Diese Aromaten können nur in sehr begrenztem Maße Dieselkraftstoffen beigemischt werden, da sie sehr schlechte Zünd- und Kältefließigenschaften besitzen, zu Ruß- und Partikelbildung neigen und durch ihren niedrigen Wasserstoffgehalt einen hohen Ausstoß an CO₂ verursachen. Allerdings führt eine Ringöffnung, bei der die Anzahl der Kohlenstoffatome gleich bleibt, zu Alkanen mit stark verbesserten Eigenschaften. Für eine solche Umsetzung müssen die Aromaten zunächst zu Naphthenen hydriert werden, wonach dann die selektive Ringöffnung erfolgen kann. Im Gegensatz zur Hydrierung von Aromaten, die schon Stand der Technik ist, gelang die selektive Ringöffnung von Naphthenen zu offenkettigen Alkanen in der Vergangenheit nicht zufriedenstellend.

Das Ziel dieser Arbeit war die Untersuchung der hydrierenden Umsetzung von cis-Decalin an verschiedenen edelmetallhaltigen Zeolith-Katalysatoren. Dabei sollten insbesondere Katalysatorsysteme identifiziert werden, die bei der hydrierenden Umsetzung von cis-Decalin eine Ausbeute von mindestens 25 % an offenkettigen Decanen (OCDs) erreichen. Diese Katalysatoren werden „*high-performance ring-opening catalysts*“ (HIPEROCs) genannt. Um dieses Ziel zu erreichen, wurden die Natur des Edelmetalls, die Struktur des Trägers, die Stärke der Brønsted-Säurezentren des Trägers und der Edelmetallgehalt variiert. In allen untersuchten Katalysatoren wurden die Brønsted-Säurezentren lediglich durch die Reduzierung des Edelmetalls generiert, was zu einer relativ geringen Konzentration an Säurezentren geführt hat.

In einem ersten Schritt wurde das am besten geeignete Edelmetall für die selektive Ringöffnung von Decalin gesucht. Aus der Literatur war bekannt, dass Iridium oder Platin geträgert auf Faujasit sehr vielversprechend sind: Maximale Ausbeuten an OCDs von 31 bzw. 39 % wurden erreicht. In dieser Arbeit wurden Ruthenium, Rhenium, Palladium und Rhodium geträgert auf dem Faujasiten Na-Y untersucht.

Bei geringen Umsätzen wurden an Ru/Na,H-Y fast ausschließlich Ringöffnungsprodukte mit einem verbliebenen naphthenischen Ring (ROPs) gebildet, welche durch eine zweite Ringöffnung zu offenkettigen Decanen (OCDs) umgesetzt wurden. Allerdings betrug die Ausbeute an OCDs nur 5 %. Vermutlich lag der Hauptgrund für diese niedrigen Ausbeuten an den großen Mengen gecrackter Produkte mit weniger als 10 Kohlenstoffatomen (C₉-), die sich bei allen Umsätzen bildeten. Im Falle des rheniumhaltigen Katalysators war die Menge an gebildetem C₉- sogar noch größer: Schon bei geringen Umsätzen bestanden beinahe 50 %

des umgesetzten Decalins aus Kohlenwasserstoffen mit neun oder weniger C-Atomen, und mit steigendem Umsatz stieg deren Menge stark an.

Ein gänzlich anderes Verhalten wurde bei der Umsetzung von Decalin am mit Palladium beladenen Zeolithen beobachtet: Es fand fast ausschließlich Gerüstisomerisierung des Decalins statt. Allerdings bildeten sich ab einem Umsatz von ca. 65 % vorwiegend Crackprodukte. Der beste Katalysator dieser Serie war der mit Rhodium beladene Faujasit mit einer maximalen Ausbeute an OCDs von 11 %. Bei geringen Umsätzen bildeten sich beinahe gleiche Mengen an Gerüstisomeren (sk-Isos) und ROPs, welche mit steigendem Umsatz konsekutiven Reaktionen unterlagen. Die Ergebnisse dieser Untersuchungen zeigten, dass die Natur des Edelmetalls einen großen Einfluss auf die Eigenschaften von bifunktionellen Zeolithkatalysatoren haben kann. Basierend auf diesen Ergebnissen wurden für die weiteren Untersuchungen durchweg Platin oder Iridium als Edelmetall-Komponente gewählt.

In einem zweiten Schritt wurde der Einfluss der Zeolith-Struktur auf die hydrierende Ringöffnung von Decalin untersucht. Hierfür wurden die Zeolithe Na,H-Mordenit, K,H-L, H-SAPO-5, Na,H-EMC-2, Na,H-[Al]Beta-14 und Na,H-ZSM-5 mit ca. 3 Ma.-% Platin oder Iridium beladen, und das Verhalten dieser Katalysatoren bei der Umsetzung von cis-Decalin wurde untersucht.

An den platinbeladenen Zeolithen war die Gerüstisomerisierung die vorherrschende Reaktion bei geringen Umsätzen mit Ausnahme des mittelporigen Zeoliths ZSM-5: An diesem bildeten sich hauptsächlich C₉-Produkte. Mit steigendem Umsatz wurde ein Ring der Gerüstisomeren von Decalin geöffnet, und es bildeten sich ROPs, deren Selektivität dann ein Maximum durchlief. In einer Folgereaktion wurde der zweite Ring geöffnet. Es bildeten sich OCDs. Die besten Ergebnisse (bezogen auf die maximalen Ausbeuten an OCDs), zeigten die Träger Na,H-[Al]Beta-14, K,H-L und Na,H-EMC-2 mit maximalen OCD-Ausbeuten von 15, 17 bzw. 27 %.

Die mit Iridium beladenen Zeolithe zeigten im Allgemeinen ein anderes Verhalten: Bei geringen Umsätzen bildeten sich im gleichen Maße ROPs und sk-Isos. Die Selektivitäten beider Produktgruppen gingen im Gegensatz zu den Selektivitäten der OCDs, welche mit steigendem Umsatz durch ein Maximum liefen, mit steigendem Umsatz zurück. Eine Ausnahme stellte hier das Verhalten von 0.067Ir/H-SAPO-5 dar: Die vorherrschende Reaktion bei geringem Umsatz war die Gerüstisomerisierung des Decalins. Möglicherweise war der geringe Metallgehalt des Katalysators der Grund für dieses Verhalten. Auch im Falle der mit Iridium beladenen Zeolithe sind Na,H-[Al]Beta-14, K,H-L und Na,H-EMC-2 die vielversprechendsten Träger mit OCD-Ausbeuten von 34, 17 bzw. 27 %. Auch mit Ir/Na,H-Mordenit wurden mit 14 % bemerkenswert hohe Ausbeuten an OCDs erzielt.

Eine genaue Betrachtung der Verteilung der Kohlenstoffanzahl der Hydrocrackprodukte zeigte, dass im Falle der platinbeladenen Zeolithe die so genannte paring reaction auftrat, während an den mit Iridium beladenen Zeolithen die Bindungsspaltung hauptsächlich durch Hydrogenolyse ablief. Dies konnte aus den M-förmigen Verteilungskurven im Falle der paring reaction und den einer Hängematte ähnelnden Kurven im Falle der hydrogenolytischen Bindungsspaltung geschlossen werden. Dieser Befund kam nicht unerwartet, da Iridium eine sehr viel höhere hydrogenolytische Aktivität aufweist als Platin und zusätzlich Platin die Fähigkeit besitzt, Kohlenwasserstoffe zu isomerisieren.

Mit dem Ziel die Ausbeuten an OCDs weiter zu erhöhen, wurde die Stärke der Brønsted-Säurezentren der bis dahin attraktivsten Zeolithe variiert. Dies wurde auf drei verschiedene Weisen erreicht: (i) die isomorphe Substitution von Aluminium durch Bor in Zeolith Beta, (ii) die Variation des Stoffmengenverhältnisses von Silicium zu Aluminium (ebenfalls in Zeolith Beta) und (iii) die Variation der Natur der ladungskompensierenden Alkalikationen in den Zeolithen Beta, Mordenit und L. Die unterschiedlichen Stärken der Brønsted-Säurezentren wurden mittels FT-IR Spektroskopie und Pyridin als Sondenmolekül bestimmt.

Die angewandten Methoden ermöglichten es, Zeolith Beta mit sehr unterschiedlichen Säurestärken zu präparieren. Geordnet nach aufsteigender Säurestärke wurden folgende Beta-Zeolithe präpariert: $\text{Na}_x\text{H}[\text{B}]\text{Beta-18} \ll \text{Cs}_x\text{H}[\text{Al}]\text{Beta-8} < \text{Rb}_x\text{H}[\text{Al}]\text{Beta-8} < \text{K}_x\text{H}[\text{Al}]\text{Beta-8} < \text{Na}_x\text{H}[\text{Al}]\text{Beta-8} \approx \text{Cs}_x\text{H}[\text{Al}]\text{Beta-14} < \text{Rb}_x\text{H}[\text{Al}]\text{Beta-14} < \text{K}_x\text{H}[\text{Al}]\text{Beta-14} < \text{Na}_x\text{H}[\text{Al}]\text{Beta-14} < \text{Na}_x\text{H}[\text{Al}]\text{Beta-21} < \text{Li}_x\text{H}[\text{Al}]\text{Beta-14}$. Überraschenderweise hatte der Austausch mit Cäsium fast keinen Einfluss auf die Säurestärke bei Zeolith L und Mordenit. Es konnten auch kaum Unterschiede bei den Selektivitäten der platin- bzw. iridiumhaltigen Katalysatoren festgestellt werden, zudem hatten die verschiedenen Alkalikationen keinen Einfluss auf die C-Zahl-Verteilungskurven der Hydrocrackprodukte.

Im Gegensatz dazu konnte eine klare Tendenz bei den iridiumhaltigen Katalysatoren mit Beta-Struktur beobachtet werden: Mit abnehmender Stärke der Brønsted-Säurezentren stieg die Ausbeute an OCDs bis auf einen Wert von 44 % für $3.4\text{Ir}/\text{H}_{0.58}, \text{Cs}_{0.42}[\text{Al}]\text{Beta-14}$ an. Dies ist die höchste Ausbeute an offenkettigen Decanen, die bei der hydrierenden Ringöffnung von Decalin bislang erreicht wurde. Leider führte eine weitere Reduktion der Säurestärke nicht zu höheren Ausbeuten an OCDs. Der Grund hierfür ist die nötige Balance zwischen der Hydrogenolyseaktivität des Edelmetalls und der Isomerisierungsaktivität des Katalysators. Im Falle eines nur leicht sauren Trägers, wie z. B. $[\text{B}]\text{Beta}$, reicht die Stärke der Säurezentren nicht aus, die Sechsringe des Decalins zu Fünfringen zu isomerisieren, welche hydrogenolytisch wesentlich leichter geöffnet werden können. Wenn allerdings ein Träger mit einer hohen Säurestärke, wie z. B. $\text{Li}[\text{Al}]\text{Beta-14}$, eingesetzt wird, kommt es zur so genannten paring reaction, und zusätzlich werden stark verzweigte Isomere gebildet. Da die

Bindungsspaltung von sekundär-tertiären und tertiär-tertiären C-C Bindungen an Iridium sehr viel langsamer ist als die Spaltung zwischen zwei sekundären C-Atomen (bekannt als der selektive Mechanismus), ist die Öffnung der Ringe in stark verzweigten Isomeren langsamer als bei weniger stark verzweigten. Dies führt dazu, dass ein Katalysator die richtige Balance zwischen der Aktivität der Säure- und der Edelmetallzentren aufweisen muss, um hohe Ausbeuten an OCDs zu erzielen, wie es wahrscheinlich z. B. bei $3.4\text{Ir}/\text{H}_{0.58},\text{Cs}_{0.42}\text{-[Al]Beta-14}$ der Fall ist. Die Auftragung der maximalen Ausbeuten an OCDs gegen die maximal erzielten Ausbeuten an Gerüstisomeren der iridiumhaltigen Katalysatoren lieferte weitere Anhaltspunkte für diese Annahme. Eine klare Beziehung zwischen den beiden Werten konnte gefunden werden: Mit sinkenden Ausbeuten an Gerüstisomeren stiegen die Ausbeuten an OCDs, bis sie ein Maximum erreichten. Darüber hinaus scheint es einen direkten Zusammenhang zwischen den Ausbeuten an sk-Isos und der Stärke der Brønsted-Säurezentren zu geben: Je stärker die Säurezentren waren desto mehr Gerüstisomere wurden gebildet. Dieses Ergebnis unterstreicht abermals die Wichtigkeit der Balance zwischen der Aktivität der Säure- und Edelmetallzentren.

Leider wurde für die platinhaltigen Katalysatoren kein so klarer Trend gefunden. Die maximalen Ausbeuten an OCDs lagen zwischen 15 und 27 % für die Beta-Zeolithe, und sie hingen nicht von der Säurestärke des Trägers ab. Der Grund für dieses unvorhersehbare Verhalten liegt wahrscheinlich in der Fähigkeit des Platins selbst, Kohlenwasserstoffe zu isomerisieren: Da nun nicht mehr nur die Stärke der Säurezentren allein für die Isomerisierungsaktivität verantwortlich ist, verliert der Begriff „Balance zwischen den Aktivitäten beider Arten von Zentren“ seinen Sinn.

Um die Ausbeuten an OCDs weiter zu erhöhen, wurde die Konzentration des Edelmetalls auf dem bisher besten Träger ($\text{Cs}_x\text{H}_y\text{-[Al]Beta-14}$) variiert. Es wurden vier weitere iridiumhaltige Katalysatoren hergestellt mit 1, 2, 4 bzw. 5 Ma.-% Edelmetall. Dabei konnte die maximale Ausbeute an OCDs nicht weiter gesteigert werden, aber die Katalysatoren dieser Serie erfüllen mit maximalen Ausbeuten an OCDs zwischen 38 und 43 % in hervorragender Weise das Kriterium für HIPEROCS. Eine Ausnahme stellte $1.1\text{Ir}/\text{Cs}_{0.96},\text{H}_{0.04}\text{-[Al]Beta-14}$ dar, mit diesem Katalysator wurde nur eine maximale Ausbeute von 23 % erreicht. Es scheint so, als ob die hydrogenolytische Aktivität des Katalysators zu gering war, was zur Bildung von hoch verzweigten Decalin-Isomeren führte.

In einem letzten Experiment wurde der Wasserstoffdruck von dem Standardwert 5,2 MPa auf 8,0 MPa erhöht und einer der besten Katalysatoren für die Umsetzung von Decalin eingesetzt. Dies führte zu einer Steigerung der maximalen Ausbeute an OCDs von 43 % auf 47 %.

Es lässt sich zusammenfassen, dass durch systematische Variation der sauren Eigenschaften der Zeolithe und durch Nutzung des am besten geeigneten Edelmetalls mit optimaler Beladung bifunktionelle Katalysatoren erzeugt werden konnten, welche bei der Ringöffnung des Modellkohlenwasserstoffs Decalin die höchsten Ausbeuten an offenkettigen Decanen ermöglichen, die bisher bekannt sind.

2 Summary

The aim of this work was to investigate the influence of the nature of the noble metal, the structure of the zeolite catalysts and their acidic properties on the selective ring opening of cis-decalin. In addition, catalyst systems were to be identified which are able to achieve a yield of at least 25 % of open-chain decanes (OCDs) in the hydroconversion of cis-decalin. Such catalysts are referred to as HIgh-PERformance Ring-Opening Catalysts (HIPEROCs). In all investigated catalysts solely the Brønsted acid sites generated during the reduction of the noble metal were present, thus obtaining catalysts with relatively low concentrations of acid sites.

The first step was to identify the best suited noble metal for the selective ring opening of decalin. As already known from literature, iridium and platinum supported on faujasites are very promising catalysts for this reaction: Maximum yields of OCDs as high as 31 and 39 %, respectively, had been described. In this work ruthenium, rhenium, palladium and rhodium supported on the faujasite Na,H-Y were investigated. At low conversions ring-opening products (ROPs) were prevailing on Ru/Na,H-Y which were further ring-opened to open-chain decanes (OCDs). However, a maximum yield of only 5 % of OCDs was obtained. Most likely, the main reason for the low maximum yields of OCDs was the formation of large amounts of hydrocracked products with less than ten carbons atoms (C₉-) formed over the whole range of conversions. Moreover, in the case of the rhenium-containing catalyst, the amount of C₉- was even larger: Nearly 50 % of the converted decalin were transformed into products belonging to the C₉- group at low conversions, and the amount increased sharply with increasing conversions.

A totally different behavior was observed with the palladium-loaded zeolite: Nearly exclusively skeletal isomerization took place. At high conversions above 65 %, hydrocracking became the prevailing reaction. The best catalyst with respect to the formation of OCDs of this series was the rhodium-containing faujasite. Beside the formation of hydrocracked products at high conversions, nearly equal amounts of skeletal isomers of decalin (sk-Isos) and ROPs were formed at low conversions, but their yields decreased with increasing conversion. The results obtained with the different noble metals show that the nature of the noble metal can have a significant influence on the performance of bifunctional zeolite catalysts. Based on the results all subsequent experiments were conducted on catalysts containing either iridium or platinum.

In a second step, the influence of the zeolite structure on the attainable yields of OCDs and ROPs was investigated. Zeolites Na,H-mordenite, K,H-L, H-SAPO-5, Na,H-EMC-2, Na,H-[Al]Beta-14 and Na,H-ZSM-5 were loaded with about 3 wt.-% of platinum or iridium and tested in the hydroconversion of decalin. On the platinum-loaded zeolites, skeletal

isomerization was the prevailing reaction at low conversions with the exception of the medium-pore zeolite ZSM-5. There, the formation of C₉- products was prevailing. Upon increasing the conversion, the skeletal isomers were ring-opened to ROPs, and their selectivities passed through maxima. In a consecutive reaction the second ring was opened to form OCDs. The best performance was shown by the catalysts with the zeolite structures Na,H-[Al]Beta-14, K,H-L and Na,H-EMC-2 with maximum OCDs yields of 15, 17 and 27 %, respectively.

The iridium-containing counterparts showed, in general, a different behavior: At low conversions equal amounts of ROPs and sk-Isos were formed, and the selectivities of both product groups decreased with increasing conversions. By contrast, the selectivities of OCDs initially increased with increasing conversion and then passed through maxima. An exception was 0.067Ir/H-SAPO-5: The prevailing reaction at low conversion was the isomerization of decalin. The origin of this peculiarity is most likely the very low iridium loading of this catalyst, which stems from the very low ion-exchange capacity of the support. Again, zeolites Na,H-[Al]Beta-14, K,H-L and Na,H-EMC-2 produced the highest yields of OCDs, namely 34, 17 and 27 %, respectively. In addition, zeolite Na-mordenite reached a remarkable yield of OCDs amounting to 14 %.

A closer look at the carbon number distributions of the hydrocracked products revealed that the undesired paring reaction was prevailing on the platinum-loaded zeolites, whereas hydrogenolytic cracking seemed to be dominating on the iridium-loaded zeolites. This was deduced from the M-shape of the distribution curves in the case of the platinum catalysts and hammock-shaped curves obtained on the iridium catalysts. This finding was not unexpected, since it is known that iridium possesses a much higher hydrogenolytic activity than platinum and, in addition, platinum is capable to isomerize hydrocarbons itself, *i.e.*, without the presence of acidic sites.

For a further enhancement of the yields of open-chain decanes, the strength of the Brønsted acid sites of the most promising zeolites was varied. This was done in three different ways, namely (i) the isomorphous substitution of aluminum by boron in zeolite Beta, (ii) the variation of the molar ratio $n_{\text{Si}} / n_{\text{Al}}$, again in zeolite Beta, and (iii) the exchange of the charge-compensating cations by different alkali metals in zeolites Beta, mordenite and L. The strengths of the Brønsted acid sites were determined by FT-IR spectroscopy and pyridine as a probe molecule.

The applied methods allowed the preparation of Beta zeolites with a broad variety of acid strengths. Ordered by their acid strengths, the following Beta zeolites were prepared: Na,H-[B]Beta-18 << Cs,H-[Al]Beta-8 < Rb,H-[Al]Beta-8 < K,H-[Al]Beta-8 < Na,H-[Al]Beta-8 ≈ Cs,H-[Al]Beta-14 < Rb,H-[Al]Beta-14 < K,H-[Al]Beta-14 <

Na,H-[Al]Beta-14 < Na,H-[Al]Beta-21 < Li,H-[Al]Beta-14. Surprisingly, the cesium exchange into zeolites mordenite and L seems to have no influence on their acid strengths. This finding was also reflected in the selectivities obtained in the hydroconversion of decalin with the platinum and the iridium catalysts. Only marginal differences were observed. Moreover, the carbon number distributions of the hydrocracked products were nearly identical for the alkali metal-exchanged mordenite- and L-supported catalysts.

A clear trend was observed for the iridium-containing Beta-supported catalysts: With decreasing acid strength the maximum yield of OCDs increased to 44 % for 3.4Ir/H_{0.58},Cs_{0.42}-[Al]Beta-14, which is the highest value reported so far. Unfortunately, a further reduction of the acid strengths led to decreasing yields of OCDs. The reason for this behavior seems to be the balance between the hydrogenolytic activity of the noble metal and the isomerization activity of the acid component of the catalyst: In the case of a very weakly acidic support, such as Na,H-[B]Beta, the strength of the acid sites is no longer sufficient for isomerizing the two six-membered-rings of decalin to five-membered-rings, which are much easier to open by hydrogenolysis. On the other hand, a support which possesses Brønsted acid sites of a high strength, like Li,H-[Al]Beta-14, promotes the occurrence of the paring reaction and, in addition, leads to the formation of highly branched decalin isomers. Since the rupture of secondary-tertiary and tertiary-tertiary C-C bonds is much slower on iridium than the rupture of secondary-secondary C-C bonds (known as the selective mechanism), the ring opening of highly branched isomers is slower compared to that of mildly branched ones. Thus a catalyst must possess the right balance between the activity of the acid and noble metal sites, which seems to be the case for 3.4Ir/H_{0.58},Cs_{0.42}-[Al]Beta-14. Consistent with this assumption was a plot of the maximum yield of OCDs *versus* the maximum yield of sk-Isos obtained on various iridium-containing Beta zeolites. A clear relationship between these two quantities was found: With decreasing yields of sk-Isos the yields of OCDs increased till a maximum was reached. Moreover, a direct relationship between the yield of sk-Isos and the strength of the Brønsted acid sites could not be observed. This additionally underlines the importance of the right balance between the activity of the acid and noble metal sites.

Unfortunately, the platinum-loaded catalysts did not show such clear trends. The maximum yields of OCDs obtained on the different Beta zeolites varied between 15 and 27 % and did not correlate with the strength of the acid sites. Presumably, the reason for this unpredictable behavior lies in the isomerization ability of platinum: Since the acid sites are not solely responsible for the skeletal isomerization of decalin, the mechanism is more complex, and it is much harder to find the right balance between the isomerization and the hydrogenolysis activity.

The last modification applied to enhance the yields of OCDs was the variation of the noble metal content of the best catalyst, *viz.* 3.4Ir/H_{0.58},Cs_{0.42}-[Al]Beta-14. Four additional catalysts

with iridium contents of roughly 1, 2, 4 or 5 wt.-% were prepared. All but one (1.1Ir/Cs_{0.96}H_{0.04}-[Al]Beta-14, $Y_{\text{OCDs, max.}} = 23\%$) of these catalysts turned out to be excellent HIPEROs in the decalin hydroconversion enabling maximal yields of OCDs between 38 and 44 %, but the hopes to find a catalyst leading to $Y_{\text{OCDs, max.}} > 44\%$ were not fulfilled. The relatively poor performance of the catalyst with 1.1 wt.-% of iridium can be rationalized in terms of its too low hydrogenolysis activity enabling the formation of highly branched decalin isomers the rings of which open very sluggishly on iridium.

In a last exploratory experiment, decalin was hydroconverted on one of the best catalysts, *viz.* 4.0Ir/Cs_{0.53}H_{0.47}-[Al]Beta-14 under standard reaction conditions except for the hydrogen pressure which was increased from 5.2 to 8.0 MPa. This brought about a maximal yield of OCDs of 47 %, the best value ever achieved in the hydroconversion of decalin.

Summing up, this work has demonstrated that zeolite Beta is an excellently suited starting material for high-performance catalysts for the hydrodecyclization of multi-ring naphthenes derived from polynuclear aromatic hydrocarbons. Key properties that have to be carefully optimized are the concentration and strength of the Brønsted acid sites, the nature of the noble metal, and its loading. Also vital is a good balance of the isomerization and the hydrogenolysis activities of the bifunctional catalysts.

3 Introduction and Objectives

Monocyclic aromatic hydrocarbons in a pure form are important base chemicals, *e.g.* for the manufacture of polymers. However, polycyclic aromatic hydrocarbons are undesired. In diesel fuel, for example, polycyclic aromatics may create problems due to their poor ignition characteristics (low cetane numbers), their propensity of soot formation, their poor cold-flow properties and their low hydrogen content which inevitably brings about relatively high concentrations of carbon dioxide in the off-gas. The current EU legislation limits the content of polycyclic aromatics in diesel fuels to 8 wt.-% [1], and a more far-reaching reduction is under discussion. The corresponding ring-opened products, in particular alkanes, possess much better characteristics, *e.g.* much higher cetane numbers [2].

There is a general agreement that, in order to achieve the ring-opening reaction, the aromatic rings must first be hydrogenated to the corresponding multi-ring naphthenes (see Figure 3.1). This ring hydrogenation is generally considered to be state-of-the-art catalysis. By contrast, good catalysts for the consecutive selective ring-opening reaction are lacking.

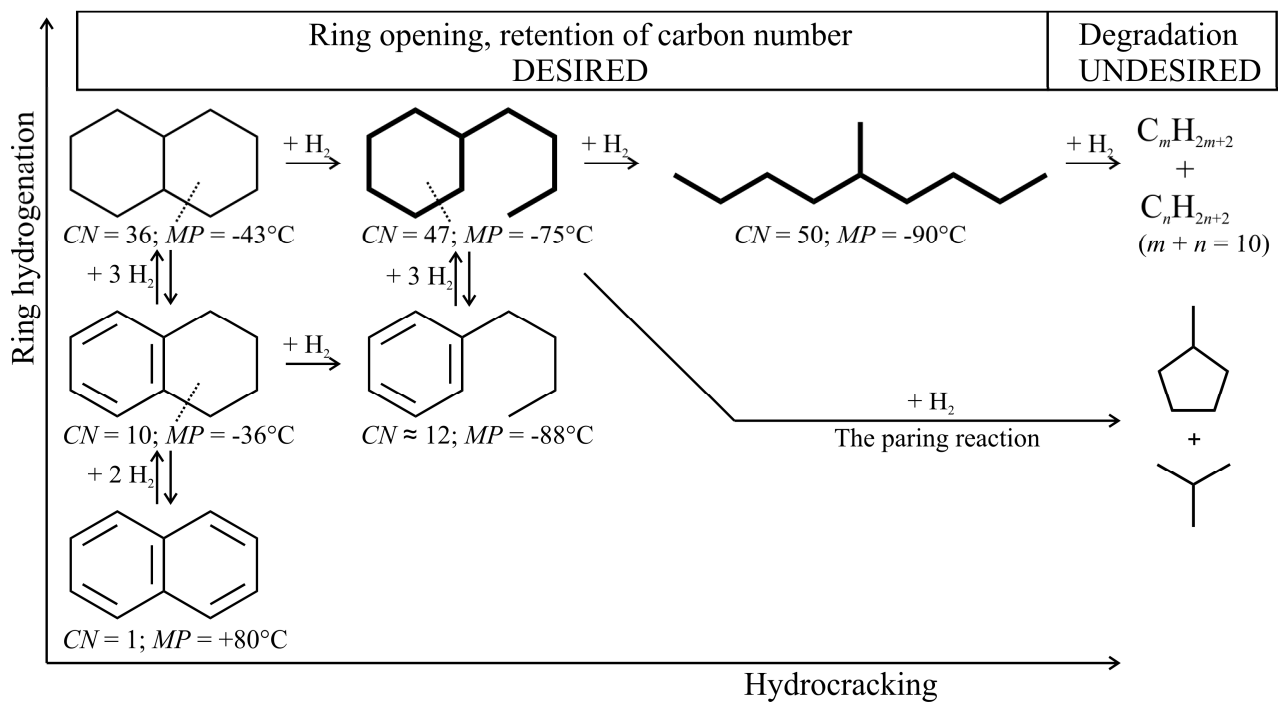


Figure 3.1: Idealized reaction network for ring opening of a multi-ring aromatic hydrocarbon into alkanes, after Ref. [2]. Available cetane numbers (CN) and melting points (MP) of the components are also indicated.

The smallest polycyclic aromatic hydrocarbon is naphthalene which is built of two condensed six-membered rings. With a cetane number of 1 and a melting point of 80 °C it is highly undesired in diesel fuels. However, the hydrogenation of this polycyclic aromatic to the corresponding naphthene, *viz.* decalin, leads to an enhancement of the cetane number to 36, and the melting point decreases to -43 °C. Even better values are obtained upon ring-opening: Butylcyclohexane possesses a cetane number of 47 and a melting point of only -75 °C, and the open-chain decane 5-methylnonane has a cetane number of 50 and a melting point of -90 °C. Although n-decane has a higher cetane number ($CN = 77$), the melting point is too high for the use in diesel fuels, with only -30 °C. Thus, the best suited compounds for diesel fuel would be mildly branched decanes. To achieve high yields of these compounds, one has to selectively open the rings of the naphthene while avoiding the loss of carbon atoms *via* excessive hydrocracking or the paring reaction.

The objective of this work was to investigate the selective ring opening of cis-decalin and to identify catalysts which are capable to achieve high yields of open-chain decanes (OCDs) while avoiding a loss of carbon atoms. To achieve these aims different noble metals supported on various 10- and 12-membered ring zeolites were investigated in the hydroconversion of cis-decalin in a catalytic high-pressure flow-type apparatus under a hydrogen atmosphere. In addition, the influence of the strength of the Brønsted acid sites of the support on the selective ring opening was investigated. To obtain supports with different acid strengths, the n_{Si} / n_{Al} ratio of the supports and the nature of the charge-compensating alkali cation, respectively, were varied. Moreover, aluminum was isomorphously substituted by boron.

4 Literature Review

4.1 Structures and Pore Architectures of Zeolites

“A zeolite mineral is a crystalline substance with a structure characterized by a framework of linked tetrahedra, each consisting of four O atoms surrounding a cation. This framework contains open cavities in the form of channels and cages. These are usually occupied by H₂O molecules and extra-framework cations that are commonly exchangeable. The channels are large enough to allow the passage of guest species. In the hydrated phases, dehydration occurs at temperatures mostly below about 400 °C and is largely reversible. The framework may be interrupted by (OH, F) groups; these occupy a tetrahedron apex that is not shared with adjacent tetrahedra.”

This is the definition of a zeolite given by the Subcommittee on Zeolites of the International Mineralogical Association in the year 1997 [3]. Today, the structure commission of the International Zeolite Association (IZA) is responsible for the approval of new zeolite structures. Until now, 201 different structures meet the definition of a zeolite [4]. A unique Framework Type Code (FTC) which consists of three letters is assigned to all of these structures by the IZA.

A framework type can consist of zeolites with different chemical compositions: In general the tetrahedrally coordinated atoms (T-atoms) in a zeolite are silicon- and aluminum cations. Nevertheless, there are also framework types, like MFI [4] which can be build from trivalent, tetravalent or even pentavalent cations like boron, germanium or phosphorus. Due to the incorporation of trivalent cations, a negative lattice charge is generated which is compensated by extra-framework cations. In the case of protons as charge-compensating cations, Brønsted acid sites are generated (see page 19). If pentavalent cations, like phosphorus, are incorporated into the zeolite framework, positive charges are generated which are compensated by an equal amount of trivalent cations. This is the case, for example, in aluminophosphates (ALPOs) and silicoaluminophosphates (SAPOs).

In general, the tetrahedra are linked entirely randomly, however, a restriction is described by Löwenstein's rule [5]: The linkage of two tetrahedra with aluminum on tetrahedral positions is forbidden. This results in a minimum molar ratio $n_{\text{Si}} / n_{\text{Al}} = 1$ of the zeolite framework.

In this work, eight zeolites with seven different structure types were used: Zeolite SAPO-5 (AFI), zeolite [Al]Beta and [B]Beta (*BEA), zeolite EMC-2 (EMT), zeolite Y (FAU), zeolite L (LTL), zeolite ZSM-5 (MFI) and zeolite mordenite (MOR). With the exception of zeolite ZSM-5, all of these zeolites possess at least one 12-membered ring (12-MR) channel. In the following, the zeolite structures will be discussed briefly.

Zeolite SAPO-5 (AFI)

Zeolite SAPO-5 is the only silicoaluminophosphate (SAPO) used in this work. It possesses a one-dimensional pore system, consisting of a linear 12-MR channel. Depicted in Figure 4.1 are the structure of the zeolite viewed along [001] (left) and a schematic drawing of the 12-MR channel (right). The corners of the structure represent T-atoms (in this case P, Al or Si) whereas the connecting lines represent T-O-T bonds. The channels have an inner diameter of 0.73 nm.

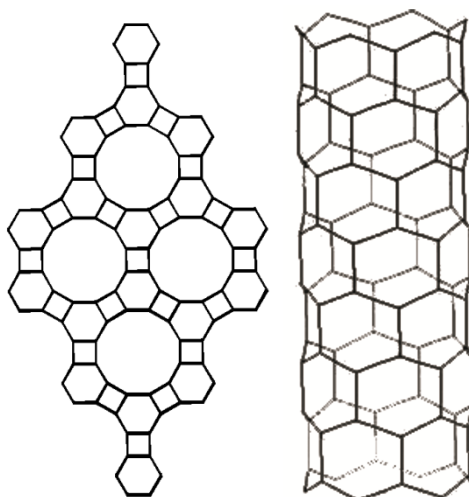


Figure 4.1: Structure of zeolite SAPO-5 (AFI) viewed along [001] (left) and the 12-MR channel viewed normal to [001] (right). After Ref. [4].

In contrast to aluminophosphate (ALPO) frameworks, SAPO frameworks can be Brønsted acidic: In general, ALPOs possess equal amounts of negatively charged trivalent aluminum and positively charged pentavalent phosphorus. If however, silicon is introduced into the ALPO framework this happens *via* two substitution mechanisms [6]: (i) one P^{5+} is substituted by one Si^{4+} or (ii) a pair of one Al^{3+} and one P^{5+} is substituted by two Si^{4+} . A substitution of one Al^{3+} by one Si^{4+} is energetically very unfavorable due to the formation of Si-O-P bridges [7]. Only *via* the first substitution mechanism, a negative lattice charge, which can be compensated by protons, is generated. The local structure of these Brønsted acid sites is similar to those of aluminosilicates, constituted by Si-O(H)-Al units (see Section 4.2, page 19). However, the first coordination sphere of the aluminum can consist of silicon or phosphorus in SAPO frameworks, whereas only silicon can be present in aluminosilicates. In addition, areas, where solely silicon-containing tetrahedra are present in the framework, so-called silicon islands, can be formed due to the energetically unfavorable Si-O-P bridges. All this results in acidic properties that are more tunable than in zeolites. However, this requires a controlled incorporation of silicon into the framework [6].

*Zeolite Beta (*BEA)*

The main part of the catalysts in this work possesses a *BEA framework type. The structure of this zeolite is peculiar since it is one of three polymorphic zeolite structures known so far. These framework types are marked by an asterisk in front of the FTC. Depicted in Figure 4.2 are the three framework structures that result from different kinds of stacking of the building layers which are present in *BEA. While the structure of polymorph C has its own FTC, namely BEC (Figure 4.2c), the intergrowth of polymorph A (Figure 4.2a) and B (Figure 4.2b) form the framework type *BEA. In the following only the structure of *BEA will be discussed.

Both polymorph A and B have a 3-dimensional pore systems consisting of three 12-MR channels which are perpendicular to each other. All three channels are interconnected. Two of these channels are linear and one is sinusoidal. The structure of polymorph A viewed along [010] is depicted in Figure 4.3. Marked with the arrows are the directions of the additional channels: From the left to the right the second linear channel and from top to down the sinusoidal channel. The dimensions of the linear and the sinusoidal channels are 0.76 x 0.66 nm and 0.56 x 0.56 nm, respectively.

In this work zeolites [Al]Beta with molar ratios $n_{\text{Si}} / n_{\text{Al}}$ of 8, 14 and 21, and additionally the borosilicate [B]Beta with a molar ratio $n_{\text{Si}} / n_{\text{B}} = 18$ have been investigated. The variation of the silicon to aluminum molar ratio, as well as the isomorphous substitution of aluminum by boron impacts the strength of the Brønsted acid sites of the zeolite strongly. A further variation of the strength was achieved by using different alkali metals as charge-compensating cations. The reasons for the different strengths of the Brønsted acid sites due to the variation of the charge-compensating cation and the molar ratios of silicon to aluminum or boron will be discussed on page 21 and 22.

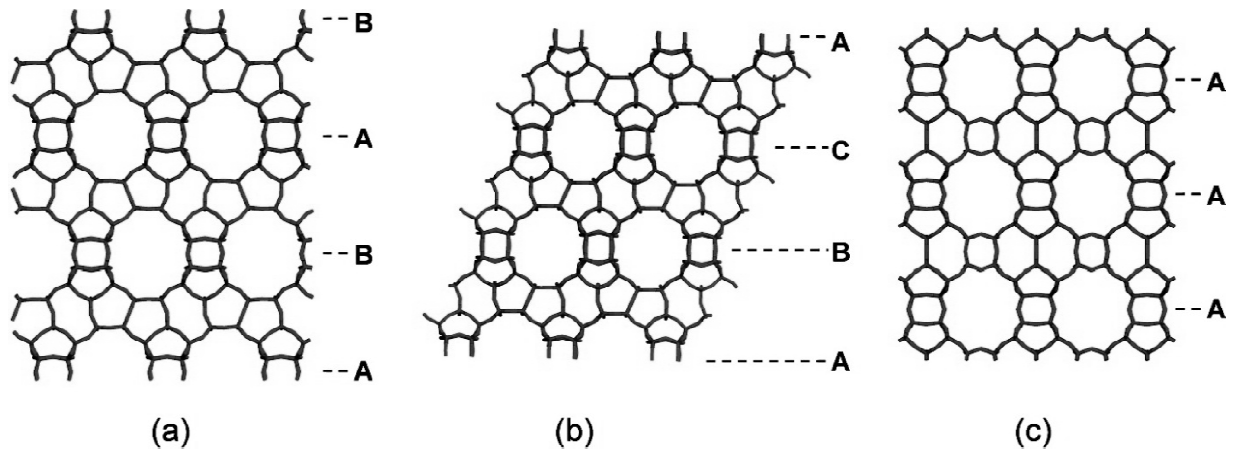


Figure 4.2: Framework structures of (a) polymorph A, (b) polymorph B and (c) polymorph C of zeolite Beta viewed along [010]. In addition, the different stackings of the 12-MR pores as (a) ABAB..., (b) ABCA... and (c) AA... are shown [8].

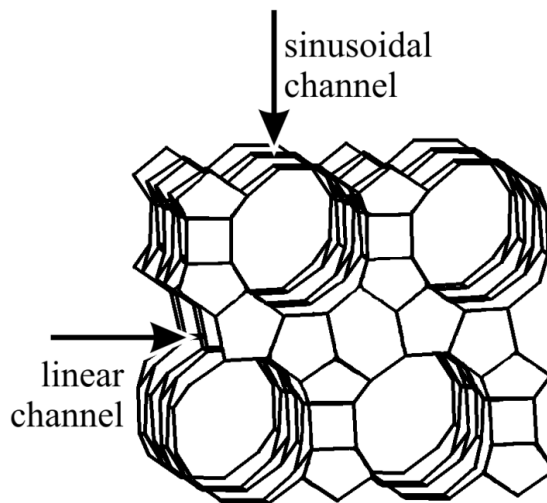


Figure 4.3: Structure of zeolite Beta (polymorph A) viewed along [010]. Marked with the arrows are the directions of the two other channel systems. After Ref. [4].

Zeolites EMC-2 (EMT) and Y (FAU)

Since the structures of EMT and FAU are very similar they will be discussed together. Both structures are built from sodalite cages which are connected by hexagonal prisms (see Figure 4.4). The only differences are the unit cells of FAU and EMT: That of FAU is cubic, whereas the unit cell of EMT is hexagonal. However, both framework types possess relatively large supercages with a diameter of 1.3 nm which are interconnected by 12-MR windows. Zeolite Y (FAU) contains four tetragonally arranged windows, whereas EMC-2 (EMT) possesses five windows which are arranged like a trigonal dipyramide (see Figure 4.4). Thereby, the

two windows that are located opposite to each other form a spacious linear channel. The other three windows of the supercage are arranged perpendicular to this channel in angles of 120° and are of elliptical shape. The diameters of the 12-MR windows are 0.73×0.73 nm and 0.75×0.65 nm, respectively. In zeolite Y the diameters of the windows assume values of 0.74×0.74 nm.

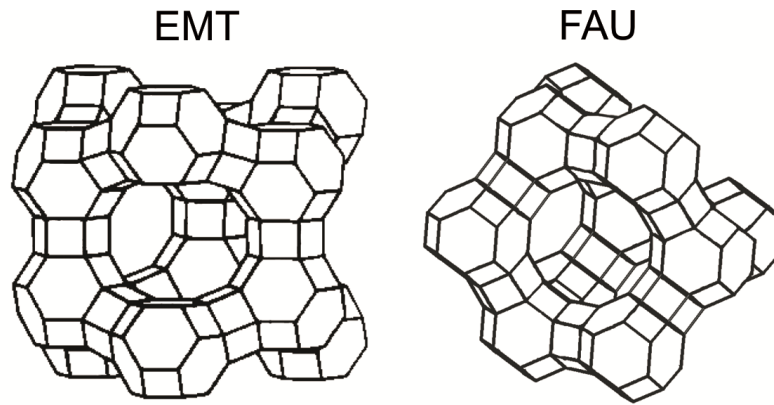


Figure 4.4: Structures of zeolite EMC-2 (EMT) (left) and zeolite Y (FAU) (right) viewed along [111]. After Ref. [4].

Zeolite L (LTL)

Zeolite L contains a one-dimensional, linear 12-MR pore system (with a diameter of 0.71 nm) which is interconnected by a perpendicular 8-MR channel system. Moreover, a narrow 8-MR channel system runs in parallel to the 12-MR main channels, separated only by 8-MR windows (see Figure 4.5, left). The main channels slightly expand at the intersections with the 8-MR channels (see Figure 4.5, right).

There are four different cation sites known in this zeolite [9, 10]: Three of them are not located in the 12-MR channel and are closely surrounded by framework O-atoms, which makes them practically not exchangeable. However, the fourth cation position is located in the cage of the 12-MR channel close to the channel wall. This specific feature makes it impossible to exchange all potassium cations incorporated in the zeolite during the synthesis by other cations.

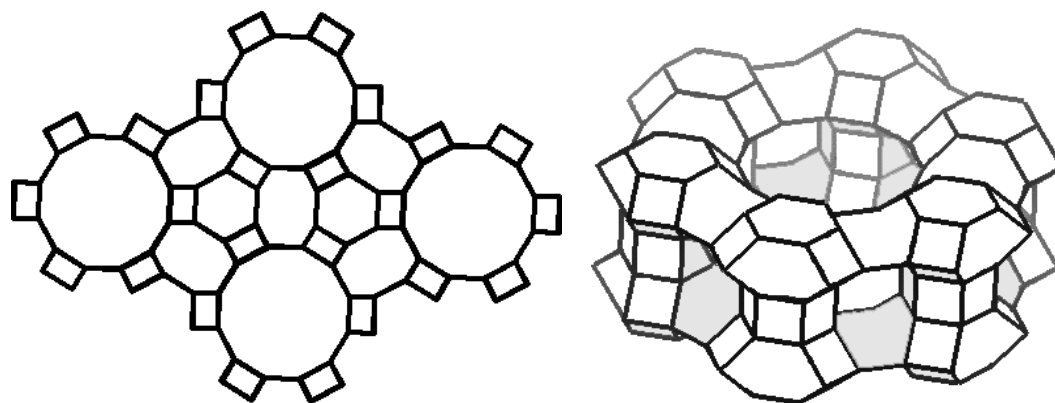


Figure 4.5: Structure of zeolite L (LTL) viewed along [001] (left) and the 12-MR channel viewed nearly normal to [001] (right). After Ref. [4].

Zeolite ZSM-5 (MFI)

Zeolite ZSM-5 is the only zeolite examined in this work which does not possess a 12-MR channel system. It rather has a 3-dimensional 10-MR channel system consisting of linear channels running along [010] with a dimension of 0.53 x 0.56 nm and intersecting sinusoidal channels running along [100] with a dimension of 0.51 x 0.55 nm (see Figure 4.6).

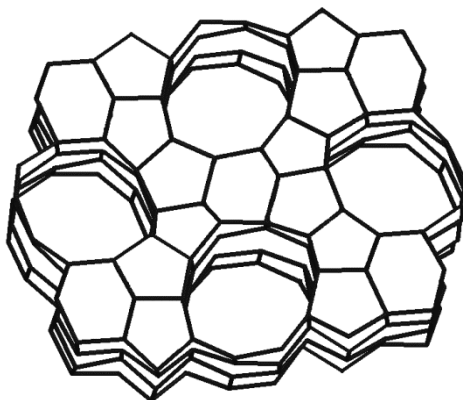


Figure 4.6: Structure of zeolite ZSM-5 (MFI) viewed along [010]. After Ref. [4].

Zeolite Mordenite (MOR)

Zeolite mordenite possesses a linear, one-dimensional 12-MR channel system which is interconnected by a sinusoidal 8-MR channel system which runs perpendicular to the 12-MR channels. Moreover, similar to zeolite L, a linear, elliptical 8-MR channel system runs in parallel to the 12-MR channels (see Figure 4.7). However, the only connection between these 8-MR channels and the 12-MR channels is the sinusoidal 8-MR channel system. The 12-MR

channels have dimensions of 0.70 x 0.65 nm whereas the linear 8-MR channels possess dimensions of only 0.57 x 0.25 nm.

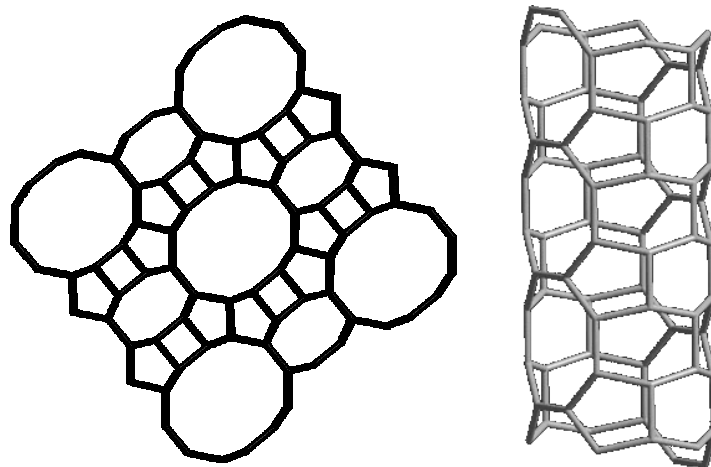


Figure 4.7: Structure of zeolite mordenite (MOR) viewed along [001] (left) and the 12-MR channel viewed normal to [001] (right). After Ref. [4].

Comparison of the Zeolites

Table 4.1 summarizes the different zeolites and their respective pore systems. In addition, the Spaciousness Indices (*SI*) of the zeolites are given [11]. This index is defined as the yield of iso-butane divided by the yield of n-butane in the hydrocracking of butylcyclohexane on bifunctional zeolites. It is used as a measure for the space inside the zeolite pores and increases with increasing pore size. The Spaciousness Index is particularly valuable for ranking 12-MR zeolites for which it covers a wide range from *ca.* 3 to more than 20. By contrast, all 10-MR zeolites have essentially the same Spaciousness Index around 1. From Table 4.1 one can see that a wide variety of zeolites will be investigated: from zeolites with very narrow pores, like ZSM-5 (*SI* = 1) over 12-MR zeolites with relatively small pores, *viz.* SAPO-5 (*SI* = 4) and mordenite (*SI* = 7) to large pore zeolites like Beta (*SI* = 18) and Y (*SI* = 21). In addition, zeolites with one-dimensional (SAPO-5, L, mordenite) as well as three-dimensional pore systems (Beta, Y, EMC-2, ZSM-5) are represented.

Table 4.1: Pore systems and Spaciousness Indices (SI) of different zeolites.

Zeolite	FTC	Pore Systems	SI [12]
SAPO-5	AFI	12-MR (1-dim)	4
Beta	*BEA	12-MR (3-dim)	18
Y	EMC	12-MR (3-dim)	21
EMC-2	EMT	12-MR (3-dim)	21
L	LTL	12-MR (1-dim); 8-MR (1-dim)	16
ZSM-5	MFI	10-MR (3-dim)	1
Mordenite	MOR	12-MR (1-dim); 8-MR (2-dim)	7

4.2 Acid Sites in Zeolites

An important feature of zeolites is their Lewis and Brønsted acidity. Whereas the chemical nature of the Brønsted acid sites is known (they are formed by bridging hydroxyl groups which act as proton donors, see Figure 4.8), the nature of the Lewis acid sites is up to now a matter of research. They can be attributed to octahedrally or tetrahedrally coordinated extra-framework aluminum (EFAL) species as well as to tri-coordinated framework aluminum [13, 14]. Kühl [15] concluded from X-ray diffractometry investigations that $[AlO]^+$ species removed from the framework act as so-called “true” Lewis acid sites. However, in the following only the Brønsted acid sites will be discussed since there is experimental evidence that the catalytic activity stems from Brønsted rather than Lewis acidic sites [16 - 18].

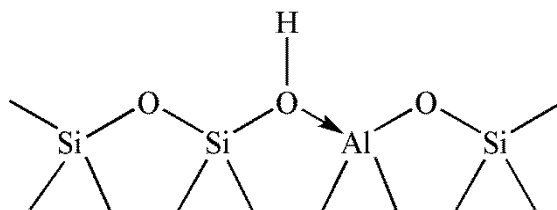
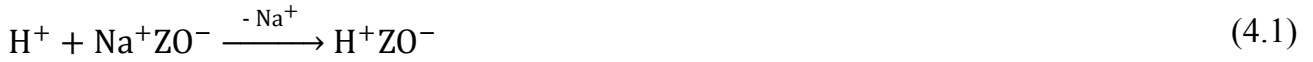


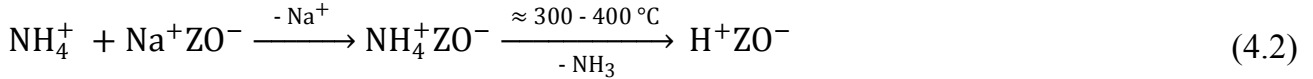
Figure 4.8: Local structure of a Brønsted acid site in a zeolite.

Generation of Brønsted Acid Sites

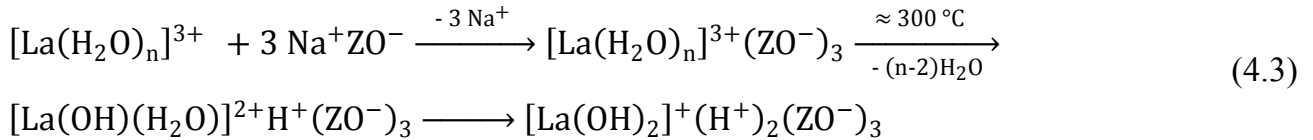
There are four methods known for the generation of Brønsted acid sites in zeolites, all of them are post-synthesis modifications. A straightforward method is the direct ion exchange of the zeolite with a mineral acid to generate the Brønsted acid sites (Eq. (4.1)). However, this is also a very unfavorable method since the exposure of the zeolite to the relatively strong mineral acid can lead to the extraction of aluminum from the framework. This in turn can lead to a collapse of the zeolite framework, especially in case of zeolites with a low n_{Si} / n_{Al} ratio [19].



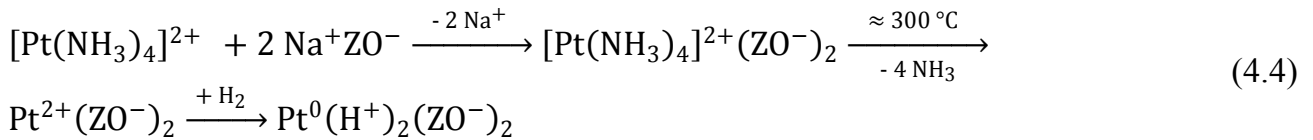
A very frequently applied method to generate Brønsted acid sites is the ion exchange with ammonium salts in aqueous solution followed by thermal decomposition of the ammonium ions (Eq. (4.2)). The salient feature of this method is that the concentration of the generated Brønsted acid sites can be adjusted easily, since it is directly related to the amount of ammonium salt used for the ion exchange.



The third method to generate Brønsted acid sites is the ion exchange with multivalent cations, like Mg^{2+} or La^{3+} followed by thermal dehydration of the cationic complex (Eq. (4.3)). This mechanism of generating Brønsted acid sites is called Hirschler-Plank mechanism [20, 21]. The removal of most of the water molecules from the cationic complexes leads to strong electrostatic fields inside the zeolite pores. Due to these strong electrostatic fields the residual water molecules dissociate into a hydroxyl proton bound to a bridging oxygen atom and an OH group bound to the extra-framework cation. It can be seen from Eq. (4.3) that a maximum of two acidic sites can be generated with one trivalent cation.



In this work the only method to generate Brønsted acid sites is the ion exchange with a metal nobler than hydrogen:



After thermal decomposition of the metal complex, the noble metal ion is reduced with molecular hydrogen leading unavoidably to Brønsted acid sites. The concentration of acid sites resulting from this reaction depends on the concentration and initial charge of the noble metal ion and is in general relatively low.

Variation of Brønsted Acid Site Strength

The strength of the Brønsted acid sites does not depend on the method applied to generate them. It rather depends on the chemical composition of the zeolite, *e.g.* the nature of the T-atoms, the molar ratio of the different T-atoms and the nature and concentration of residual charge-compensating cations. In addition, the framework type of the zeolite also influences the strength of the Brønsted acid sites [22].

The main factor influencing the strength of the Brønsted acid sites is the chemical composition of the zeolite. One approach to describe these influences is Sanderson's theory of intermediate electronegativities [23, 24]:

$$S_{\text{int}} = \left(\prod_i S_i^{\gamma_i} \right)^{\frac{1}{\sum \gamma_i}} \quad (4.5)$$

Were S_{int} , S_i , and γ_i denote, respectively, Sanderson's intermediate electronegativity, the electronegativity of the element i , and the stoichiometric coefficient of the element i in the zeolite unit cell. The basic idea of this theory is the equalization of the electronegativities of the different atoms in a zeolite framework leading to an intermediate electronegativity. Rabl *et al.* [25] studied the influence of the nature of the charge-compensating cation on the hydrodeacyclization of decalin. They observed with M,H-Y zeolites ($M = \text{Li, Na, K, Rb or Cs}$) that the strength of Brønsted acid sites decreases in the following order: $\text{Li,H-Y} > \text{Na,H-Y} > \text{K,H-Y} > \text{Rb,H-Y} > \text{Cs,H-Y}$. This order was also found earlier by other groups [26, 27] and is in-line with Sanderson's intermediate electronegativity approach.

However, a prediction of the acid strength of isomorphously substituted silicates does not seem to be possible with this approach. The calculated values of S_{int} of isomorphously substituted aluminosilicates increase in the following order $\text{Fe} < \text{Al} < \text{B} < \text{Ga}$ [28], which means an increase of the acid strength. Nevertheless, experimental data revealed a different order: $\text{B} < \text{Fe} < \text{Ga} < \text{Al}$ [29 - 31]. These discrepancies may be due to structural changes of the zeolite unit cell caused by the different ionic radii of the atoms, bond lengths and angles, which also influence the strength of the Brønsted acid sites. However, with quantum mechanical calculations it is possible to confirm the experimentally derived order [32, 33].

In addition, Sanderson's intermediate electronegativity concept does not explain the different strengths of the acid sites in a given zeolite. To account for the inhomogeneous acid strength distribution, a more detailed consideration is needed, namely the next-nearest neighbors (NNN) approach [34].

If Löwenstein's rule [5] is obeyed the first coordination sphere of the trivalent atom close to an OH group consists of four silicon atoms and nine T-atoms in the second coordination sphere, the so-called next-nearest neighbors (NNN). For a molar ratio $n_{\text{Si}} / n_{\text{Al}} = 1$ or $n_{\text{Si}} / n_{\text{B}} = 1$, all NNN T-atoms would be Al or B. With increasing molar ratio, more and more NNN aluminum or boron atoms will be replaced by silicon atoms, until the number of NNN aluminum or boron atoms is zero and isolated hydroxyl groups result. These isolated hydroxyl groups possess the highest Brønsted acid strength and with higher amounts of aluminum or boron as NNN T-atoms the strength decreases [34].

Determination of the Concentration and Strength of Brønsted Acid Sites

In most publications dealing with the acid strength of zeolites, FT-IR spectroscopic techniques are used for its characterization, but there are several other methods which can be used for that purpose, like MAS NMR spectroscopy, temperature-programmed desorption (TPD) of probe molecules and microcalorimetry. All of these techniques utilize, in one way or the other, probe molecules for the determination of the strength of the Brønsted acid sites.

One of the first tasks to be achieved is the choice of the best-suited probe molecule. Knözinger [35] reviewed infrared spectroscopy as a technique for characterizing zeolites and formulated nine criteria for the choice of the probe molecule:

- Criterion I: The probe molecule should discriminate between protic (Brønsted) and aprotic (Lewis) acid sites.
- Criterion II: The probe molecule should interact selectively either with basic or acidic sites.
- Criterion III: Frequency shifts induced by the interaction of the probe molecule and the acidic / basic sites should be larger than the bandwidth of the normal vibration.
- Criterion IV: The extinction coefficients of the vibration modes should be high, so that the detection sensitivity is high.
- Criterion V: The extinction coefficients for the characteristic vibrational modes should be experimentally available.
- Criterion VI: The probe molecule should have the appropriate acid or base strength to induce the optimal interaction.

Criterion VII: The probe molecule should interact specifically with sites of different acid or basic strength.

Criterion VIII: The probe molecule should have the appropriate size to interact with the surface sites which are to be measured.

Criterion IX: The reactivity of the probe molecule should be, at the applied measurement conditions, as low as possible to avoid surface transformations.

In general, in a real experiment not all of these criteria can be fulfilled, but one should try to fulfill as many as possible. The most commonly used probe molecules for the determination of the acid strength and concentration of acid sites are pyridine and ammonia. One of these two probe molecules is used in nearly every publication dealing with the determination of the acid site strength of zeolites.

There are three different interactions which can occur between the acidic surface of a zeolite and a basic probe molecule:



Equation (4.6) illustrates the interaction between the Brønsted acidic zeolite surface OH_s and the basic probe molecule B *via* hydrogen bonding. Equation (4.7) represents the proton transfer which can occur if the hydroxyl group has a sufficient acid strength. The third equation (4.8) illustrates the interaction of a Lewis acid site L with the basic probe molecule which leads to a Lewis acid-base adduct. These three different interactions can be easily studied by spectroscopic methods. However, the differentiation between Brønsted and Lewis acid sites with sorption methods must happen through the probe molecule. With IR spectroscopy the interaction of the hydrogen bonded base B and the hydroxyl group can be studied by the perturbation of the O-H bond [36]. Proton transfer (Eq. (4.7)) can either be studied by discrimination of the parent base B and the protonated base H^+B or by H-bonding of the H^+B species to the surface base O_s^- . The interaction of the Lewis acid site on the surface with the probe molecule can only be studied by the perturbation of the vibration modes of the probe molecule.

In the following the determination of the Brønsted acid site strength and concentration only *via* FT-IR spectroscopy will be discussed in more depth since it was the only method applied in this work. In general two different FT-IR techniques can be used for the study of acidic sites, namely diffuse reflection and transmission IR spectroscopy. For the transmission technique a thin wafer of the zeolite is required. This wafer should be self-supporting, *i.e.*

pressed without KBr which is, in some cases used to dilute and stabilize the sample. The absence of KBr is important because of the interactions which could occur between the probe molecule and KBr. The diffuse reflectance technique used to play an important role in UV-visible spectroscopy of zeolites. Since the 1980s DRIFT (diffuse reflectance IR Fourier transform) spectroscopy is also used in the near IR region for zeolites [37] where transmission spectroscopy essentially fails due to the severe scattering of the zeolite sample. These two techniques have been discussed in detail by Karge *et al.* [38] and will not be discussed more deeply here.

The different interactions of pyridine with acid sites are given by the reaction equations (4.6), (4.7) and (4.8). All three interactions can be easily distinguished by infrared spectroscopy [39, 40]. In general, only the ring vibration modes 8a and 19b (Figure 4.9) are used for the study of the acid strength, because they respond most sensitively to the interaction of the nitrogen lone-pair electrons.

In Table 4.2 the infrared bands of adsorbed pyridine are given. In general, only the bands at 1400 to 1460 cm^{-1} for the Lewis acid-base adduct and 1540 cm^{-1} for the pyridinium ion are taken into account for the determination of the acid site concentration, due to the overlap of some of the bands.

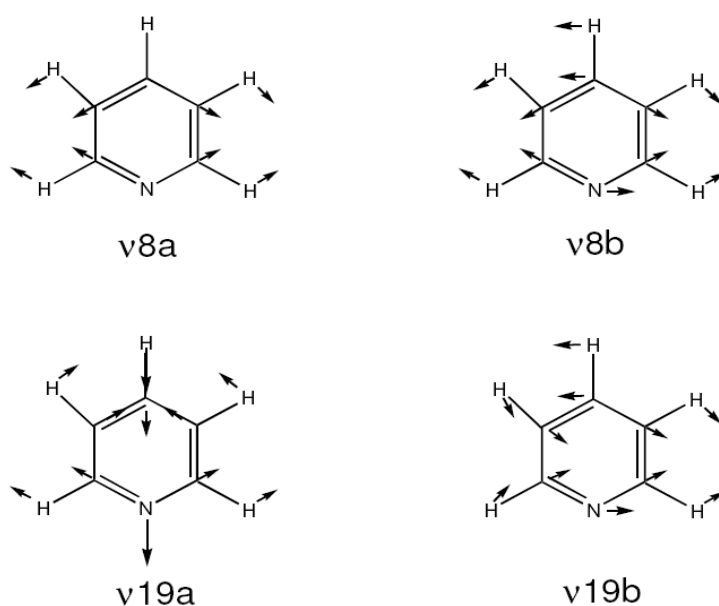


Figure 4.9: Ring vibration modes 8a/b and 19a/b of pyridine. After Ref. [41].

Table 4.2: Infrared bands (cm^{-1}) of pyridine adsorbed on acid sites [35].

H-bonded pyridine	Coordinatively bonded pyridine	Pyridinium ion
1400 - 1447	1447 - 1460	1485 - 1500
1485 - 1490	1488 - 1503	1540
1580 - 1600	1580	1640
	1600 - 1633	

For the determination of the strength of acid sites, the concentration of the adsorbed pyridine at different temperatures is needed, and for this purpose, the extinction coefficients have to be known. In Table 4.3 some extinction coefficients ϵ are given which are commonly used in the literature. Since the values range from $0.73 \text{ cm}\cdot\mu\text{mol}^{-1}$ to $3.03 \text{ cm}\cdot\mu\text{mol}^{-1}$ it is important to ascertain the coefficients by experiments with the own spectroscopic equipment to obtain values which are comparable with other groups. However, for comparative in-house analyses at the same spectrometer this is not necessary.

Table 4.3: Experimentally derived IR integrated extinction coefficients of pyridine on acidic materials for the band at 1545 cm^{-1} for Brønsted acid sites and 1455 cm^{-1} for Lewis acid sites.

Authors	$\epsilon_{\text{BA}} / \text{cm}\cdot\mu\text{mol}^{-1}$	$\epsilon_{\text{LA}} / \text{cm}\cdot\mu\text{mol}^{-1}$	Ref.
Hughes and White	3.03 ± 0.13	3.26 ± 0.13	[42]
Take <i>et al.</i>	1.3	1.5	[43]
Datka	0.73	1.11	[44]
Emeis	1.67 ± 0.12	2.22 ± 0.21	[45]
Khabtou <i>et al.</i>	1.8	-	[46]
Guisnet <i>et al.</i>	1.13	1.28	[47]

The methodology of the measurements, for example the time allotted to ad- and desorption or the adsorption temperature, may have an even greater influence on the measured concentration of the probe molecule than the extinction coefficients. Given in Table 4.4 are some pyridine concentrations determined by FT-IR spectroscopy on different zeolites. The values for the two USY zeolites are in good agreement with the $n_{\text{Si}} / n_{\text{Al}}$ ratios: Twice the number of aluminum leads to twice the number of pyridine adsorbed on acidic sites. This was not unexpected since the two zeolites were measured by the same group, so the methodology of the measurements and the equipment were the same. A comparison of the four Beta zeolites of Table 4.4 appears to reveal a worse correlation of these values: The first two Beta zeolites seems to have comparable silicon to aluminum molar ratios, but the concentration of H^+Py at a desorption temperature of $250 \text{ }^\circ\text{C}$ differs by a factor of 20.

Table 4.4: Pyridine concentrations at different desorption temperatures as determined by FT-IR spectroscopy.

Zeolite	$n_{\text{Si}} / n_{\text{Al}}$	H^+Py concentration in $\mu\text{mol}_{\text{Py}} \cdot \text{g}^{-1}$ at different temperatures			Ref.
		250 °C	350 °C	400 °C	
H-USY	15	44	16	5	[48]
H-USY	28	20.4	8.3	n.d.	[49]
H-Beta	11	444 ^a	n.d.	142 ^b	[50]
H-Beta	16	22	9	5	[48]
H-Beta	25	269	207	120 ^b	[51]
H-Beta	25	150 ^a	n.d.	n.d.	[52]

^a desorption temperature = 150 °C

^b desorption temperature = 450 °C

However, considering that a zeolite with an $n_{\text{Si}} / n_{\text{Al}}$ of 11 possesses 50 % more aluminum than one with a $n_{\text{Si}} / n_{\text{Al}}$ of 16 and that the desorption temperature for the measurements used by the authors differed by 100 °C, the discrepancy between the two values gets smaller. Nevertheless, the pyridine concentrations are not really the same which is probably the consequence of the different pretreatment conditions of the samples. Unfortunately, the authors did not mention the exact pretreatment procedure applied to the zeolites. Another example for the lack of experimental precision are the data for the last two Beta zeolites in Table 4.4. As they possess the same molar silicon to aluminum ratio they would be expected to show the same amount of adsorbed pyridine. However, the experimental values measured, deviate considerably from each other. Most likely these deviations have their origin in the different desorption temperatures and extinction coefficients used by the authors.

In spite of these methodological shortcomings, FT-IR spectroscopic measurements with pyridine as probe molecule have been applied in this work. Due to the use of the same equipment and methodology of the measurements for all catalysts, a comparison of the obtained data between these catalysts was possible.

4.3 Hydrodecyclization of Multi-Ring Aromatics, Naphthenoaromatics and Multi-Ring Naphthenes

4.3.1 Mechanistic Principles of the Ring-Opening Reaction

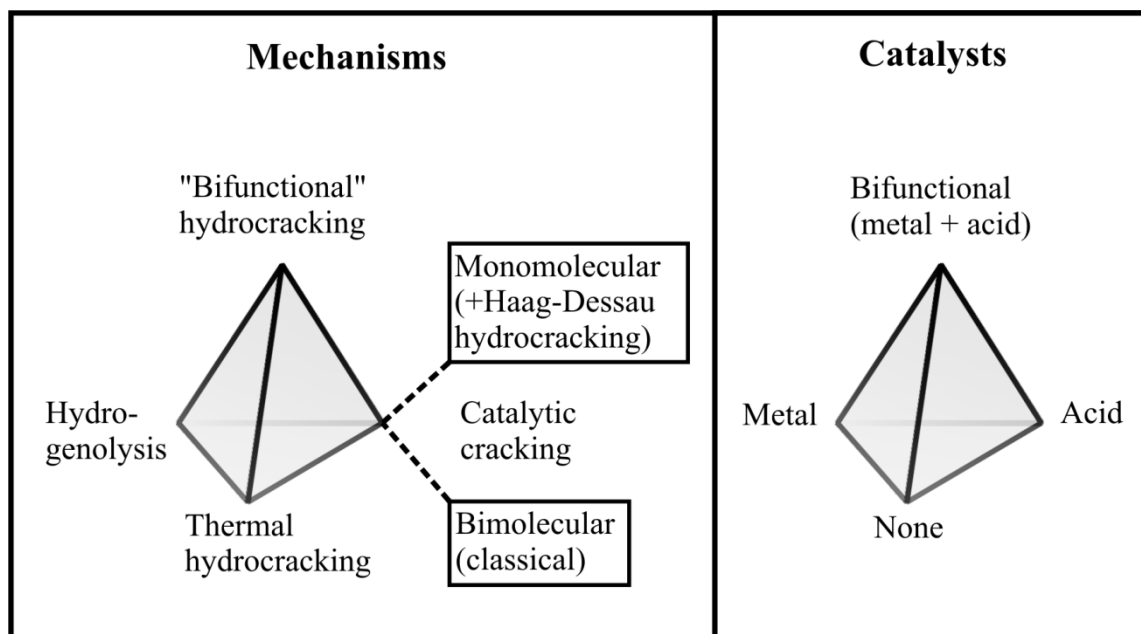


Figure 4.10: Pure cracking mechanisms and corresponding catalysts. After Ref. [2].

Depicted in Figure 4.10 (left) are the four hydrocracking mechanisms, namely thermal hydrocracking, hydrogenolysis, catalytic cracking and bifunctional hydrocracking and the corresponding catalyst systems (right). Since the hydrodecyclization reaction is a special case of hydrocracking in which the C-C bond rupture occurs in naphthenic structures, these four mechanisms will be briefly presented in the following Sections.

Thermal Hydrocracking

Thermal hydrocracking is the only cracking mechanism which is non-catalytic. Above temperatures of around 500 °C carbon-carbon bond rupture can occur *via* radical mechanisms. Unfortunately, thermal hydrocracking produces large amounts of light hydrocarbons [53] which makes this kind of cracking very undesired for the selective hydrodecyclization of multi-ring naphthenes.

Hydrogenolysis on Metal Catalysts

Pure hydrogenolysis occurs only on non-acidic metal-containing catalysts like *e.g.* Pt/silica or Ir/silica [54]. The bond rupture proceeds *via* the interaction of hydrogen and the carbon-carbon bond while both species are adsorbed on the metal surface: At sufficiently elevated temperatures, the chemisorbed, hydrogen-deficient hydrocarbon undergoes carbon-carbon bond cleavage, whereupon the adsorbed products are hydrogenated and desorbed. It is evident from such a mechanism that the nature of the metal has a large influence on the hydrogenolytic activity. Sinfelt [55] studied the hydrogenolysis activity of some metals at 205 °C with ethane as reactant. He found the following order of reaction rates: Os > Ru > Ni > Rh > Ir > Re > Co > Fe > Cu > Pt \approx Pd. In addition, the mode of adsorption, which depends mainly on the dispersion of the metal, is crucial for the selectivity of hydrogenolysis.

Besides hydrocracking, skeletal isomerization of the adsorbed hydrocarbon can also occur on a non-acidic metal-containing catalyst. For platinum a relatively high isomerization activity is known, whereas rhodium, iridium, palladium and ruthenium are less active in the isomerization of hydrocarbons [56 - 58]. For this isomerization, two different mechanisms can be distinguished, namely the bond shift mechanism (see Figure 4.11) and the cyclic mechanism (see Figure 4.12). While the cyclic mechanism can only occur on hydrocarbons with more than five carbon atoms, the bond shift mechanism has no such limitation.

There are two different pathways proposed for the bond shift mechanism (see Figure 4.11a and b). The pathway depicted in Figure 4.11a proceeds *via* a cyclopropanoid intermediate formed from an α,γ -diadsorbed species on two metal atoms. The rupture of a carbon-carbon bond other than the one formed before, leads to a skeletal isomer. The second pathway, depicted in Figure 4.11b, involves a metallacyclobutane intermediate which is formed from an α,γ -diadsorbed species, as well. However, this species is only adsorbed on a single metal atom. Through C-C bond rupture a metal-carben complex with a π -adsorbed allylic species is formed. The rotation of the allylic specie and the subsequent formation of a metallacyclobutane intermediate followed by desorption and hydrogenation result in an isomerized hydrocarbon.

The cyclic mechanism for the isomerization of alkanes on a metal is depicted in Figure 4.12. It involves the formation of a substituted cyclopentane intermediate adsorbed on a metal atom *via* a 1,5-dehydrocyclization step. Through the interconversion between isomeric adsorbed cyclopentyl species, all C-C bond ruptures at positions different from the one that was formed in the 1,5-dehydrocyclization step lead to isomerization of the hydrocarbon.

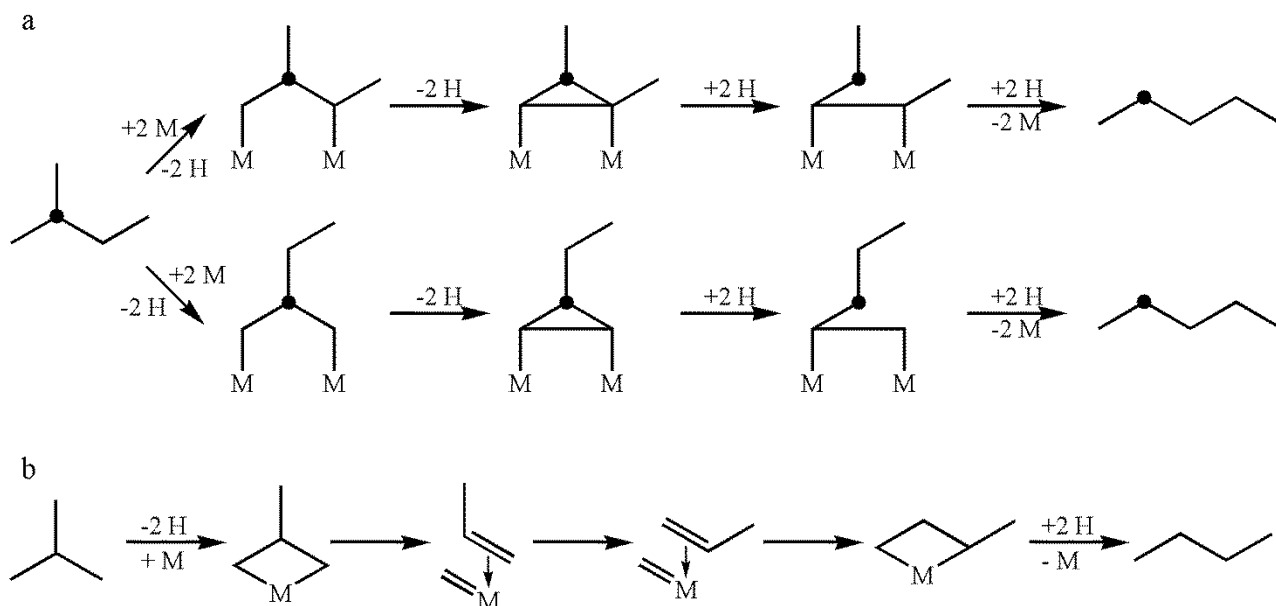


Figure 4.11: The bond shift mechanism *via* a) a cyclopropanoid species and b) a metallacyclic intermediate. 2-Methylbutane is ^{13}C -labeled. After Refs. [56, 59].

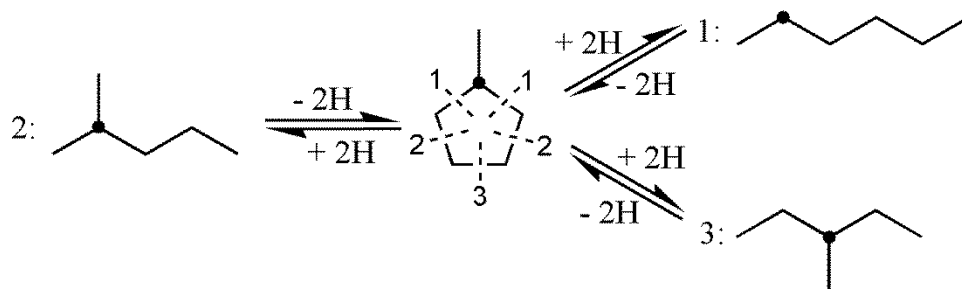


Figure 4.12: Isomerization of ^{13}C labeled 2-methylpentane *via* the cyclic mechanism. After Ref. [56].

An example for the large influence of the metal dispersion on the regioselectivities is the hydrogenolysis of methylcyclopentane on Pt/Al₂O₃ catalysts [60]. As shown in Figure 4.13, the regioselectivity of ring-opening is markedly determined by the metal dispersion: On small, highly dispersed metal particles, non-selective ring opening of all endocyclic carbon-carbon bonds occur. Whereas, on large metal particles with a low dispersion the ring opening is selective and only endocyclic bonds between two secondary carbon atoms are broken. The non-selective ring-opening reaction or multiplet mechanism presumably involves a flat adsorption of cyclopentane, which occurs only on highly dispersed platinum particles. The selective ring-opening reaction is also called dicarben mechanism. It presumably involves a perpendicular adsorption of the cyclopentane ring *via* two adjacent secondary carbon atoms. It occurs on low dispersed platinum particles, as well as on Ru, Rh and Ir independent of the dispersion.

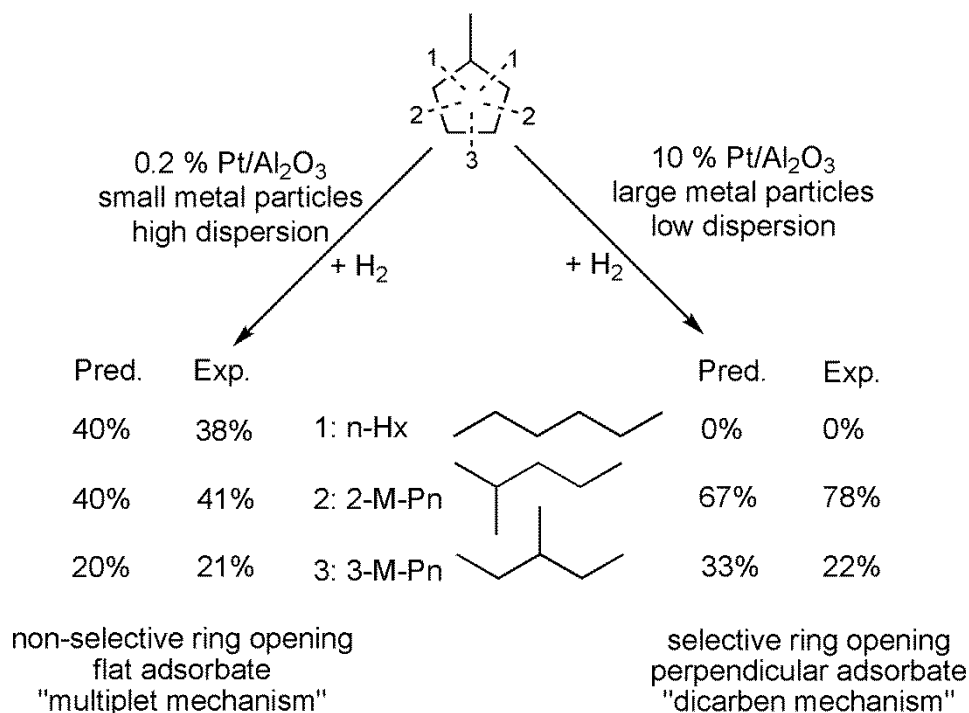


Figure 4.13: Non-selective and selective ring opening of methylcyclopentane on Pt/Al₂O₃ catalysts of high and low metal dispersion. n-Hx: n-hexane; 2-M-Pn: 2-methylpentane; 3-M-Pn: 3-methylpentane. After Ref. [60].

However, Maire *et al.* [60] also found a relatively high selectivity of n-hexane in the hydroconversion of methylcyclopentane on 10Pt/ γ -alumina with a low metal dispersion at high conversions. They explained their findings with the occurrence of a third mechanism, called partially selective mechanism. There, the ring-opening proceeds through the rupture of endocyclic C-C bonds between secondary-tertiary or two tertiary carbon atoms. The mechanism is analogous to the metallacyclobutane bond shift mechanism mentioned above (see Figure 4.11b).

Catalytic Cracking on Acidic Catalysts

There are two mechanisms known in literature for the catalytic cracking on monofunctional acidic catalysts: The bimolecular- or classical cracking mechanism and the monomolecular or Haag-Dessau cracking mechanism. The bimolecular mechanism proceeds *via* two principle reactions, namely skeletal rearrangements and β -scissions. The skeletal rearrangements are subdivided in two types: (i) type A rearrangements, in which the number of branchings of the carbenium ion remains constant and (ii) type B rearrangements in which the number of branchings increases or decreases. While type A rearrangements proceed *via* intramolecular shifts of hydride and alkyl groups, type B rearrangements proceed *via*

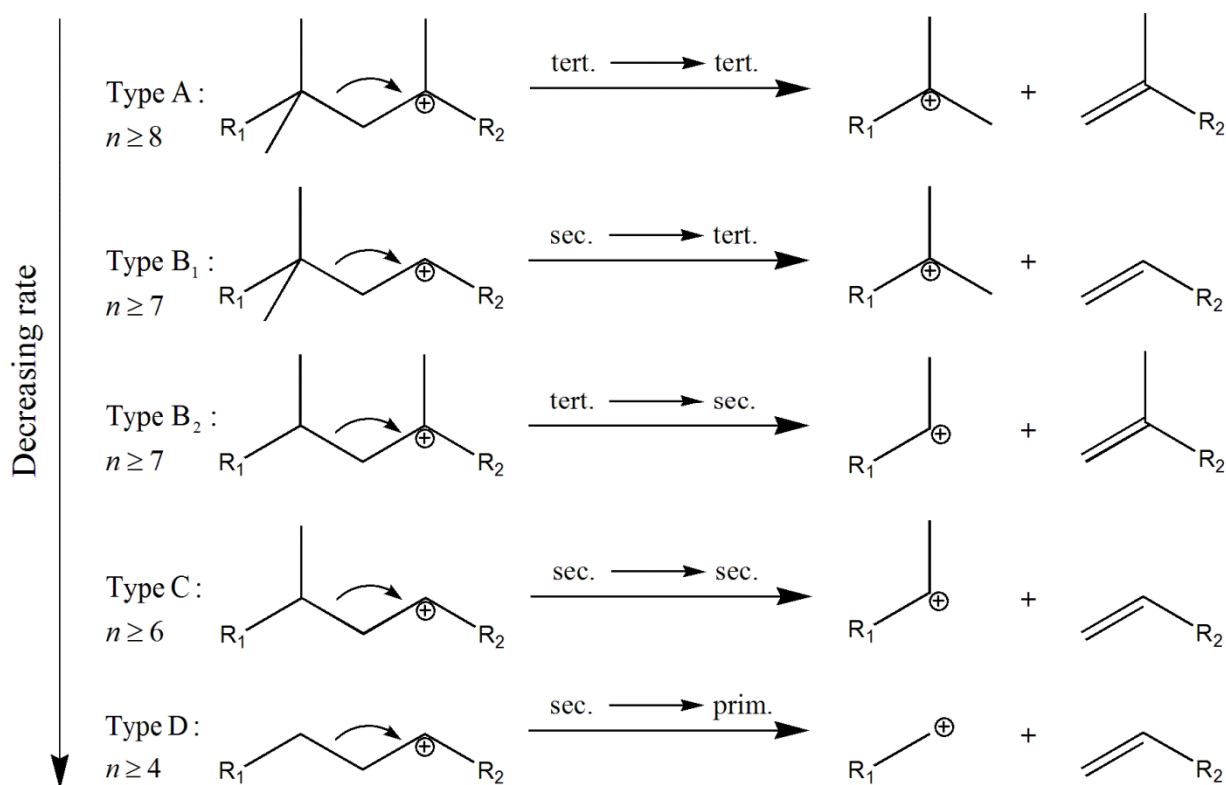


Figure 4.14: Classification of β -scissions of alkylcarbenium ions; n is the number of carbon atoms of alkylcarbenium ions that can undergo the respective type of β -scission. After Refs. [61, 62].

protonated cyclopropanes (PCPs). In general, type A rearrangements are faster than type B rearrangements. A detailed discussion about these mechanisms is given in Ref. [61].

The β -scissions have been classified in a similar manner [62]. As shown in Figure 4.14 five different types are distinguished. From type A to type D the reaction rate decreases strongly. This can be explained by the stability of the formed cations which decreases in the same order.

Figure 4.15 depicts the catalytic cycle of the bimolecular cracking of n-hexane. In the first step a secondary hexyl cation is formed by protonation of either n-hexane or n-hexene (which might be present as an impurity). The hexyl cation then undergoes a type B rearrangement into a branched tertiary cation (step I). Subsequently, an intermolecular hydride shift (step II) leads to the precursor for a type C β -scission into propene and a propyl-(2) cation (step III). The eponymous step of the catalytic cycle is the intermolecular hydride shift between a new reactant molecule and the propyl-(2) cation which is displaced as propane (step IV). This mechanism cannot lead to the formation of methane or ethane due to the low stability of the primary carbenium cations (type D β -scission). In contrast to the hydrocracking on bifunctional catalysts (see below), large amounts of alkenes are formed.

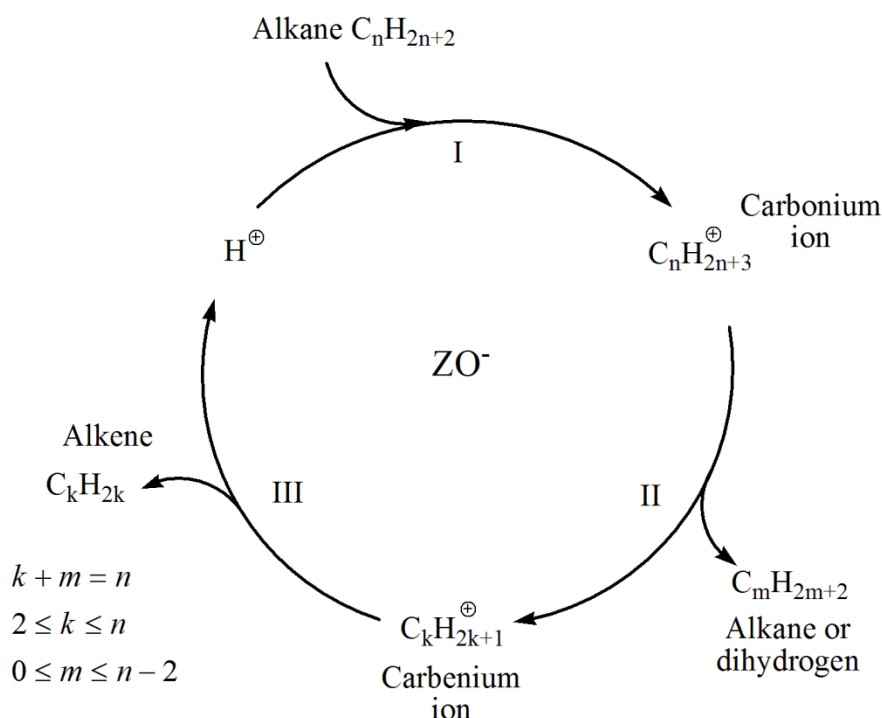


Figure 4.16: Monomolecular (non-classical, protolytic or Haag-Dessau) cracking of an alkane on a Brønsted-acidic catalyst, e.g. a zeolite. ZO⁻ stands for anionic framework oxygen of the zeolite. After Ref. [61].

Hydrocracking on Bifunctional Catalysts

The widely accepted course of this mechanism involves, as a first step, the dehydrogenation of the adsorbed n-alkanes at metallic sites to form a mixture of the corresponding n-alkenes in their equilibrium ratio. After desorption, these alkenes diffuse through the zeolite pores until they readsorb at a Brønsted acid site. There the alkenes are protonated to secondary alkylcarbenium cations which subsequently undergo skeletal rearrangements and β -scissions exactly in the same manner as stated above for the bimolecular cracking mechanism (see Figure 4.15). The formed alkenes diffuse to metal sites, where they are finally hydrogenated to skeletal isomers of the feed hydrocarbon or hydrocracked products. An important feature of this mechanism is the mass transfer between both types of catalytic sites by diffusion of alkenes. As a matter of fact, the olefinic intermediates could be directly detected in the conversion of n-dodecane on a Pd/Ca-Y zeolite [64].

However, Sullivan *et al.* [65] found in experiments with cyclic C_{10} hydrocarbons and bifunctional catalysts, such as NiS/SiO₂-Al₂O₃, that the β -scission of endocyclic carbon-carbon bonds is unexpectedly slow. They found essentially two products, *viz.* iso-butane and methylcyclopentane with remarkably high selectivities. This kind of hydrocracking was

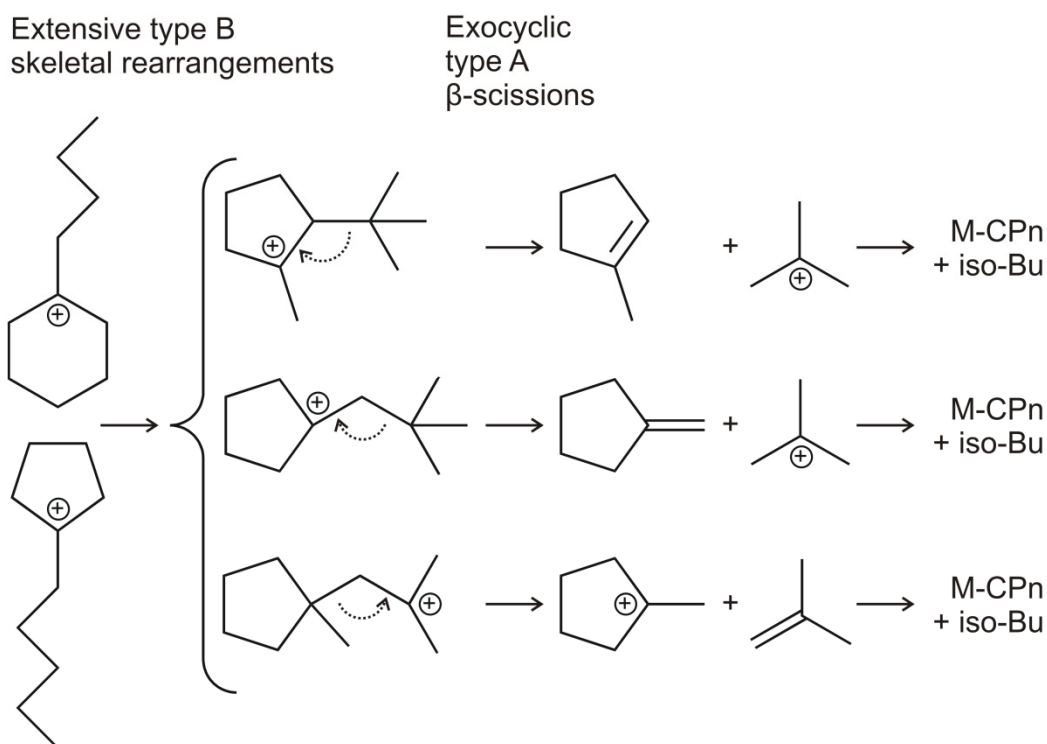


Figure 4.17: The three possible C_{10} cycloalkylcarbenium ions that can undergo exocyclic type A β -scission. M-CPn: methylcyclopentane; iso-Bu: iso-butane. After Ref. [2].

named the “paring reaction”, because methyl groups are pared from the cyclic hydrocarbon and released as iso-butane. A rationale for the paring reaction can easily be given: Any cyclic C_{10} hydrocarbon undergoes a series of type A and B isomerizations until one out of three possible precursors for an exocyclic type A β -scission is reached (see Figure 4.17). The β -scission of all three carbenium ions leads to the formation of iso-butane and methylcyclopentane. Since these precursors of the paring reaction are relatively bulky, it proceeds only in large-pore zeolites. In zeolites with 10-MR pores, hydrocracking of C_{10} cycloalkanes proceeds mainly *via* type B β -scissions, which lead to a much broader spectrum of hydrocracked products.

A generally accepted explanation for the slow rupture of endocyclic carbon-carbon bonds has been given by Brouwer and Hogeveen [66] (see Figure 4.18): Whereas the α -bond in an alkylcarbenium ion can rotate freely, which allows a coplanar conformation of the vacant p-orbital and the β -bond to be broken, this is not possible in a cycloalkylcarbenium ion. There the vacant p-orbital is fixed in a perpendicular or near-perpendicular orientation to the β -bond, which is very unfavorable for the required orbital overlap.

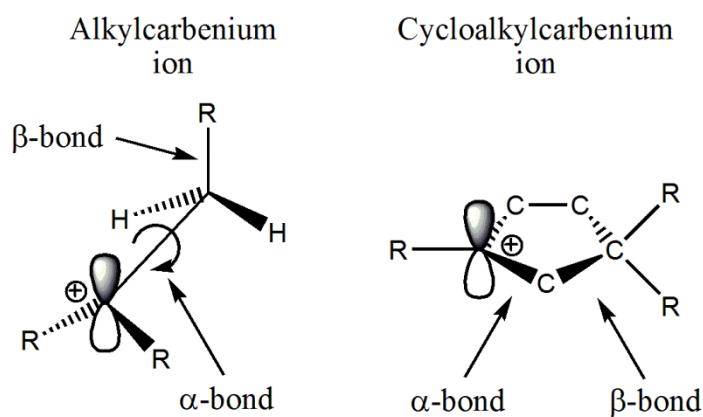


Figure 4.18: Possible role of orbital orientation for the fast β -scission in alkylcarbenium ions compared to cycloalkylcarbenium ions. After Ref. [66].

4.3.2 Hydrodecyclization on Bifunctional and Monofunctional Catalysts

Kubička *et al.* [67] studied the zeolites H-Beta-25, H-Beta-75, H-Y-12, H-mordenite-20 and H-MCM-41 in the hydroconversion of a decalin isomer mixture. They used a batch reactor and reaction temperatures of 200 to 300 °C at a total pressure of 2 MPa. A general trend they observed was an increasing initial activity of the catalysts with increasing concentration of Brønsted acid sites with the exception of zeolite H-mordenite. This peculiarity was explained by a fast blockage of the one-dimensional 12-MR pore system of zeolite mordenite. Over the whole range of temperatures, the mesoporous material H-MCM-41 showed nearly no conversion, due to the extremely low concentration of Brønsted acid sites. On all catalysts they observed a strong deactivation during the reaction. The rate of deactivation depended on the concentration of Brønsted acid sites: With increasing concentration the rate of deactivation also increased. In addition, they found that the deactivation is also influenced by the structure of the zeolite. A comparison of H-Y-12 and H-Beta-25, showed that the faujasite deactivates faster than the Beta zeolite. The authors explained this by the presence of large cavities in H-Y, which enables the formation of bulky organic molecules blocking the pores. However, the faster deactivation of H-Y-12 could also stem from the different concentrations of Brønsted acid sites, which is for H-Y-12 twice as high as for H-Beta-25. Nevertheless, they observed yields of ring-opening products of 10 % for zeolite H-Beta-25, accompanied by the formation of large amounts of dehydrogenated products and products with more than 10 carbon atoms. The formation of open-chain decanes (OCDs) was not mentioned.

In another publication, the same authors [68] compared the results obtained on the monofunctional acidic catalysts H-Beta-25, H-Y-12 and H-mordenite-20 with those measured on their bifunctional counterparts containing 2 wt.-% platinum. The reaction

conditions were similar to the ones chosen in their earlier publication [67]. A significant increase in activity was observed after impregnation of the catalysts with platinum. The initial activity of the catalysts was in the same order for both types of catalysts, *i.e.*, monofunctional or bifunctional: Beta > Y > mordenite. Experiments at different hydrogen pressures compared to experiments under argon atmosphere led the authors to conclude that the ring-opening is a zero-order reaction with respect to hydrogen. Moreover, they observed a strong deactivation during the experiments without hydrogen. However, they found that the formation of dehydrogenated products and products with more than 10 carbon atoms as well as deactivation are suppressed by the addition of platinum.

In a third paper, Kubička *et al.* [69] proposed a reaction network (see Figure 4.19) for Pt-modified H-Beta zeolites. In a first step, decalin (Dec) is dehydrogenated on a metal site. Afterwards, the resulting olefin diffuses to a Brønsted acid site where it isomerizes to form skeletal isomers (sk-Isos). At this point two reactions are possible: (i) diffusion to metal sites and hydrogenation to saturated isomers or (ii) ring-opening at acidic sites which leads to dienic ring-opening products (ROPs). These dienic ROPs get either hydrogenated at metal sites to olefinic or saturated ROPs or they get cracked at acid sites in an alkyl side chain to hydrocarbons with less than ten carbon atoms (C₉-). It was stated that this reaction scheme suits also for monofunctional acidic catalysts. In its essence, the scheme is just an adoption of the classical hydrocracking mechanism to the conversion of decalin.

Another comparative study was done by Santikunaporn *et al.* [70]. They tested three H-Y zeolites with different concentrations of Brønsted acid sites (H1-Y < H2-Y < H3-Y) and 1.0Pt/H3-Y as a bifunctional catalyst in the hydroconversion of a mixture of decalin isomers at 260 °C and a total pressure of 2 MPa. The best catalyst concerning the yield of ROPs was H3-Y with $Y_{\text{ROPs, max.}} = 19.1 \%$. In accordance with the results obtained by Kubička *et al.* [67 - 69] on all three monofunctional catalysts a strong deactivation was observed which could be suppressed by the incorporation of platinum.

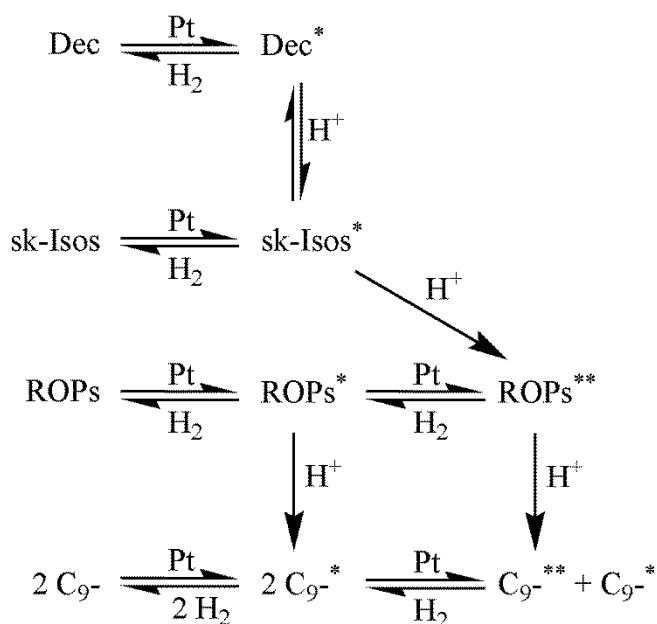


Figure 4.19: Proposed reaction scheme of decalin conversion on Pt-modified H-Beta zeolites. The asterisks * and ** denote an olefin and a diene, respectively. After Ref. [69].

In addition, the hydroconversion of tetralin was also studied at 325 °C and a total pressure of 2 MPa [70]. A large increase of the activity was observed by the addition of platinum. This increase is mainly attributed to the hydrogenation of tetralin. This was also found by Arribas and Martínez [71] during the hydroconversion of naphthalene on 1.0Pt/H-Y. The initial step of the reaction was the hydrogenation of naphthalene to tetralin and decalin. In addition, with a series of experiments (physical mixtures of H-Y and Pt/SiO₂ and separated beds of both catalysts in alternating order), they found that Pt is responsible for the hydrogenation and isomerization and that the acid sites are responsible for the ring opening which was found to be easier for decalin than for tetralin.

The results discussed so far lead to the same conclusion: The performance of monofunctional acidic catalysts in the hydrodeacyclization of naphthenes is not promising. Due to the strong deactivation tendency and the formation of high amounts of undesired products, like hydrocracked products and dehydrogenated products, they are not suitable for the selective ring opening of decalin.

McVicker *et al.* [72] investigated the ring opening of the bicyclic naphthenes bicyclo[3.3.0]octane, perhydroindane and decalin on a monofunctional metallic 0.9Ir/Al₂O₃ catalyst. They obtained very high conversions for bicyclo[3.3.0]octane at 225 °C with good selectivities of open-chain octanes between 26 and 83 %. With perhydroindane as feed hydrocarbon they obtained much lower conversions and only traces of acyclic paraffins. Even worse results were obtained in the hydroconversion of decalin. Hardly any conversion

was observed, even not at reaction temperatures that were 50 °C higher, and only traces of OCDs were formed. The authors explained this behavior with the different structures of the naphthenes: Whereas bicyclo[3.3.0]octane possesses two five-membered rings and perhydroindane one five-membered ring and one six-membered ring, decalin possesses two six-membered rings which are much harder to open by hydrogenolysis. From ancillary experiments with other cycloalkanes like methylcyclohexane, methylcyclopentane, trimethylcyclohexane or butylcyclohexane they concluded that the ring opening of mildly branched five-membered rings is much easier than the ring opening of highly branched six-membered rings. Depicted in Figure 4.20 are a reaction scheme of the skeletal isomerization and ring opening of methylcyclohexane and the different ring opening rates depending on the structure of the C₇ naphthene to be opened. The preferred reaction path is the ring contraction to ethylcyclopentane not only due to the higher ring opening reaction rates of ethylcyclopentane compared to methylcyclohexane but also due to the formation of open-chain heptanes with a lower degree of branching which possess much higher cetane numbers than highly branched heptanes. These would be obtained by the ring opening of dimethylcyclopentane at bissecondary C-C bonds. The direct ring opening of the six-membered ring of methylcyclohexane would also lead to moderately branched heptanes; however, the corresponding reaction rate is very low.

In conclusion, the authors proposed that for the selective ring opening of decalin a metal catalyst combined with a balanced acid function for the isomerization of the six-membered rings would be preferable. This concept has already been proven for the ring opening of methylcyclohexane: By adding an isomerization catalyst (Pt/USY) to the monofunctional Ir/Al₂O₃ catalyst the ring opening yield was significantly enhanced [72].

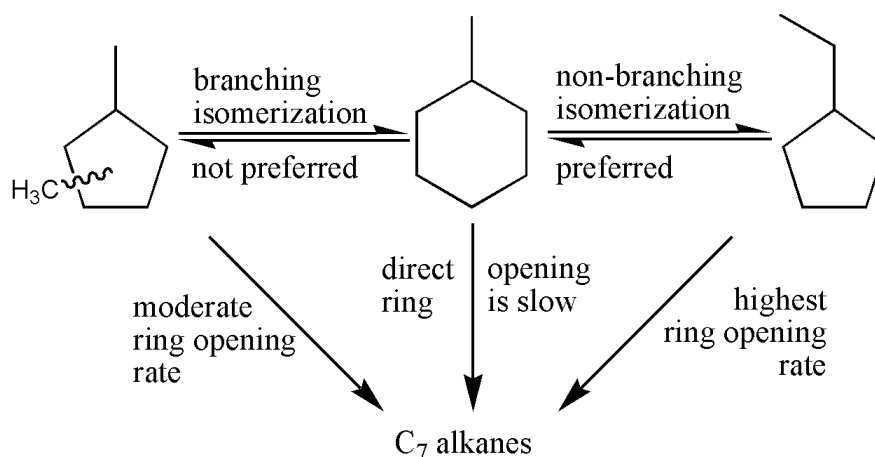


Figure 4.20: Different ring opening rates of five- and six-membered rings. After Ref. [72].

Arribas *et al.* [73] investigated the influence of the proximity of the two catalytically active sites in Pt/USY catalysts on the ring opening of tetralin. For varying the distance of the metallic and acid sites in the bifunctional catalyst they used different bed configurations (see Figure 4.21). The largest distance was achieved by a two-bed arrangement with 1.0Pt/Al₂O₃ and USY separated by quartz wool. A much smaller distance was achieved by a physical mixture of 1.0Pt/Al₂O₃ and USY. And finally, the smallest distance between both types of sites was realized by an USY zeolite impregnated with 1.0 wt.-% of platinum. With decreasing distance between the two types of sites they observed increasing yields of ROPs and sk-Isos. This finding is in-line with the mechanism for ideal hydrocracking (see page 33), where the mass transfer between the two catalytic sites plays an important role. With their best catalyst, 1.0Pt/USY they reached $Y_{\text{ROPs, max.}} = 16.0 \%$.

In another work, Arribas *et al.* [74] investigated the influence of the pore size on the ring-opening reaction of tetralin with different medium- and large-pore zeolites loaded with 1.0 wt.-% platinum at a total pressure of 3 MPa and reaction temperatures between 250 and 325 °C. The results are listed in Table 4.5, page 41, together with the results obtained by other groups. High yields of ROPs are formed mainly on large-pore zeolites with a three-dimensional pore system, in particular Beta and USY. The poor results obtained with the 10-MR pore zeolite ZSM-5 have been attributed to diffusional limitations, which were confirmed by molecular docking simulations of butylcyclohexane and diethylcyclohexane as representative molecules for ROPs. Again, the low yields obtained with 1.0Pt/H-mordenite were explained by accumulation of carbonaceous deposits in the narrow one-dimensional pores. The best performance concerning the maximum yield of ring-opening products was obtained with 1.0Pt/H-Beta ($Y_{\text{OCDs, max.}} = 22.4 \%$). However, high amounts of cracked products were also formed ($Y_{\text{C}_9} = 30 \%$).

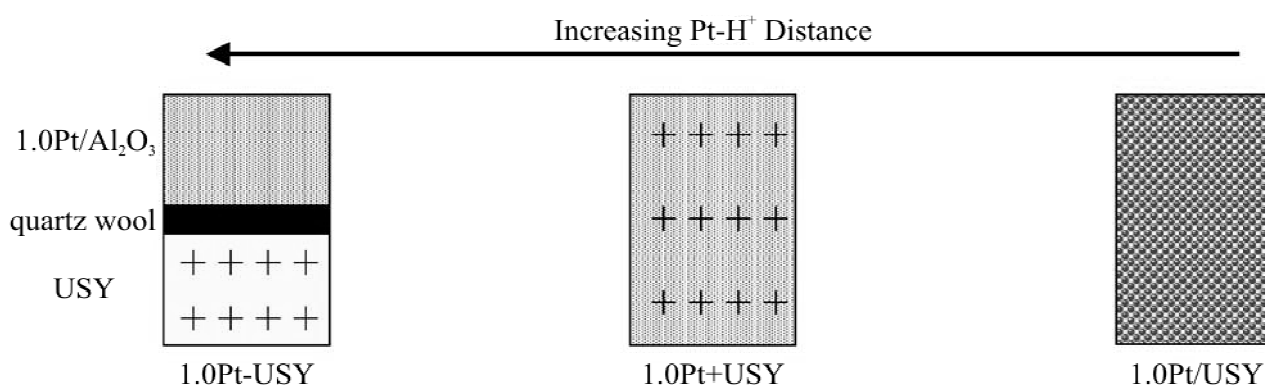


Figure 4.21: Schematic representation of the different bed configurations used by Arribas *et al.* for studying the influence of the proximity between metallic and acid sites. After Ref. [73].

In a more recent publication, the same authors investigated the behavior of 1.0Pt/H-ITQ-21 in the hydroconversion of tetralin [75]. They expected higher yields of ROPs due to the very spacious pore system of ITQ-21 (six 12-MR windows in the supercages *vs.* four windows in the supercage of faujasite). In-line with their expectations, the yield of ROPs obtained with 1.0Pt/H-ITQ-21 was higher compared to 1.0Pt/USY (see Table 4.5, page 41). Attempts to increase the yield by decreasing the concentration of acid sites *via* steaming were unsuccessful.

In an earlier work of the same group [76], the reduction of the concentration of the Brønsted acid sites of 1.0Pt/H-Beta *via* steaming led to increasing yields of ring-opening products in the hydroconversion of tetralin and 1-methylnaphthalene. In addition, the reaction temperature at which the maximum yield of ROPs was obtained increased with decreasing concentration of acid sites, indicating a lower cracking and dealkylation activity of the catalysts.

Moreover, they found that the yield of ROPs increases with decreasing crystallite size of zeolite Beta. Both yield enhancements were explained by a faster diffusion of the ring-opening products through either the steamed Pt/Beta zeolite or the smaller crystallites of Pt/Beta, thus decreasing the probability of secondary reactions. The maximum yields of ROPs obtained in the hydroconversion of tetralin are summarized in Table 4.5, page 41.

Ma *et al.* [77] also investigated the influence of the Brønsted acid sites on the ring opening of tetralin. They lowered the strength of the acid sites by impregnation of zeolite USY with different amounts of potassium nitrate. Compared to the non-modified 0.5Pt/USY, which gave a yield of hydrocracked products as high as 98 %, the potassium-impregnated catalysts showed much better performances: The yield of hydrocracked products decreased rapidly upon impregnation of the catalyst with increasing amounts of potassium, whereas the yield of ROPs passed through a maximum of 45.6 % for 0.5Pt/1.2K-USY.

The influence of the incorporation method of the noble metal on the ring opening of decalin has also been examined. Platinum or ruthenium were incorporated into H-MCM-41 by *in situ* synthesis, ion exchange and impregnation [78, 79]. In addition, Vuori *et al.* [80] incorporated iridium into H-Beta zeolite by impregnation and atomic layer deposition. The results of all these studies have to be taken with care because the metal contents of the catalysts in this series differ strongly. Nevertheless, in all studies the impregnated catalysts showed the worst performance concerning the yield of ring-opening products.

Publications about the influence of the hydrogen pressure on the hydroconversion of naphthenes are very scarce. Only Kubička *et al.* [81] investigated this influence on the hydroconversion of decalin. They found that an increase of the hydrogen pressure has a

Table 4.5: Maximum yields of ring-opening products (ROPs) obtained from bicyclic C₁₀ hydrocarbons on various bifunctional catalysts.

Feed	Catalyst	$T / ^\circ\text{C}$	$p_{\text{H}_2} / \text{MPa}$	$Y_{\text{ROPs, max.}} / \%$	Ref.
Decalins	2.0Pt/H-Beta	250	2.0	30.2	[68]
Decalins	2.0Pt/H-Y	250	2.0	27.2	[68]
Decalins	2.0Pt/H-mordenite	270	2.0	8.8	[68]
Tetralin	1.0Pt/H-Y	325	2.0	15.0	[70]
Tetralin	4.0Pt/USY	275	3.0	21.2	[73]
Tetralin	1.0Pt/H-ZSM-5	300	3.0	0.9	[74]
Tetralin	1.0Pt/H-MCM-22	300	3.0	4.6	[74]
Tetralin	1.0Pt/H-mordenite	275	3.0	6.8	[74]
Tetralin	1.0Pt/H-Beta	250	3.0	22.4	[74]
Tetralin	1.0Pt/USY	275	3.0	16.1	[74]
Tetralin	1.0Pt/H-ITQ-21	300	3.0	20.1	[75]
Tetralin	1.0Pt/USY	275	3.0	16.1	[75]
Tetralin	1.0Pt/H-Beta	300	3.0	14.5	[75]
Tetralin	1.0Pt/H-Beta	300	3.0	26	[76]
Tetralin	0.5Pt/1.2K-USY	250	4.0	45.6	[77]

beneficial influence on the ring opening of decalin: At higher hydrogen pressures the selectivity of ROPs increased more strongly with the conversion and reached higher final values. Moreover, at $p_{\text{H}_2} = 6.0$ MPa also slightly lower selectivities of C₉- products were obtained than in experiments at $p_{\text{H}_2} = 2.0, 3.0$ or 5.0 MPa. However, in addition, they found that the activity of the catalysts decreased at higher hydrogen pressures.

Until 2011 in only three publications the formation of open-chain decanes from the hydroconversion of a C₁₀ naphthene was reported: Contreras *et al.* [82] reported, in a qualitative manner, about the formation of small quantities of n-decane during the hydroconversion of decalin on a Pt/MFI-SBA-15 hybrid catalyst. Mouli *et al.* [83] tested bimetallic catalysts made from iridium and platinum (loaded with 0 – 1.5 wt.-%) on H-Zr-MCM-41 in the ring opening of decalin. They qualitatively reported about the formation of 3,5-dimethyloctane as a product. In a later publication [84] they reported for the ring opening

of decalin on a Pt,Ir/H-Y catalyst a maximal selectivity of open-chain decanes of 5 % and a maximal yield of 4 %.

In 2010/2011 two publications [85, 86] dealing with the hydrodecyclization of decalin on the bifunctional zeolites $0.85\text{Ir}/\text{La}_{0.30},\text{H}_{0.06},\text{Na}_{0.04}\text{-X}$, $1.0\text{Pt}/\text{La}_{0.30},\text{H}_{0.06},\text{Na}_{0.04}\text{-X}$ and $5.0\text{Rh}/\text{H}_{0.99},\text{Na}_{0.01}\text{-Beta}$ catalysts appeared. The authors had used improved techniques for the analysis of the complex product mixtures and observed the formation of open-chain decanes with maximal yields of up to 14 %. In their opinion these relatively high yields were not caused by improved properties of the catalysts used, but rather due to their advanced product analyses. They also paid, for the first time, attention to a reliable analysis of the hydrocracked products with one to nine carbon atoms. Iso-butane and methylcyclopentane turned out to be the dominating products. This was strong evidence for the paring reaction (Figure 4.17, page 34) occurring on bifunctional catalysts. The carbon number distribution curves of the hydrocracked products (see Figure 4.22) of all three catalysts showed pronounced maxima at C_4 and C_6 originating from iso-butane and methylcyclopentane. The authors denoted the curves as “M-shaped”. Moreover, they were able to unambiguously detect spiro[4.5]decane as a primary product from decalin which accounted for up to 15 % of all skeletal isomers formed at low conversion. The occurrence of this hydrocarbon was rationalized in terms of a so-called type A rearrangement at the level of carbocations adsorbed on the acid sites of the catalysts [86].

Most recently Moraes *et al.* [87] reported about the hydroconversion of decalin and methylcyclohexane at a total pressure of 5 MPa in the temperature range from 250 to 350 °C on two alumina-based monofunctional catalysts, *viz.* on acidic $\text{WO}_3/\text{alumina}$ and on non-acidic Ir/alumina containing 0.6, 1.2 or 1.8 wt.-% iridium. They used up-to-date product analysis methods including comprehensive two-dimensional gas chromatography (GCxGC) and GC/MS and reported yields of open-chain decanes of around 8 % on 1.8Ir/alumina. However, the yield of open-chain decanes obtained on the monofunctional acidic catalysts was only 2 %. Based on their experimental data, they proposed two reaction networks for the hydroconversion of decalin on the monofunctional acidic and the metallic catalyst (see Figure 4.23).

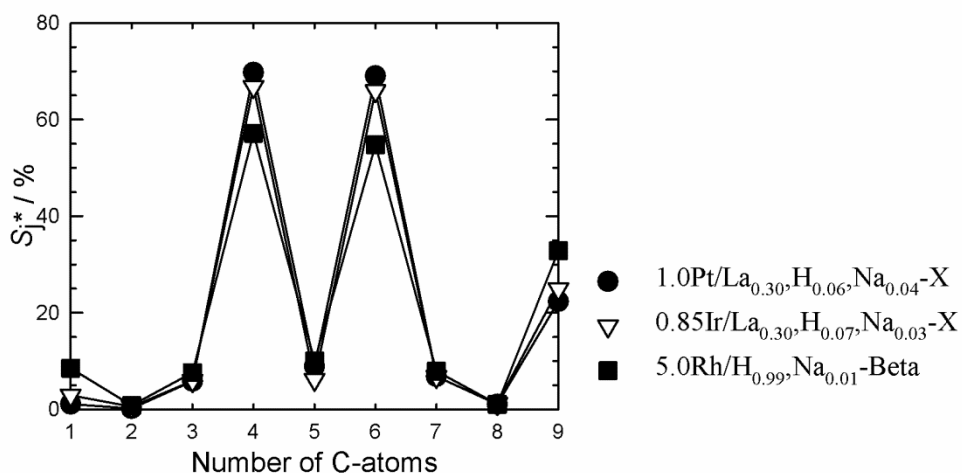


Figure 4.22: Distribution of the hydrocracked products on the zeolite catalysts 1.0Pt/La_{0.30},H_{0.06},Na_{0.04}-X, 0.85Ir/La_{0.30},H_{0.06},Na_{0.04}-X and 5.0Rh/H_{0.99},Na_{0.01}-Beta in the hydroconversion of decalin. After Refs. [85, 86].

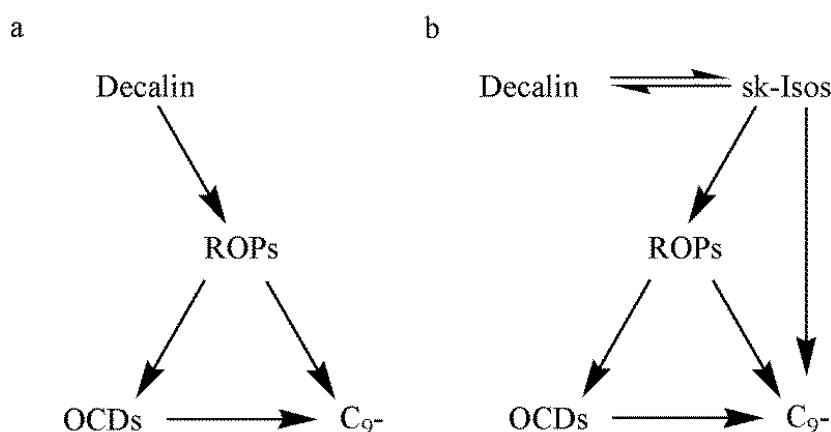


Figure 4.23: Proposed reaction scheme of decalin hydroconversion on (a) Ir/alumina and (b) WO₃/alumina. After Ref. [87].

The authors concluded that monofunctional acidic catalysts are not suitable for the upgrading of light cycle oils since only low yields of ROPs and OCDs are formed. Much better suited for this purpose are monofunctional metallic catalysts: They yield much higher amounts of OCDs and ROPs.

In addition, Haas *et al.* [88] very recently published their results obtained on non-acidic Ir/silica and Pt/silica in the hydroconversion of decalin. Their results are in-line with those obtained by Moraes *et al.* [87] on a monofunctional Ir/alumina catalyst: On Ir/silica mainly ring-opening occurred at low conversions (see Figure 4.24). Nevertheless, they reached much

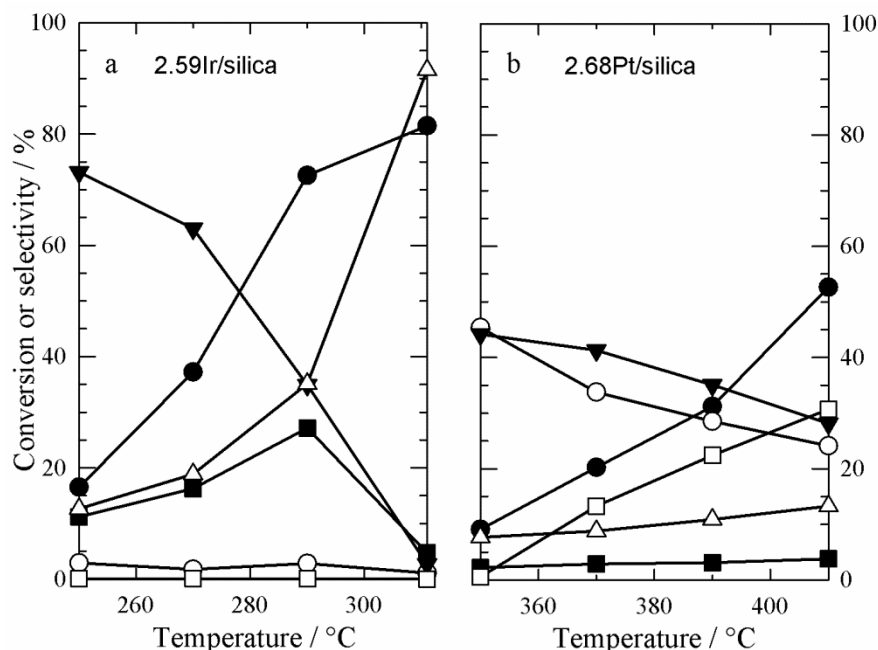


Figure 4.24: Conversion of decalin and selectivities of the different groups of products in dependence of the reaction temperature for 2.59Ir/silica and 2.68Pt/silica. (● X_{Dec} , ■ S_{OCDs} , ▼ S_{ROPs} , ○ $S_{sk-Isos}$, △ S_{C9-} , □ S_{DHPs}). After Ref. [88].

higher maximum yields of OCDs on 2.59Ir/silica ($Y_{OCDs, max.} = 20\%$) than Moraes *et al.* on 1.8Ir/alumina [87]. Moreover, the work by Haas *et al.* [88] elucidated the reaction paths of decalin on iridium catalysts lacking Brønsted acid sites much more deeply. They found (see Figure 4.25) that, on such catalysts, one six-membered ring of decalin is opened *directly*, *i.e.* without prior skeletal isomerization, by hydrogenolysis on the noble metal, the obvious products being butylcyclohexane, cis- and trans-1-methyl-2-propylcyclohexane, and cis- and trans-1,2-diethylcyclohexane (these “direct ROPs” were also detected by Moraes *et al.* [87]). Haas *et al.* furthermore showed that the above-mentioned direct ROPs undergo consecutive hydrogenolysis on iridium already at moderate decalin conversions (Figure 4.25, [88]): (i) Opening of the remaining six-membered ring leads to seven possible open-chain decanes (“direct OCDs”); (ii) hydrogenolysis of C-C bonds in the alkyl side chains gives a small alkane, typically methane, and the C₉ naphthenes propylcyclohexane and cis- and trans-1-ethyl-2-methylcyclohexane (“direct C₉ ROPs”); (iii) the latter undergo again ring opening by hydrogenolysis whereby seven possible open-chain nonanes (“direct OCNs”) are formed. It is noteworthy that all individual product hydrocarbons predicted by this direct ring-opening mechanism were indeed found in the products of decalin hydroconversion on Ir/silica [88]. Moreover, based on this mechanism, Haas *et al.* were able to simulate the characteristic carbon-number distributions of the C₉- products repeatedly observed in the hydroconversion of decalin on iridium-containing catalysts. Their salient features are large amounts of methane and C₉ hydrocarbons, smaller amounts of ethane and C₈ hydrocarbons and hardly

any C₃ to C₇ hydrocarbons. Due to their characteristic shape the term “hammock-type” curves was coined [25, 89, 90].

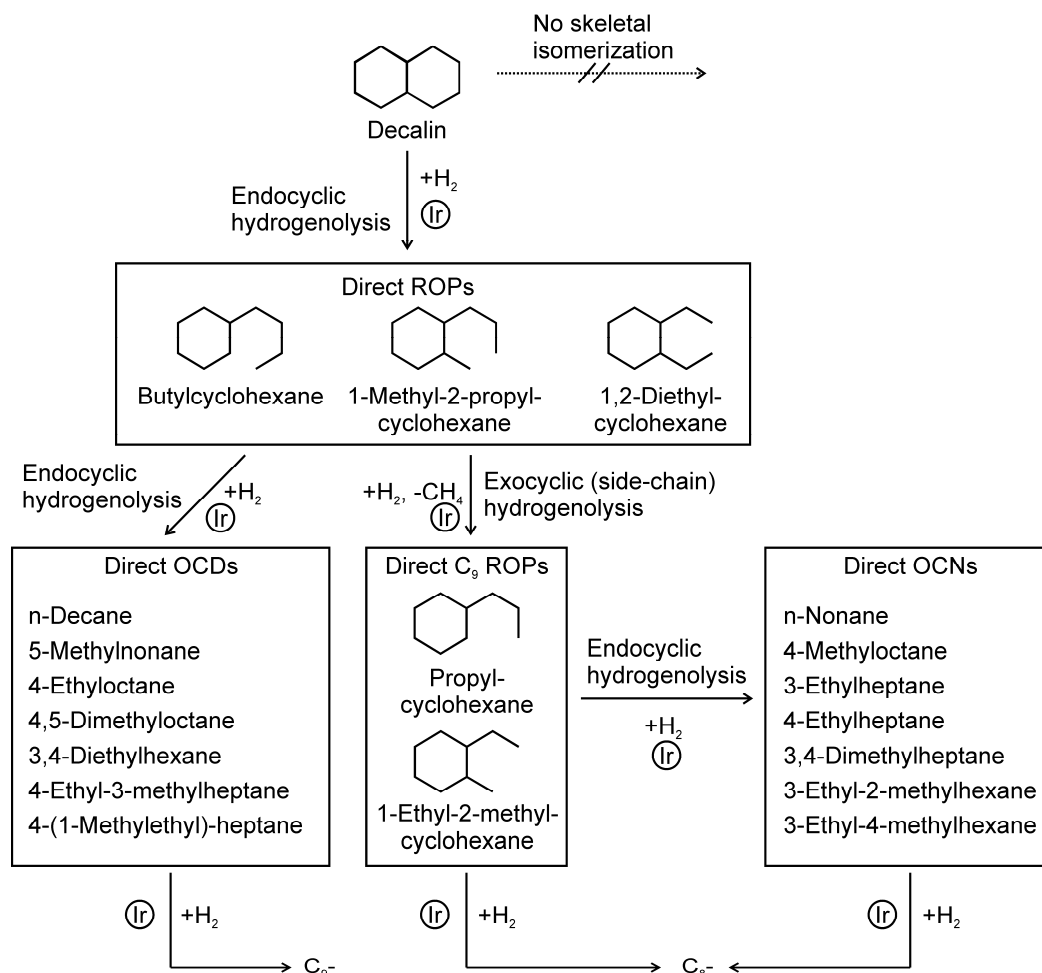


Figure 4.25: The *direct ring-opening mechanism* for hydrogenolytic hydrodecyclization of decalin and consecutive hydrogenolysis reactions over iridium on non-acidic supports. After Ref. [88].

4.3.3 High-Performance Ring-Opening Catalysts (HIPEROCs)

A new family of ring-opening catalysts was introduced by Rabl *et al.* [25]: They prepared iridium- and platinum-containing zeolites Y with unusually low concentrations of Brønsted acid sites and relatively high amounts of noble metal (around 3 wt.-%). In addition, the strengths of the Brønsted acid sites were tuned by ion exchange of the charge-compensating cations with different alkali metals. These catalysts were tested in the hydroconversion of *cis*-decalin at reaction temperatures between 240 and 380 °C and at a hydrogen partial pressure of 5.2 MPa. The Brønsted acid sites were generated in low concentrations by the

reduction of the noble metal with hydrogen (see Eq. (4.4), page 20) after introduction of the noble metal *via* ion exchange.

Using as a quality criterion the maximum attainable yields of open-chain decanes, the two best catalysts made in this way were 2.9Ir/Na_{0.90},H_{0.10}-Y and 3.0Pt/Na_{0.88},H_{0.12}-Y. With these, unprecedented yields of OCDs amounting to 31 and 41 %, respectively, were reached [25]. They referred to such catalysts that fulfill the criterion

$$Y_{\text{OCDs, max.}} > 25 \% \quad (4.9)$$

in the hydroconversion of decalin as “High-PERformance Ring-Opening Catalysts” (HIPEROcs). Their main mechanistic feature is their ability to promote a mild skeletal isomerization of decalin into bicycloalkanes containing one five-membered and one six-membered ring *via* bifunctional catalysis. As already known since the work of McVicker *et al.* [72], ring opening of such hydrocarbons *via* hydrogenolysis on the metal proceeds much more readily than ring opening of decalin itself. In addition, due to the low concentration and strength of the Brønsted acid sites, the strongly undesired paring reaction (see Figure 4.17, page 34) is suppressed. This can be clearly seen from the carbon number distribution curves of the hydrocracked products (see Figure 4.26): Instead of the M-shaped curves measured on conventional bifunctional catalysts (see Figure 4.22, page 43) – and restricting the discussion for a while to HIPEROcs containing iridium as the metal component – the characteristic hammock-shaped distribution curves are observed which are depicted in Figure 4.26.

It has also been found [25] that, while 2.9Ir/Na_{0.90},H_{0.10}-Y zeolite is a good catalyst for ring opening of decalin, the replacement of sodium by potassium, or the partial replacement of sodium by rubidium or cesium changes the performance of the catalyst fundamentally: These catalysts are no longer HIPEROcs, but the acid strength is reduced to such an extent that they rather behave like monofunctional metallic catalysts, such as non-acidic Ir/silica [88] (see Section 4.3.2, pages 43 - 45).

If the catalysts contain platinum instead of iridium, the chemistry of ring opening is more complex, in part because platinum is capable to isomerize decalin in the absence of acid sites. Also, the carbon number distribution of the C₉- products is fundamentally different from the hammock-type curves observed on iridium [25]. Again, in the series of platinum-loaded Y-type zeolites exchanged with alkali cations, the sodium version 3.0Pt/Na_{0.88},H_{0.12}-Y turned out to be an excellent catalyst for ring opening of decalin with $S_{\text{OCDs, max.}}$ and $Y_{\text{OCDs, max.}}$ of 41 % and 39 %, respectively [25]. As a major conclusion from this prior work, both the opening of the first ring to ROPs and the opening of the second ring to OCDs, *i.e.* the rupture of endocyclic C-C-bonds on HIPEROcs proceeds *via* hydrogenolysis on the respective metal rather than *via* carbocations on the acid sites.

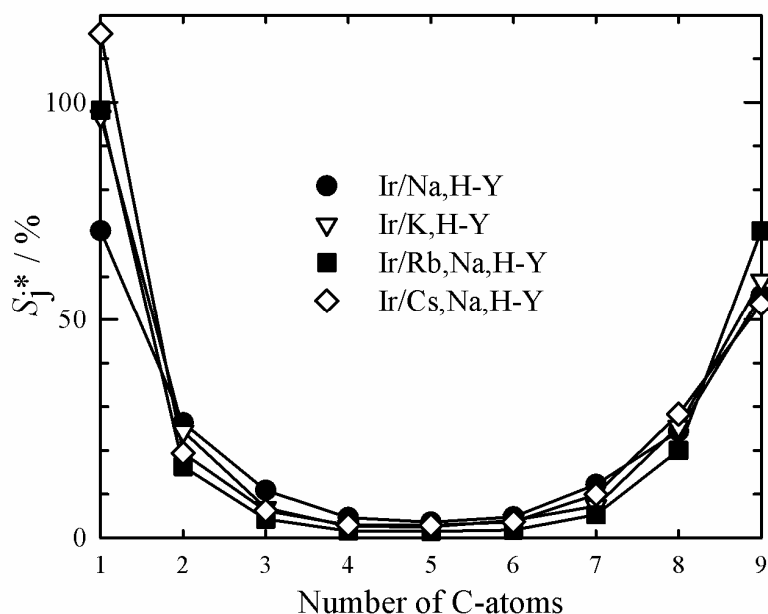


Figure 4.26: Carbon number distributions of the hydrocracked products on iridium-containing Y zeolites with different charge-compensating cations in the hydroconversion of cis-decalin [25].

In another recent study [90], HIPEROs based on zeolite Y, *viz.* 3.0Ir/Na_{0.90}H_{0.10}-Y and 3.7Pt/Na_{0.88}H_{0.12}-Y, were used in the hydroconversion of perhydroindane (bicyclo[4.3.0]nonane) in which a six- and a five-membered naphthenic ring are combined. Maximum yields of open-chain nonanes amounting to 49 and 55 %, respectively, were achieved, *i.e.*, significantly better results than with decalin as model hydrocarbon. This result probably has its origin in the more facile hydrogenolysis of five-membered compared to six-membered naphthenic rings. In the same study [90], zeolite 1.1Pd/Na_{0.70}H_{0.30}-Beta enabled only low yields of open-chain nonanes ($Y_{\text{OCNs, max.}} = 6\%$) reflecting the poor performance of this metal in the hydrogenolytic cleavage of endocyclic C-C bonds.

Summing up, the pertinent literature clearly shows that monofunctional catalysts, either acidic or metallic, are not suitable to gain high yields of open-chain alkanes: Monofunctional acidic catalysts suffer from a strong deactivation due to coke formation and the formation of large amounts of dehydrogenated and hydrocracked products. Monofunctional metallic catalysts perform slightly better: Due to the dehydrogenation/hydrogenation ability of noble metals, the formation of coke is suppressed, and, especially at the elevated hydrogen pressures usually applied, the formation of dehydrogenated products is much less favored. Although the hydrogenolytic ring opening of bicyclic naphthenes is possible on a non-acidic noble metal catalyst, the ring opening of six-membered rings is too slow to yield open-chain alkanes in high amounts.

However, it has been demonstrated in a few very recent publications [25, 89, 90] that bifunctional catalysts with a low concentration of Brønsted acid sites and a relatively large amount of the noble metals iridium or platinum are promising for the selective ring opening of multi-ring naphthenes. In this field, there seems to be room for further catalyst improvement. In particular, the concept of combining low concentrations of Brønsted acid sites with high amounts of noble metals to generate HIPEROs can be extended to other zeolite structures. In addition, the variation of the strength of the Brønsted acid sites may be used to optimize the catalysts for a further improvement of the yields of open-chain decanes from decalin.

5 Experimental Section

The chemicals and purchased zeolites used in this work are listed in Table 5.1.

Table 5.1: Used chemicals and purchased zeolites.

Chemical	Producer, Purity / Composition
18-crown-6	Fluka, purum
Aluminum isopropoxide	Merck, > 98 wt.-%
Aluminum sulfate 18 hydrate	Riedel-de Haën, chemically pure
Ammonium nitrate	Merck, > 99 wt.-%
Cesium chloride	Sigma, > 99 wt.-%
Chromosorb	Merck, particle size: 0.25 - 0.60 mm, P/AW
cis-Decalin	Merck, 97.4 wt.-%
Hydrofluoric acid	Merck, 40 wt.-%
Hydrogen 5.0	Westfalen AG, 99.999 vol.-%
Levasil 200N	Akzo Nobel, 30 wt.-% SiO ₂ in H ₂ O
Lithium chloride	Sigma-Aldrich, > 99 wt.-%
Ludox AS-40	Sigma-Aldrich, 40 wt.-% SiO ₂ in H ₂ O, average particle size: 22 nm
Ludox HS-40	Aldrich, 40 wt.-% SiO ₂ in H ₂ O, average particle size: 12 nm
Ludox SM-30	Sigma-Aldrich, 30 wt.-% SiO ₂ in H ₂ O, average particle size: 7 nm
Pentaamminechloroiridium(III) chloride	Colonial Metals, 49.9 wt.-% Ir
Pentaamminechlororhodium(III) chloride	Alfa Aesar, 34.5 wt.-% Rh
Phosphoric acid	Sigma-Aldrich, 99.999 wt.-%
Potassium chloride	Riedel-de Haën, > 99.5 wt.-%
Rhenium(III) chloride	Alfa Aesar, > 99 wt.-%
Rubidium chloride	Aldrich, > 99 wt.-%
Ruthenium(III) chloride	Alfa Aesar, > 99 wt.-%
Sodium aluminum oxide	Riedel-de Haën, 54 wt.-% Al ₂ O ₃ , 41 wt.-% Na ₂ O, 5 wt.-% H ₂ O
Sodium hydroxide	ChemSolute, 99 wt.-%
Sodium nitrate	Merck, > 99 wt.-%
Sulfuric acid	unknown, 96 %
Tetraamminepalladium(II) chloride hydrate	ChemPur, 40.62 wt.-% Pd
Tetraammineplatinum(II) chloride hydrate	ChemPur, 55.63 wt.-% Pt
Tetraethylammonium hydroxide solution	Sigma-Aldrich, 40 wt.-%
Triethylamine	Merck-Schuchardt, > 99 wt.-%
Zeolite [B]Beta	Eni S.p.A.
Zeolite L	Tosoh, lot No. 50KA8802
Zeolite mordenite	Strem Chemicals, lot No. 14-763
Zeolite Y	Strem Chemicals, lot No. 148 960
Zeolite ZSM-5	Degussa, lot No. KM-426

5.1 Preparation of the Catalysts

5.1.1 Dry-Gel Conversion

For the synthesis of [Al]Beta and SAPO-5 the so-called dry-gel conversion (DGC) was used [91]. The essential feature of this method is the use of a dry gel which comes in contact with vapors only. After drying in air, the powdered gel was placed on a porous plate in a Teflon-lined autoclave (Figure 5.1). Pure water is provided from the gas phase. After each conversion the resulting zeolite was filtered, washed with 1 dm³ demineralized water and dried for at least 12 h at 80 °C in an oven. The template was removed by heating under a nitrogen flow rate of 58 dm³·h⁻¹ from room temperature to 450 °C with a heating rate of 1 K · min⁻¹ and holding at 450 °C for 24 h and then switching the gas to synthetic air with a flow rate of 58 dm³·h⁻¹ and holding the temperature for another 24 h.

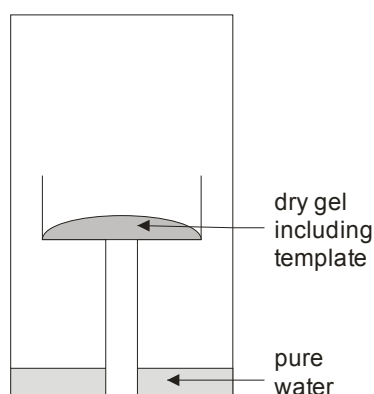


Figure 5.1: Schematic drawing of the autoclave used for the DGC.

5.1.2 Starting Materials

Zeolites Y (lot No. 148 960) and mordenite (lot No. 14-763) were purchased from Strem Chemicals, zeolite L was purchased from Tosoh (lot No. 50KA8802) and Zeolite ZSM-5 from Degussa (lot No. KM-426). Zeolite [B]Beta was kindly provided by Eni S.p.A. Zeolites [Al]Beta, EMC-2 and SAPO-5 were synthesized according to the procedures described in the next paragraphs. Some of these zeolites were prepared by Dr. Sandra Rabl, Dipl.-Chem. Dennis Wan Hussin, Dipl.-Chem. Gregor Näfe, Dipl.-Chem. Matthias Aimer and Dipl.-Chem. Daniel Pötsch.

Zeolites [Al]Beta

Na-[Al]Beta-24 seeds [92]

Aluminum-rich Beta zeolites were synthesized by hydrothermal synthesis after a recipe that needed nano-crystalline [Al]Beta zeolite as seeds. For the synthesis of these seeds 49.714 g tetraethylammonium hydroxide solution (TEAOH) and 0.450 g NaOH were mixed and stirred for 30 min at room temperature. Afterwards, 1.581 g aluminum isopropoxide were added, and stirring was continued till a solution was obtained. Finally, 75.200 g Ludox SM-30 were added, and the gel was stirred for another 30 min. The crystallization was carried out for 2 d at 100 °C in stainless steel autoclaves with Teflon inlets. The resulting solid was separated by centrifugation for 45 min at 15000 rpm. Afterwards the zeolite was suspended in demineralized water and the nanocrystallites were separated from each other by means of an ultrasonic bath. Finally, the water was removed by freeze drying. No calcination step was applied. The $n_{\text{Si}} / n_{\text{Al}}$ ratio of the gel was 48.5, and the $n_{\text{Si}} / n_{\text{Al}}$ ratio of the solid sample determined by ICP-OES amounted to 24.2.

Na-[Al]Beta-8 [92]

For the synthesis of Na-[Al]Beta-8 zeolite, 3.082 g aluminum isopropoxide, 6.192 g NaOH, and 50.082 g Ludox SM-30 were mixed and stirred for 30 min at room temperature. 1.020 g Na-[Al]Beta-24 seeds were added, and the gel was stirred for another 30 min. The crystallization was carried out for 12 d at 100 °C in stainless steel autoclaves with Teflon inlets. Finally, the resulting zeolite was filtered, washed with 1 dm³ demineralized water and dried for at least 12 h at 80 °C in an oven. The template was removed by heating under a nitrogen flow rate of 58 dm³ · h⁻¹ from room temperature to 450 °C with a heating rate of 1 K · min⁻¹ and holding at 450 °C for 24 h and then switching the gas to synthetic air with a flow rate of 58 dm³ · h⁻¹ and holding the temperature for another 24 h. Subsequently, the zeolite sample was stirred two times for 4 h at 80 °C in 40 cm³ of a 1 M aqueous solution of NaNO₃ per 1 g of dry zeolite sample. After each treatment the sample was filtrated and washed with demineralized water until no nitrate ions could be detected any more and dried for at least 12 h at 80 °C in an air oven. The $n_{\text{Si}} / n_{\text{Al}}$ ratio of the gel was 16.6, and the $n_{\text{Si}} / n_{\text{Al}}$ ratio of the solid sample determined by ²⁹Si MAS NMR amounted to 7.7.

Na-[Al]Beta-14 [93, 94]

The synthesis was carried out according to the dry-gel synthesis method described in Section 5.1.1, page 50. 9.980 g aluminum sulfate 18 hydrate were dissolved in 5.0 g demineralized water, heated to 80 °C and stirred for 30 min. Meanwhile, 69.190 g colloidal silica (Ludox HS-40), 66.842 g TEAOH and 12.977 g NaOH solution (4 mol · dm⁻³) were mixed and stirred for 30 min at room temperature. Subsequently, the two solutions were put together and stirred for another 2 h at room temperature. After this, the resulting gel was heated to 80 °C with an oil bath and dried while stirring. Approximately 1.5 g of the dry gel were placed in the Teflon-lined autoclave described in Section 5.1.1 with 2 g of demineralized water. The conversion was carried out at 175 °C for 48 h. The $n_{\text{Si}} / n_{\text{Al}}$ ratio of the dry gel was 15.4, and the $n_{\text{Si}} / n_{\text{Al}}$ ratio of the solid sample determined by ICP-OES amounted to 14.0.

Na-[Al]Beta-21 [93, 94]

The synthesis was carried out according to the dry-gel synthesis method described in Section 5.1.1, page 50. 7.291 g aluminum sulfate 18 hydrate were dissolved in 5.0 g demineralized water, heated to 80 °C and stirred for 30 min. Meanwhile, 69.190 g colloidal silica (Ludox HS-40), 66.842 g TEAOH and 12.977 g NaOH solution (4 mol · dm⁻³) were mixed and stirred for 30 min at room temperature. Subsequently, the two solutions were put together and stirred for another 2 h at room temperature. After this, the resulting gel was heated to 80 °C with an oil bath and dried while stirring. Approximately 1.5 g of the dry gel were placed in the Teflon-lined autoclave described in Section 5.1.1 with 2 g of demineralized water. The conversion was carried out at 175 °C for 48 h. The $n_{\text{Si}} / n_{\text{Al}}$ ratio of the dry gel was 21.1, and the $n_{\text{Si}} / n_{\text{Al}}$ ratio of the solid sample determined by ICP-OES amounted to 20.9.

Zeolite SAPO-5

The SAPO-5 samples were also prepared by the DGC-method after Ref. [95]. First, 20.43 g aluminum isopropoxide were dissolved in 15.81 g of demineralized water. Then, 11.53 g of 85 wt.-% H_3PO_4 which were diluted by addition of 15.81 g of water, were added dropwise under continuous stirring, followed by addition of 4.51 g of Ludox AS-40 to the gel. Afterwards, 5.05 g of triethylamine were added, and stirring was continued until the gel became homogeneous. The gel was then dried at 80 °C in an oil bath with continuous stirring, allowing the evaporation of water. Approximately 1.5 g of the resulting solid were placed in a Teflon-lined autoclave described in Section 5.1.1, page 50 with 2 g of demineralized water. The crystallization of the dry gel was carried out at 175 °C for 24 h under autogenous pressure. The $n_{\text{Si}} / n_{\text{Al}}$ ratio of the solid sample determined by ICP-OES amounted to 0.28, the $n_{\text{Si}} / n_{\text{P}}$ ratio to 0.29, and the $n_{\text{Na}} / (n_{\text{Al}} - n_{\text{P}})$ ratio to 0.04.

Zeolite EMC-2

The synthesis gel for the crystallization of zeolite EMC-2 [96] was prepared by dissolving 7.27 g sodium aluminate, 8.81 g 18-crown-6, and 6.05 g of a 50 wt.-% NaOH solution in 39 g of demineralized water. The resulting solution was then mixed with 77.0 g of silica sol (Levasil 200N) under vigorous stirring until a homogeneous gel was formed. The gel was placed in a Teflon-lined stainless steel autoclave and aged at room temperature for 24 h without stirring. The conversion was carried out at 110 °C for 12 days. For template removal, the material was first heated from room temperature to 540 °C with a heating rate of 1 K·min⁻¹ under a nitrogen flow of 43 dm³ · h⁻¹. After 24 h at 540 °C the flow was switched to air with the same flow rate, and the sample was held at this temperature for another 24 h. The $n_{\text{Si}} / n_{\text{Al}}$ ratio of the gel was 5.0, and the $n_{\text{Si}} / n_{\text{Al}}$ ratio of the solid sample determined by ICP-OES amounted to 4.3.

5.1.3 Modification of the Zeolites

Prior to any modification step all zeolite samples except for zeolites K-L and K,Cs-L were stirred for 4 h at 80 °C in 40 cm³ of a 1 M aqueous solution of NaNO_3 per 1 g of dry zeolite sample. After the treatment the samples were filtered and washed with demineralized water until no nitrate ions could be detected any more and dried for at least 12 h at 80 °C in an air oven. The purpose of this procedure was to ensure that all exchangeable cation positions were occupied by sodium, such as to start from a well-defined zeolite composition for each modification step. Zeolite K-L was used as purchased for the noble-metal exchange.

Ion Exchange with Alkali Metals

The starting materials for all alkali metal ion exchanges were the sodium forms of the zeolites.

Li_{0.72}H_{0.28}-[Al]Beta-14

Zeolite Li-[Al]Beta-14 was prepared by ion exchange of Na-[Al]Beta-14 with LiCl. The starting material was slurried under stirring in 33 g of a 1 M aqueous solution of LiCl per gram of dry Na-[Al]Beta-14. The suspension was stirred for 4 h at 80 °C. Upon filtration, the zeolite was washed with demineralized water and dried at 80 °C for 12 h in an air oven. The final $n_{\text{Li}} / n_{\text{Al}}$ ratio as determined by ICP-OES amounted to 0.72. Sodium could not be detected.

K_{0.87}Na_{0.13}-[Al]Beta-14

Zeolite Na-[Al]Beta-14 was slurried under stirring in 33 g of a 1 M aqueous solution of KCl per gram of dry Na-[Al]Beta-14. The suspension was stirred for 4 h at 80 °C. Upon filtration, the zeolite was washed with demineralized water and dried at 80 °C for 12 h in an air oven. The final $n_{\text{K}} / n_{\text{Al}}$ ratio as determined by ICP-OES amounted to 0.87 and the $n_{\text{Na}} / n_{\text{Al}}$ ratio to 0.13.

Rb_{0.95}Na_{0.05}-[Al]Beta-14

Zeolite Na-[Al]Beta-14 was slurried under stirring in 42 g of a 0.1 M aqueous solution of RbCl per gram of dry Na-[Al]Beta-14. The suspension was stirred for 4 h at 80 °C. Upon filtration, the zeolite was washed with demineralized water and dried at 80 °C for 12 h in an air oven. The final $n_{\text{Rb}} / n_{\text{Al}}$ ratio as determined by ICP-OES amounted to 0.95 and the $n_{\text{Na}} / n_{\text{Al}}$ ratio to 0.05.

Cs_{0.97}Na_{0.03}-[Al]Beta-14

Zeolite Na-[Al]Beta-14 was slurried under stirring in 42 g of a 0.1 M aqueous solution of CsCl per gram of dry Na-[Al]Beta-14. The suspension was stirred for 4 h at 80 °C. Upon filtration, the zeolite was washed with demineralized water and dried at 80 °C for 12 h in an

air oven. The final $n_{\text{Cs}} / n_{\text{Al}}$ ratio as determined by ICP-OES amounted to 0.97 and the $n_{\text{Na}} / n_{\text{Al}}$ ratio to 0.03.

$\text{K}_{0.81}, \text{Na}_{0.13}, \text{H}_{0.06}$ -[Al]Beta-8

The procedure for making K,Na-[Al]Beta-8 zeolite was similar to the potassium ion exchange mentioned above, except for the starting material which was Na-[Al]Beta-8. The final $n_{\text{K}} / n_{\text{Al}}$ ratio as determined by ICP-OES amounted to 0.81 and the $n_{\text{Na}} / n_{\text{Al}}$ ratio to 0.13.

$\text{Rb}_{0.65}, \text{Na}_{0.25}, \text{H}_{0.10}$ -[Al]Beta-8

The procedure for making Rb,Na-[Al]Beta-8 zeolite was similar to the rubidium ion exchange mentioned above, except for the starting material which was Na-[Al]Beta-8. The final $n_{\text{Rb}} / n_{\text{Al}}$ ratio as determined by ICP-OES amounted to 0.65 and the $n_{\text{Na}} / n_{\text{Al}}$ ratio to 0.25.

$\text{Cs}_{0.65}, \text{Na}_{0.25}, \text{H}_{0.10}$ -[Al]Beta-8

The procedure for making Cs,Na-[Al]Beta-8 zeolite was similar to the cesium ion exchange mentioned above, except for the starting material which was Na-[Al]Beta-8. The final $n_{\text{Cs}} / n_{\text{Al}}$ ratio as determined by ICP-OES amounted to 0.65 and the $n_{\text{Na}} / n_{\text{Al}}$ ratio to 0.25.

$\text{K}_{0.66}, \text{Cs}_{0.34}$ -L-2.9

The procedure for making K,Cs-L zeolite was similar to the cesium ion exchange mentioned above, except for the starting material which was K-L-2.9. The final $n_{\text{Cs}} / n_{\text{Al}}$ ratio as determined by ICP-OES amounted to 0.34 and the $n_{\text{K}} / n_{\text{Al}}$ ratio to 0.66.

$\text{Cs}_{0.97}, \text{Na}_{0.03}$ -mordenite-5.8

The procedure for making Cs-mordenite zeolite was similar to the cesium ion exchange mentioned above, except for the starting material which was Na-mordenite-5.8. The final $n_{\text{Cs}} / n_{\text{Al}}$ ratio as determined by ICP-OES amounted to 0.97 and the $n_{\text{Na}} / n_{\text{Al}}$ ratio to 0.03.

Incorporation of the Noble Metal

Solid-state ion exchange with ReCl_3

For the preparation of the rhenium-containing Na-Y zeolite, a physical mixture of ReCl_3 and Na-Y was heated from room temperature to 550 °C with a rate of 0.5 K · min⁻¹ in a fixed-bed reactor with a nitrogen flow of 175 cm³ · min⁻¹. The resulting solid was directly, *i.e.* without washing, used as a catalyst.

Ion exchange with $[\text{Pt}(\text{NH}_3)_4]\text{Cl}_2$ or $[\text{Ir}(\text{NH}_3)_5\text{Cl}]\text{Cl}_2$

The zeolites were suspended in 12 - 15 g demineralized water per gram of dry solid. An aqueous solution of $[\text{Pt}(\text{NH}_3)_4]\text{Cl}_2$ or $[\text{Ir}(\text{NH}_3)_5\text{Cl}]\text{Cl}_2$ in 50 g demineralized water was slowly added by means of a dropping funnel within 20 min under vigorous stirring. For the exchange with the platinum complex the amount of complex was calculated under the assumption that all platinum was loaded on the zeolite sample. In case of iridium an excess of 20 % was used in comparison to the calculated amount. At the end, the suspension was stirred for another 4 h at 80 °C. The solid was then filtered off, washed with demineralized water and dried for at least 12 h at 80 °C in an air oven.

Ion exchange with $[\text{Pd}(\text{NH}_3)_4]\text{Cl}_2 \cdot \text{H}_2\text{O}$, $[\text{Rh}(\text{NH}_3)_5\text{Cl}_2]\text{Cl}$ and RuCl_3

The three metals palladium, rhodium and ruthenium were introduced into the zeolites in a way similar to the above-described method except for the used metal salts, which were $[\text{Pd}(\text{NH}_3)_4]\text{Cl}_2 \cdot \text{H}_2\text{O}$, $[\text{Rh}(\text{NH}_3)_5\text{Cl}_2]\text{Cl}$ or RuCl_3 and that the mixtures were stirred at 80 °C for 24 h instead of 12 h.

Zeolites ZSM-5, Y, EMC-2, mordenite, L, [Al]Beta and [B]Beta exchanged with different alkali metals were used as supports. Table 6.2 and Table 6.3 in Section 6.1, pages 71 and 72, summarize the utilized zeolitic supports for the different ion exchanges and the resulting catalyst designations and chemical compositions.

5.1.4 Decomposition of the Noble-Metal Complex

After ion exchange, the Ir-, Pt-, Re-, Rh- and Ru-containing catalysts were calcined in air at 300 °C for 3 h in an oven with a heating rate of 0.5 K · min⁻¹ and a flow rate of 58 dm³ · min⁻¹ of synthetic air. This pretreatment was conducted to obtain catalysts in which

the noble metals are highly dispersed [97]. In the case of the palladium-loaded catalysts this step was omitted to achieve catalysts with high isomerization activity [90].

5.1.5 *Forming of the Catalyst Powder*

To avoid the high pressure drop catalyst powders would produce in a fixed-bed reactor, the zeolite powders were pressed without a binder at 127 MPa for 15 min, and the tablets thereby formed were crushed. The size fraction of $0.20 \text{ mm} < d_{\text{cat}} < 0.32 \text{ mm}$ was used for the catalytic experiments.

5.1.6 *Reduction of the Noble Metal*

The reduction of the noble metal on the catalysts was carried out in the catalytic flow-type apparatus described in Section 5.3, page 61, under a hydrogen pressure of 5.2 MPa and a hydrogen flow of $130 \text{ cm}^3 \cdot \text{min}^{-1}$ (referenced to 25 °C and 0.10 MPa) while heating the sample from room temperature to 360 °C with a rate of $2 \text{ K} \cdot \text{min}^{-1}$ and holding at 360 °C for 2 h. Moreover, the reduction of the divalent noble metal cation leads to the formation of two Brønsted acid sites (see Section 4.2).

5.2 Characterization of the Catalysts and Starting Materials

X-Ray Diffraction

To ensure that the synthesized zeolites were phase-pure and had retained their structures after the various modification steps powder X-ray diffractometry (XRD) was applied. A Bruker D8 Advance diffractometer and $\text{CuK}\alpha$ radiation ($\lambda = 0.154 \text{ nm}$) were used. The diffraction patterns were recorded between 2θ values of 5 and 50 ° with a step size of 0.02 ° and a step time of 0.2 s.

Chemical and Thermogravimetric Analysis

Silicon, aluminum, boron, sodium, potassium, rubidium, cesium and the noble metals iridium, platinum, palladium, rhenium, rhodium and ruthenium were determined by means of a Varian optical emission spectrometer with an inductively coupled plasma (ICP-OES) Vista-MPX CCD ICP-OES. For the analysis, *ca.* 100 mg of the zeolite sample were dissolved in 3 cm^3 of diluted hydrofluoric acid (10 wt.-% HF in doubly distilled water) and 6 cm^3 of

nitrohydrochloric acid. This mixture was filled up to 250 cm³ with doubly distilled water and was then analyzed. The main part of the measurements was kindly conducted by Mrs. Heike Fingerle.

The water content of the zeolites was measured by means of a Setaram Thermogravimetric Analyzer (TGA) Setsys TG-16/18. Prior to the analysis the zeolites were stored in a desiccator over a saturated aqueous solution of calcium nitrate for at least 24 h. In the TGA experiment, the zeolites were heated in a nitrogen flow from room temperature to 600 °C with a heating rate of 20 K · min⁻¹. The determined water content of the zeolites was used to calculate the mass of the dry samples. The measurements were kindly conducted by Mrs. Barbara Gering, Dipl.-Chem. Ines Kley, Dipl.-Chem. Nicole Weiß, Dipl.-Chem. Dennis Wan Hussin and Dr. Frank Salzbauer.

MAS NMR Spectroscopy

A Bruker MSL 400 spectrometer was used for measuring the ¹¹B, ²⁷Al and ²⁹Si MAS NMR spectra.

The ¹¹B MAS NMR spectra were measured in a 9 mm rotor at a resonance frequency of 128.4 MHz with 2400 accumulations. The spinning rate was 8.0 kHz, the pulse length 1 µs and the repetition time was 2 s. The spectrum was recorded against tetrahydroxoborate sodalite, and the WINFIT program from Bruker was used to simulate and integrate the signals.

For the measurements of the ²⁷Al MAS NMR spectra the zeolites were hydrated by storing them over a saturated aqueous sodium chloride solution at room temperature. The measurements were conducted in a rotor with a diameter of 9 mm at a resonance frequency of 104.3 MHz with 800 accumulations. The spinning rate was 9 kHz. The spectra were recorded against aluminum nitrate using a pulse length of 0.61 µs and a repetition time of 0.5 s.

A rotor with a diameter of 7 mm and a resonance frequency of 79.5 MHz with 380 to 1250 accumulations were used for the measurements of the ²⁹Si HPDEC MAS NMR spectra. A spinning rate of 4.0 kHz, a pulse length of 5 µs and a repetition time of 10 s were applied. The spectra were recorded against tetramethylsilane (TMS). The program WINFIT from Bruker was used to simulate and integrate the signals.

The quantitative measurements of ²⁹Si MAS NMR spectra allowed the determination of the $n_{\text{Si}} / n_{\text{T}}$ ratio (T = Al or B) of the zeolite framework by means of Eq. (5.1) [98], whereas ICP-OES measurements provide only the $n_{\text{Si}} / n_{\text{T}}$ ratio of the whole solid, which may contain, *e.g.*

amorphous silica or extra-framework aluminum. In general, the ^{29}Si MAS NMR spectra of zeolites consist of different signals which can be attributed to silicon atoms which are coordinated to zero, one, two, three or four aluminum or boron atoms. In Eq. (5.1), k is the number of aluminum or boron atoms coordinated to a silicon atom and F is the relative fraction of the different signals.

$$n_{\text{Si}}/n_{\text{T}} = \frac{\sum_{k=0}^4 F_{\text{Si}(k\text{T})}}{\sum_{k=0}^4 0.25 \cdot k \cdot F_{\text{Si}(k\text{T})}} \quad (5.1)$$

The measurements were kindly conducted by the working group of Prof. Dr. Michael Hunger.

H₂ Chemisorption

A Quantachrome Autosorb-1-C instrument was used for the determination of the noble-metal dispersion. Prior to the measurement the samples were reduced with the same temperature program as used in the reactor of the catalytic flow-type apparatus. The actual measurement consist of two isotherms measured at $T = 40\text{ }^\circ\text{C}$, where the first one is considered to be a combination of physis- and chemisorption, and the second isotherm, measured after evacuating the sample, is interpreted as physisorption only. The difference of these two isotherms originating from irreversibly and strongly adsorbed molecules is applied for calculating the noble-metal dispersion. For all samples an adsorption stoichiometry of $n_{\text{H}} / n_{\text{noble metal}} = 1$ was assumed. The measurements were kindly conducted by Dipl.-Chem. Andreas Haas and Mr. Matthias Scheibe.

N₂ Physisorption

For studying the porous properties of the catalysts, nitrogen physisorption in a Quantachrome Autosorb-1-C instrument was conducted. The sample was degassed for 16 h at $T_{\text{deg}} = 350\text{ }^\circ\text{C}$ prior to the N_2 physisorption experiment at the temperature of liquid nitrogen. For the calculation of the specific surface area A_{BET} according to Brunauer, Emmett and Teller (BET), those values of p / p_0 were chosen which led to a linear BET plot and a positive C -value (usually between 0.1 and 0.3). The measurements were kindly conducted by Dipl.-Chem. Andreas Haas and Mr. Matthias Scheibe.

Scanning Electron Microscopy

A scanning electron microscope (SEM) Cam Scan 44 was used to determine the morphology and the size of the zeolite crystals. The samples were coated with an ultrathin layer of gold by a sputter coating equipment K550 of Emitech. An excitation voltage of 5 kV was used to achieve a high resolution. The measurements were kindly conducted by Dipl.-Chem. Ines Kley, Dipl.-Chem. Arne Bressel, Dipl.-Chem. Christian Lieder and Dipl.-Chem. Daniel Geiß.

FT-IR Spectroscopy

To investigate the acid properties of the zeolites, FT-IR spectroscopic measurements with pyridine as probe molecule were applied. The used spectrometer was a Vector 22 from Bruker with a high-vacuum sample cell. Prior to the measurements the samples were pressed into very thin, rectangular self-supporting wafers with edge lengths of 10 mm and *ca.* 20 mm. The discs were placed in a metal IR cell with CaF₂ windows, a vacuum system and a separated oven (see Figure 5.2). The metal-loaded zeolites were reduced in a flow of 100 cm³ · min⁻¹ of hydrogen with a heating rate of 2 K · min⁻¹ up to 500 °C and holding for 2 h in the oven. After the reduction, the sample cell and the oven were evacuated for 4 h at 100 °C with a vacuum of 2.0 · 10⁻⁶ Pa. After that, pyridine vapor was introduced into the cell for 30 min with $p_{\text{pyridine}} = 3.3$ Pa. The physically adsorbed pyridine was removed by evacuating for 1 h at 200 °C. Subsequently, the wafer was placed into the measurement cell, and a spectrum was recorded at 80 °C. Afterwards, the wafer was moved back into the oven, the temperature was raised in 50 °C steps from 200 to 500 °C, and a spectrum was recorded at every step. For the evaluation of the spectra the band of the Brønsted acid sites at 1544 cm⁻¹ [35] was integrated.

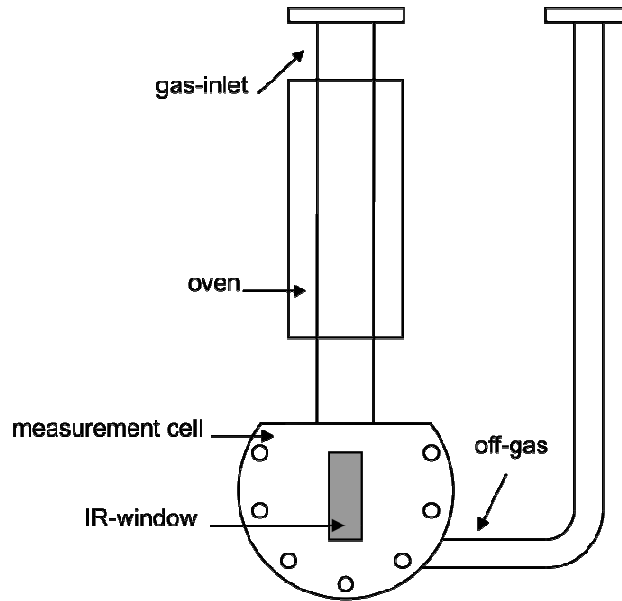


Figure 5.2: Scheme of the FT-IR sample cell with oven.

For the calculation of the concentration of adsorbed pyridine the following equation was used [16]:

$$c_{\text{pyridine}} = \frac{\bar{A} \cdot l_1 \cdot l_2}{m \cdot \varepsilon} \quad (5.2)$$

\bar{A} stands for the integral absorption coefficient with the unit $[\text{cm}^{-1}]$; l_1 and l_2 indicate the edge lengths and m the mass of the dry wafer, while ε is the extinction coefficient. The value for ε is taken from the literature [45] and is for Brønsted acid sites $1.67 \text{ cm} \cdot \mu\text{mol}^{-1}$.

5.3 Conditions in the Catalytic Experiments

In all catalytic experiments cis-decalin (purity 97.4 wt.-%; impurities: trans-decalin 0.9 wt.-%; other impurities 1.7 wt.-%, mainly skeletal isomers of decalin and hydrocarbons with more than 10 carbon atoms) was used as feed hydrocarbon. The mass of dry catalyst was varied between 0.17 and 0.22 g corresponding to a bulk volume of 0.4 cm^3 . The reaction temperature was varied between 195 and $370 \text{ }^\circ\text{C}$. The total pressure was 5.2 MPa, while the partial pressure of cis-decalin at the reactor entrance was 25 kPa corresponding to a saturator temperature of $135 \text{ }^\circ\text{C}$. Corresponding to a hydrogen flow of $130 \text{ cm}^3 \cdot \text{min}^{-1}$ (referenced to $25 \text{ }^\circ\text{C}$ and 0.10 MPa) the *LHSV* assumed values between 0.3 and 0.4 h^{-1} . One experiment was conducted at 8.0 MPa total pressure. For this experiment the partial pressure of cis-decalin at the reactor entrance, the *LHSV* and the bulk volume of catalyst were kept at the same values as for the other experiments, *viz.* 25 kPa, 0.4 h^{-1} and 0.4 cm^3 , respectively. To achieve this,

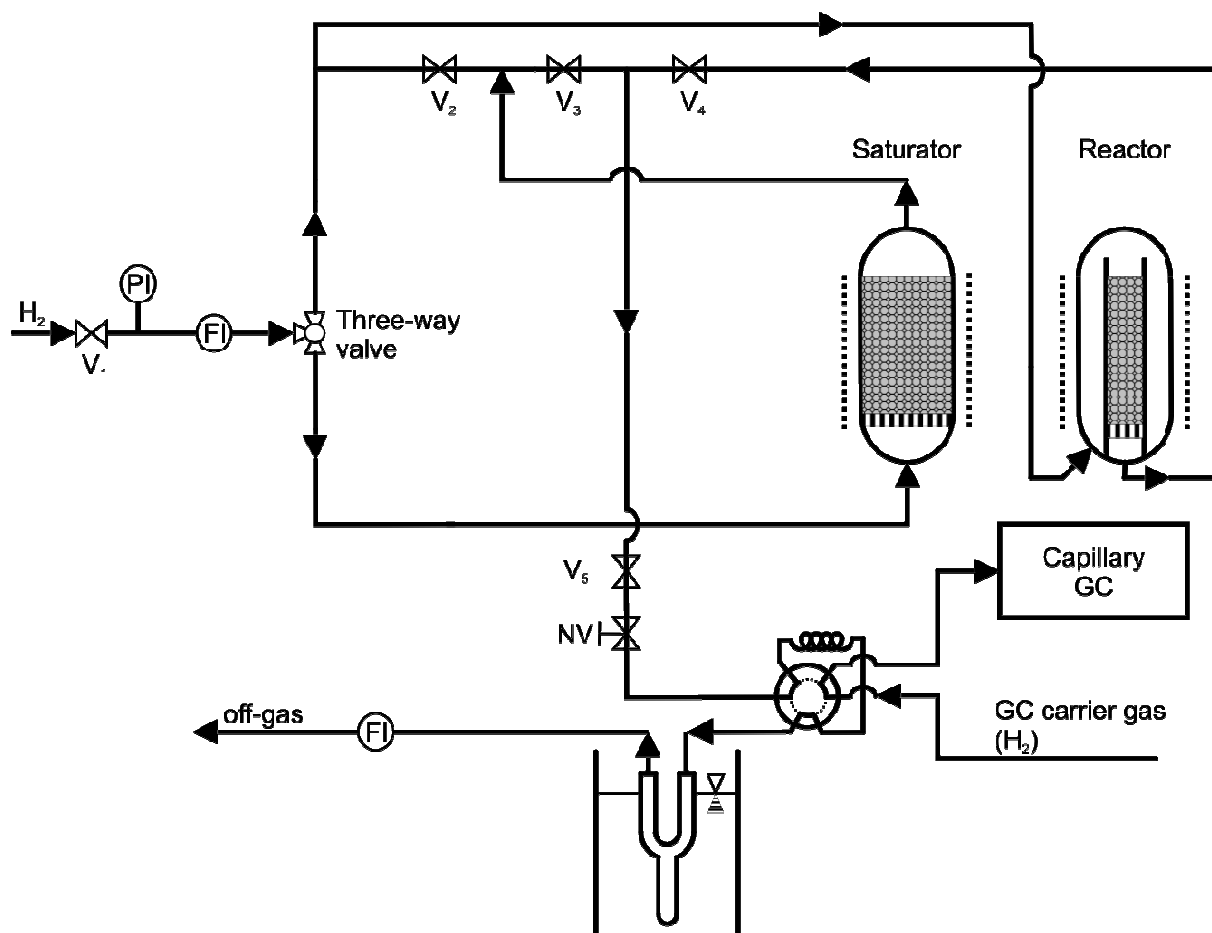


Figure 5.3: Scheme of the high-pressure flow-type apparatus used for the catalytic hydroconversion of cis-decalin (FI: flow indicator; GC: gas chromatograph; NV: needle valve; PI: pressure indicator; V: shut-off valve).

the saturator temperature was decreased to 133 °C and the hydrogen flow was raised to $180 \text{ cm}^3 \cdot \text{min}^{-1}$. Usually, two samples of gaseous products were injected into the capillary gas chromatograph (GC) for analysis at each reaction temperature. The first sample was taken after 45 min time-on-stream and the second after 205 min time-on-stream. For the evaluation of the experiments, usually the results of the second analysis were chosen.

All catalytic experiments were conducted in a high-pressure flow-type apparatus shown schematically in Figure 5.3. The main parts of this apparatus were a fixed-bed saturator filled with an inert solid (chromosorb P/AW, 0.25 - 0.60 mm) and impregnated with cis-decalin, a fixed-bed reactor and a heated gas sampling valve which was connected to a capillary gas chromatograph. All parts downstream the saturator were kept at elevated temperature to avoid condensation of the hydrocarbon vapors. The saturator and the reactor were heated separately, and the temperatures were controlled by temperature controllers (Omega CN3000).

Hydrogen was taken from a pressurized cylinder, and the pressure was reduced to 5.2 MPa by means of a pressure reducer. Through a three-way valve, the hydrogen flow could be directed either to the saturator or the reactor. For the reduction of the noble metal, the hydrogen flow was directed directly through the fixed-bed reactor (see Figure 5.4) and afterwards through valves V_4 and V_5 to a needle valve where the gas was expanded to ambient pressure. Subsequently, the gas flow was directed *via* a heated 6-port-2-position valve to the off-gas. The feed gas entered the reactor at the bottom and flowed upwards while it was preheated to the desired reaction temperature. At the top of the reactor the flow direction was changed, and the feed gas passed downwards through the fixed-bed of catalyst.

For the catalytic experiments, the feed gas was previously directed through the saturator where it was loaded with vapor of cis-decalin. For that purpose, the hydrogen flow was directed *via* the three-way valve to the saturator and afterwards through valve V_2 to the reactor. After the reaction, the product gas flow was directed to the needle valve *via* the opened valve V_4 . The valve V_3 remained closed. By means of the 6-port-2-position valve the product gas flow could either be automatically injected into the GC for product analysis or routed to the off-gas where the product gas flow was cooled to $-10\text{ }^\circ\text{C}$ by means of a cooling trap. In the cooling trap, storable liquid product samples were gained. These samples were used for qualitative product identification by GC/MS. All quantitative evaluations were based on the analysis of the gaseous products by the capillary gas chromatograph.

For the calibration of the saturator temperature for the desired $n_{\text{H}_2} / n_{\text{c-Dec}}$ ratio the hydrogen flow was routed directly through the saturator. After the expansion of the gas *via* the needle valve the mixture was analyzed by the GC.

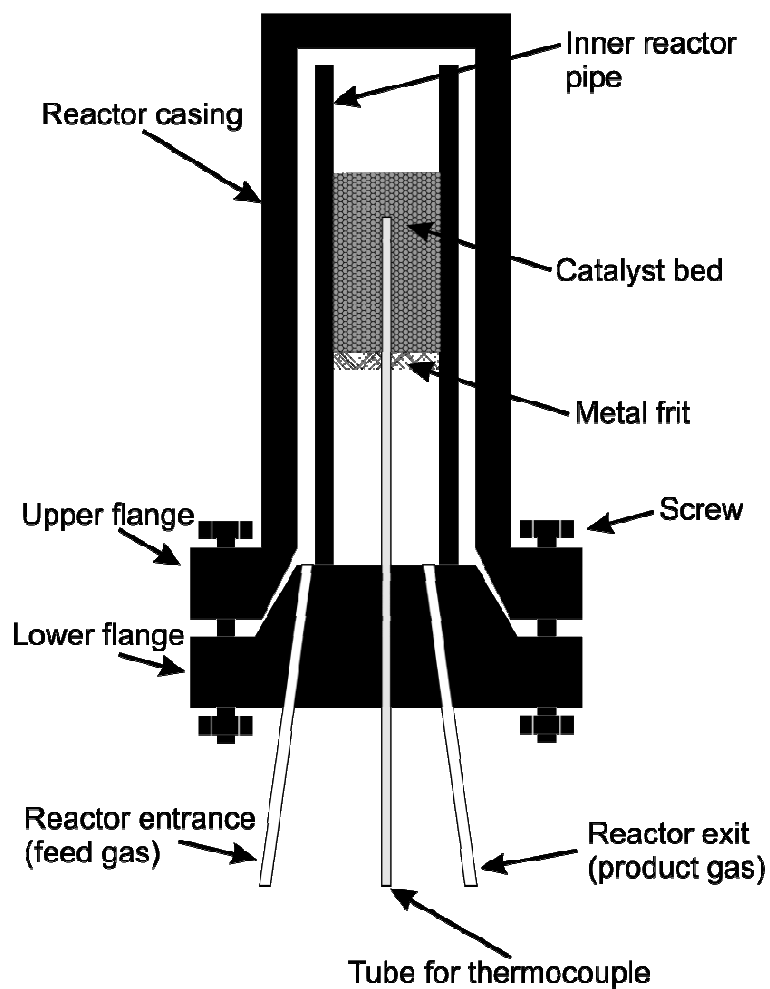


Figure 5.4: Detailed drawing of the fixed-bed reactor. After Ref. [89].

5.4 Product Analysis by Capillary Gas Chromatography

On-Line Gas Chromatography

For the quantitative analysis the gaseous reaction products were injected into a capillary gas chromatograph *via* a gas sampling valve (see Figure 5.3). An Agilent 7890 A instrument and a PC with an Agilent Chemstation software was used. Details of the analytical conditions are listed in Table 5.2.

Table 5.2: Conditions of the on-line analyses of the products of the cis-decalin hydroconversion by capillary gas chromatography.

Column	Petrocol DH 150
Stationary phase	Dimethyl polysiloxane
Length	150 m
Internal diameter	0.25 mm
Film thickness	1.0 μm
Temperature program	10 min at 35 °C; heating with 1 K · min ⁻¹ to 100 °C; heating with 0.5 K · min ⁻¹ to 140 °C; hold for 1 min
Carrier gas	Hydrogen
Pressure at column entrance	193 - 267 kPa
Flow through column	1.5 cm ³ · min ⁻¹
Injection	<i>via</i> gas sampling loop
Volume of sampling loop	250 μl
Split ratio	5 : 1
Injector temperature	250 °C
Detector	Flame ionization detector (FID)
Temperature	250 °C
\dot{V}_{H_2} to FID	35 cm ³ · min ⁻¹
\dot{V}_{air} to FID	350 cm ³ · min ⁻¹

Off-Line Gas Chromatography / Mass Spectrometry

A second gas chromatograph (Agilent 6890 N) coupled with a mass spectrometer (Agilent 5876 B inert XL MSD) was used for the analysis of the liquid product samples collected in the cooling trap. The aims of these analyses were the qualitative peak assignments. Summarized in Table 5.3 are the conditions of the GC/MS analyses.

Table 5.3: Conditions of the off-line analyses of the products of the cis-decalin hydroconversion by capillary gas chromatography / mass spectrometry.

Column	Petrocol DH 150
Stationary phase	Dimethyl polysiloxane
Length	150 m
Internal diameter	0.25 mm
Film thickness	1.0 μm
Temperature program	10 min at 35 $^{\circ}\text{C}$; heating with 1 $\text{K} \cdot \text{min}^{-1}$ to 100 $^{\circ}\text{C}$; heating with 0.5 $\text{K} \cdot \text{min}^{-1}$ to 180 $^{\circ}\text{C}$; hold for 1 min
Carrier gas	Helium
Pressure at column entrance	320 - 473 kPa
Flow through column	1.5 $\text{cm}^3 \cdot \text{min}^{-1}$
Injection	Liquid, <i>via</i> syringe
Injected volume	0.1 μl
Split ratio	5 : 1
Injector temperature	250 $^{\circ}\text{C}$
Detector	Flame ionization detector (FID)
Temperature	250 $^{\circ}\text{C}$
\dot{V}_{H_2} to FID	35 $\text{cm}^3 \cdot \text{min}^{-1}$
\dot{V}_{air} to FID	350 $\text{cm}^3 \cdot \text{min}^{-1}$
Mass spectrometer	
Acceleration voltage	70 eV
Temperature of ion source	230 $^{\circ}\text{C}$
Temperature of quadrupole analyzer	150 $^{\circ}\text{C}$

5.5 Evaluation of the Catalytic Experiments

Terminology of the Reactions and Products

Due to the high complexity of the product mixture obtained in the hydroconversion of cis-decalin, a classification of the possible reactions and products into classes is useful. Five different reactions are possible during the hydroconversion of cis-decalin which are summarized in Table 5.4. In addition, the short designations of the resulting products used in this work are given. Since trans-decalin is formed in a very fast isomerization reaction it is lumped together with cis-decalin to the pseudo-reactant decalin (Dec).

Table 5.4: Reactions occurring in the catalytic conversion of cis-decalin (c-Dec) with hydrogen.

Reaction	Products	Formula	Short Designation
Isomerization	Isomers	$C_{10}H_{18}$	Isos
	a) trans-decalin		tr-Dec
	b) skeletal isomers		sk-Isos
Ring opening	Ring-opening products	$C_{10}H_{20}$	ROPs
	a) alkylcyclopentanes		
	b) alkylcyclohexanes		
Double ring opening	Open-chain decanes	$C_{10}H_{22}$	OCDs
Dehydrogenation	Dehydrogenated products		DHPs
	a) tetralin	$C_{10}H_{12}$	Ttr
	b) naphthalene	$C_{10}H_8$	Nap
Hydrocracking	Hydrocarbons with less than 10 carbon atoms		C_9^-
	a) gaseous hydrocarbons		$C_1 - C_4$
	b) liquid hydrocarbons		$C_5 - C_9$

Assignment of the GC Signals

The assignment of the GC signals was mainly achieved by GC/MS analyses of the liquid samples collected in the cooling trap. Although it was not possible to assign each signal to a specific hydrocarbon, the molar mass of each signal could be determined. This in turn made it possible to assign the signals to the different product groups listed in Table 5.4.

For a further advancement of the assignment of the GC signals, pure hydrocarbons, whenever they were commercially available, and hydrocarbon mixtures with known compositions were co-injected with the liquid product samples. The hydrocarbon mixtures were generated by catalytic isomerization of n-octane, n-nonane and n-decane (see Refs. [54, 89] for further information). Especially the co-injection of the iso-decane mixture was useful for the safe assignment of the peaks of OCDs. In the Appendix 9.1, page 148, the most up-to-date version of the peak assignment is given.

Calculations of Conversion, Yields and Selectivities

The calculations of the conversion X_{Dec} , the yield of products Y_j and the selectivity of products S_j were based on equations for a continuously operated flow-type reactor:

$$X_{Dec} = \frac{(\dot{n}_{Dec})_{in} - (\dot{n}_{Dec})_{out}}{(\dot{n}_{Dec})_{in}} \quad (5.3)$$

$$Y_j = \frac{(\dot{n}_j)_{out} - (\dot{n}_j)_{in}}{(\dot{n}_{Dec})_{in}} \cdot \frac{|\gamma_{Dec}|}{\gamma_j} \quad (5.4)$$

$$S_j = \frac{(\dot{n}_j)_{out} - (\dot{n}_j)_{in}}{(\dot{n}_{Dec})_{in} - (\dot{n}_{Dec})_{out}} \cdot \frac{|\gamma_{Dec}|}{\gamma_j} \quad (5.5)$$

\dot{n} and γ are the molar flux and the stoichiometric factor, respectively. While $(\dot{n}_{Dec})_{out}$ and $(\dot{n}_j)_{out}$ can be directly calculated from the areas of the cis- and trans-decalin peak A_{Dec} and the area of the respective product peak A_j (see Appendix 0, page 156), the calculation of $(\dot{n}_{Dec})_{in}$ is not so straightforward. The derivations of the equations for the calculation of the conversion, the yields and selectivities are given in Appendix 9.2, page 152. Equations (5.6) to (5.8) are used for the calculation of X_{Dec} , Y_j and S_j , respectively.

$$X_{Dec} = \frac{\sum_j \frac{|\gamma_{Dec}|}{\gamma_j} \cdot \frac{M_{Dec}}{M_j} \cdot f_j \cdot A_j}{f_{Dec} \cdot A_{Dec} + \sum_j \frac{|\gamma_{Dec}|}{\gamma_j} \cdot \frac{M_{Dec}}{M_j} \cdot f_j \cdot A_j} \quad (5.6)$$

$$Y_j = \frac{f_j \cdot A_j}{f_{Dec} \cdot A_{Dec} + \sum_j \frac{|\gamma_{Dec}|}{\gamma_j} \cdot \frac{M_{Dec}}{M_j} \cdot f_j \cdot A_j} \cdot \frac{|\gamma_{Dec}|}{\gamma_j} \cdot \frac{M_{Dec}}{M_j} \quad (5.7)$$

$$S_j = \frac{f_j \cdot A_j}{\sum_j \frac{|\gamma_{Dec}|}{\gamma_j} \cdot \frac{M_{Dec}}{M_j} \cdot f_j \cdot A_j} \cdot \frac{|\gamma_{Dec}|}{\gamma_j} \cdot \frac{M_{Dec}}{M_j} \quad (5.8)$$

A , f and M are the peak area in the chromatogram, the FID correction factor and the molar mass, respectively. For a better understanding of the hydrocracking mechanisms the hydrocracked products were analyzed in detail. The results will be presented in terms of the modified hydrocracking selectivity S_j^* . It is defined as the molar amount of hydrocarbons with j carbon atoms formed ($j = 1$ to 9) divided by the molar amount of decalin converted into hydrocracked products (Eq. (5.9)):

$$S_j^* = \frac{(\dot{n}_j)_{\text{out}}}{(\dot{n}_{\text{Dec}})_{\text{converted to C}_9\text{-}}} = \frac{f_j \cdot A_j}{\sum_j \frac{|\gamma_{\text{Dec}}|}{\gamma_j} \cdot \frac{M_{\text{Dec}}}{M_j} \cdot f_j \cdot A_j} \cdot \frac{M_{\text{Dec}}}{M_j} \quad (5.9)$$

Liquid Hourly Space Velocity

The liquid hourly space velocity (*LHSV*) is defined as the hourly volume of liquid decalin at room temperature and 1 bar divided by the bulk volume of the catalyst bed (Eq. (5.10)). The *LHSV* was kept constant around 0.4 h⁻¹ in all experiments. The volume of liquid decalin was calculated from the hourly mass flux and the density of liquid cis-decalin. To determine the mass flux of liquid decalin, the gaseous cis-decalin generated in the saturator was condensed in a cooling trap, and the mass of liquid collected during one hour was determined. In all experiments the mass flux of liquid decalin was around 0.14 g · h⁻¹, and the bulk volume of catalyst was 0.4 cm³.

$$LHSV = \frac{\dot{V}_{\text{Dec, liquid, RT}}}{V_{\text{bulk, cat}}} \quad (5.10)$$

6 Characterization of the Catalysts and Respective Zeolitic Supports

6.1 Chemical Composition

The chemical compositions of the zeolitic supports and the catalysts were determined by means of an optical emission spectrometer with an inductively coupled plasma (ICP-OES) (see Section 5.2, page 57). For the calculation of the metal loading in weight percent, the mass of the dry zeolites was determined by thermogravimetric analysis (TGA) (see Section 5.2, page 57). In addition, ^{29}Si MAS NMR spectroscopy was applied for the determination of the framework $n_{\text{Si}} / n_{\text{T}}$ ratios (T = Al or B) (see Section 5.2, page 58). Summarized in Table 6.1 are the chemical compositions and short designations of the zeolitic supports. In Table 6.2 and Table 6.3 the chemical compositions of the prepared catalysts and their respective zeolitic supports are summarized. For a better readability, Table 6.3 is sub-divided to form catalyst groups according to the Sections in which their catalytic results are discussed (Chapter 7).

From the zeolites presented in Table 6.1 zeolites L and [Al]Beta-8 deserve particular mention. On both zeolites a 100 % exchange degree with the alkali metal cations could not be reached. In the case of zeolite L four different cation locations are known [9] but only one of these four sites is located in the 12-MR channels and exchangeable. This leads to the very low exchange degree of sodium and cesium of around 30 %. The reason for the occurrence of residual sodium after the ion exchange of [Al]Beta-8 with potassium, rubidium or cesium is not exactly known. However, the amorphous silica in the sample might play a role (*vide infra*).

The catalysts presented in Table 6.2 are all based on Na-Y zeolite but loaded either with palladium, rhodium, ruthenium or rhenium. They were prepared to investigate the influence of the nature of the noble metal on the hydrodecyclization of cis-decalin. A comparison of the noble metal contents and the mole fractions of protons reveal that 3.5Re/Na_{0.97}H_{0.03}-Y is exceptional. Due to the solid-state ion exchange applied to this catalyst the amount of noble metal is lower compared to the other three catalysts of this group. Moreover, the mole fraction of protons is very low. The origin of this peculiarity can be found in the preparation method and in the calculation of the mole fractions: Due to the solid-state ion exchange the catalyst was not washed with water prior to the catalytic experiments which led to residual sodium in the zeolite pores. Since the mole fraction of protons is calculated as the molar amount of aluminum minus the sum of equivalents of all metal cations (in this case solely sodium), the calculated mole fraction of the protons is too low.

Table 6.1: Chemical compositions and short designations of the used zeolitic supports.

Short Designation	Zeolitic Support	Short Designation	Zeolitic Support
Na-mordenite	Na _{0.99} ,H _{0.01} -mordenite-5.8	Na-[Al]Beta-21	Na _{0.90} ,H _{0.10} -[Al]Beta-20.9
Cs-mordenite	Cs _{0.97} ,H _{0.03} -mordenite-5.8	Li-[Al]Beta-14	Li _{0.72} ,H _{0.28} -[Al]Beta-14.0
K-L	K _{0.94} ,H _{0.06} -L-2.9	Na-[Al]Beta-14	Na _{0.96} ,H _{0.04} -[Al]Beta-14.0
K,Na-L	K _{0.68} ,Na _{0.29} ,H _{0.03} -L-2.9	K-[Al]Beta-14	K _{0.87} ,H _{0.13} -[Al]Beta-14.0
K,Cs-L	K _{0.66} ,Cs _{0.34} -L-2.9	Rb-[Al]Beta-14	Rb _{0.88} ,H _{0.12} -[Al]Beta-14.0
Na-SAPO-5	Na-SAPO-5	Cs-[Al]Beta-14	Cs _{0.97} ,H _{0.03} -[Al]Beta-14.0
Na-ZSM-5	Na _{0.96} ,H _{0.04} -ZSM-5-18	Na-[Al]Beta-8	Na _{0.90} ,H _{0.10} -[Al]Beta-7.7
Na-EMC-2	Na _{0.92} ,H _{0.08} -EMC-2-4.3	K-[Al]Beta-8	K _{0.81} ,Na _{0.13} ,H _{0.06} -[Al]Beta-7.7
Na-[B]Beta-18	Na _{0.94} ,H _{0.06} -[B]Beta-18.4	Rb-[Al]Beta-8	Rb _{0.65} ,Na _{0.25} ,H _{0.10} -[Al]Beta-7.7
		Cs-[Al]Beta-8	Cs _{0.77} ,Na _{0.23} -[Al]Beta-7.7

Table 6.2: Chemical compositions and designations of the palladium-, rhodium-, ruthenium- and rhenium-containing catalysts and their respective zeolitic support (for catalytic results see Section 7.1).

Zeolitic Support	Catalyst
Na-Y	5.3Pd/Na _{0.72} ,H _{0.28} -Y
Na-Y	4.9Rh/Na _{0.64} ,H _{0.36} -Y
Na-Y	4.8Ru/Na _{0.61} ,H _{0.39} -Y
Na-Y	3.5Re/Na _{0.97} ,H _{0.03} -Y

A noble metal loading of around 3 wt.-% was aimed at for all catalysts presented in Table 6.3 apart from the last group where the amount of iridium was varied. However, Na-SAPO-5 and Na,H-ZSM-5 possess relatively low amounts of noble metal. In case of Na-SAPO-5 the molar composition was 0.11 Na : 3.63 P : 3.74 Al : 1.00 Si, determined by ICP-OES. Due to the very low difference of the molar ratios between the positively charged phosphorus and the negatively charged aluminum, only low metal loadings *via* ion exchange are possible. The reason for the low amount of iridium on Na-ZSM-5 could be the narrow pores of MFI type zeolites which hamper the diffusion of the iridium complex into the pores during the ion exchange. Catalyst 3.3Ir/H_{0.58},Cs_{0.42}-[Al]Beta-14 was prepared to ensure the reproducibility of the catalysts and the experimental data obtained with them. For that purpose the preparation of this catalyst was started from a completely new batch of dry gel.

Table 6.3: Chemical compositions and designations of the iridium- and platinum-containing catalysts and their respective zeolitic supports.

Zeolitic Support	Iridium Catalysts	Platinum Catalysts
<i>Influence of the zeolite structure (see Section 7.2)</i>		
Na-mordenite	2.9Ir/Na _{0.90} ,H _{0.10} -mordenite	3.9Pt/Na _{0.79} ,H _{0.21} -mordenite
K-L	2.8Ir/K _{0.86} ,H _{0.14} -L	3.5Pt/K _{0.79} ,H _{0.21} -L
Na-SAPO-5	0.067Ir/H _{0.91} ,Na _{0.09} -SAPO-5	0.72Pt/H _{1.00} -SAPO-5
Na-ZSM-5	0.52Ir/H _{0.59} ,Na _{0.41} -ZSM-5	2.6Pt/H _{0.89} ,Na _{0.11} -ZSM-5
Na-EMC-2	3.0Ir/Na _{0.80} ,H _{0.20} -EMC-2	2.8Pt/Na _{0.83} ,H _{0.17} -EMC-2
Na-[Al]Beta-14	3.0Ir/Na _{0.53} ,H _{0.47} -[Al]Beta-14	3.2Pt/H _{0.57} ,Na _{0.43} -[Al]Beta-14
<i>Isomorphous substitution (see Section 7.3.1)</i>		
Na-[B]Beta-18	2.3Ir/H _{0.88} ,Na _{0.12} -[B]Beta-18	2.0Pt/H _{0.91} ,Na _{0.09} -[B]Beta-18
<i>Variation of the molar ratio of silicon to aluminum (see Section 7.3.2)</i>		
Na-[Al]Beta-21	3.4Ir/H _{0.56} ,Na _{0.44} -[Al]Beta-21	3.1Pt/H _{0.56} ,Na _{0.44} -[Al]Beta-21
Na-[Al]Beta-8	3.1Ir/Na _{0.82} ,H _{0.18} -[Al]Beta-8	2.8Pt/Na _{0.83} ,H _{0.17} -[Al]Beta-8
<i>Variation of the charge-compensating cation (see Section 7.3.3)</i>		
Cs-mordenite	2.0Ir/Cs _{0.84} ,H _{0.16} -mordenite	3.0Pt/Cs _{0.87} ,H _{0.13} -mordenite
K,Na-L	2.9Ir/K _{0.68} ,Na _{0.21} ,H _{0.11} -L	2.9Pt/K _{0.68} ,Na _{0.19} ,H _{0.13} -L
K,Cs-L	2.0Ir/K _{0.65} ,Cs _{0.34} ,H _{0.01} -L	2.9Pt/K _{0.63} ,Cs _{0.29} ,H _{0.08} -L
Li-[Al]Beta-14	3.3Ir/H _{0.74} ,Li _{0.26} -[Al]Beta-14	2.8Pt/H _{0.74} ,Li _{0.26} -[Al]Beta-14
K-[Al]Beta-14	3.2Ir/H _{0.61} ,K _{0.39} -[Al]Beta-14	2.8Pt/H _{0.55} ,K _{0.45} -[Al]Beta-14
Rb-[Al]Beta-14	3.5Ir/Rb _{0.52} ,H _{0.48} -[Al]Beta-14	2.8Pt/Rb _{0.58} ,H _{0.42} -[Al]Beta-14
Cs-[Al]Beta-14	3.4Ir/H _{0.58} ,Cs _{0.42} -[Al]Beta-14	2.9Pt/Cs _{0.51} ,H _{0.49} -[Al]Beta-14
Cs-[Al]Beta-14	3.3Ir/H _{0.58} ,Cs _{0.42} -[Al]Beta-14	
K-[Al]Beta-8	3.4Ir/K _{0.66} ,H _{0.22} ,Na _{0.12} -[Al]Beta-8	
Rb-[Al]Beta-8	3.4Ir/Rb _{0.56} ,H _{0.25} ,Na _{0.19} -[Al]Beta-8	
Cs-[Al]Beta-8	3.5Ir/Cs _{0.62} ,H _{0.22} ,Na _{0.16} -[Al]Beta-8	
<i>Variation of the iridium content (see Section 7.4)</i>		
Cs-[Al]Beta-14	1.1Ir/Cs _{0.96} ,H _{0.04} -[Al]Beta-14	
Cs-[Al]Beta-14	2.0Ir/Cs _{0.80} ,H _{0.20} -[Al]Beta-14	
Cs-[Al]Beta-14	4.0Ir/Cs _{0.53} ,H _{0.47} -[Al]Beta-14	
Cs-[Al]Beta-14	4.8Ir/H _{0.61} ,Cs _{0.39} -[Al]Beta-14	

In addition to the ICP/OES analyses, the framework $n_{\text{Si}} / n_{\text{T}}$ ratios of some zeolites were determined by ^{29}Si MAS NMR spectroscopy (see Section 5.2, page 58). With some exceptions, namely [Al]Beta-8 and [B]Beta-18 zeolites, the bulk $n_{\text{Si}} / n_{\text{T}}$ ratios determined by ICP/OES are in-line with the framework $n_{\text{Si}} / n_{\text{T}}$ ratios determined by ^{29}Si MAS NMR. In Figure 6.1 the ^{29}Si MAS NMR spectra and their deconvolution of Na-[Al]Beta-8, Na-[Al]Beta-14 and Na-[B]Beta-18 are shown exemplarily. The ^{29}Si MAS NMR spectra of the two aluminum-containing zeolites (Figure 6.1a and b) show four signals. The signals at around -115 and -110 ppm originate from silicon atoms with four other silicon atoms as next neighbors [99]. There are two resonances due to the partial resolution of the different crystallographic sites in the zeolite. The signals at around -104 ppm are created by silicon atoms which have one aluminum or boron in the direct neighborhood. The signals at around -99 ppm originate from a silicon atom with one OH-group or amorphous silica. In the case of Na-[B]Beta-18, one additional signal at -101 ppm occurs. This signal is also attributed to a silicon atom with one boron atom in the direct neighborhood. Signals corresponding to silicon atoms with more than one Al or B in the direct neighborhood were not detected.

The greatest difference in the NMR spectra of the three zeolites is the signal at -104 ppm originating from silicon atoms which have one aluminum or boron in the direct neighborhood: It decreases in the row Na-[Al]Beta-8 > Na-[Al]Beta-14 > Na-[B]Beta-18 (see also Table 6.4). This finding is in-line with the decreasing amount of aluminum in the zeolites.

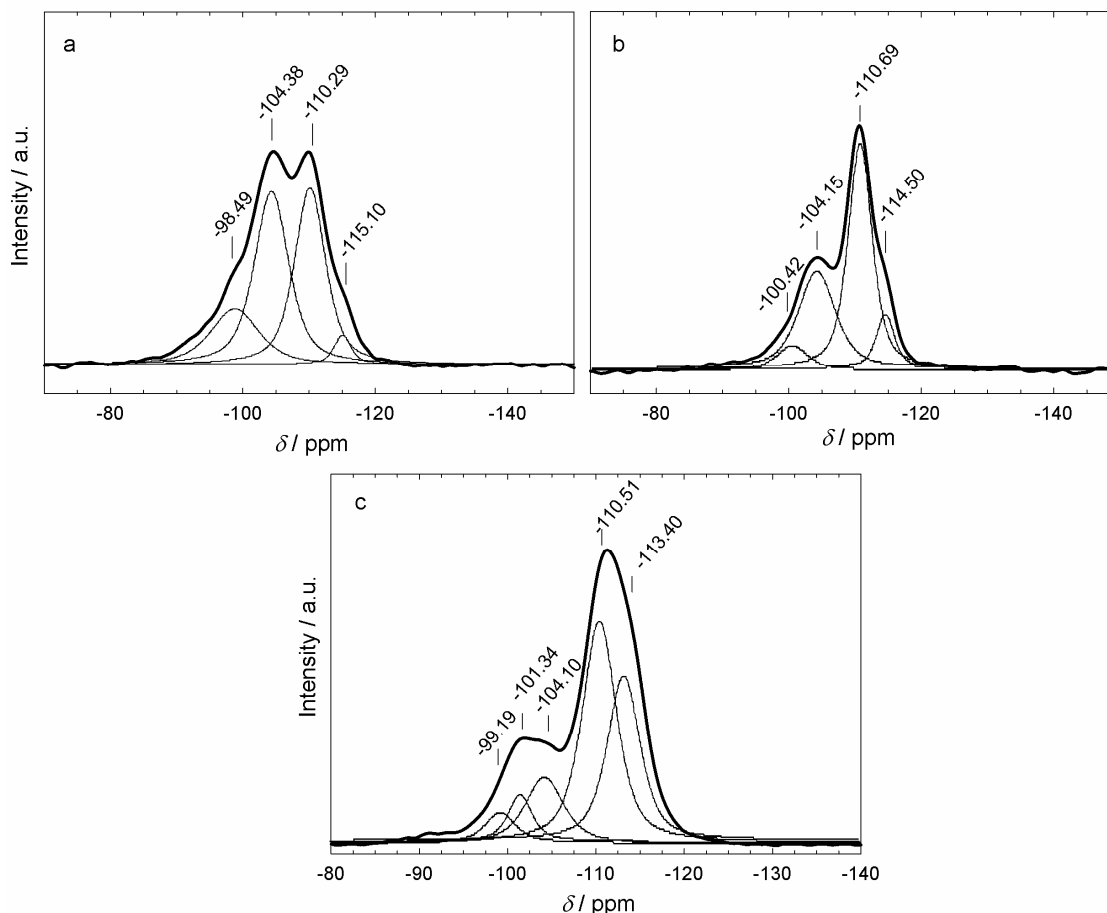


Figure 6.1: ^{29}Si MAS NMR spectra and their deconvolution for Na-[Al]Beta-8 (a), Na-[Al]Beta-14 (b) and Na-[B]Beta-18 (c).

In Table 6.4 the integrals of the deconvoluted signals of the ^{29}Si MAS NMR spectra of the three zeolites are given. From these values the molar ratios of the samples were calculated (see Section 5.2, page 59, Eq. (5.1)). For the Na-[Al]Beta-14 and Na-[Al]Beta-8 samples the calculated $n_{\text{Si}} / n_{\text{Al}}$ ratios are 12.1 and 7.7, respectively. For the aluminum rich Beta zeolite the bulk $n_{\text{Si}} / n_{\text{Al}}$ ratio determined by ICP/OES amounted to 5.5. This deviation stems from amorphous silica which is not considered for the framework $n_{\text{Si}} / n_{\text{Al}}$ ratio determined by ^{29}Si MAS NMR. The $n_{\text{Si}} / n_{\text{B}}$ ratio of the sample Na-[B]Beta-18 was calculated to 18.4 which also strongly deviates from the $n_{\text{Si}} / n_{\text{B}}$ ratio determined by ICP/OES which amounts to 40. Very likely, the too low amount of boron determined by ICP/OES stems from the formation of volatile BF_3 during the dissolution of the sample in hydrofluoric acid and nitrohydrochloric acid. After ion exchange with iridium salt and calcination a second ^{29}Si MAS NMR spectrum was recorded (not shown). From this spectrum a framework $n_{\text{Si}} / n_{\text{B}}$ ratio of 19.7 was calculated for $2.3\text{Ir}/\text{H}_{0.88}, \text{Na}_{0.12}$ -[B]Beta-18. The increase of the molar ratio can be explained by the further treatment of the sample which leads to a slight deboronation of the zeolite (see Section 6.2, page 83).

Table 6.4: Integrals and origins of the deconvoluted ^{29}Si MAS NMR spectra of Na-[Al]Beta-8, Na-[Al]Beta-14 and Na-[B]Beta-18.

Na-[Al]Beta-8		
Signal / ppm	Origin	Integral / %
-98.49	Si(3Si,1OH)	14.0
-104.38	Si(3Si,1Al)	44.9
-110.29	Si(4Si)	37.2
-115.10	Si(4Si)	3.9
Na-[Al]Beta-14		
Signal / ppm	Origin	Integral / %
-100.42	Si(3Si,1OH)	6.4
-104.15	Si(3Si,1Al)	33.0
-110.69	Si(4Si)	51.1
-114.5	Si(4Si)	9.5
Na-[B]Beta-18		
Signal / ppm	Origin	Integral / %
-99.19	Si(3Si,1OH)	5.3
-101.34	Si(3Si,1B)	6.6
-104.10	Si(3Si,1B)	15.1
-110.51	Si(4Si)	42.6
-113.40	Si(4Si)	30.4

6.2 Physical and Structural Properties

This Section will deal with the physical and structural properties of the zeolitic supports. The results of the FT-IR spectroscopy measurements for the determination of the strength and concentration of the Brønsted acid sites will be discussed in Section 6.4, page 89.

Zeolite Y

The Y zeolite used in this work was purchased from Strem Chemicals, lot No. 148 960, and was treated two times with NaNO_3 before any further modification (see Section 5.1.3, page 53). The powder X-ray diffractogram depicted in Figure 6.2 reveals, in comparison to a simulated diffraction pattern (not shown) [4], that the zeolite is phase-pure.

The ^{27}Al MAS NMR spectrum of Na-Y (Figure 6.3) consists of one signal at *ca.* 60 ppm which originates from tetrahedrally coordinated aluminum [98]. A signal at 0 ppm, which would have originated from octahedrally coordinated extra-framework aluminum [98], was not detected. These extra-framework aluminum species would indicate framework defects of the zeolite. The sample consists of crystals with a diameter between 0.5 and 1.5 μm as can be seen from the SEM image depicted in Figure 6.4. The specific surface area according to Brunauer, Emmett and Teller (A_{BET}) determined by N_2 physisorption amounts to 885 $\text{m}^2 \cdot \text{g}^{-1}$.

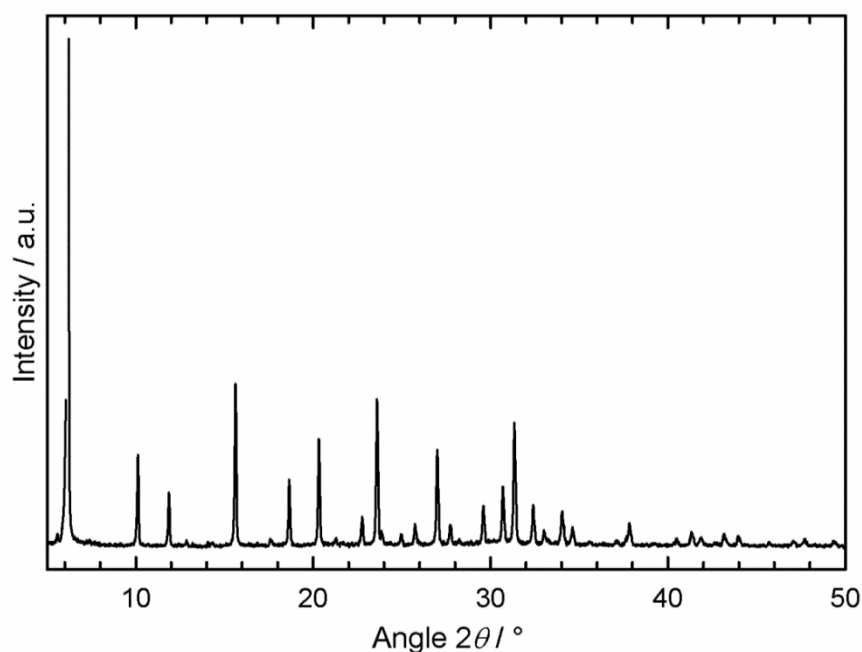


Figure 6.2: X-ray diffractogram of zeolite Na-Y.

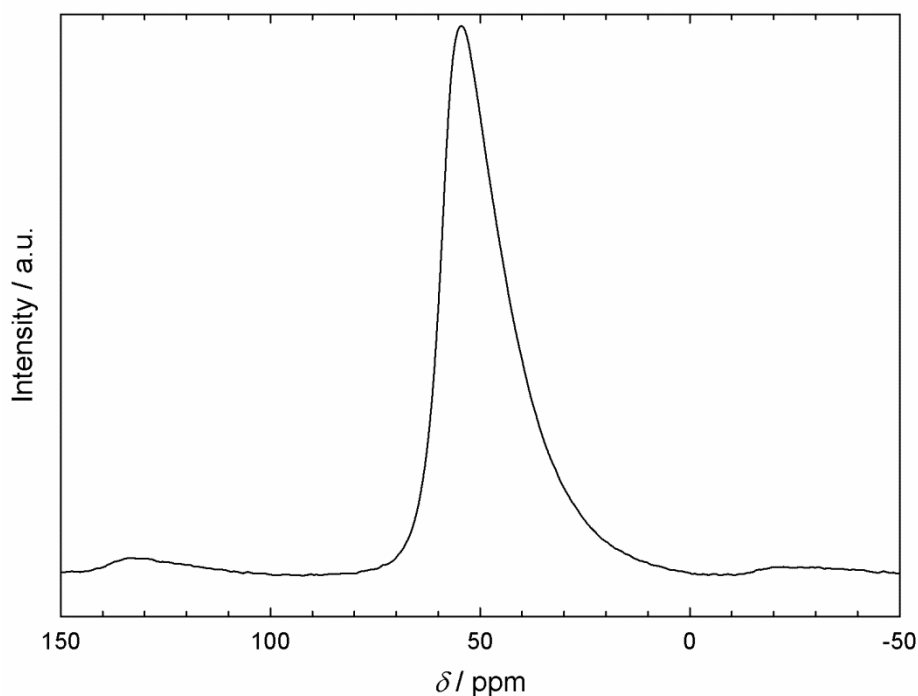


Figure 6.3: ^{27}Al MAS NMR spectrum of zeolite Na-Y.

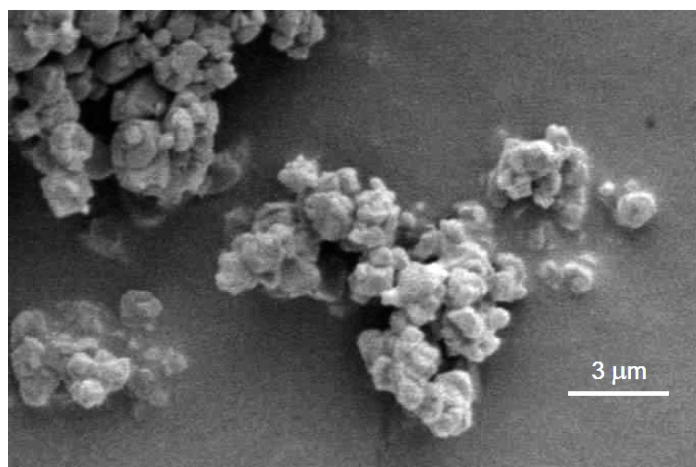


Figure 6.4: SEM image of zeolite Na-Y.

Zeolite Mordenite

Zeolite mordenite was purchased from Strem Chemicals, lot No. 14-763. The comparison of a simulated diffraction pattern (not shown) [4] and the determined powder X-ray diffractogram, which is depicted in Figure 6.5, indicates that Na-mordenite is phase-pure. The ion exchange with cesium did not lead to a change in the XRD pattern (not shown). The SEM image of Na-mordenite is depicted in Figure 6.6. One can see that the sample forms

agglomerates of *ca.* 1 to 10 μm diameter. The specific surface area, A_{BET} , amounted to $320 \text{ m}^2 \cdot \text{g}^{-1}$.

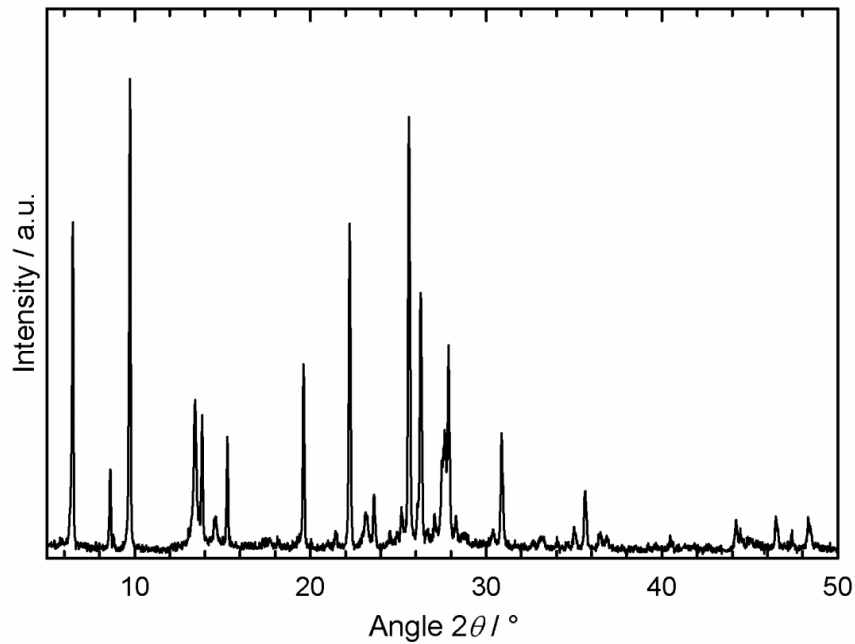


Figure 6.5: X-ray diffractogram of zeolite Na-mordenite.

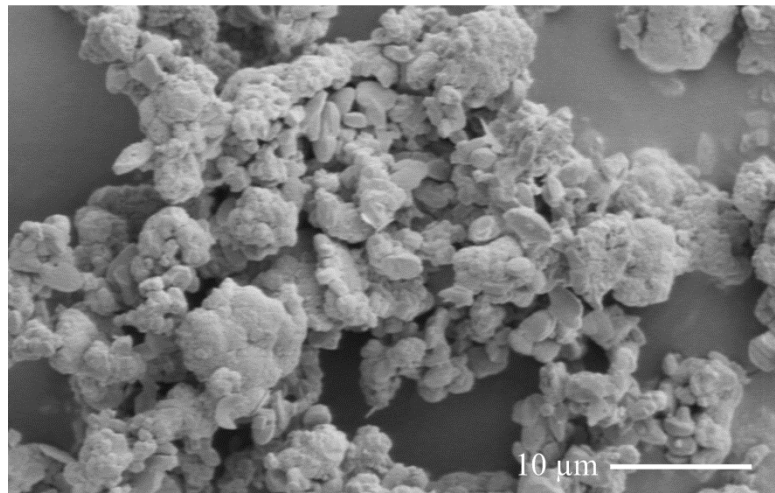


Figure 6.6: SEM image of Na-mordenite.

Zeolite L

Zeolite K-L was purchased from Tosho, lot No. 50KA8802. The X-ray diffractogram is depicted in Figure 6.7. A comparison with a simulated diffraction pattern (not shown) [4] indicated that the zeolite is phase-pure. The ion exchange with sodium or cesium did not lead

to a change in the diffractogram (not shown). The SEM image (Figure 6.8) revealed that the sample consisted of thin disks with a diameter of around 0.2 μm .

The ^{27}Al MAS NMR spectrum (not shown) showed only one signal at *ca.* 60 ppm originating from tetrahedrally coordinated aluminum. Extra-framework aluminum could not be detected. The specific surface area A_{BET} determined by N_2 physisorption amounted to 398 $\text{m}^2 \cdot \text{g}^{-1}$.

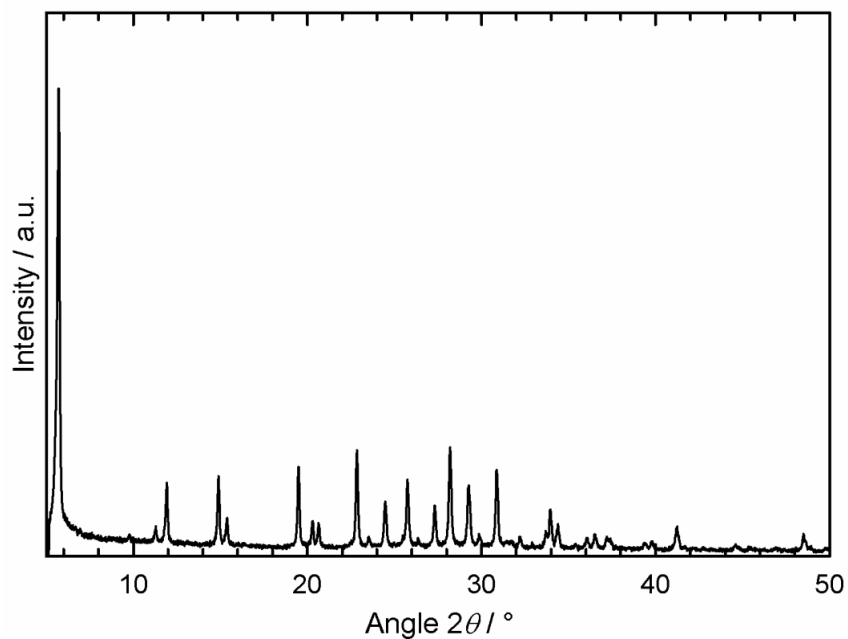


Figure 6.7: X-ray diffractogram of zeolite K-L.

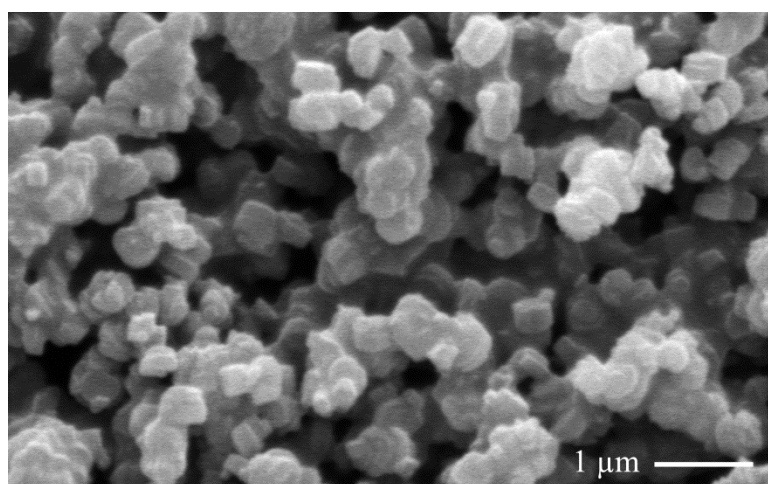


Figure 6.8: SEM image of zeolite K-L.

Zeolite SAPO-5

A powder X-ray diffractogram of the calcined SAPO-5 zeolite is depicted in Figure 6.9. It reveals that the material is phase-pure. From the SEM image depicted in Figure 6.10 one can see that the particle size varies very strongly between 5 μm and 300 μm . The specific surface area A_{BET} amounted to 223 $\text{m}^2 \cdot \text{g}^{-1}$.

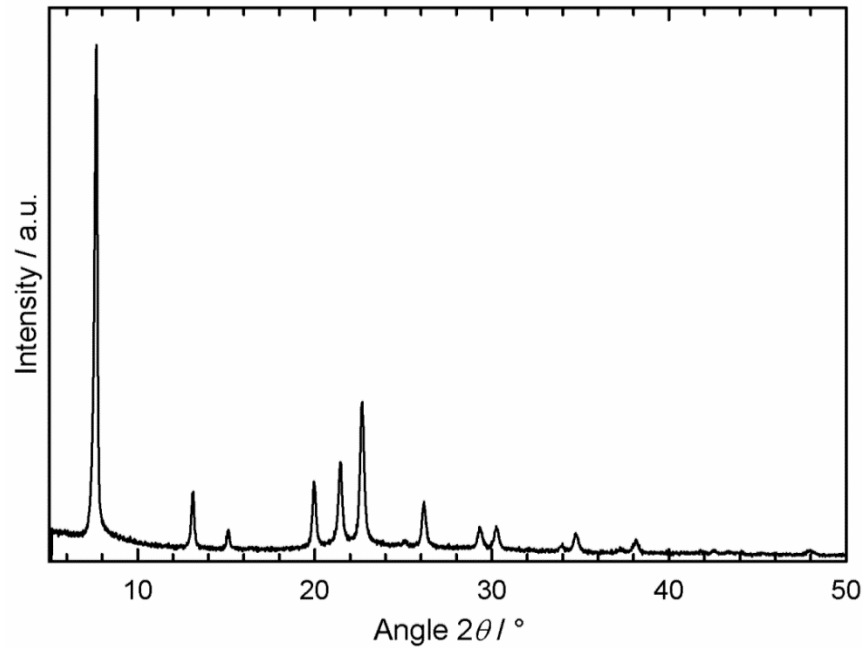


Figure 6.9: X-ray diffractogram of SAPO-5 after calcination.

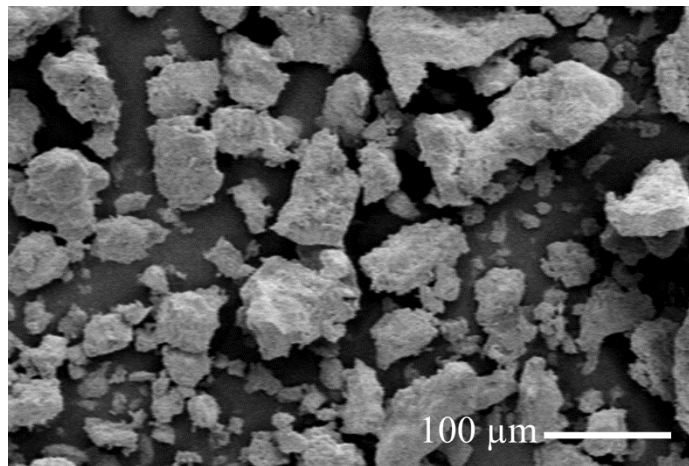


Figure 6.10: SEM image of SAPO-5.

Zeolite ZSM-5

Zeolite ZSM-5 was purchased from Degussa, lot No. KM-426. A comparison of a simulated diffraction pattern (not shown) with the determined X-ray diffractogram depicted in Figure 6.11 indicated that the sample was phase-pure. Depicted in Figure 6.12 is the SEM image of zeolite Na-ZSM-5. It reveals that the zeolite consists of spheres with a diameter of around 1 μm which form agglomerates of around 6 μm . The specific surface area amounts to 424 $\text{m}^2 \cdot \text{g}^{-1}$. The ^{27}Al MAS NMR spectrum (not shown) consists of only one signal at *ca.* 60 ppm. No extra-framework aluminum could be detected.

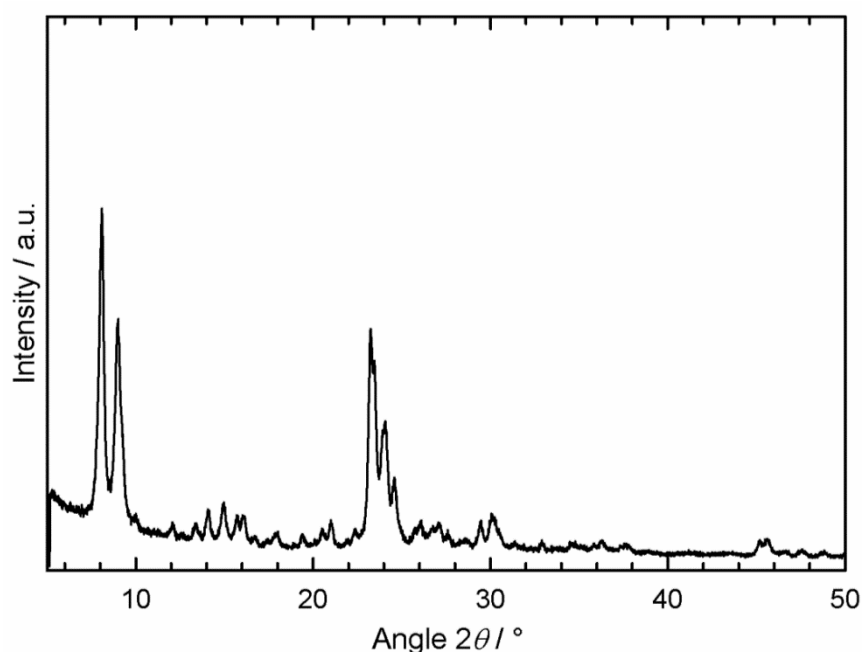


Figure 6.11: X-ray diffractogram of zeolite Na-ZSM-5.

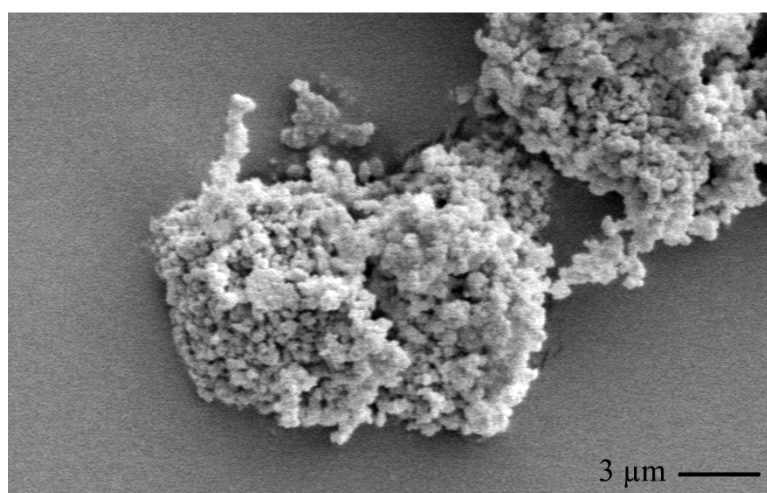


Figure 6.12: SEM image of Na-ZSM-5.

Zeolite EMC-2

Depicted in Figure 6.13 is the X-ray diffractogram of zeolite Na-EMC-2. It reveals that the sample is phase-pure and possesses a high degree of crystallinity. The high degree of crystallinity can be confirmed by the SEM image, depicted in Figure 6.14, which reveals octagonal discs with a diameter of *ca.* 3 μm and a thickness of around 1.5 μm . The specific surface area determined by N_2 physisorption amounts to 325 $\text{m}^2 \cdot \text{g}^{-1}$. The ^{27}Al MAS NMR spectra did not show a signal at 0 ppm (not shown).

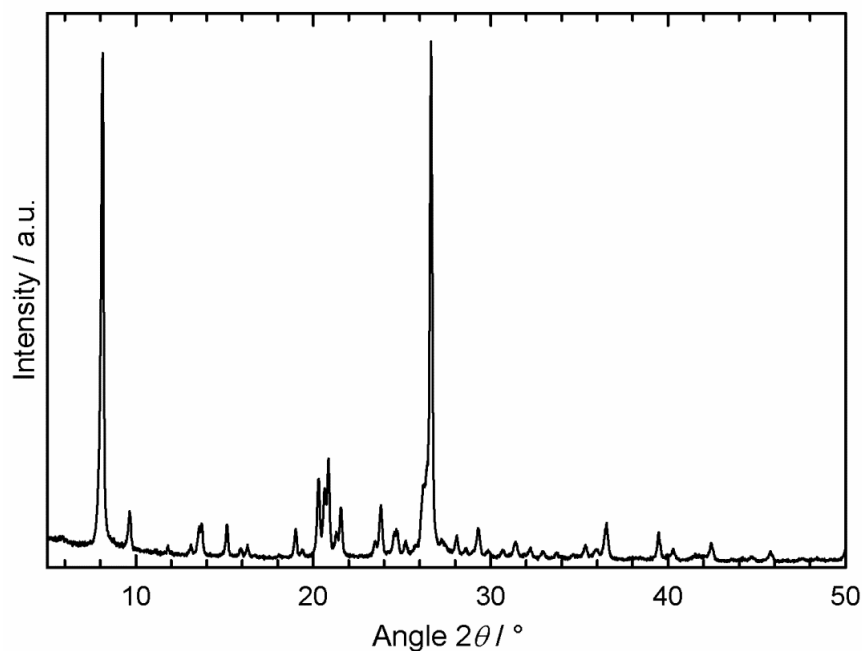


Figure 6.13: X-ray diffractogram of zeolite Na-EMC-2 after calcination.

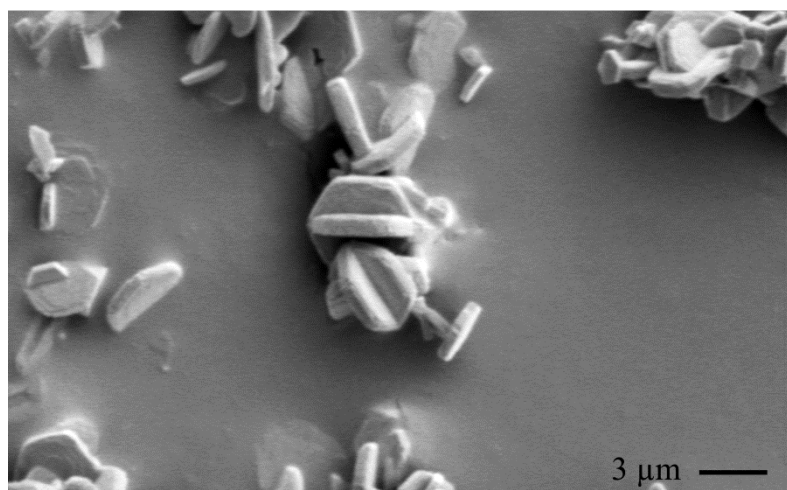


Figure 6.14: SEM image of Na-EMC-2.

Zeolite Beta

Depicted in Figure 6.15 are the X-ray diffractograms of zeolites Na-[Al]Beta-21, Na-[Al]Beta-14, Na-[Al]Beta-8 and Na-[B]Beta-18, after calcination. As already discussed in Section 4.1, page 14, zeolite Beta has a disordered structure, which leads to broad reflexes, e.g. the one at *ca.* 8°. All four X-ray diffraction patterns show the typical reflexes for *BEA type zeolites without any impurities [4]. However, whereas the diffraction patterns of Na-[Al]Beta-21, Na-[Al]Beta-14 and Na-[Al]Beta-8 are nearly identical, the diffractogram of Na-[B]Beta-18 is slightly different. The reflex at 23° is shifted to higher 2θ values compared to the other three diffractograms. Most likely the different T-atoms of the samples lead to this shift. A change of the pattern due to the exchange with different alkali metals was not observed.

In Figure 6.16 the SEM images of Na-[Al]Beta-21, Na-[Al]Beta-14, Na-[Al]Beta-8 and Na-[B]Beta-18 are depicted. One can see that the zeolites form agglomerates of about 5 to 30 μm diameter. A crystalline structure is in all cases not observable. The BET surface areas of the four Beta zeolites are summarized in Table 6.5. The low value for Na-[Al]Beta-8 stems most likely from the relatively high amount of amorphous silica in the sample (see Section 6.1, Table 6.4, page 75).

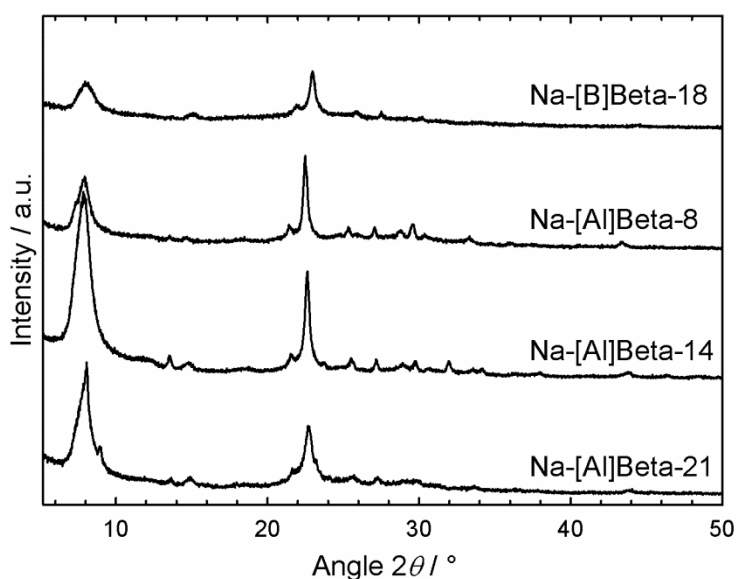


Figure 6.15: X-ray diffractograms of zeolites Na-[Al]Beta-21, Na-[Al]Beta-14, Na-[Al]Beta-8 and Na-[B]Beta-18 after calcination.

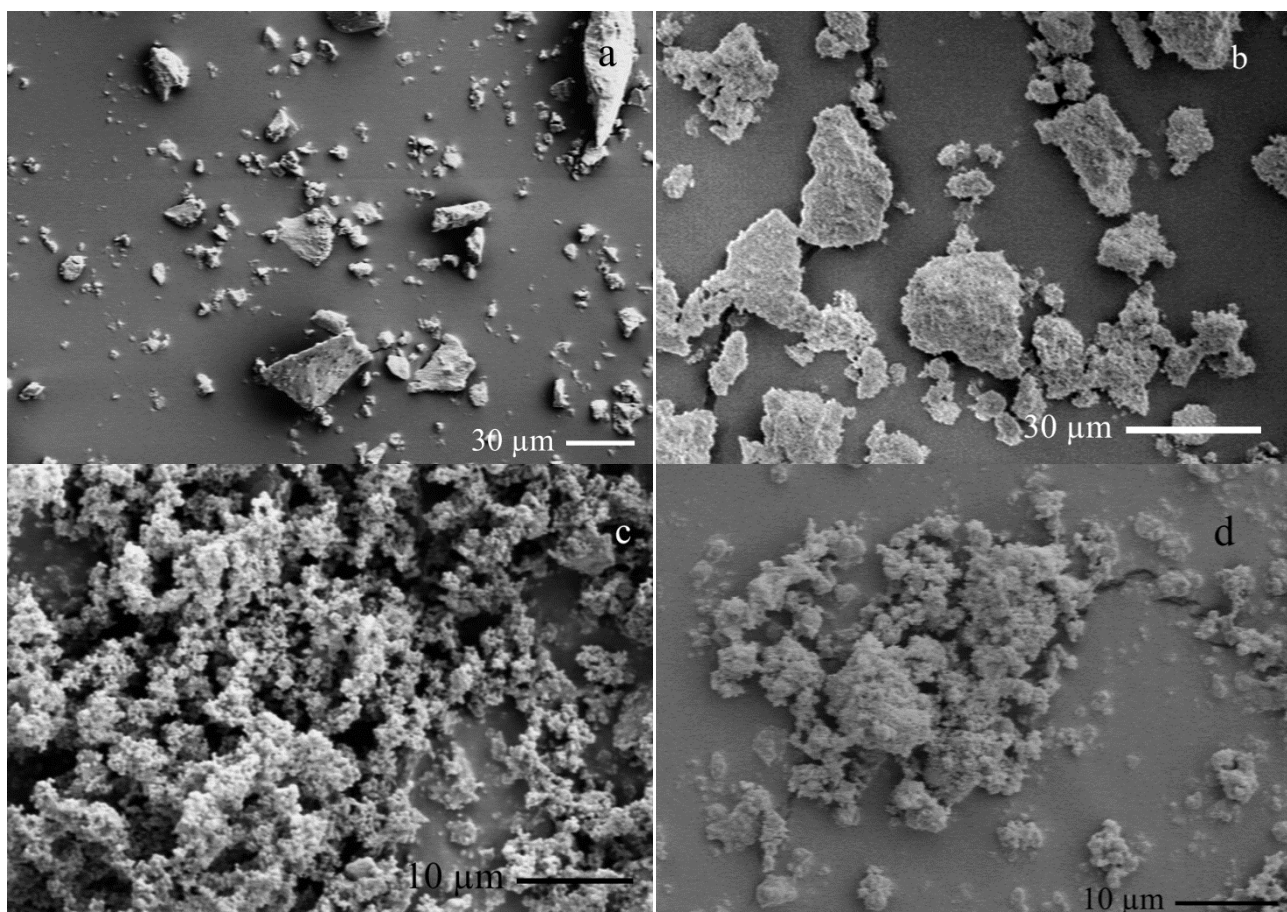


Figure 6.16: SEM pictures of Na-[Al]Beta-21 (a), Na-[Al]Beta-14 (b), Na-[Al]Beta-8 (c) and Na-[B]Beta-18 (d).

Table 6.5: Specific surface areas A_{BET} determined by N_2 physisorption of the four Beta zeolites.

Catalyst	$A_{\text{BET}} / \text{m}^2 \cdot \text{g}^{-1}$
Na-[Al]Beta-21	1143
Na-[Al]Beta-14	609
Na-[Al]Beta-8	360
Na-[B]Beta-18	520

The ^{27}Al MAS NMR spectra of Na-[Al]Beta-21, Na-[Al]Beta-14 and Na-[Al]Beta-8 depicted in Figure 6.17, consist of one signal only at around 55 ppm originating from tetrahedrally coordinated aluminum. A signal at 0 ppm was not observed. However, the signal of Na-[Al]Beta-8 is much broader compared to the signal of the other two samples. This line broadening can be explained by a lower degree of short-range order of this sample, caused for example by amorphous silica. This is in-line with the results obtained by ^{29}Si MAS NMR spectroscopy (see Figure 6.1, page 74), which gave clear evidence for amorphous silica in the sample.

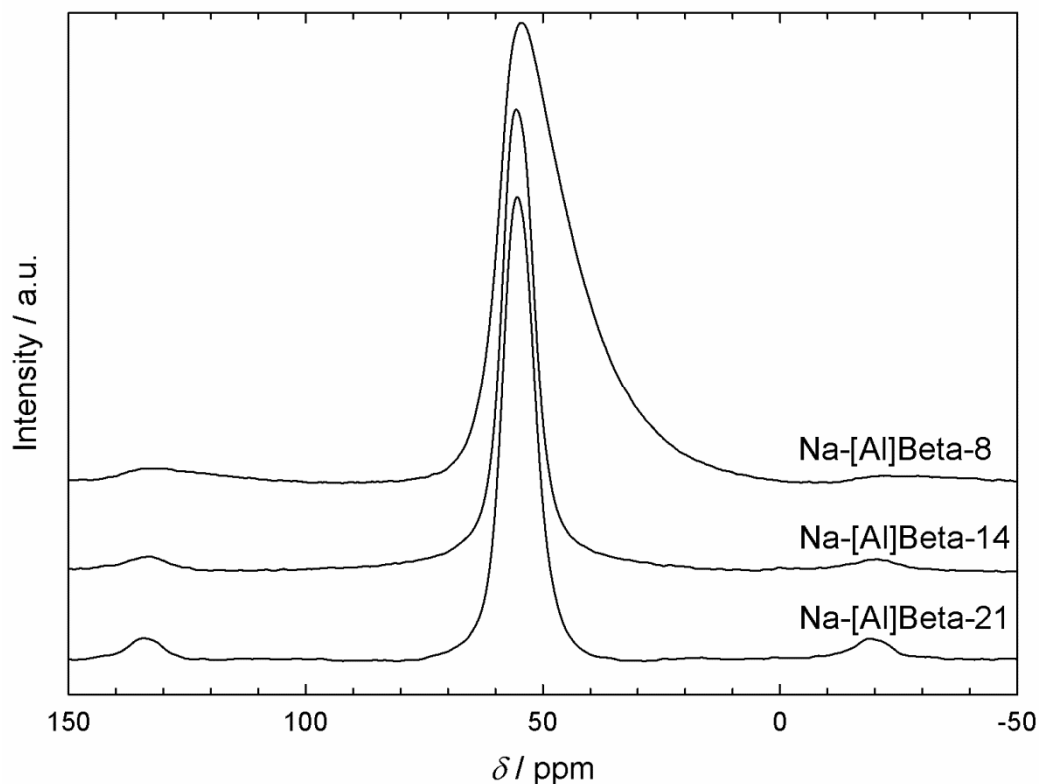


Figure 6.17: ^{27}Al MAS NMR spectra of Na-[Al]Beta-21, Na-[Al]Beta-14 and Na-[Al]Beta-8.

Figure 6.18 depicts the deconvoluted ^{11}B MAS NMR spectrum of Na-[B]Beta-18. The signals at -1.56 and -0.41 ppm are assigned to tetravalent boron in the zeolite framework with either sodium or a proton as charge-compensating cation, respectively. The component affected by second-order quadrupole interaction is clearly distinguished ($C_q = 2.6$ MHz, $\delta = 13.62$ ppm) and is assigned to trivalent boron in the framework [100, 101]. This indicates that no extra-framework boron is present in this sample. Nevertheless, after ion exchange with iridium salt and calcination, a second ^{11}B MAS NMR spectrum has been recorded (see Figure 6.19), which is significantly different: A fourth signal at 21.30 ppm ($C_q = 2.4$ MHz) emerged, which is affected by a second-order quadrupole interaction and can be attributed to tetragonal boron without B-O-Si bridges (extra-framework species) [100, 101]. Integration of the signals reveals 13 % of extra-framework species and 87 % of framework species. These findings are in-line with the results of ^{29}Si MAS NMR investigations (see Section 6.1, Table 6.4, page 75).

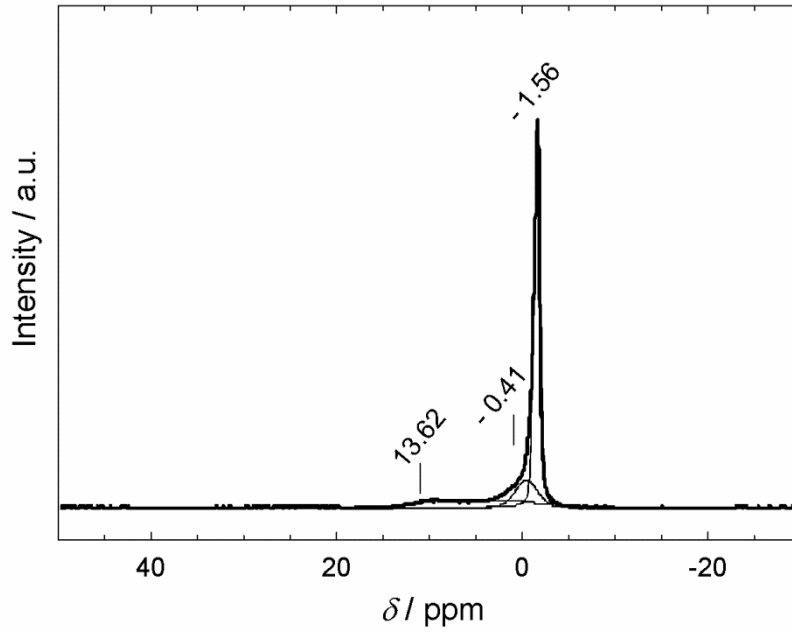


Figure 6.18: ^{11}B MAS NMR spectrum of Na-[B]Beta-18 and its deconvolution.

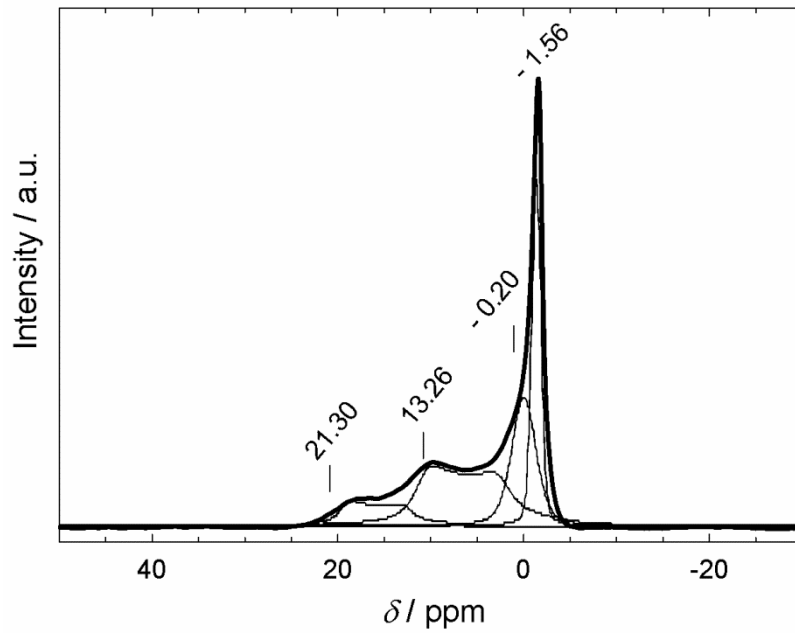


Figure 6.19: ^{11}B MAS NMR spectrum of $2.3\text{Ir}/\text{H}_{0.88},\text{Na}_{0.12}$ -[B]Beta-18 and its deconvolution.

6.3 Metal Dispersion

The metal dispersions of some catalysts tested in the hydroconversion of cis-decalin are summarized in Table 6.6. Although the catalysts were prepared, calcined and reduced under nearly identical conditions huge variations are observable. These may be due to the different nature of the noble metals and the supports. Overall, one can say that the mean metal dispersion of the platinum-containing catalysts, which is around 0.6, is much lower than that of the iridium-containing catalysts, which is without the extreme cases around 1.0. The values above unity may be due to adsorption stoichiometries $n_H / n_M > 1$. The reason for the extremely low metal dispersions measured for some catalysts, namely the Cs-[Al]Beta-14- and the Li-[Al]Beta-14-supported catalysts is unknown. Presumably, the use of a different batch of iridium salt for the ion exchange or unintended changes in the conditions of the calcination and reduction caused the low values. For 3.5Re/Na_{0.97}H_{0.03}-Y the determination of the metal dispersion was not applicable due the nature of the noble metal or the partial blockage of the active sites by residual sodium. However, the improvement of the metal dispersion was not a subject of this work, although higher metal dispersions would lead to lower amounts of noble metal needed for the same activity of the catalysts.

Table 6.6: Metal dispersions of various catalysts (n.a.: not applicable).

Catalyst	Metal Dispersion	Catalyst	Metal Dispersion
2.9Ir/Na _{0.90} ,H _{0.10} -mordenite	1.49	3.9Pt/Na _{0.79} ,H _{0.21} -mordenite	0.50
2.8Ir/K _{0.86} ,H _{0.14} -L	1.86	3.5Pt/K _{0.79} ,H _{0.21} -L	1.16
0.067Ir/H _{0.91} ,Na _{0.09} -SAPO-5	0.44	0.72Pt/H _{1.00} -SAPO-5	0.29
0.52Ir/H _{0.59} ,Na _{0.41} -ZSM-5	0.73	2.6Pt/H _{0.89} ,Na _{0.11} -ZSM-5	0.27
3.0Ir/Na _{0.80} ,H _{0.20} -EMC-2	0.91	2.8Pt/Na _{0.83} ,H _{0.17} -EMC-2	0.81
3.0Ir/Na _{0.53} ,H _{0.47} -[Al]Beta-14	0.87	3.2Pt/H _{0.57} ,Na _{0.43} -[Al]Beta-14	0.54
2.3Ir/H _{0.88} ,Na _{0.12} -[B]Beta-18	0.34	2.0Pt/H _{0.91} ,Na _{0.09} -[B]Beta-18	0.51
3.4Ir/H _{0.56} ,Na _{0.44} -[Al]Beta-21	0.62	3.1Pt/H _{0.56} ,Na _{0.44} -[Al]Beta-21	0.67
3.1Ir/Na _{0.82} ,H _{0.18} -[Al]Beta-8	0.45	2.8Pt/Na _{0.83} ,H _{0.17} -[Al]Beta-8	0.59
2.0Ir/Cs _{0.84} ,H _{0.16} -mordenite	1.07	3.0Pt/Cs _{0.87} ,H _{0.13} -mordenite	0.56
2.9Ir/K _{0.68} ,Na _{0.21} ,H _{0.11} -L	1.66	2.9Pt/K _{0.68} ,Na _{0.19} ,H _{0.13} -L	0.90
2.0Ir/K _{0.65} ,Cs _{0.34} ,H _{0.01} -L	1.32	2.9Pt/K _{0.63} ,Cs _{0.29} ,H _{0.08} -L	0.69
3.3Ir/H _{0.74} ,Li _{0.26} -[Al]Beta-14	0.18	2.8Pt/H _{0.74} ,Li _{0.26} -[Al]Beta-14	0.40
3.2Ir/H _{0.61} ,K _{0.39} -[Al]Beta-14	1.48	2.8Pt/H _{0.55} ,K _{0.45} -[Al]Beta-14	0.72
3.5Ir/Rb _{0.52} ,H _{0.48} -[Al]Beta-14	0.51	2.8Pt/Rb _{0.58} ,H _{0.42} -[Al]Beta-14	0.52
3.4Ir/H _{0.58} ,Cs _{0.42} -[Al]Beta-14	0.86	2.9Pt/Cs _{0.51} ,H _{0.49} -[Al]Beta-14	0.58
3.4Ir/K _{0.66} ,H _{0.22} ,Na _{0.12} -[Al]Beta-8	0.60		
3.4Ir/Rb _{0.56} ,H _{0.25} ,Na _{0.19} -[Al]Beta-8	0.61	5.3Pd/Na _{0.72} ,H _{0.28} -Y	0.02
3.5Ir/Cs _{0.62} ,Na _{0.19} ,H _{0.19} -[Al]Beta-8	0.20	4.9Rh/Na _{0.64} ,H _{0.36} -Y	0.49
		4.8Ru/Na _{0.61} ,H _{0.39} -Y	0.15
1.1Ir/Cs _{0.96} ,H _{0.04} -[Al]Beta-14	0.17	3.5Re/Na _{0.97} ,H _{0.03} -Y	n.a.
2.0Ir/Cs _{0.80} ,H _{0.20} -[Al]Beta-14	0.28		
4.0Ir/Cs _{0.53} ,H _{0.47} -[Al]Beta-14	0.41		
4.8Ir/H _{0.61} ,Cs _{0.39} -[Al]Beta-14	0.28		

6.4 Acidic Properties

The strength and concentration of the Brønsted acid sites of the catalysts were determined by FT-IR spectroscopy with pyridine as probe molecule. The concentrations of adsorbed pyridine were calculated using Eq. (5.2), page 61. The determined pyridine concentrations at different desorption temperatures of various catalysts used in this work are summarized in the Appendix 9.3, page 163, Table 9.3.

In Figure 6.20 the spectra of 3.0Ir/Na_{0.53}H_{0.47}-[Al]Beta-14 loaded with pyridine desorbed at different temperatures are exemplarily depicted. Listed in Table 6.7 are the five occurring FT-IR bands of pyridine adsorbed at acid sites in the range of 1400 cm⁻¹ to 1580 cm⁻¹ and their supposed origins. For the evaluation of the strength and concentration of the Brønsted acid sites, only the band at 1544 cm⁻¹ was taken into account.

Table 6.7: FT-IR bands of pyridine adsorbed at acid sites [35, 102, 103].

Pyridine band / cm ⁻¹	Assignment
1444	Pyridine bond at weak Lewis acid sites
1458	Pyridine bond at strong Lewis acid sites
1462	
1490	Pyridine bond at Brønsted or Lewis acid sites
1544	Pyridine bond at Brønsted acid sites

The increase of the signal at 1462 cm⁻¹ (see Figure 6.20) with increasing temperature could arise from a redistribution of the coordinatively held pyridine from framework aluminum to extra-framework aluminum. The dependency of the intensity of the signal on the temperature could originate from the fact that, at higher temperatures, [Al]Beta zeolite undergoes dealumination, and extra-framework Al³⁺ sites thereby generated readsorb the pyridine. Christner *et al.* [102] observed an analogous behavior with an Mg-Y zeolite. They assumed that the pyridine desorbed from residual Na⁺ and moved to stronger Mg²⁺ sites.

Hattori *et al.* [103] discovered that the signal at 1444 cm⁻¹ originates from weaker Lewis acid sites than that at 1458 cm⁻¹, which is in good agreement with the results obtained with 3.0Ir/Na_{0.53}H_{0.47}-[Al]Beta-14. With increasing desorption temperatures the signal which originates from the weaker Lewis acid sites vanishes much faster than the signal originating from the stronger Lewis acid sites. The signal at 1544 cm⁻¹ originating from pyridine adsorbed on Brønsted acid sites decreased over the whole range of desorption temperatures.

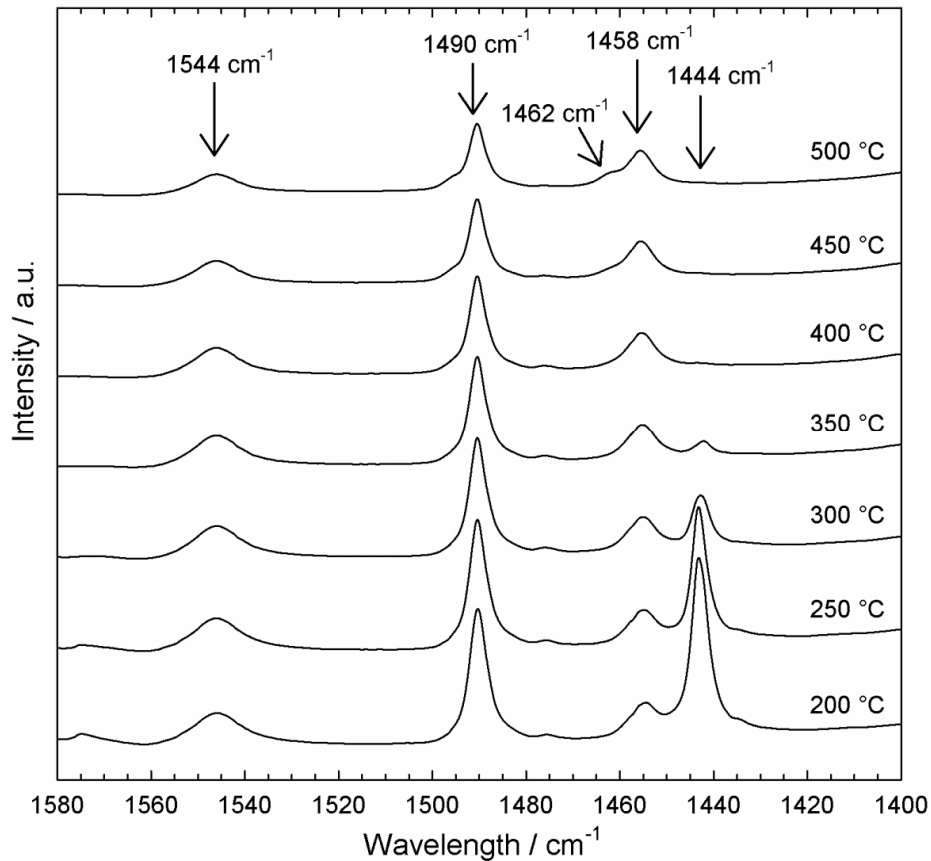


Figure 6.20: FT-IR spectra of 3.0Ir/Na_{0.53}H_{0.47}-[Al]Beta-14 loaded with pyridine desorbed at different temperatures.

In the following the determined strengths and concentrations of the Brønsted acid sites obtained for the various catalysts will be discussed. For that purpose the relative pyridine concentrations were plotted against the desorption temperatures. The relative pyridine concentration c_{rel} is defined as:

$$c_{\text{rel}} = \frac{c_{\text{pyridine}}(T_{\text{des}})}{c_{\text{pyridine}}(200\text{ °C})} \quad (6.1)$$

This kind of presentation of the data was chosen in order to generate a comparable value for the acid site concentration at a given desorption temperature independent from the overall Brønsted acid site concentration.

Since pyridine which is adsorbed at stronger acid sites needs higher temperatures till it desorbs, the decrease of the relative concentration with increasing temperature can be taken as a semiquantitative measure of the strength of the Brønsted acid sites. Depicted in Figure 6.21 are the relative pyridine concentrations determined by FT-IR spectroscopy at different desorption temperatures for the iridium- and platinum-containing alkali metal-exchanged [Al]Beta-14 zeolites. A clear trend of the strengths of the acid sites can be seen: In-line with

the behavior found with alkali metal-exchanged faujasites [25], the strength of the Brønsted acid sites decreases in the row from lithium to cesium. Whereas 3.3Ir/H_{0.74},Li_{0.26}-[Al]Beta-14 retains, after the treatment at 500 °C, nearly 60 % of the initial pyridine concentration, 3.4Ir/H_{0.58},Cs_{0.42}-[Al]Beta-14 possesses only 10 %.

For the platinum-containing zeolites this trend is much less pronounced but it is still observable. Nevertheless, it seems that the strength of Brønsted acid sites is higher for platinum-containing zeolites than for the iridium-containing ones, which can be seen from slower decrease of the determined pyridine concentrations. This is confirmed for the faujasite-supported catalysts (see Figure 6.22). Nevertheless, the trend of decreasing acid site strength is clearly reflected in the catalytic behavior in the hydrodecyclization of cis-decalin for both the platinum- as well as the iridium-containing catalysts (see Section 7.3.3, page 116).

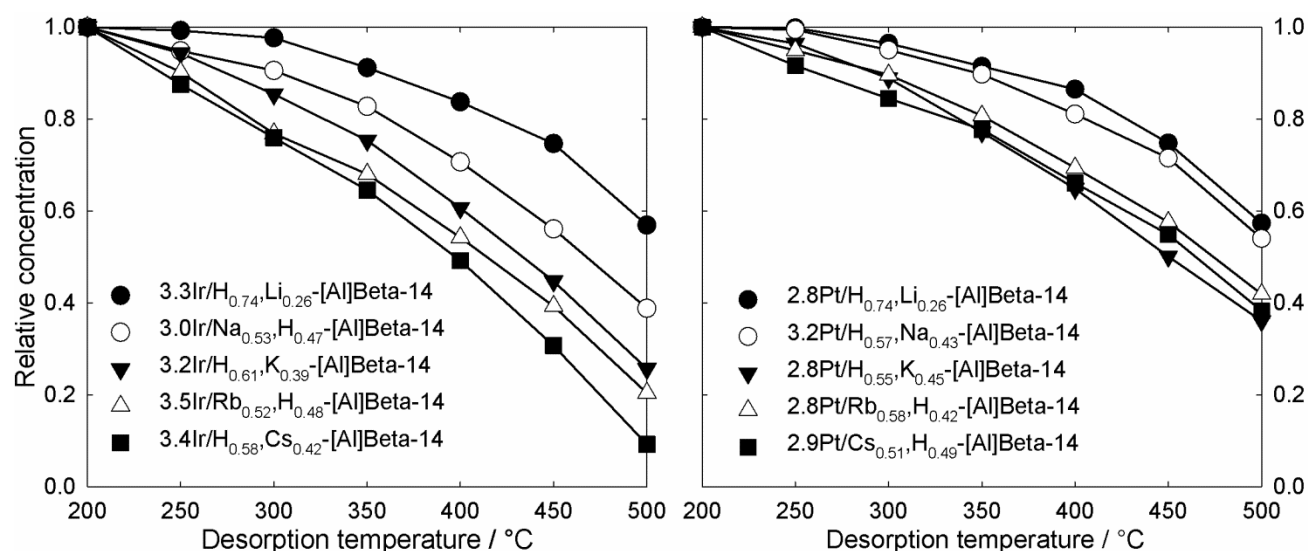


Figure 6.21: Relative pyridine concentrations on the iridium- and platinum-containing alkali metal-exchanged [Al]Beta-14 zeolites determined by FT-IR spectroscopy.

Due to the similar tendencies found for iridium- and platinum-containing catalysts, FT-IR spectroscopy was only applied the palladium, rhodium and rhenium loaded zeolites Y (Figure 6.22) and the iridium-containing catalysts. The ruthenium-containing zeolite Y could not be measured, since it shows a too strong adsorption in the region of the ring deformation bands of pyridine.

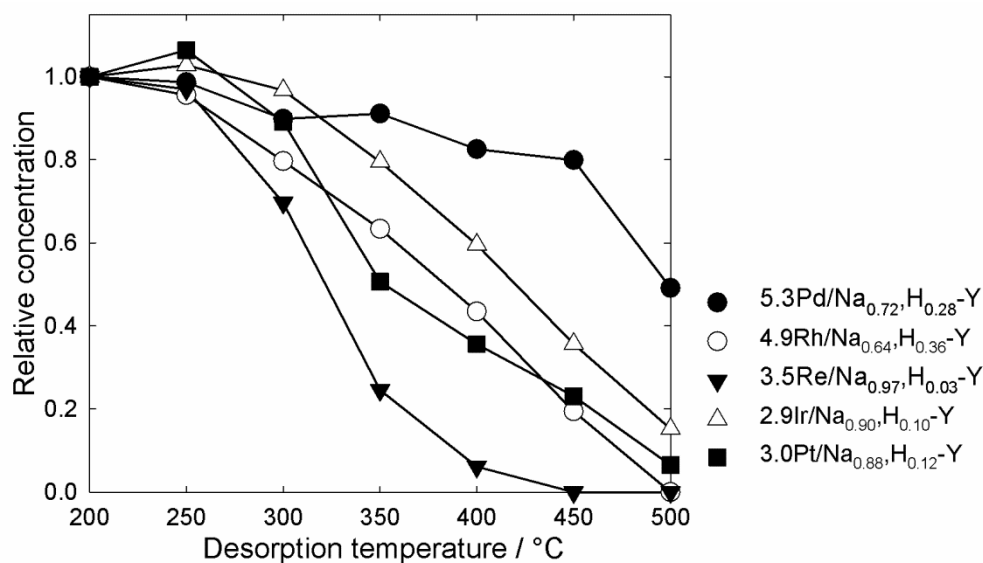


Figure 6.22: Relative pyridine concentrations on Y zeolites loaded with different noble metals determined by FT-IR spectroscopy (data for 2.9Ir/Na_{0.90},H_{0.10}-Y and 3.0Pt/Na_{0.88},H_{0.12}-Y were taken from Ref. [25]).

In Figure 6.22 the relative pyridine concentrations of the Na,H-Y zeolites are depicted. The main differences between the catalysts are the nature of the noble metal and the amount of noble metal. Nevertheless, large differences in the strengths of the Brønsted acid sites can be observed. These differences can be explained by Sanderson's intermediate electronegativities [23, 24] which predict the same order of acid site strengths (see also Section 4.2, page 21). The slight increase in the pyridine concentration with increasing temperature found on 2.9Ir/Na_{0.90},H_{0.10}-Y and 3.0Pt/Na_{0.88},H_{0.12}-Y may be due to experimental errors.

The relative pyridine concentrations determined for the iridium-loaded zeolites Na,H-mordenite, K,H-L, H-SAPO-5, Na,H-ZSM-5, Na,H-EMC-2 and Na,H-[Al]Beta-14 are depicted in Figure 6.23. The fact that 2.9Ir/Na_{0.90},H_{0.10}-mordenite and 3.0Ir/Na_{0.53},H_{0.47}-[Al]Beta-14 have similar Brønsted acid site strengths and that 2.8Ir/K_{0.86},H_{0.14}-L possesses a much lower acid strength than 3.0Ir/Na_{0.53},H_{0.47}-[Al]Beta-14 has to be kept in mind for the discussion of the results obtained in the catalytic experiments with these two catalysts (see Section 7.2.2, page 104).

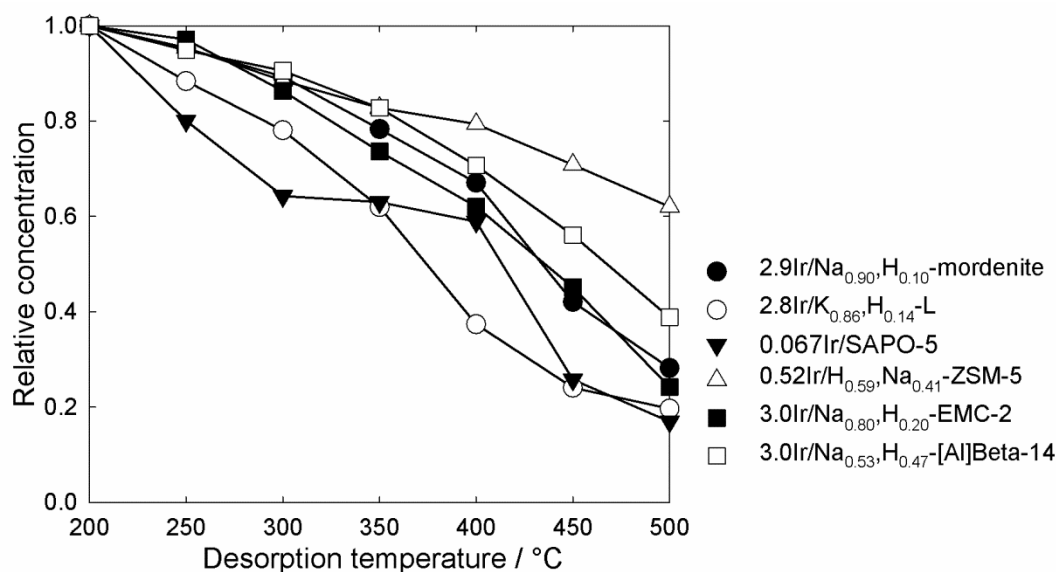


Figure 6.23: Relative pyridine concentrations on various iridium-containing zeolites determined by FT-IR spectroscopy.

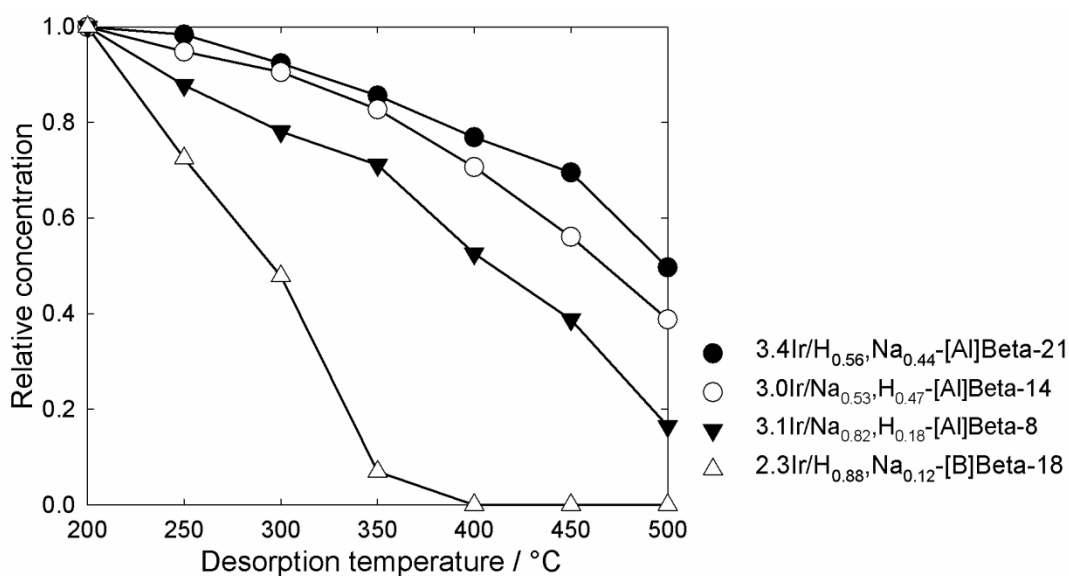


Figure 6.24: Relative pyridine concentrations on iridium-containing H,Na-[B]Beta and Na,H-[Al]Beta zeolites with varying aluminum content determined by FT-IR spectroscopy.

The relative pyridine concentrations on iridium-containing H,Na-[B]Beta and Na,H-[Al]Beta zeolites with varying aluminum content depicted in Figure 6.24 revealed the expected trend: The higher the molar ratio n_{Si} / n_{Al} the higher the acid strength of the catalyst. The isomorphous substitution of aluminum by boron results in a much lower acid strength of the support.

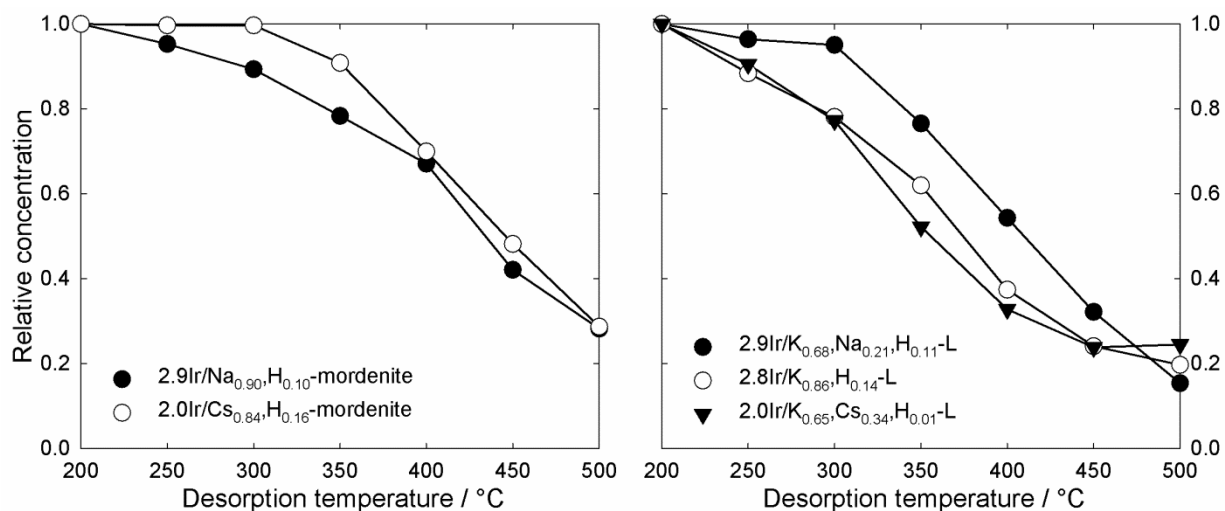


Figure 6.25: Relative pyridine concentrations on iridium-containing alkali metal-exchanged mordenite (left) and L zeolites (right) determined by FT-IR spectroscopy.

Surprisingly, the cesium exchange of mordenite does not lead to a reduction of the acid site strength of the zeolite (see Figure 6.25, left) it rather leads to increasing strengths. The same effect was observed for zeolite L (see Figure 6.25, right). Only the sodium exchange seems to enhance the acid strength of zeolite L. The reason for these peculiarities may be experimental errors, especially in the case of increasing acid site strengths, or the pore architecture of the two zeolites. Both zeolites possess a one-dimensional 8-MR pore system (see Sections 0 and 0, pages 16 and 17, respectively) in which the cesium may be adsorbed thus not influencing the accessible acid sites.

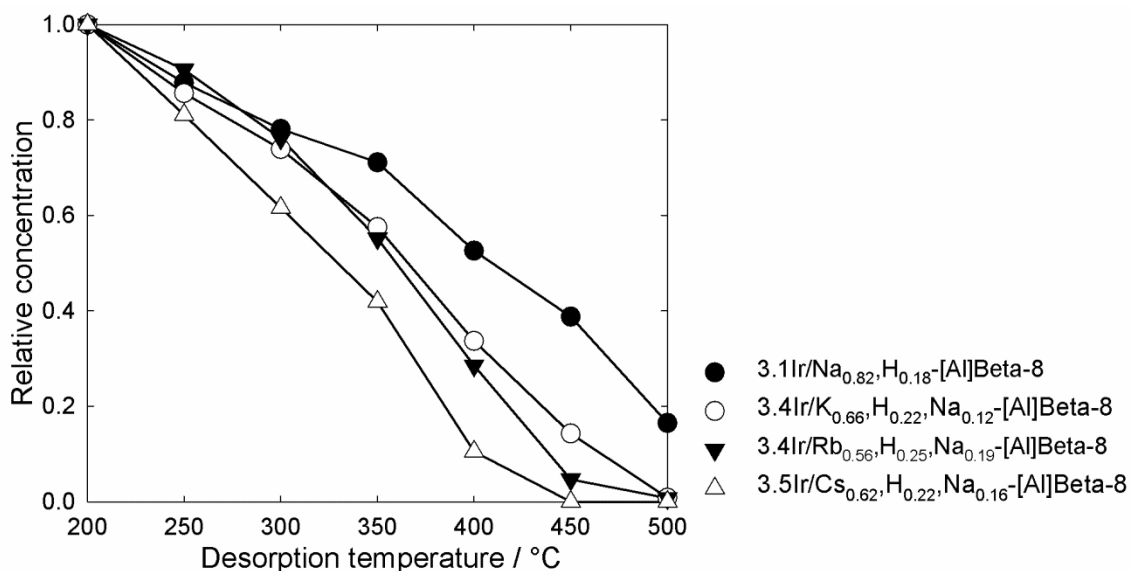


Figure 6.26: Relative pyridine concentrations of iridium-containing alkali metal-exchanged aluminum-rich Beta zeolites determined by FT-IR spectroscopy.

In-line with the results obtained for the alkali metal-exchanged [Al]Beta-14 zeolites (see Figure 6.21, page 91), the strength of the Brønsted acid sites of the aluminum-rich Beta zeolites (Figure 6.26) decreases upon exchange with potassium, rubidium or cesium. However, the strengths of the sites are throughout lower compared to the ones obtained on the [Al]Beta-14 zeolites, which is in-line with the results obtained for the [Al]Beta zeolite with varying aluminum content (see Figure 6.24, page 93).

Figure 6.27 depicts the relative pyridine concentrations on cesium-exchanged [Al]Beta-14 with varying iridium content. With decreasing iridium content the Brønsted acid site strength also decreases. This is in-line with Sandersons intermediate electronegativities [23, 24] which decrease from 4.13 for 4.8Ir/H_{0.61},Cs_{0.39}-[Al]Beta-14 to 4.00 for 1.1Ir/Cs_{0.96},H_{0.04}-[Al]Beta-14. The decreasing acid strengths of the catalysts can be explained by the decreasing amount of cesium and the increasing amount of protons in the catalysts. The very low acid site concentrations of 3.4Ir/H_{0.58},Cs_{0.42}-[Al]Beta-14 and 2.0Ir/Cs_{0.80},H_{0.20}-[Al]Beta-14 are near the detection limit of the spectrometer which can explain the similar acid strengths of these two catalysts.

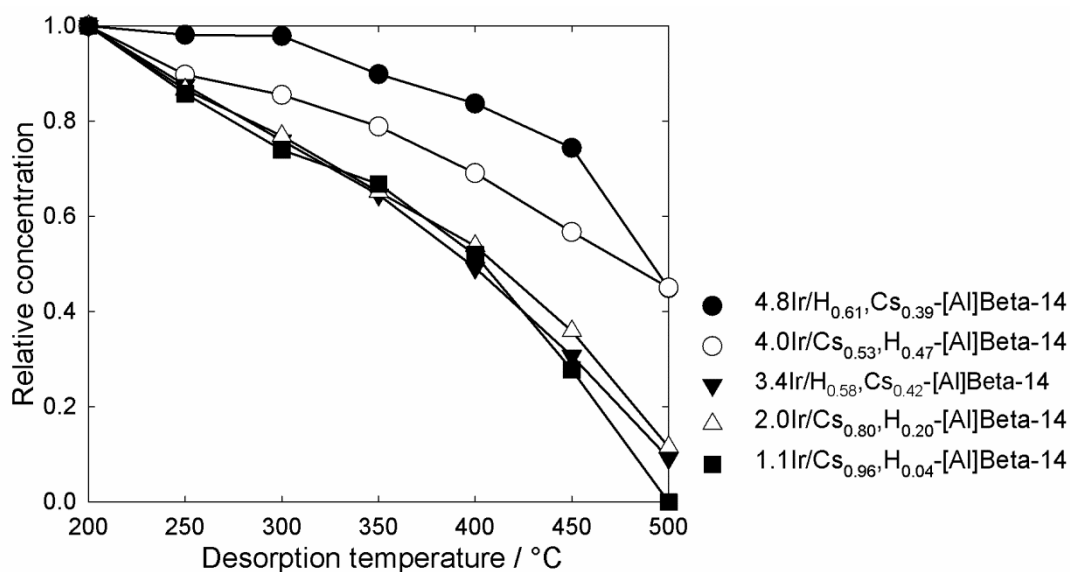


Figure 6.27: Relative pyridine concentrations on Beta zeolites with varying iridium content determined by FT-IR spectroscopy.

7 Hydrodecyclization of Decalin

In the following Sections the results obtained with the various noble metal-containing zeolites in the hydroconversion of cis-decalin will be discussed. Although the results obtained with these catalysts were very different, for none of the catalysts considerable deactivation occurred up to times-on-stream of 60 h.

7.1 Influence of the Noble Metal

A series of four Na,H-Y zeolites loaded either with ruthenium, rhenium, palladium or rhodium were prepared to identify the most promising noble metal for the hydrodecyclization of decalin. In Figure 7.1 the conversion of decalin and selectivities of the different groups of products in dependence of the reaction temperature for the four prepared Na,H-Y zeolites are depicted. For comparison, the results obtained by Rabl *et al.* [25] on 2.9Ir/Na_{0.90}H_{0.10}-Y and 3.0Pt/Na_{0.88}H_{0.12}-Y are also shown in Figure 7.1e and f.

The results observed on 4.8Ru/Na_{0.61}H_{0.39}-Y (Figure 7.1a) seem to be very promising at low conversions since the prevailing products are ROPs, and the selectivity of open-chain decanes increases to 13.6 %. However, the catalyst is very active for carbon-carbon bond cleavage, so that already at 260 °C and a decalin conversion of *ca.* 70 %, hydrocracked products are dominating. The rhenium catalyst (Figure 7.1b) exhibits a similar behavior: Ring-opening and hydrocracking govern the chemistry at low decalin conversions, and upon increasing the conversion, hydrocracking to C₉- products becomes the sole reaction. Only small amounts of open-chain decanes are formed on both catalysts (see Table 7.1).

On the palladium-containing catalyst skeletal isomers of decalin are formed with very high selectivities at low to moderate conversions (Figure 7.1c). As the reaction temperature and conversion increase, the selectivities of ring-opening products and open-chain decanes increase as well. At still higher conversions, both selectivities pass through maxima, and from thereon, the selectivities of hydrocracked products increase sharply. The maximum yield and selectivity of OCDs observed on 5.3Pd/Na_{0.72}H_{0.28}-Y amounts to only 3 and 5 %, respectively (see also Table 7.1).

The most promising catalyst concerning the selectivities of OCDs among this series is 4.9Rh/Na_{0.64}H_{0.36}-Y (Figure 7.1d): At low conversions nearly equal amounts of ring-opening products and skeletal isomers are formed. With increasing conversion the selectivities of these two product groups decrease, whereas the selectivity of OCDs raises and passes through a maximum at 295 °C of 17.1 %. Note that the height of the maximum yield of OCDs

increase in the order $3.5\text{Re}/\text{Na}_{0.97},\text{H}_{0.03}\text{-Y} > 5.3\text{Pd}/\text{Na}_{0.72},\text{H}_{0.28}\text{-Y} > 4.8\text{Ru}/\text{Na}_{0.61},\text{H}_{0.39}\text{-Y} > 4.9\text{Rh}/\text{Na}_{0.64},\text{H}_{0.36}\text{-Y} > 2.9\text{Ir}/\text{Na}_{0.90},\text{H}_{0.10}\text{-Y} > 3.0\text{Pt}/\text{Na}_{0.88},\text{H}_{0.12}\text{-Y}$ (see Table 7.1).

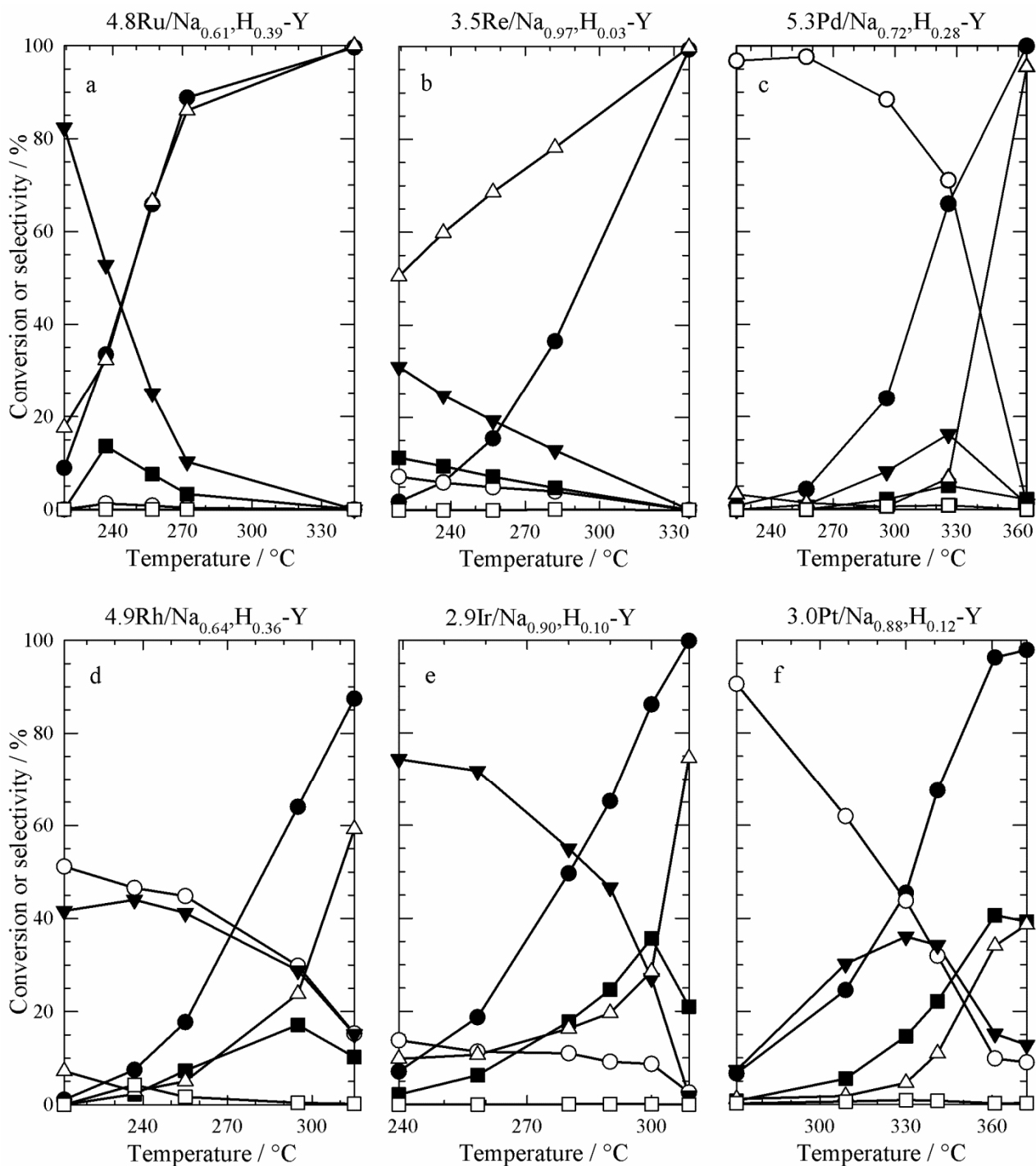


Figure 7.1: Conversion of decalin and selectivities of the different groups of products in dependence of the reaction temperature for Na,H-Y zeolites loaded with different noble metals. (\bullet X_{Dec} , \blacksquare S_{OCDs} , \blacktriangledown S_{ROPs} , \circ $S_{\text{sk-Isos}}$, \triangle S_{C_9} , \square S_{DHPs}). Data for $2.9\text{Ir}/\text{Na}_{0.90},\text{H}_{0.10}\text{-Y}$ (e) and $3.0\text{Pt}/\text{Na}_{0.88},\text{H}_{0.12}\text{-Y}$ (f) taken from Ref. [25].

Table 7.1: Maximum yields and selectivities of open-chain decanes (OCDs), combined yields of ring-opening products (ROPs) and OCDs and yields of C₉-hydrocarbons at reaction conditions of maximal OCD yields in the hydroconversion of decalin on the Na,H-Y zeolites loaded with different noble metals.

Catalyst	$T_r / ^\circ\text{C}$	$X_{\text{Dec}} / \%$	$S_{\text{OCDs}} / \%$	$Y_{\text{OCDs, max.}} / \%$	$(Y_{\text{OCDs, max.}} + Y_{\text{ROPs}}) / \%$	$Y_{\text{C}_9} / \%$
4.8Ru/Na _{0.61} ,H _{0.39} -Y	257	66	8	5	22	44
3.5Re/Na _{0.97} ,H _{0.03} -Y	282	37	5	2	6	29
5.3Pd/Na _{0.72} ,H _{0.28} -Y	326	66	5	3	14	5
4.9Rh/Na _{0.64} ,H _{0.36} -Y	295	64	17	11	29	15
2.9Ir/Na _{0.90} ,H _{0.10} -Y *	300	86	36	31	54	25
3.0Pt/Na _{0.88} ,H _{0.12} -Y *	361	96	41	39	54	33

* Data taken from Ref. [25].

The carbon number distributions of the hydrocracked products formed on the four catalysts are depicted in Figure 7.2. Catalysts 4.8Ru/Na_{0.61},H_{0.39}-Y and 3.5Re/Na_{0.97},H_{0.03}-Y mainly produce methane, and both suffer from secondary cracking, which is indicated by values of ΣS_j^* greater than 200 % (see Section 9.2.5, page 161). In contrast, the carbon number distribution curve for 5.3Pd/Na_{0.72},H_{0.28}-Y is clearly M-shaped, which is a strong indication for the occurrence of the paring reaction. However, bearing in mind the higher strength of the acid sites determined for this catalyst compared to the other three catalysts of this series (see Section 6.4, page 92, Figure 6.22), the occurrence of the paring reaction is not unexpected. The distribution curve obtained for 4.9Rh/Na_{0.64},H_{0.36}-Y is quite similar to the one obtained for the HIPEROX 2.9Ir/Na_{0.90},H_{0.10}-Y (see Section 4.3.3, page 47, Figure 4.26): High amounts of methane and C₉ hydrocarbons and nearly equal amounts of C₂ to C₈ hydrocarbons. The slightly higher amounts of methane compared to the C₉ hydrocarbons originate from secondary cracking.

The results discussed in this Section show that the nature of the noble metal can have a significant influence on the performance of bifunctional zeolite catalysts. Based on the results all subsequent experiments were conducted on catalysts containing either iridium or platinum.

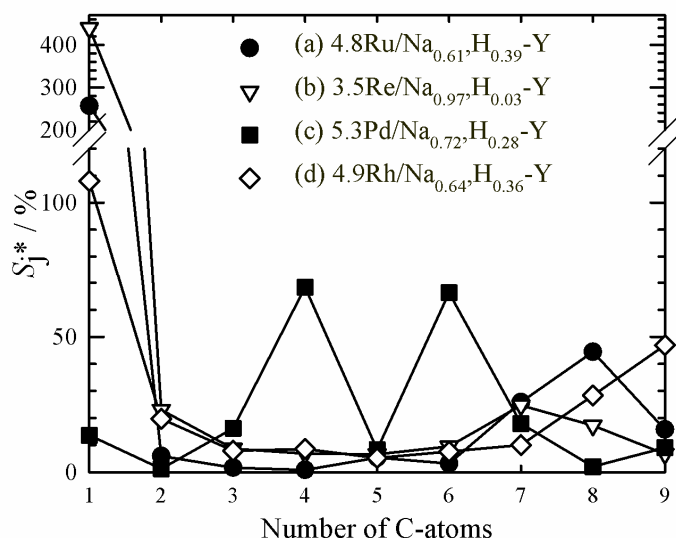


Figure 7.2: Carbon number distributions of the hydrocracked products obtained on four Na,H-Y catalysts:

- | | | | | |
|------|-------------------------------------|------------------------------------|------------------------------------|-----------------------------------|
| (a): | $T_r = 257\text{ }^\circ\text{C}$; | $X_{\text{Dec}} = 66\text{ } \%$; | $Y_{\text{C}_9} = 44\text{ } \%$; | $\Sigma S_j^* = 359\text{ } \%$. |
| (b): | $T_r = 282\text{ }^\circ\text{C}$; | $X_{\text{Dec}} = 37\text{ } \%$; | $Y_{\text{C}_9} = 29\text{ } \%$; | $\Sigma S_j^* = 543\text{ } \%$. |
| (c): | $T_r = 326\text{ }^\circ\text{C}$; | $X_{\text{Dec}} = 66\text{ } \%$; | $Y_{\text{C}_9} = 5\text{ } \%$; | $\Sigma S_j^* = 203\text{ } \%$. |
| (d): | $T_r = 295\text{ }^\circ\text{C}$; | $X_{\text{Dec}} = 64\text{ } \%$; | $Y_{\text{C}_9} = 15\text{ } \%$; | $\Sigma S_j^* = 242\text{ } \%$. |

7.2 Influence of the Zeolite Structure

In the following two Sections the influence of the zeolite structure on the hydrodeacyclization of decalin will be investigated. In Section 7.2.1 the results obtained on catalysts Pt/Na,H-mordenite, Pt/K,H-L, Pt/H-SAPO-5, Pt/Na,H-EMC-2, Pt/H,Na-[Al]Beta-14 and Pt/H,Na-ZSM-5 will be discussed, whereas Section 7.2.2 is dealing with the results on the respective zeolites loaded with iridium. This screening was done in order to learn more about the impact of the structure of the zeolitic support on the selectivities of ring opening of decalin.

7.2.1 Platinum-Containing Zeolites

In Figure 7.3 the conversions and selectivities of the different groups of products for the various platinum-loaded zeolites are depicted. The behavior of the five large-pore zeolite catalysts, *viz.* Pt/Na,H-mordenite (Figure 7.3a), Pt/K,H-L (Figure 7.3b), Pt/H-SAPO-5 (Figure 7.3c), Pt/Na,H-EMC-2 (Figure 7.3d) and Pt/H,Na-[Al]Beta-14 (Figure 7.3e) are quite similar: Over a wide range of reaction temperatures mainly skeletal isomers are formed. With increasing conversions the selectivities of ring-opening products pass through maxima, whereas the selectivities of open-chain decanes increase till they also pass through maxima or the highest measured temperature was reached. At conversions around 60 % the formation

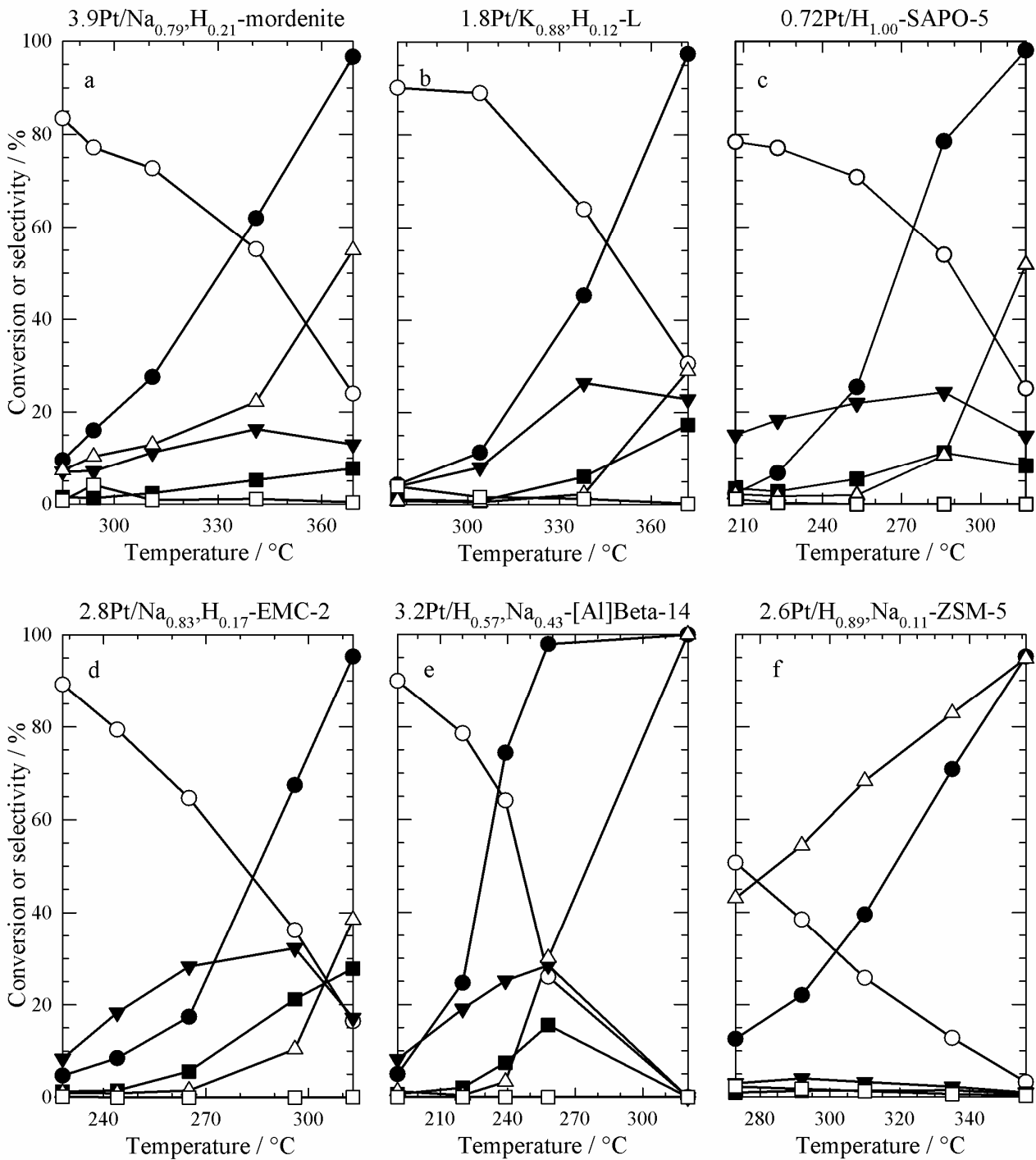


Figure 7.3: Conversion of decalin and selectivities of the different groups of products in dependence of the reaction temperature for the platinum-loaded zeolites. (● X_{Dec} , ■ S_{OCDs} , ▼ S_{ROPs} , ○ $S_{sk-Isos}$, △ S_{C9-} , □ S_{DHPs}).

of hydrocracked products is the prevailing reaction. Dehydrogenation of decalin to tetralin and naphthalene was nearly absent over the whole range of conversions.

The medium-pore zeolite 2.6Pt/H_{0.89},Na_{0.11}-ZSM-5 shows a totally different behavior: Only traces of OCDs, ROPs and DHPs are formed, and the selectivity of the C₉- products increases strongly with increasing temperature, whereas the selectivity of skeletal isomers decreases with increasing conversion. A possible reason for the completely different behavior will be discussed later in this Section. In view of an industrial ring-opening process, Pt/H₃Na-ZSM-5 shows a very poor selectivity pattern.

Summarized in Table 7.2 are the maximum yields and selectivities of open-chain decanes (OCDs) and combined yields of ring-opening products (ROPs) and OCDs of the catalysts of this series. The best performance, in terms of the maximum yield of OCDs showed 2.8Pt/Na_{0.83},H_{0.17}-EMC-2 with $Y_{\text{OCDs, max.}} = 27\%$ at 313 °C. These promising results are not totally unexpected, since the framework structure of EMC-2 is closely related to the one of faujasites. In addition, Pt/K₃H-L and Pt/H₃Na-[Al]Beta-14 also showed encouraging results with 17 and 15 % maximum yields of OCDs, respectively. If one considers the sum of Y_{OCDs} and Y_{ROPs} (Table 7.2, column 6), these two supports show similar results as the Na₃H-EMC-2-supported catalyst, moreover, both produce 10 % less hydrocracked products. Remarkably, the best zeolitic supports possess a spaciousness index of 16 or above (see Table 4.1, page 19).

The relatively high amounts of isomers formed on all these supports can have two origins: (i) type A and B rearrangements *via* carbocations (see Section 4.3.1, page 30) at Brønsted acid sites generated during the reduction of platinum or (ii) the isomerization on platinum itself [56 - 58]. A closer look at the carbon number distributions of the hydrocracked products, presented in Figure 7.4, reveals M-shaped distribution curves for Pt/K₃H-L, Pt/H-SAPO-5, Pt/Na₃H-EMC-2- and Pt/H₃Na-[Al]Beta-14. This indicates, as mentioned in the previous Section, the occurrence of the paring reaction. This in turn, may be taken as a hint for isomerization of decalin occurring at the Brønsted acid sites. The small amounts of methane and C₉ formed stem from a small contribution of hydrogenolytic carbon-carbon bond rupture.

The very high sum of modified hydrocracking selectivities obtained on 3.9Pt/Na_{0.79},H_{0.21}-mordenite ($\sum S_j^* = 441\%$) is an indicator for an extremely strong secondary hydrocracking. This explains that only traces of C₅ to C₉ are observed. However, the reason for the formation of the large amounts of propane is not known.

Table 7.2: Maximum yields and selectivities of OCDs, combined yields of ROPs and OCDs and yields of C₉- hydrocarbons at reaction conditions of maximal OCD yields in the hydroconversion of decalin on the platinum-loaded zeolites.

Catalyst	$T_r /$ °C	$X_{Dec} /$ %	$S_{OCDs} /$ %	$Y_{OCDs, max.} /$ %	$(Y_{OCDs, max.} +$ $Y_{ROPs}) /$ %	$Y_{C_9-} /$ %
3.9Pt/Na _{0.79} ,H _{0.21} -mordenite	369	97	8	7	20	53
1.8Pt/K _{0.88} ,H _{0.12} -L	372	97	17	17	39	28
0.72Pt/H _{1.00} -SAPO-5	286	78	11	9	28	8
2.8Pt/Na _{0.83} ,H _{0.17} -EMC-2	313	95	28	27	43	37
3.2Pt/H _{0.57} ,Na _{0.43} -[Al]Beta-14	258	98	16	15	43	29
2.6Pt/H _{0.89} ,Na _{0.11} -ZSM-5	335	71	1	1	3	59

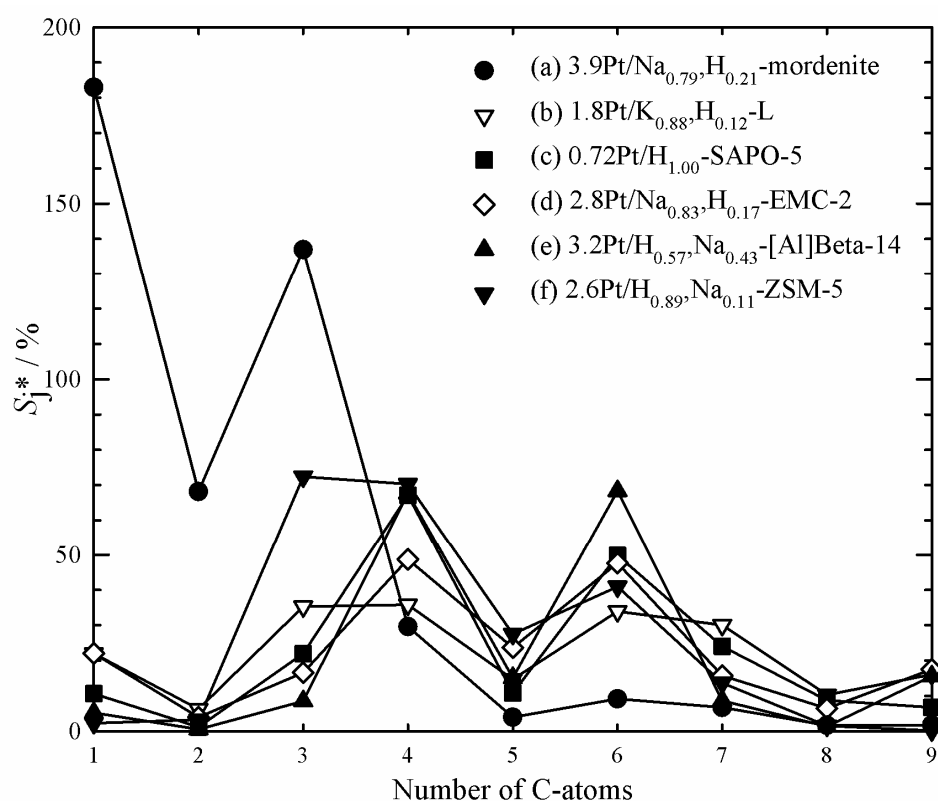


Figure 7.4: Carbon number distributions of the hydrocracked products obtained on the platinum-loaded zeolite catalysts:

- (a): $T_r = 369$ °C; $X_{Dec} = 97$ %; $Y_{C_9-} = 53$ %; $\Sigma S_j^* = 441$ %.
 (b): $T_r = 372$ °C; $X_{Dec} = 97$ %; $Y_{C_9-} = 28$ %; $\Sigma S_j^* = 205$ %.
 (c): $T_r = 286$ °C; $X_{Dec} = 78$ %; $Y_{C_9-} = 8$ %; $\Sigma S_j^* = 201$ %.
 (d): $T_r = 313$ °C; $X_{Dec} = 95$ %; $Y_{C_9-} = 37$ %; $\Sigma S_j^* = 202$ %.
 (e): $T_r = 258$ °C; $X_{Dec} = 98$ %; $Y_{C_9-} = 29$ %; $\Sigma S_j^* = 191$ %.
 (f): $T_r = 335$ °C; $X_{Dec} = 71$ %; $Y_{C_9-} = 59$ %; $\Sigma S_j^* = 232$ %.

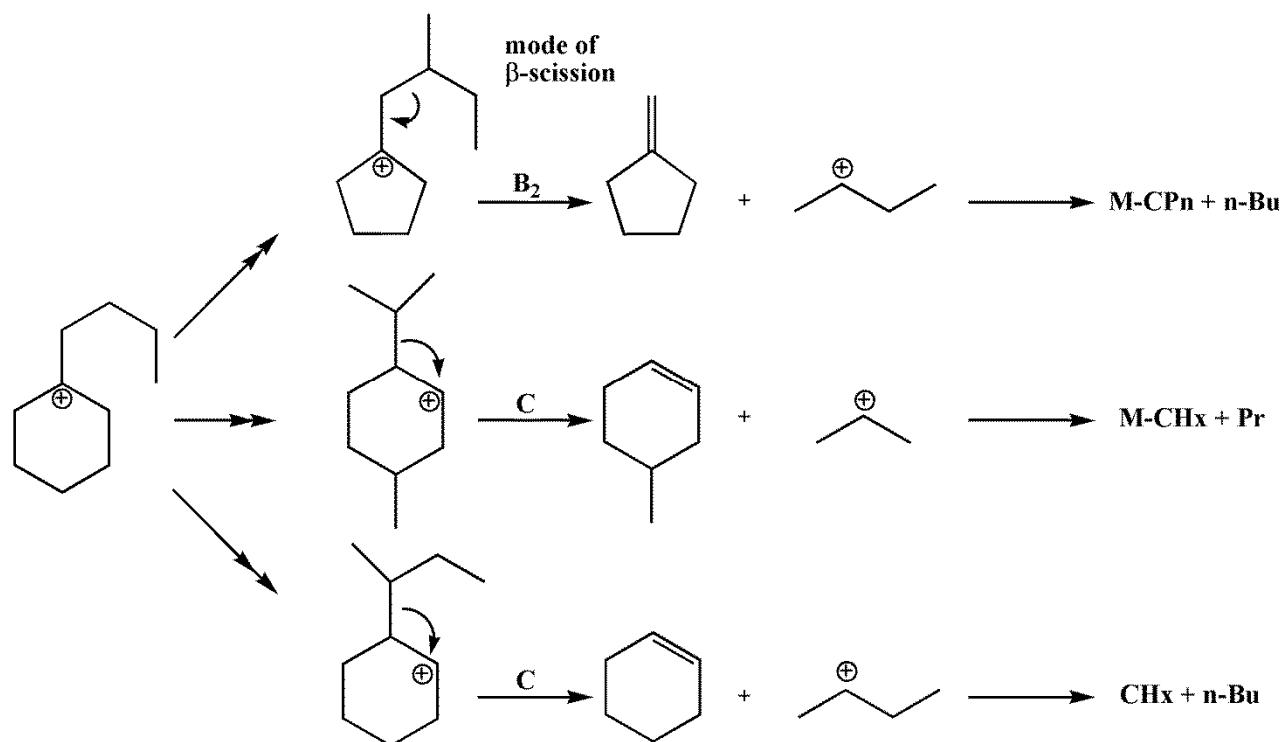


Figure 7.5: Exocyclic type B_2 and type C β -scissions of cycloalkylcarbenium ions with 10 carbon atoms. (M-CPn: methylcyclopentane; n-Bu: n-butane; M-CHx: methylcyclohexane; Pr: propane; CHx: cyclohexane). After Ref. [104].

In the case of 2.6Pt/H_{0.89},Na_{0.11}-ZSM-5 the M-shape of the distribution curve is distorted: More C₃ and C₄ are formed than C₆ and C₇. Furthermore, the C₆ fraction does not mainly consist of methylcyclopentane, and the content of iso-butane in the C₄ fraction amounts to 50 % only. These are hints for the absence of the paring reaction. In addition, the hydrocracking is much less selective than with 12-membered-ring zeolites. In principle, this loss of selectivity of the C₉- products has been found earlier in hydrocracking of alkanes on Pt/H-ZSM-5 [62] and of naphthenes on Pd/H-ZSM-5 [104]. The authors concluded that the bulky precursors for type A β -scissions, which are necessary for the paring reaction, cannot be formed in the small channels of ZSM-5. In Figure 7.5 possible pathways for the formation of various hydrocracked products *via* type B_2 and C β -scissions are depicted starting from butylcyclohexane.

In order to get more information about the number of branchings in the group of open-chain decanes, the OCDs are subdivided into non-branched decane (n-C₁₀), monobranched decanes with a methyl group (M-C₉) or an ethyl group (E-C₈) and multiply branched decanes (MBDe). For a better comparability of the results obtained on different catalysts, the distribution of these groups among the OCDs is given. In Figure 7.6 the distribution of the differently branched decanes on the catalysts 3.9Pt/Na_{0.79},H_{0.21}-mordenite, 0.72Pt/H-SAPO-5 and 3.2Pt/H_{0.57},Na_{0.43}-[Al]Beta-14 are depicted. On all three catalysts the multiply

branched decanes are the main OCDs formed, whereas only traces of n-decane and ethyloctanes are formed. The most pronounced difference between the three catalysts is the amount of methylnonanes formed: On the Na-mordenite- and Na-SAPO-5-supported catalysts they account for around 25 % of all OCDs formed, whereas nearly 40 % of all OCDs are methylnonanes in the case of 3.2Pt/H_{0.57},Na_{0.43}-[Al]Beta-14. This is much better than the distributions obtained for the other catalysts, since mildly branched decane isomers possess much higher cetane numbers than their highly branched isomers.

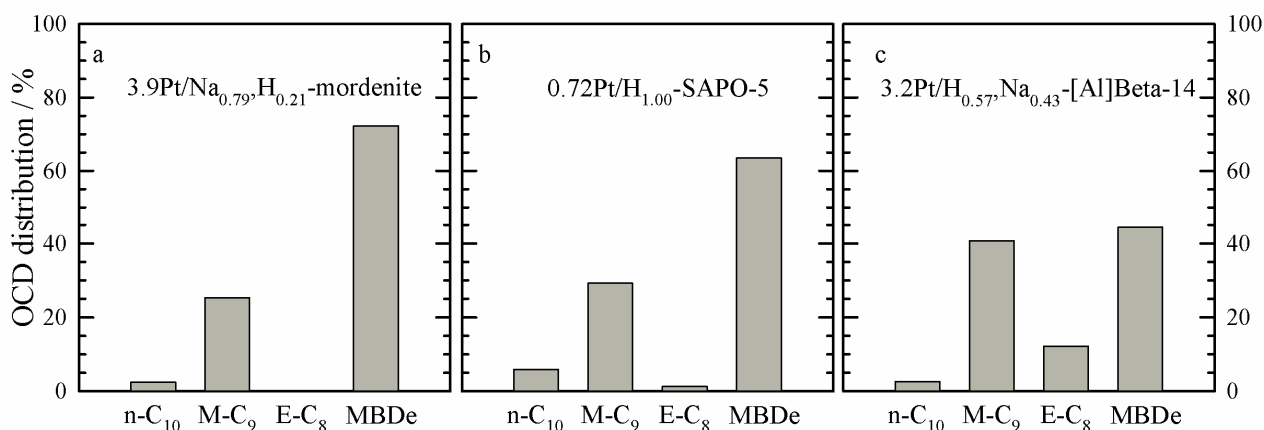


Figure 7.6: Breakdown of the selectivities of OCDs into differently branched decanes on Pt/Na,H-mordenite, Pt/H-SAPO-5 and Pt/H,Na-[Al]Beta-14 (n-C₁₀: n-decane; M-C₉: methylnonanes; E-C₈: ethyloctanes; MBDe: multiply branched decanes):
 (a): $T_r = 369\text{ }^\circ\text{C}$; $X_{\text{Dec}} = 97\text{ }%$; $Y_{\text{OCDs}} = 7\text{ }%$; $S_{\text{OCDs}} = 8\text{ }%$.
 (b): $T_r = 286\text{ }^\circ\text{C}$; $X_{\text{Dec}} = 78\text{ }%$; $Y_{\text{OCDs}} = 9\text{ }%$; $S_{\text{OCDs}} = 11\text{ }%$.
 (c): $T_r = 258\text{ }^\circ\text{C}$; $X_{\text{Dec}} = 98\text{ }%$; $Y_{\text{OCDs}} = 15\text{ }%$; $S_{\text{OCDs}} = 16\text{ }%$.

7.2.2 Iridium-Containing Zeolites

For the iridium-containing catalysts discussed in this Section the same supports were used as for the platinum-containing catalysts described in Section 7.2.1. However, the conversions and selectivities of the different groups of products on the six iridium-containing catalysts, which are depicted in Figure 7.7, have a totally different behavior compared to the platinum-loaded catalysts: Ir/Na,H-mordenite, Ir/K,H-L, Ir/Na,H-EMC-2 and Ir/Na,H-[Al]Beta-14 produce nearly equal amounts of ring-opening products and skeletal isomers of decalin at low conversions. With increasing conversion their selectivities decrease, and the selectivity of OCDs increases until maxima are reached. The amount of ROPs obtained on 2.0Ir/K_{0.86},H_{0.14}-L first increases and then decreases very fast. At even higher conversions the formation of hydrocracked products (C₉-) becomes the prevailing reaction, with the exception of 3.0Ir/Na_{0.53},H_{0.47}-[Al]Beta-14. There, the selectivity of C₉- stays below 20 % until $T_r = 260\text{ }^\circ\text{C}$.

It is likely, that the unusual behavior of 0.067Ir/H_{0.91},Na_{0.09}-SAPO-5 (Figure 7.7c) has its origin in the low amount of iridium loaded onto this zeolite. Skeletal isomers are formed with high selectivities which decrease with increasing conversion. The selectivities of ROPs and OCDs only slightly increase and pass through maxima at a conversion of around 70 %. As usually, the formation of hydrocracked products becomes more and more prevailing with increasing reaction temperature until they are nearly exclusively formed at 99 % conversion. These results are quite similar to the ones obtained with 0.72Pt/H_{1.00}-SAPO-5 (see Figure 7.3c, page 100), which means that the nature of the noble metal has no great influence on the selectivities on these two catalysts. However, as already stated, this is likely to have its origin in the low amounts of noble metal.

The selectivities obtained on 0.52Ir/H_{0.59},Na_{0.41}-ZSM-5 are comparable with those obtained on the Na-mordenite-supported catalyst, except for the high amounts of hydrocracked products formed even at very low conversions. However, this resembles the findings with the platinum-loaded H,Na-ZSM-5 zeolite.

The maximum yields and selectivities of OCDs and the combined yields of ROPs and OCDs obtained on the catalysts of this series are summarized in Table 7.3. As can be seen, two high-performance ring-opening catalysts (HIPEROCS) are present in this series, *viz.* 3.0Ir/Na_{0.80},H_{0.20}-EMC-2 and 3.0Ir/Na_{0.53},H_{0.47}-[Al]Beta-14, with maximum yields of OCDs of 27 and 34 %, respectively. Not only is the maximum yield of OCDs higher on the Beta-supported catalyst, but also the combined yields of OCDs and ROPs are 9 % higher. Moreover, the amounts of hydrocracked products at the conditions of maximum OCDs yields are very low on both catalysts ($Y_{C_9} = 14\%$). All this makes zeolite [Al]Beta a very promising support for further investigations. It remains to be stated that the results obtained on the two Na,H-mordenite- and K,H-L-supported catalysts are also quite good.

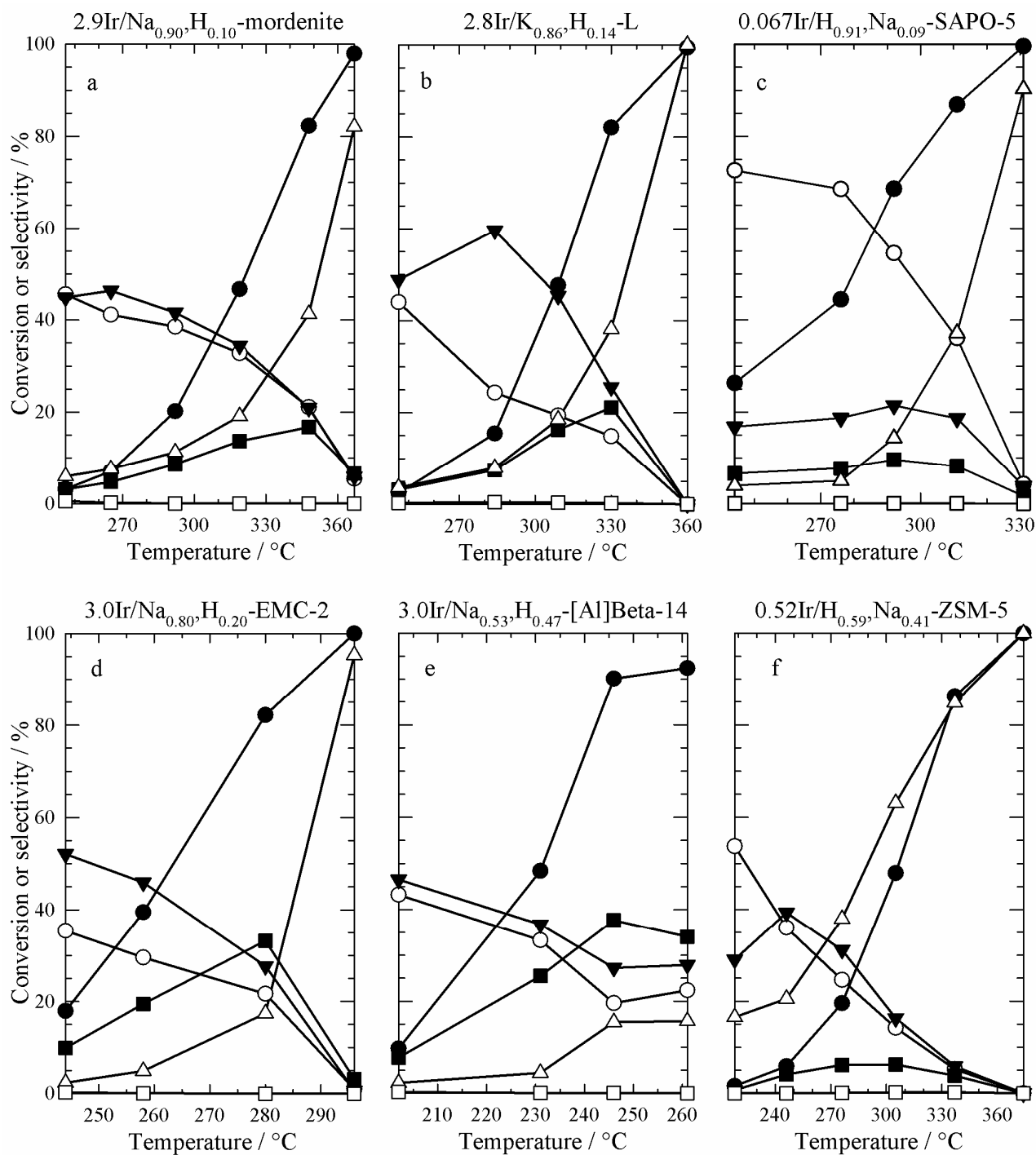


Figure 7.7: Conversion of decalin and selectivities of the different groups of products in dependence of the reaction temperature for the iridium-loaded zeolites. (●- X_{Dec} , ■- S_{OCDs} , ▼- S_{ROPs} , ○- $S_{sk-Isos}$, △- S_{C_9-} , □- S_{DHPs}).

Table 7.3: Maximum yields and selectivities of OCDs, combined yields of ROPs and OCDs and yields of C₉- hydrocarbons at reaction conditions of maximal OCD yields in the hydroconversion of decalin on the iridium-loaded zeolites.

Catalyst	T_r / °C	X_{Dec} / %	S_{OCDs} / %	$Y_{OCDs, max.}$ / %	$(Y_{OCDs, max.} + Y_{ROPs})$ / %	Y_{C_9-} / %
2.9Ir/Na _{0.90} ,H _{0.10} -mordenite	348	82	17	14	31	34
2.8Ir/K _{0.86} ,H _{0.14} -L	330	82	21	17	38	31
0.067Ir/H _{0.91} ,Na _{0.09} -SAPO-5	311	87	8	7	23	32
3.0Ir/Na _{0.80} ,H _{0.20} -EMC-2	280	82	33	27	50	14
3.0Ir/Na _{0.53} ,H _{0.47} -[Al]Beta-14	246	90	38	34	59	14
0.52Ir/H _{0.59} ,Na _{0.41} -ZSM-5	337	86	4	3	8	73

The carbon number distributions of the hydrocracked products depicted in Figure 7.8 indicate for 0.067Ir/H_{0.91},Na_{0.09}-SAPO-5, by contrast to the other catalysts, a bifunctional hydrocracking mechanism (indicated by the M-shaped distribution curve). 2.9Ir/Na_{0.90},H_{0.10}-mordenite and 2.8Ir/K_{0.86},H_{0.14}-L show hammock-shaped curves with a higher amount of methane than C₉ hydrocarbons. The higher amount of methane is also mirrored by the high sum of the modified hydrocracking selectivities of 386 % and 250 % for Ir/Na,H-mordenite and Ir/K,H-L, respectively, which are indicators for the occurrence of secondary hydrocracking. However, the high amounts of propane obtained for 3.9Pt/Na_{0.79},H_{0.21}-mordenite (see Figure 7.4, page 102) was not found for the iridium-containing mordenite. Thus this peculiarity, most probably stems from the platinum rather than from the structure of the supporting zeolite. Ir/Na,H-EMC-2 possesses a modified hammock curve in that the S_j^* values are nearly equally distributed from C₁ to C₉. In the case of Ir/Na,H-[Al]Beta-14 the S_j^* values of C₄ and C₆ are somewhat elevated, indicating a certain contribution of the paring reaction. For the medium-pore zeolite H_{0.59},Na_{0.41}-ZSM-5 nearly identical carbon number distribution curves are obtained for both the platinum- and the iridium-containing catalyst (see also Figure 7.4, page 102).

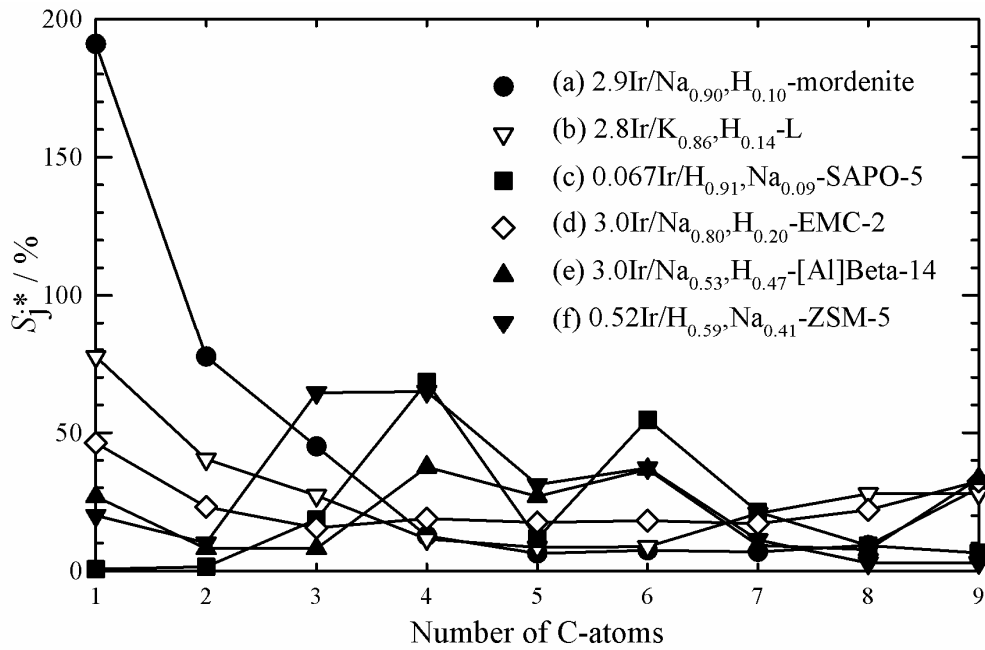


Figure 7.8: Carbon number distributions of the hydrocracked products obtained on the iridium-loaded zeolite catalysts:

(a):	$T_r = 348\text{ }^\circ\text{C}$;	$X_{\text{Dec}} = 82\text{ } \%$;	$Y_{\text{C}_9} = 34\text{ } \%$;	$\Sigma S_j^* = 386\text{ } \%$.
(b):	$T_r = 330\text{ }^\circ\text{C}$;	$X_{\text{Dec}} = 82\text{ } \%$;	$Y_{\text{C}_9} = 31\text{ } \%$;	$\Sigma S_j^* = 250\text{ } \%$.
(c):	$T_r = 311\text{ }^\circ\text{C}$;	$X_{\text{Dec}} = 87\text{ } \%$;	$Y_{\text{C}_9} = 32\text{ } \%$;	$\Sigma S_j^* = 192\text{ } \%$.
(d):	$T_r = 280\text{ }^\circ\text{C}$;	$X_{\text{Dec}} = 82\text{ } \%$;	$Y_{\text{C}_9} = 14\text{ } \%$;	$\Sigma S_j^* = 211\text{ } \%$.
(e):	$T_r = 246\text{ }^\circ\text{C}$;	$X_{\text{Dec}} = 90\text{ } \%$;	$Y_{\text{C}_9} = 14\text{ } \%$;	$\Sigma S_j^* = 194\text{ } \%$.
(f):	$T_r = 337\text{ }^\circ\text{C}$;	$X_{\text{Dec}} = 86\text{ } \%$;	$Y_{\text{C}_9} = 73\text{ } \%$;	$\Sigma S_j^* = 245\text{ } \%$.

Nearly identical distributions of the differently branched decanes were observed for the platinum- and iridium-loaded catalysts (see Figure 7.9): High amounts of multiply branched decanes are formed and nearly no n-decane. It seems that the structure of the support has a much greater influence on the distribution than the nature of the noble metal. However, a comparison of the distribution obtained on 3.2Pt/H_{0.57},Na_{0.43}-[Al]Beta-14 with the one obtained on 3.0Ir/Na_{0.53},H_{0.47}-[Al]Beta-14 reveals that much more methylnonanes and less multiply branched decanes are formed on the platinum-containing catalyst.

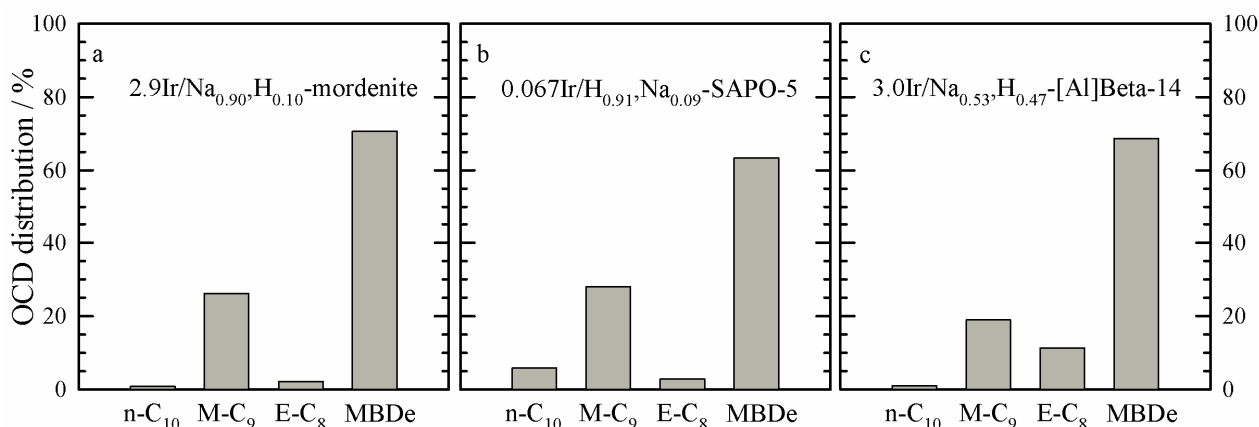


Figure 7.9: Breakdown of the selectivities of OCDs into differently branched decanes on the iridium-loaded zeolites Na-mordenite, SAPO-5 and Na-[Al]Beta-14 (n-C₁₀: n-decane; M-C₉: methylnonanes; E-C₈: ethyloctanes; MBDe: multiply branched decanes):

(a): $T_r = 348$ °C; $X_{Dec} = 82$ %; $Y_{OCDs} = 14$ %; $S_{OCDs} = 17$ %.

(b): $T_r = 311$ °C; $X_{Dec} = 87$ %; $Y_{OCDs} = 7$ %; $S_{OCDs} = 8$ %.

(c): $T_r = 246$ °C; $X_{Dec} = 90$ %; $Y_{OCDs} = 34$ %; $S_{OCDs} = 38$ %.

In conclusion, ZSM-5 and SAPO-5 are not a good choice as zeolites for the selective ring opening of decalin, the former due its the narrow pores and the latter due to the low ion-exchange capacity leading to very low metal loadings. Zeolites mordenite and L seem to possess the potential for a further improvement of OCD yields by modifying the strength of the Brønsted acid sites. A reduction of the strength of the Brønsted acid sites of zeolite mordenite could lead to enhanced yields of OCDs, since it is very active in the hydroconversion of decalin and exhibits a high tendency for secondary hydrocracking which may be reduced by a lower strength of the acid sites. Since the formation of ring-opening products is prevailing at low conversions in the case of zeolite L, indicating that the hydrogenolytic activity of iridium is prevailing, a variation in both directions, lowering and heightening of the acidic strength could lead to higher yields of OCDs. Nevertheless, the best supports so far are zeolites [Al]Beta-14 and EMC-2, which both possess spaciousness indices above 18. However, since EMC-2 has a structure very similar to the faujasites studied by Rabl *et al.* [25, 89] this zeolite will not be used for further modification, emphasis will rather be placed on zeolite Beta.

As already shown by Rabl *et al.* [25], the strength of the Brønsted acid sites has a marked influence on the yields and selectivities of the different products formed in the hydroconversion of decalin. This concept of modifying the strength of the acid sites to enhance the yield of OCDs will be applied to zeolites mordenite, L and Beta.

7.3 Influence of the Strength of the Brønsted Acid Sites

In general there are three ways to influence the strength of Brønsted acid sites in zeolites: (i) isomorphous substitution of framework elements, (ii) variation of the molar ratio $n_{\text{Si}} / n_{\text{Al}}$, and (iii) variation of the nature of the charge-compensating cations (see also Section 4.2, page 21). These three methods were applied to zeolite Beta and, in addition, the variation of the nature of the charge-compensating cation was applied to zeolites mordenite and L. In the following, the results of the hydroconversion of decalin obtained on the thus modified zeolites will be discussed.

7.3.1 Isomorphous Substitution

The isomorphous substitution of aluminum by boron leads to much weaker Brønsted acid sites in zeolite Beta (see Figure 6.24, page 93). Unfortunately, it seems that the reduction is even too strong: In Figure 7.10 the conversion of decalin and the selectivities of the different groups of products for the two Na,H-[B]Beta-18 zeolites are depicted. The results obtained with Ir/H,Na-[B]Beta-18 are nearly identical to the results obtained with the monofunctional metallic Ir/silica in the hydroconversion of decalin by Haas *et al.* (see Figure 4.24, page 44) [88]: By far the prevailing reaction at low conversions is direct ring opening of decalin by hydrogenolysis leading nearly exclusively to the direct ROPs butylcyclohexane, cis- and trans-1-methyl-2-propylcyclohexane and cis- and trans-1,2-diethylcyclohexane. With increasing conversion the amount of ROPs decreases, and the formation of hydrocracked products becomes the prevailing reaction. The amount of open-chain decanes and skeletal isomers remains nearly constant at around 10 % selectivity over the whole range of conversions. Pt/Na,H-[B]Beta-18 shows, in contrast to 2.3Ir/H_{0.88},Na_{0.12}-[B]Beta-18, a totally different behavior, which is not comparable with the results obtained with Pt/silica. In a first step, skeletal isomers of decalin are formed which undergo, with increasing conversion, ring-opening reactions to form ROPs and OCDs. With none of the [B]Beta catalysts, dehydrogenated products were observed.

In comparison to the Ir/Na,H-[Al]Beta-14 catalyst (see Figure 7.7e, page 106), the maximum yield of OCDs decreases from 34 % to only 9 %. However, they increased for the platinum-loaded catalysts from $Y_{\text{OCDs,max.}} = 15 \%$ to 23 % (see also Table 7.4). Presumably, the decreasing yields of OCDs on the iridium-containing catalyst originate from the lack of sufficiently strong acid sites for the isomerization of decalin on Na,H-[B]Beta. As already stated by various groups [72, 87, 88] the isomerization of the six-membered-rings of decalin to substituted five-membered-rings enhances the rate of the ring-opening reaction. In the case of the two platinum-loaded catalysts, the enhancement of the yields of OCDs can have its origin in the reduction of the activity of the [B]Beta-supported catalyst compared to the [Al]Beta-supported one.

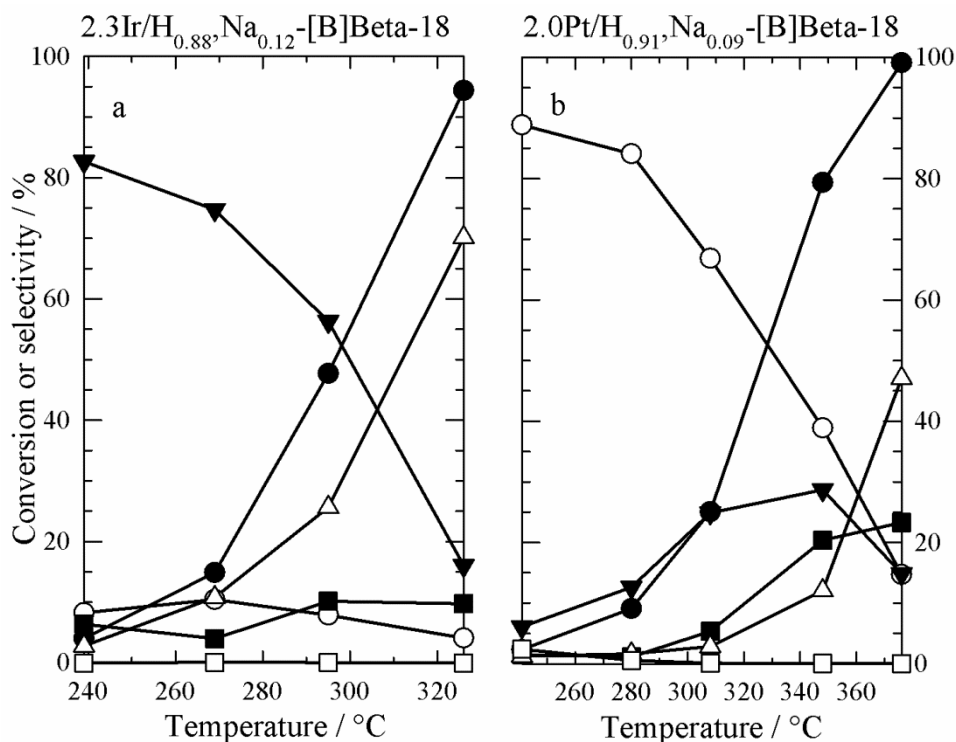


Figure 7.10: Conversion of decalin and selectivities of the different groups of products in dependence of the reaction temperature for the two [B]Beta catalysts. (● X_{Dec} , ■ S_{OCDs} , ▼ S_{ROPs} , ○ $S_{sk-Isos}$, △ S_{C_9-} , □ S_{DHPs}).

Table 7.4: Maximum yields and selectivities of OCDs, combined yields of ROPs and OCDs and yields of C₉- hydrocarbons at reaction conditions of maximal OCD yields in the hydroconversion of decalin on the two [B]Beta catalysts.

Catalyst	$T_r /$ °C	$X_{Dec} /$ %	$S_{OCDs} /$ %	$Y_{OCDs, max.} /$ %	$(Y_{OCDs, max.} +$ $Y_{ROPs}) /$ %	$Y_{C_9-} /$ %
2.3Ir/H _{0.88} ,Na _{0.12} -[B]Beta-18	326	94	10	9	24	66
2.0Pt/H _{0.91} ,Na _{0.09} -[B]Beta-18	376	99	23	23	38	47

The carbon number distribution of the hydrocracked products, depicted in Figure 7.11, mirrors the very weak Brønsted acid sites of the support: For 2.3Ir/H_{0.88},Na_{0.12}-[B]Beta-18 a hammock-shaped curve is obtained with a high amount of methane, which stems from secondary cracking. The distribution curve obtained for 2.0Pt/H_{0.91},Na_{0.09}-[B]Beta-18 is completely different: A nearly equal distribution of hydrocracked products is obtained. Just the amounts of C₂ and C₈ hydrocarbons are somewhat lower.

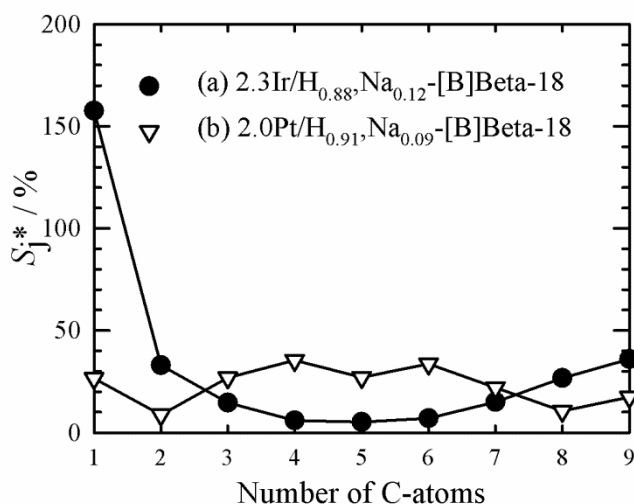


Figure 7.11: Carbon number distributions of the hydrocracked products obtained on the two [B]Beta catalysts:

- (a): $T_r = 326\text{ }^\circ\text{C}$; $X_{\text{Dec}} = 94\text{ }%$; $Y_{\text{C}_9} = 66\text{ }%$; $\Sigma S_j^* = 301\text{ }%$.
 (b): $T_r = 376\text{ }^\circ\text{C}$; $X_{\text{Dec}} = 99\text{ }%$; $Y_{\text{C}_9} = 47\text{ }%$; $\Sigma S_j^* = 208\text{ }%$.

Summing up, the isomorphous substitution of aluminum by boron in zeolite Beta leads to a considerable reduction of the strength of the Brønsted acid sites (see Section 6.4, Figure 6.24, page 93). The catalytic data show that the resulting acid strength is too low for a formation of five-membered rings *via* skeletal isomerization, which seems to be essential for the ring opening of decalin.

7.3.2 Variation of the Molar Ratio of Silicon to Aluminum

In this series of catalysts the molar ratio of silicon to aluminum of zeolite [Al]Beta was varied. This led to different Brønsted acid strengths of the supports, with the acid strength increasing in the order H,Na-[Al]Beta-8 < H,Na-[Al]Beta-14 < H,Na-[Al]Beta-21 (see Section 6.4, Figure 6.24, page 93). However, even H,Na-[Al]Beta-8 has a higher acid strength than H,Na-[B]Beta-18.

Depicted in Figure 7.12 are the conversions of decalin and selectivities of different groups of products on the six catalysts supported on the Na,H-[Al]Beta zeolites. The results obtained on Na,H-[Al]Beta-14 were already discussed in Sections 7.2.1 and 7.2.2, pages 99 and 104, respectively, and are shown for comparison only.

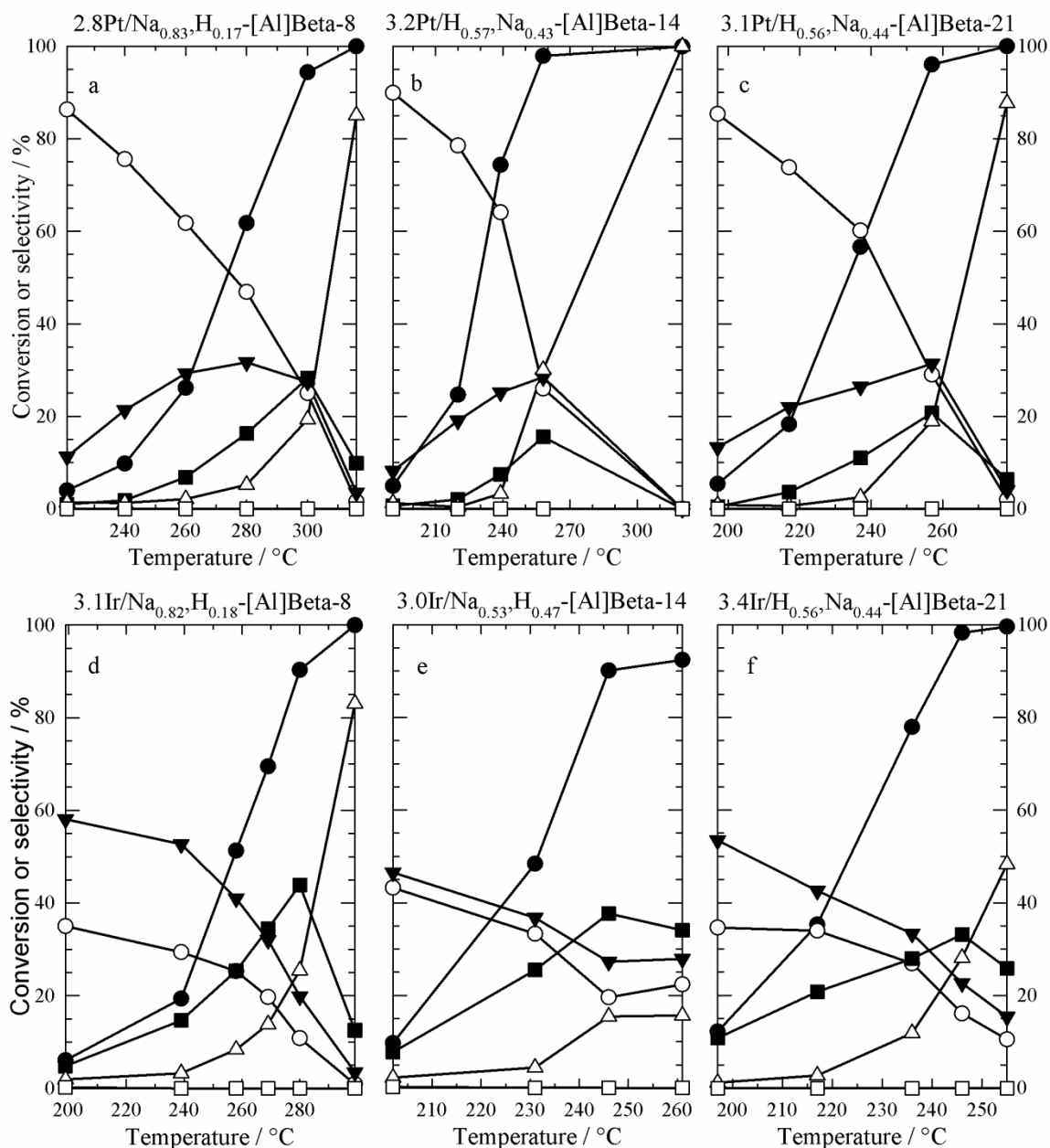


Figure 7.12: Conversion of decalin and selectivities of the different groups of products in dependence of the reaction temperature for the six [Al]Beta-supported catalysts. (\bullet X_{Dec} , \blacksquare S_{OCDs} , \blacktriangledown S_{ROPs} , \circ $S_{sk-Isos}$, \triangle S_{C_9-} , \square S_{DHPs}).

The platinum-containing catalysts, *viz.* 2.8Pt/Na_{0.83}H_{0.17}-[Al]Beta-8 (Figure 7.12a), 3.2Pt/H_{0.57},Na_{0.43}-[Al]Beta-14 (Figure 7.12b) and 3.1Pt/H_{0.56},Na_{0.44}-[Al]Beta-21 (Figure 7.12c) produce mainly skeletal isomers at low conversions. With increasing reaction temperature the selectivities of ring-opening products and open-chain decanes rise till maxima are reached at $T_r = 300$, 258 and 257 °C, respectively. These differences in the temperatures of the maxima can be attributed to the different strength of the Brønsted acid sites of the three supports: With increasing strength of the acid sites, $S_{ROPs, max.}$ and $S_{OCDs, max.}$ are shifted to lower temperatures. The maximum in S_{OCDs} of 2.8Pt/Na_{0.83}H_{0.17}-[Al]Beta-8

amounted to 28 %, which is together with the value of 2.8Pt/Na_{0.83},H_{0.17}-EMC-2 (see Section 7.2.1, page 99) the highest selectivity of OCDs reached in this work so far for platinum-containing catalysts. However, the stronger Brønsted acid sites of 3.1Pt/H_{0.56},Na_{0.44}-[Al]Beta-21 led to a higher activity but also to lower selectivities of OCDs ($S_{\text{OCDs, max.}} = 21 \%$).

Catalysts 3.1Ir/Na_{0.82},H_{0.18}-[Al]Beta-8 and 3.4Ir/H_{0.56},Na_{0.44}-[Al]Beta-21, both show the typical behavior of iridium-containing bifunctional catalysts (see Figure 7.12): The prevailing product groups at low conversions are the ring-opening products with S_{ROPs} around 55 %, whereas skeletal isomerization only accounts for 35 % in both cases. With increasing conversion the selectivity of both product groups decreases, while the selectivity of open-chain decanes increases till $S_{\text{OCDs, max.}} = 44$ and 33 % at $T_{\text{r}} = 280$ and 246 °C, respectively (see Table 7.5). At higher reaction temperatures hydrocracking is the prevailing reaction. However, to reach the same level of conversion 40 °C higher temperatures are needed in the case of 3.1Ir/Na_{0.82},H_{0.18}-[Al]Beta-8 compared to 3.4Ir/H_{0.56},Na_{0.44}-[Al]Beta-21. The activity difference stems from the higher strength of the Brønsted acid sites of the latter support.

Remarkably, four out of the six catalysts supported on Na-[Al]Beta meet the requirement for a HIPEROCC ($Y_{\text{OCDs, max.}} > 25 \%$), and with 3.1Ir/Na_{0.82},H_{0.18}-[Al]Beta-8 a yield of OCDs as high as 40 % was achieved, which is the highest yield of OCDs reached so far for iridium-containing catalysts and it is only 1 % less than the value reached with 3.0Pt/Na_{0.88},H_{0.12}-Y by Rabl *et al.* [25].

Table 7.5: Maximum yields and selectivities of OCDs, combined yields of ROPs and OCDs and yields of C₉- hydrocarbons at reaction conditions of maximal OCD yields in the hydroconversion of decalin on the six Na-[Al]Beta-supported catalysts.

Catalyst	$T_{\text{r}} /$ °C	$X_{\text{Dec}} /$ %	$S_{\text{OCDs}} /$ %	$Y_{\text{OCDs, max.}} /$ %	$(Y_{\text{OCDs, max.}} +$ $Y_{\text{ROPs}}) / \%$	$Y_{\text{C}_9-} /$ %
2.8Pt/Na _{0.83} ,H _{0.17} -[Al]Beta-8	300	94	28	27	53	18
3.2Pt/H _{0.57} ,Na _{0.43} -[Al]Beta-14	258	98	16	15	43	29
3.1Pt/H _{0.56} ,Na _{0.44} -[Al]Beta-21	257	96	21	20	50	18
3.1Ir/Na _{0.82} ,H _{0.18} -[Al]Beta-8	280	90	44	40	58	23
3.0Ir/Na _{0.53} ,H _{0.47} -[Al]Beta-14	246	90	38	34	59	14
3.4Ir/H _{0.56} ,Na _{0.44} -[Al]Beta-21	246	98	33	33	55	28

A closer look at the carbon number distribution of the hydrocracked products (Figure 7.13) reveals a hammock-type curve with slightly higher amounts of C₄ to C₆ for 3.1Ir/Na_{0.82},H_{0.18}-[Al]Beta-8, whereas 3.4Ir/H_{0.56},Na_{0.44}-[Al]Beta-21 produces even higher amounts of C₄ to C₆ hydrocarbons and much less methane and C₉ hydrocarbons. The higher

amounts of C₄ and C₆ hydrocarbons presumably stem from the paring reaction which is favored on catalysts with a higher acid strength. The two platinum-containing catalysts show pronounced M-shaped distribution curves. It seems that the varying strength of the Brønsted acid sites does not have any influence on the shape of the distribution curve obtained with the platinum-containing catalysts.

The breakdown of the selectivities of OCDs into differently branched decanes, shown in Figure 7.14, reveals no peculiarities: High amounts of multi-branched decanes, only traces of n-decane and slightly higher amounts of methylnonanes than ethyloctanes are formed.

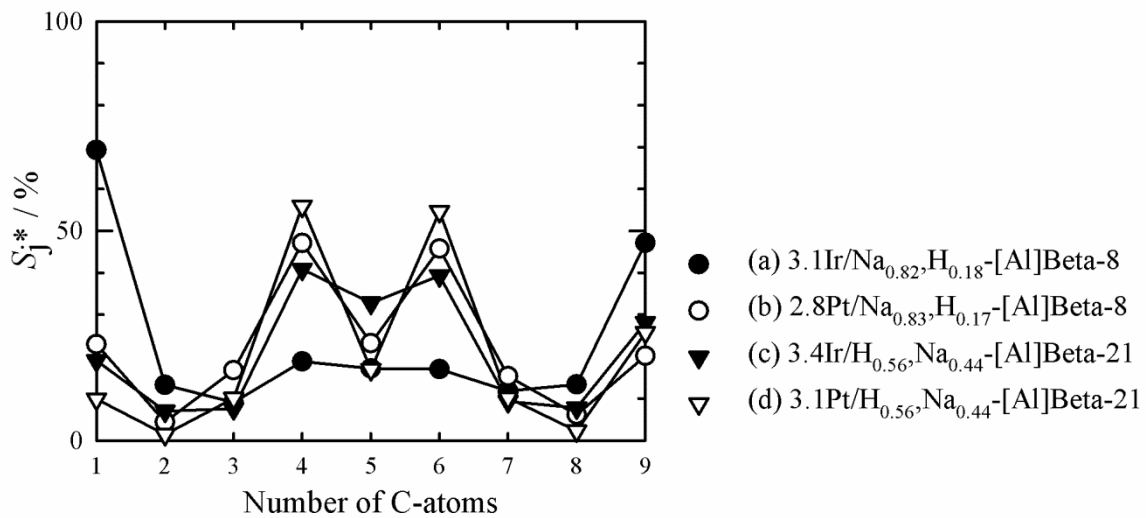


Figure 7.13: Carbon number distributions of the hydrocracked products obtained on four Na-[Al]Beta-supported catalysts:

- | | | | | |
|------|--------------------------------------|-------------------------------------|-------------------------------------|------------------------------------|
| (a): | $T_r = 280 \text{ }^\circ\text{C}$; | $X_{\text{Dec}} = 90 \text{ } \%$; | $Y_{\text{C}_9} = 23 \text{ } \%$; | $\Sigma S_j^* = 217 \text{ } \%$. |
| (b): | $T_r = 300 \text{ }^\circ\text{C}$; | $X_{\text{Dec}} = 94 \text{ } \%$; | $Y_{\text{C}_9} = 18 \text{ } \%$; | $\Sigma S_j^* = 202 \text{ } \%$. |
| (c): | $T_r = 246 \text{ }^\circ\text{C}$; | $X_{\text{Dec}} = 98 \text{ } \%$; | $Y_{\text{C}_9} = 28 \text{ } \%$; | $\Sigma S_j^* = 192 \text{ } \%$. |
| (d): | $T_r = 257 \text{ }^\circ\text{C}$; | $X_{\text{Dec}} = 96 \text{ } \%$; | $Y_{\text{C}_9} = 18 \text{ } \%$; | $\Sigma S_j^* = 187 \text{ } \%$. |

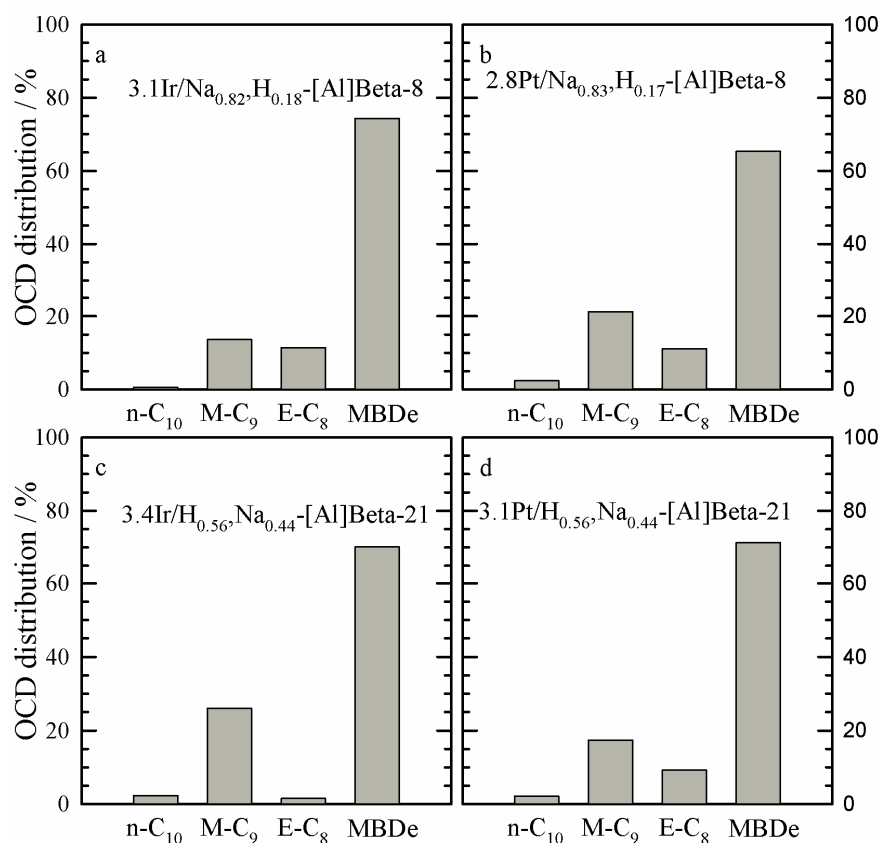


Figure 7.14: Breakdown of the selectivities of OCDs into differently branched decanes on the four [Al]Beta-supported catalysts (n-C₁₀: n-decane; M-C₉: methylnonanes; E-C₈: ethyloctanes; MBDe: multiply branched decanes):

- (a): $T_r = 280\text{ }^\circ\text{C}$; $X_{\text{Dec}} = 90\%$; $Y_{\text{OCDs}} = 40\%$; $S_{\text{OCDs}} = 44\%$.
 (b): $T_r = 300\text{ }^\circ\text{C}$; $X_{\text{Dec}} = 94\%$; $Y_{\text{OCDs}} = 27\%$; $S_{\text{OCDs}} = 28\%$.
 (c): $T_r = 246\text{ }^\circ\text{C}$; $X_{\text{Dec}} = 98\%$; $Y_{\text{OCDs}} = 33\%$; $S_{\text{OCDs}} = 33\%$.
 (d): $T_r = 257\text{ }^\circ\text{C}$; $X_{\text{Dec}} = 96\%$; $Y_{\text{OCDs}} = 20\%$; $S_{\text{OCDs}} = 21\%$.

7.3.3 Variation of the Nature of the Charge-Compensating Cation

The third method for the variation of the strength of the Brønsted acid sites, applied in this work, is the exchange of the charge-compensating cations. As previously discussed (see Section 4.2, page 21) the strength of the acid sites in zeolites depends on the nature of the charge-compensating cations and decreases in the order $\text{Li} > \text{Na} > \text{K} > \text{Rb} > \text{Cs}$. The sodium-form of a zeolite is mostly used as a support for catalysts. However, in this work the Li-, K-, Rb- and Cs-exchanged forms of [Al]Beta-8 and [Al]Beta-14 were also studied (see Sections 0 and 0, pages 121 and 124). In addition, Na-mordenite was exchanged with cesium, and zeolite K-L with sodium and cesium.

Cesium- or Sodium-Exchanged Zeolites Mordenite and L

Bearing in mind the excellent results obtained by the reduction of the strength of the Brønsted acid sites of [Al]Beta zeolites (see Section 7.3.2, page 112), zeolites Cs-mordenite, K,Na-L and K,Cs-L were also tested in the hydroconversion of cis-decalin. However, the variation of the strength of the acid sites is much less pronounced on the alkali-exchanged zeolites compared to the effect obtained by variation of the molar ratio $n_{\text{Si}} / n_{\text{Al}}$ (see Figure 6.25 and Figure 6.26, page 94). Nevertheless, with the exception of 2.0Ir/K_{0.65},Cs_{0.34},H_{0.01}-L, the exchange of the charge-compensating cation by cesium or sodium led to higher yields of open-chain decanes. Unfortunately, this did only result in one HIPEROC, *viz.* 2.9Pt/K_{0.63},Cs_{0.29},H_{0.08}-L. Moreover, the combined yields of ROPs and OCDs remained nearly unchanged. In addition, the yields of the undesired C₉- products increased markedly, especially for the platinum-loaded zeolites L. Table 7.6 summarizes the maximum yields and selectivities obtained on the catalysts of this series.

In Figure 7.15, the conversions and selectivities of the different groups of products of the catalysts of this series are depicted. One can clearly see that, at low conversions, the iridium-loaded catalysts produce more ring-opening products compared to the platinum-loaded catalysts. Furthermore, a comparison with the results of the platinum- or iridium-containing Na-mordenite and K-L zeolites (see Figure 7.3 and Figure 7.7, pages 100 and 106, respectively) does not show major differences; even the activities of the catalysts are similar. The breakdown of the selectivities of OCDs into differently branched decanes (not shown) does not show peculiarities either: The major products are multiply branched decanes followed by methylnonanes.

One explanation for the relatively low yields of OCDs could be the high strength of the Brønsted acid sites of the supports. However, 2.0Ir/Cs_{0.84},H_{0.16}-mordenite and its corresponding sodium form have Brønsted acid site strengths which are comparable to 3.0Ir/Na_{0.53},H_{0.47}-[Al]Beta-14 (see Figure 6.21, page 91), which is a HIPEROC with $Y_{\text{OCDs, max.}} = 34 \%$. Thus, the Brønsted acid site strength cannot be the only reason for the low yields of OCDs.

Another peculiarity of the mordenite- and L-supported catalysts are the relatively high amounts of C₉- products formed (up to 74 %, see Table 7.6). The carbon number distribution of the hydrocracked products depicted in Figure 7.16 shows that mainly methane is formed, especially in case of the iridium-containing catalysts.

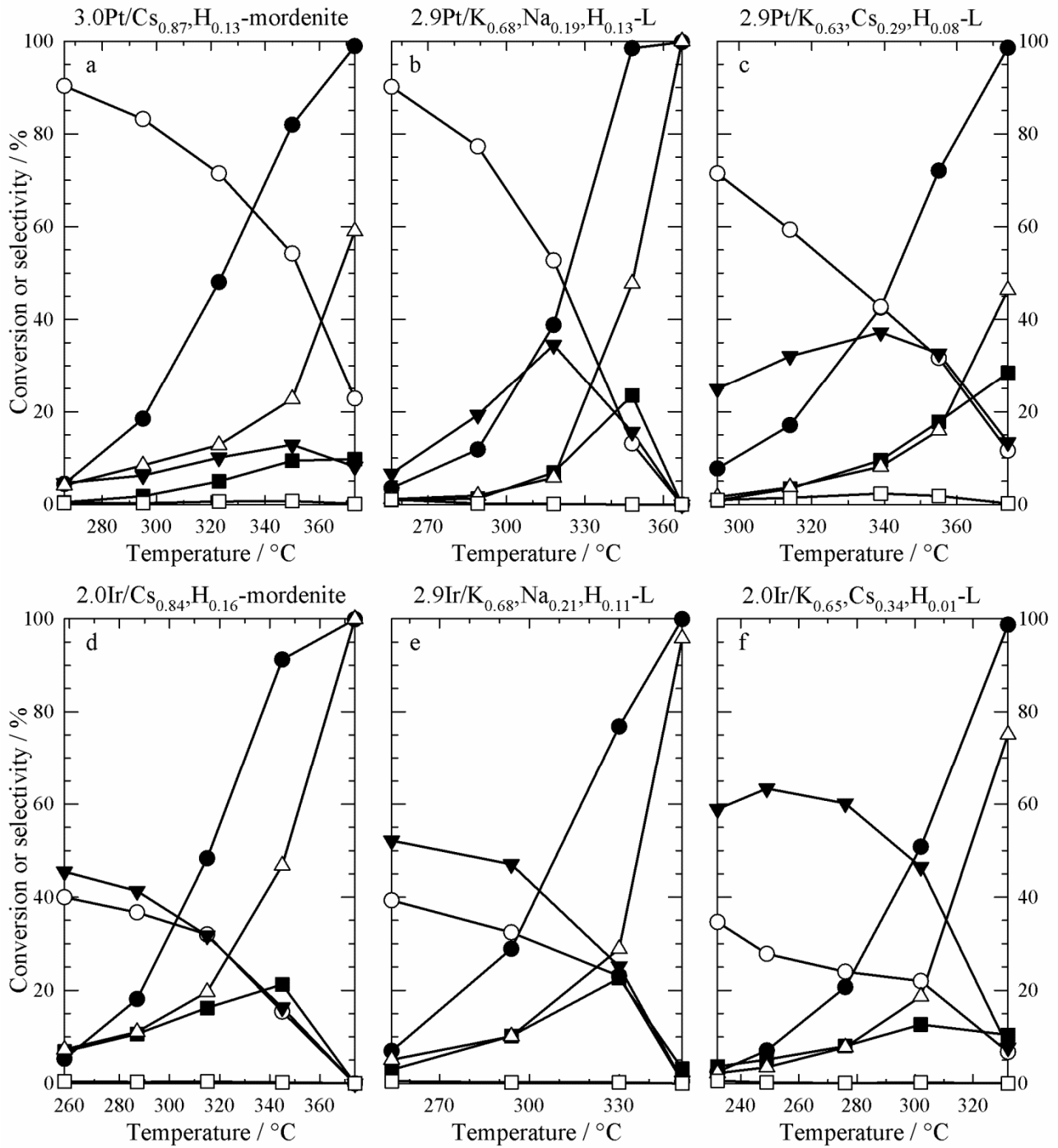


Figure 7.15: Conversion of decalin and selectivities of the different groups of products in dependence of the reaction temperature for platinum- or iridium-loaded zeolites Cs,H-mordenite, K,Na,H-L and K,Cs,H-L. (● X_{Dec} , ■ S_{OCDs} , ▼ S_{ROPs} , ○ $S_{sk-Isos}$, △ S_{C9-} , □ S_{DHPs}).

Table 7.6: Maximum yields and selectivities of OCDs, combined yields of ROPs and OCDs and yields of C₉- hydrocarbons at reaction conditions of maximal OCD yields in the hydroconversion of decalin on platinum- or iridium-loaded zeolites Cs,H-mordenite, K,Na,H-L and K,Cs,H-L and, for comparison, zeolites Na,H-mordenite and K,H-L.

Catalyst	T_r / °C	X_{Dec} / %	S_{OCDs} / %	$Y_{OCDs, max.}$ / %	$(Y_{OCDs, max.} + Y_{ROPs})$ / %	Y_{C_9-} / %
3.9Pt/Na _{0.79} ,H _{0.21} -mordenite	369	97	8	7	20	53
3.0Pt/Cs _{0.87} ,H _{0.13} -mordenite	373	99	10	10	18	58
1.8Pt/K _{0.88} ,H _{0.12} -L	372	97	17	17	39	28
2.9Pt/K _{0.68} ,Na _{0.19} ,H _{0.13} -L	348	98	23	23	38	47
2.9Pt/K _{0.63} ,Cs _{0.29} ,H _{0.08} -L	374	99	28	28	41	46
2.9Ir/Na _{0.90} ,H _{0.10} -mordenite	348	82	17	14	31	34
2.0Ir/Cs _{0.84} ,H _{0.16} -mordenite	345	91	21	19	34	43
2.8Ir/K _{0.86} ,H _{0.14} -L	330	82	21	17	38	31
2.9Ir/K _{0.68} ,Na _{0.21} ,H _{0.11} -L	330	77	23	17	37	22
2.0Ir/K _{0.65} ,Cs _{0.34} ,H _{0.01} -L	332	99	10	10	18	74

An explanation for the excessive hydrocracking of hydrocarbons could be the pore structure of the zeolites: Both zeolites possess 1-dimensional pore systems, consisting of 12-membered ring (12-MR) channels and in the case of LTL 8-MR channels running in parallel (see Figure 7.17). Moreover, mordenite possesses also a 2-dimensional 8-MR channel system. Due to the 1-dimensional pore systems, diffusion limitations can occur which lead to longer residence times, and the longer the residence time of the hydrocarbons in the pores the greater the probability for secondary hydrocracking. Nevertheless, since the ΣS_j^* values are higher for mordenite than for L zeolite, a second effect must be involved in this process. This second effect could originate from the architecture of the interconnecting 8-MR channels: In the case of mordenite, the two differently sized parallel pores are interconnected *via* perpendicularly arranged 8-MR channels and 5-MR windows, while L zeolite possesses only 8-MR windows which connect them. Hence, there is no direct link of the two parallel pore systems in the case of mordenite, while the 8-MR pores of L zeolite are interconnected by 8-MR windows.

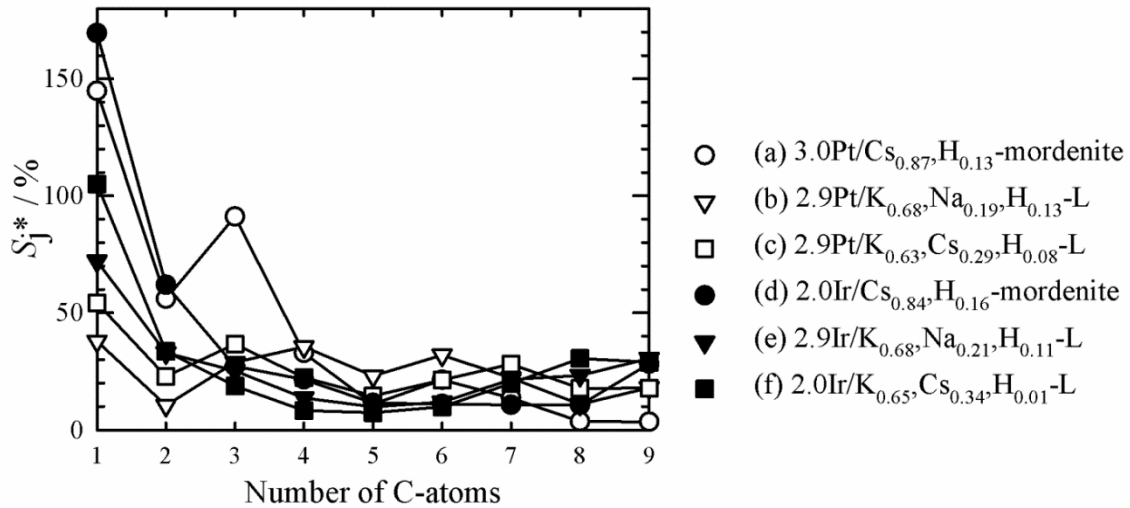


Figure 7.16: Carbon number distributions of the hydrocracked products obtained on platinum- or iridium-loaded zeolites Cs,H-mordenite, K,Na,H-L and K,Cs,H-L:

- (a): $T_r = 373\text{ }^\circ\text{C}$; $X_{\text{Dec}} = 99\text{ }%$; $Y_{\text{C}_9} = 59\text{ }%$; $\Sigma S_j^* = 378\text{ }%$.
 (b): $T_r = 348\text{ }^\circ\text{C}$; $X_{\text{Dec}} = 98\text{ }%$; $Y_{\text{C}_9} = 47\text{ }%$; $\Sigma S_j^* = 219\text{ }%$.
 (c): $T_r = 374\text{ }^\circ\text{C}$; $X_{\text{Dec}} = 99\text{ }%$; $Y_{\text{C}_9} = 46\text{ }%$; $\Sigma S_j^* = 236\text{ }%$.
 (d): $T_r = 345\text{ }^\circ\text{C}$; $X_{\text{Dec}} = 91\text{ }%$; $Y_{\text{C}_9} = 43\text{ }%$; $\Sigma S_j^* = 352\text{ }%$.
 (e): $T_r = 330\text{ }^\circ\text{C}$; $X_{\text{Dec}} = 77\text{ }%$; $Y_{\text{C}_9} = 22\text{ }%$; $\Sigma S_j^* = 241\text{ }%$.
 (f): $T_r = 332\text{ }^\circ\text{C}$; $X_{\text{Dec}} = 99\text{ }%$; $Y_{\text{C}_9} = 74\text{ }%$; $\Sigma S_j^* = 262\text{ }%$.

Based on the different pore architectures of the two zeolites one can assume that hydrocracked products diffuse into the 8-MR pores were they cannot be expelled by decalin and have thus a much longer residence time which favors secondary hydrocracking. However, the differences of the two supports originate from the fact that the 8-MR pores of mordenite are separated from the 12-MR pores by perpendicular 8-MR channels which hinders the diffusion of hydrocarbons back into the 12-MR pores while this diffusion is much easier in L zeolite.

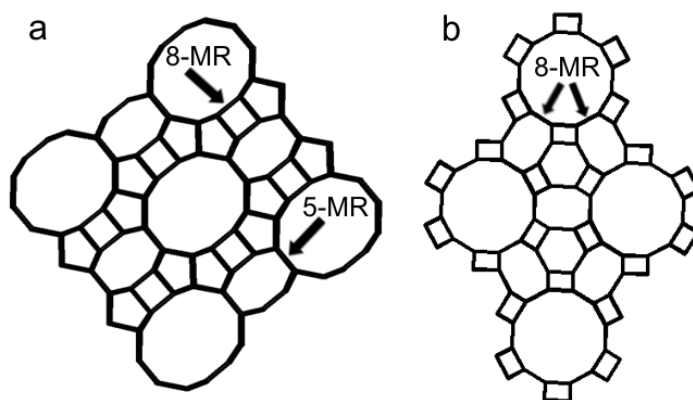


Figure 7.17: Pore systems of mordenite (MOR) (a) and L zeolite (LTL) (b) (view along [001]). After Ref. [4].

Alkali-Exchanged [Al]Beta Zeolites Loaded with Platinum

In Figure 7.18 the selectivities and conversions of the five platinum-containing alkali-exchanged [Al]Beta-14 zeolites are depicted. An activity increase can be observed with increasing Brønsted acid site strength from Pt/Cs,H-[Al]Beta-14 to Pt/H,Li-[Al]Beta-14. However, the increase is much smaller than the one found with platinum-faujasites [25], but it is more pronounced than with zeolites mordenite and L. Nevertheless, all platinum-containing catalysts are less active than their iridium-containing counterparts, which is in line with the findings of the faujasite-supported catalysts [25].

The selectivity patterns of the five catalysts (Figure 7.18) reflect the results of the FT-IR spectroscopic measurements: No great differences in the strength of the Brønsted acid sites between the catalysts can be observed. On all five platinum-containing [Al]Beta-14 zeolites skeletal isomerization is the prevailing reaction, and none of the catalysts reaches higher OCD selectivities than 22 % (Table 7.7). This is in contrast to the faujasite-supported platinum catalysts [25], on 3.0Pt/Na_{0.88},H_{0.12}-Y OCDs selectivities and yields of 41 % and 39 %, respectively, were reached. However, these results underline the considerable importance of the balance between the amount of noble metal and Brønsted acid site strength distribution.

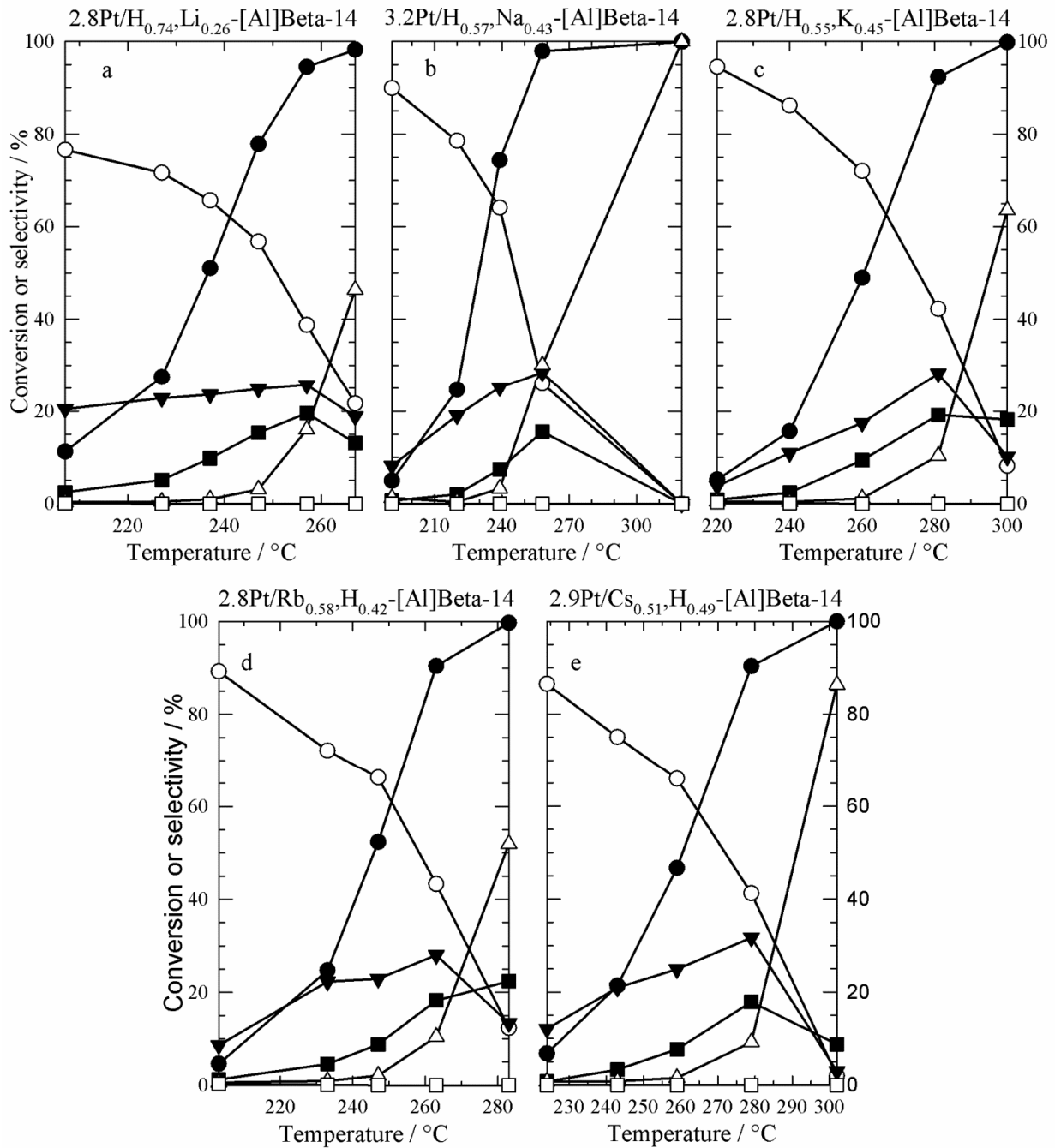


Figure 7.18: Conversion of decalin and selectivities of the different groups of products in dependence of the reaction temperature for alkali-exchanged [Al]Beta-14 zeolites loaded with platinum. (● X_{Dec} , ■ S_{OCDs} , ▼ S_{ROPs} , ○ $S_{sk-Isos}$, ▲ S_{C_9-} , □ S_{DHPs}).

The high isomerization selectivities of the catalysts can be explained by the lower hydrogenolysis activity of platinum compared to iridium and the fact that platinum itself is able to isomerize hydrocarbons at temperatures around 300 °C [56 - 58]. In addition, the high isomerization activity could be the reason for the low open-chain decane selectivities. It seems that the Brønsted acid site strength of zeolite Beta is too high, with the effect that the

isomerization activity of the acid sites in addition to the isomerization which occurs on the platinum sites leads to the formation of highly branched isomers where the ring is more difficult to open than in mildly branched isomers.

Table 7.7: Maximum yields and selectivities of OCDs, combined yields of ROPs and OCDs and yields of C₉- hydrocarbons at reaction conditions of maximal OCD yields in the hydroconversion of decalin on the alkali-exchanged [Al]Beta-14 zeolites loaded with platinum.

Catalyst	$T_r /$ °C	$X_{Dec} /$ %	$S_{OCDs} /$ %	$Y_{OCDs, max.} /$ %	$(Y_{OCDs, max.} + Y_{ROPs}) /$ %	$Y_{C_9-} /$ %
2.8Pt/H _{0.74} ,Li _{0.26} -[Al]Beta-14	257	95	20	18	43	15
3.2Pt/H _{0.57} ,Na _{0.43} -[Al]Beta-14	258	98	16	15	43	29
2.8Pt/H _{0.55} ,K _{0.45} -[Al]Beta-14	300	100	18	18	28	63
2.8Pt/Rb _{0.58} ,H _{0.42} -[Al]Beta-14	283	100	22	22	36	52
2.9Pt/Cs _{0.51} ,H _{0.49} -[Al]Beta-14	279	90	18	16	45	8

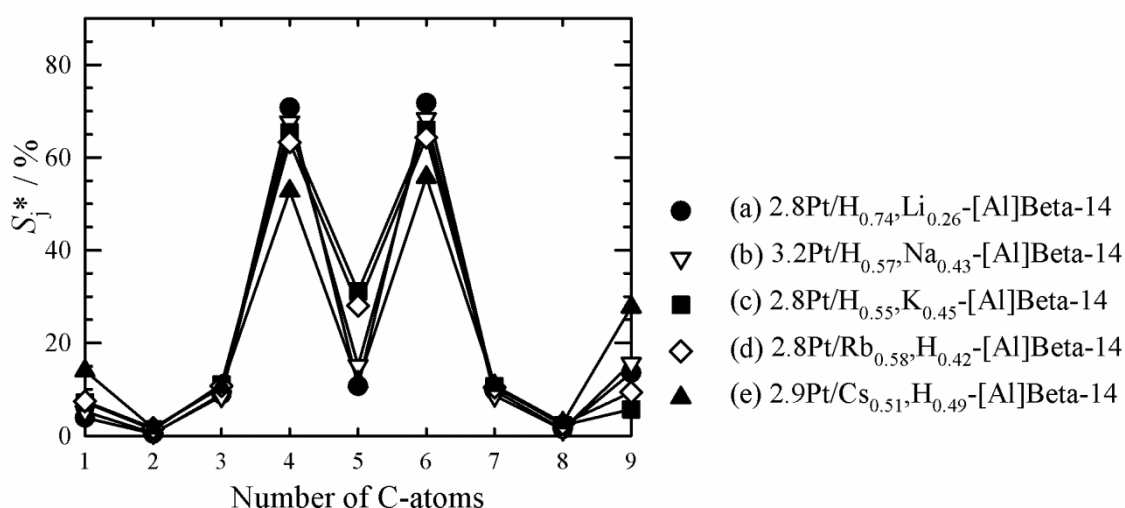


Figure 7.19: Carbon number distributions of the hydrocracked products obtained on alkali-exchanged [Al]Beta-14 zeolites loaded with platinum:

- (a): $T_r = 257$ °C; $X_{Dec} = 95$ %; $Y_{C_9-} = 15$ %; $\Sigma S_j^* = 191$ %.
- (b): $T_r = 258$ °C; $X_{Dec} = 98$ %; $Y_{C_9-} = 29$ %; $\Sigma S_j^* = 191$ %.
- (c): $T_r = 300$ °C; $X_{Dec} = 100$ %; $Y_{C_9-} = 63$ %; $\Sigma S_j^* = 201$ %.
- (d): $T_r = 283$ °C; $X_{Dec} = 100$ %; $Y_{C_9-} = 52$ %; $\Sigma S_j^* = 198$ %.
- (e): $T_r = 279$ °C; $X_{Dec} = 90$ %; $Y_{C_9-} = 8$ %; $\Sigma S_j^* = 187$ %.

A closer look at the hydrocracked products (Figure 7.19) reveals that mainly iso-butane and methylcyclopentane are formed, which is strong evidence for a hydrocracking at the acid

sites *via* the paring reaction. Even though the strength of the Brønsted acid sites have been varied (see Figure 6.21, page 91) the shapes of the distribution curves of all five catalysts are nearly identical. Two factors lead to this behavior: (i) the strength of the Brønsted acid sites, even that of 2.9Pt/C_{S0.51},H_{0.49}-[Al]Beta-14, is too high for the low hydrogenolysis activity of platinum and (ii) the isomerization ability of platinum itself. Both properties, high acid strength and isomerization ability, favor the paring reaction.

Alkali-Exchanged [Al]Beta Zeolites Loaded with Iridium

This Section is dealing with the results obtained in the hydroconversion of decalin on alkali-exchanged [Al]Beta-14 and [Al]Beta-8 zeolites loaded with iridium. First of all the results of zeolite [Al]Beta-14 will be discussed and afterwards the ones obtained with zeolite [Al]Beta-8.

Shown in Figure 7.20 are the decalin conversions and the product selectivities observed on the five alkali metal-exchanged [Al]Beta-14 zeolites containing *ca.* 3 wt.-% of iridium in dependence of the reaction temperature. A comparison of the conversions reveals that the nature of the alkali cation present in the zeolite has hardly any influence on its catalytic activity. The lack of a pronounced influence of the nature of the alkali cation in zeolite [Al]Beta-14 on the catalytic activity can be understood in view of its relatively high n_{Si} / n_{Al} ratio of 14.0 and the resulting low absolute concentration of cations.

Concerning the product selectivities, Figure 7.20 shows a number of interesting effects: Generally, $S_{sk-Isos}$ decreases with increasing temperature indicating that these products undergo consecutive reactions at higher conversions. The selectivities of ring-opening products either pass through maxima or show a monotonous decrease, as the temperature is increased. The selectivities of open-chain decanes, the most desirable products from the fuel quality point of view, show maxima for all five catalysts reflecting that OCDs are formed by opening the remaining ring in ROPs and, at higher severities, consumed by hydrocracking to C₉- hydrocarbons. This last-mentioned product group is almost absent at low to medium decalin conversions, but S_{C_9} increases sharply at severe reaction conditions. More or less the same behavior has been observed for all iridium-containing catalysts tested in this work.

With respect to the influence of the nature of the alkali cation, Figure 7.20 reveals two trends: Firstly, in the row from 3.3Ir/H_{0.74},Li_{0.26}-[Al]Beta-14 to 3.4Ir/H_{0.58},Cs_{0.42}-[Al]Beta-14, the selectivities of skeletal isomers at low conversion strongly decrease. Whereas skeletal isomers of decalin are by far the prevailing products on 3.3Ir/H_{0.74},Li_{0.26}-[Al]Beta-14 at the lowest conversion measured ($S_{sk-Isos} = 71\%$), this value drops to 25 % on the cesium-exchanged [Al]Beta-14. The same qualitative trend was found by Rabl *et al.* [25] with the

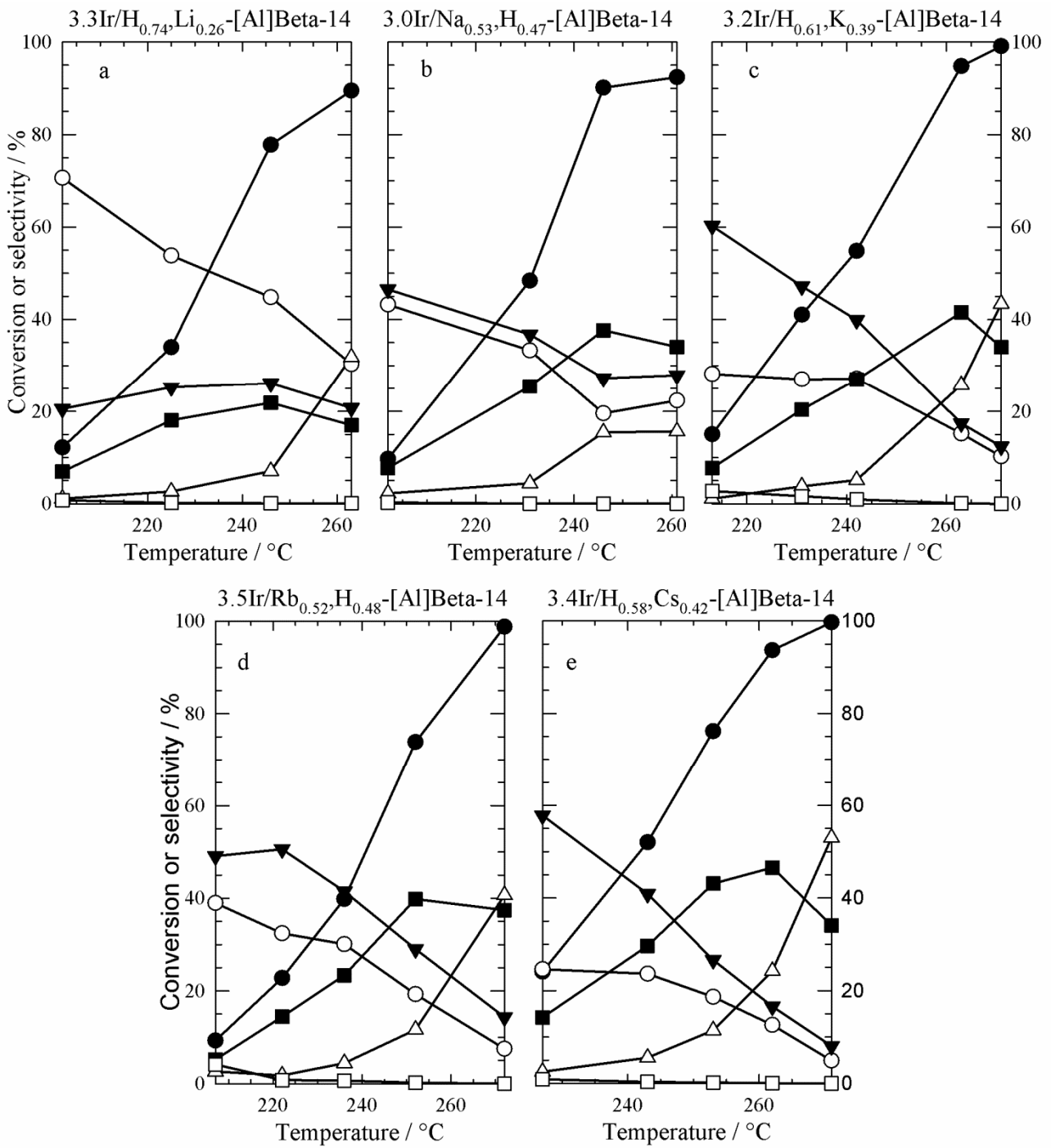


Figure 7.20: Conversion of decalin and selectivities of the different groups of products in dependence of the reaction temperature for alkali-exchanged [Al]Beta-14 zeolites loaded with iridium. (● X_{Dec} , ■ S_{OCDs} , ▼ S_{ROPs} , ○ $S_{sk-Isos}$, △ S_{C_9} , □ S_{DHPs}).

series of faujasite catalysts, *i.e.* from Ir/Li,Na,H-Y ($S_{\text{sk-Isos}} = 34\%$) to Ir/Cs,Na,H-Y ($S_{\text{sk-Isos}} = 5\%$). In addition, a comparison with 2.3Ir/H_{0.88},Na_{0.12}-[B]Beta-18 (Figure 7.10a, page 111), a catalyst which possesses weaker acid sites than the [Al]Beta-supported catalysts, reveals the same trend ($S_{\text{sk-Isos}} = 8\%$). As recently demonstrated [88] in a study of decalin hydroconversion over iridium on non-acidic silica, this metal lacks activity for skeletal isomerization. The formation of sk-Isos on 3.3Ir/H_{0.74},Li_{0.26}-[Al]Beta-14 has hence to be ascribed to a conversion of decalin at Brønsted acid sites, and in view of the decreasing strength of these sites (see Figure 6.21, page 91) the strongly decreasing activity for skeletal isomerization from the lithium-exchanged to the cesium-exchanged [Al]Beta-14 is fully expected. It should also be mentioned that, on all five iridium-containing alkali-cation-exchanged [Al]Beta-14 zeolites, spiro[4.5]decane was observed, and it accounts for up to 30 % of all skeletal isomers formed. The formation of this particular isomer of decalin is in-line with an acid-catalyzed type A isomerization *via* carbocations [86].

Secondly, the maxima in the selectivities of open-chain decanes increase markedly from the lithium-exchanged zeolite Beta to the cesium-exchanged zeolite. With the latter catalyst, the maximal selectivity of OCDs amounts to 47 % (Figure 7.20e) which is even noticeably higher than the value reported for the best faujasite-based HIPERO C (High-Performance Ring-Opening Catalyst), *viz.* 41 % on 3.0Pt/Na_{0.88},H_{0.12}-Y [25].

From an industrial point of view the yields of the target products are of even greater interest than their selectivities. In column 5 of Table 7.8 the maximal yields of open-chain decanes are listed for the five catalysts based on zeolite [Al]Beta-14 exchanged with the various alkali cations and loaded with *ca.* 3 wt.-% iridium. If the maximal yield of OCDs is used as the sole criterion, 3.4Ir/H_{0.58},Cs_{0.42}-[Al]Beta-14 and its reproduction 3.3Ir/H_{0.58},Cs_{0.42}-[Al]Beta-14 show the best performances. If the yields of ROPs attained at the same reaction conditions are added (bearing in mind that these hydrocarbons with one remaining naphthenic ring are also valuable products with a high cetane number), then values close to 60 % are reached on four catalysts of the series. Finally, these high yields should be reached at an as low as possible yield of C₉- hydrocarbons. It is seen from the last column of Table 7.8 that the four above-mentioned catalysts possess yields of hydrocracked products of 14 to 24 %, which compares very favorably to $S_{\text{C}_9} = 33\%$ for the faujasite-supported HIPERO C 3.0Pt/Na_{0.88},H_{0.12}-Y by Rabl *et al.* [25].

In addition, the results obtained with 3.3Ir/H_{0.58},Cs_{0.42}-[Al]Beta-14 are given in Table 7.8. This catalyst is the reproduction of 3.4Ir/H_{0.58},Cs_{0.42}-[Al]Beta-14, starting from a complete new batch of dry gel. It can be seen that the very good results of the latter catalyst are reproducible. The reproduced catalyst even showed a slightly better combined yield of OCDs and ROPs.

Table 7.8: Maximum yields and selectivities of OCDs, combined yields of ROPs and OCDs and yields of C₉- hydrocarbons at reaction conditions of maximal OCD yields in the hydroconversion of decalin on the alkali-exchanged [Al]Beta-14 zeolites loaded with iridium.

Catalyst	T_r / °C	X_{Dec} / %	S_{OCDs} / %	$Y_{OCDs, max.}$ / %	$(Y_{OCDs, max.} + Y_{ROPs})$ / %	Y_{C_9-} / %
3.3Ir/H _{0.74} ,Li _{0.26} -[Al]Beta-14	246	78	22	17	37	5
3.0Ir/Na _{0.53} ,H _{0.47} -[Al]Beta-14	246	90	38	34	59	14
3.2Ir/H _{0.61} ,K _{0.39} -[Al]Beta-14	263	95	42	39	56	24
3.5Ir/Rb _{0.52} ,H _{0.48} -[Al]Beta-14	272	99	37	37	51	40
3.4Ir/H _{0.58} ,Cs _{0.42} -[Al]Beta-14	262	94	47	44	59	23
3.3Ir/H _{0.58} ,Cs _{0.42} -[Al]Beta-14	257	96	46	44	62	24

The carbon number distribution of the hydrocracked products depicted in Figure 7.21 reveals that on all five alkali Beta zeolites hydrogenolysis of C₁₀ hydrocarbons on iridium occurs. This can be deduced from the high amounts of methane and C₉ hydrocarbons [86]. Nevertheless, the lithium-exchanged [Al]Beta-14 zeolite also shows the M-shaped distribution curve which is typical for the paring reaction with high amounts of iso-butane (C₄) and methylcyclopentane (C₆). With decreasing strength of the Brønsted acid sites the M-shape gradually vanishes, and distribution curves with elevated values of C₃ to C₇ occur. A similar behavior was found for the four iridium-containing Cs-[Al]Beta-14 zeolites where the S_j^* values for C₄, C₅ and C₆ were elevated (see Figure 7.27, page 134).

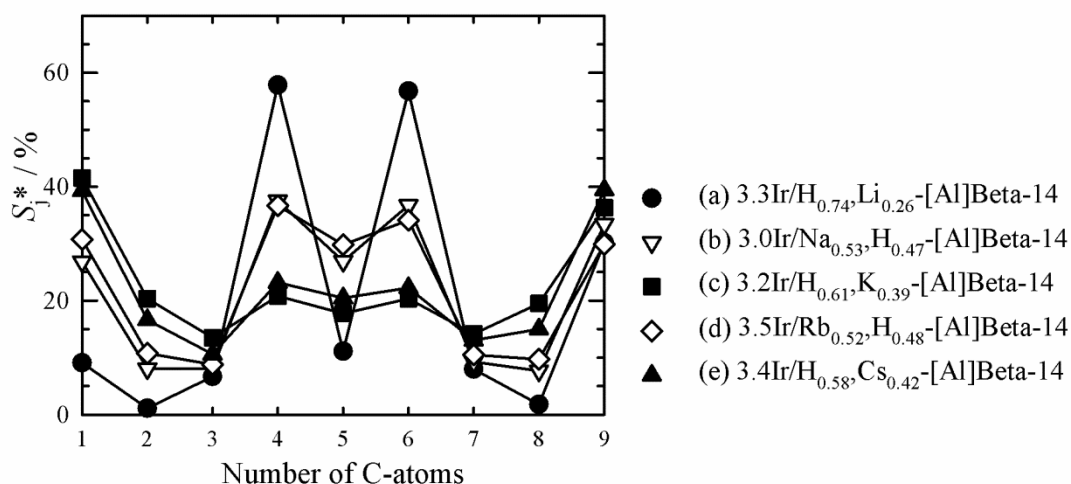


Figure 7.21: Carbon number distributions of the hydrocracked products obtained on alkali-exchanged [Al]Beta-14 zeolites loaded with iridium:

- (a): $T_r = 257\text{ }^\circ\text{C}$; $X_{\text{Dec}} = 95\%$; $Y_{\text{C}_9^-} = 15\%$; $\Sigma S_j^* = 191\%$.
 (b): $T_r = 258\text{ }^\circ\text{C}$; $X_{\text{Dec}} = 98\%$; $Y_{\text{C}_9^-} = 29\%$; $\Sigma S_j^* = 191\%$.
 (c): $T_r = 300\text{ }^\circ\text{C}$; $X_{\text{Dec}} = 100\%$; $Y_{\text{C}_9^-} = 63\%$; $\Sigma S_j^* = 201\%$.
 (d): $T_r = 283\text{ }^\circ\text{C}$; $X_{\text{Dec}} = 100\%$; $Y_{\text{C}_9^-} = 52\%$; $\Sigma S_j^* = 198\%$.
 (e): $T_r = 279\text{ }^\circ\text{C}$; $X_{\text{Dec}} = 90\%$; $Y_{\text{C}_9^-} = 8\%$; $\Sigma S_j^* = 187\%$.

Until now 3.4Ir/H_{0.58},Cs_{0.42}-[Al]Beta-14 and its reproduction showed the best performance concerning the yield of OCDs. In addition, this catalyst also produces high amounts of ROPs at the same conditions, and the yield of hydrocracked products is relatively low ($Y_{\text{C}_9^-} = 23\%$). Since this catalyst possesses the lowest strength of Brønsted acid sites of the alkali metal-exchanged [Al]Beta zeolites, one can think of a further reduction of the acid strength to obtain even higher yields of OCDs. This further reduction can be achieved by a potassium, rubidium or cesium exchange of [Al]Beta-8. In Figure 7.22 the conversions of decalin and the selectivities of different groups of products on these three catalysts are depicted at different temperatures. Unfortunately, with decreasing strength of the acid sites of the catalysts, $S_{\text{OCDs, max}}$ is decreasing from 37 to only 18 % (see Table 7.9). In-line with the findings on the alkali metal-exchanged [Al]Beta-14 zeolites, the isomerization activity of the catalysts decreases with decreasing acid strength. However, since the catalysts of this series possess very weak acid sites (see Figure 6.26, page 94) the prevailing carbon-carbon bond rupture mechanism must be hydrogenolysis. Evidence for hydrogenolysis as the prevailing bond rupture mechanism is obtained from the carbon number distribution curves of the hydrocracked products (see Figure 7.23): Clear hammock-shaped curves result for the three catalysts of this series. In contrast to the sodium-containing 3.1Ir/Na_{0.82},H_{0.18}-[Al]Beta-8 catalyst (Figure 7.13, page 115) even the slightly elevated amounts of C₄ to C₆ hydrocarbons are not observed indicating the very low strength of the acid sites.

The breakdown of the selectivities of OCDs into differently branched decanes on the catalysts of this series (not shown) reveals nothing peculiar: High amounts of multiply-branched OCDs and only low amounts of n-C₁₀, M-C₉ and E-C₈ are formed.

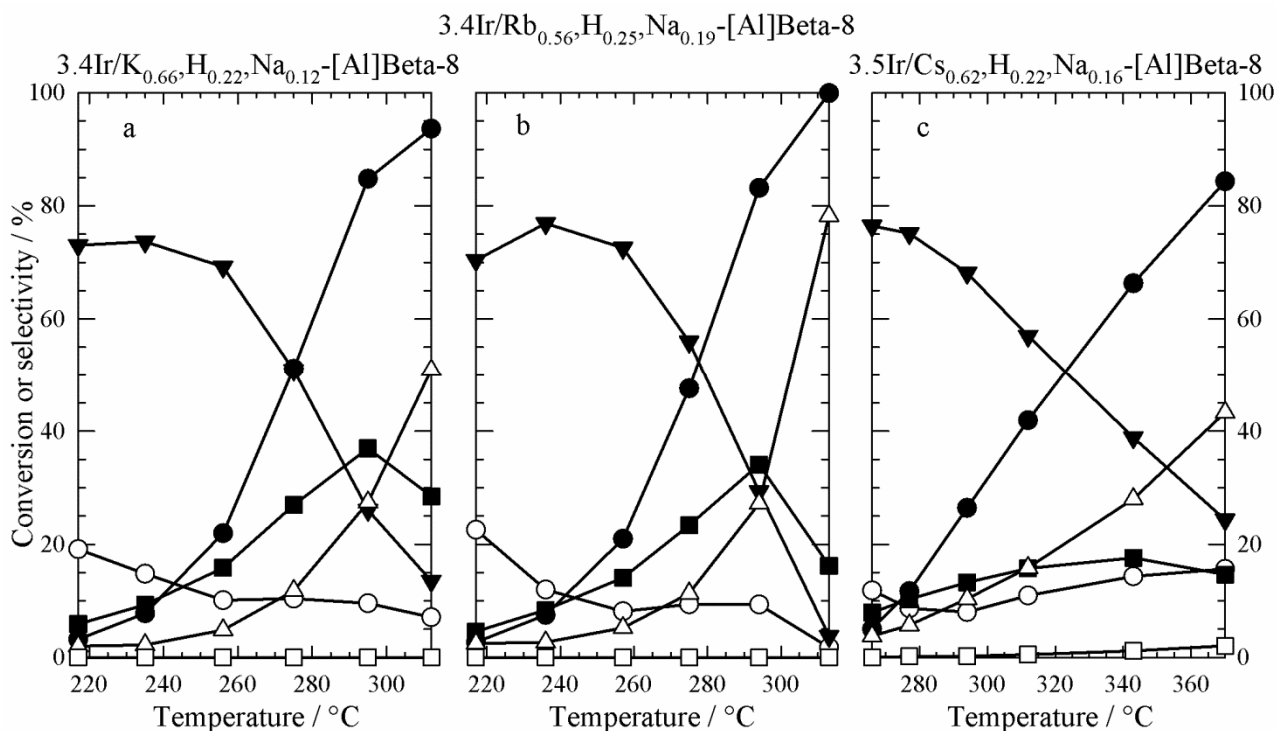


Figure 7.22: Conversion of decalin and selectivities of the different groups of products in dependence of the reaction temperature for alkali-exchanged [Al]Beta-8 zeolites loaded with iridium. (—●— X_{Dec} , —■— S_{OCDs} , —▼— S_{ROPs} , —○— $S_{sk-Isos}$, —△— S_{C_9} , —□— S_{DHPs}).

Table 7.9: Maximum yields and selectivities of OCDs, combined yields of ROPs and OCDs and yields of C₉- hydrocarbons at reaction conditions of maximal OCD yields in the hydroconversion of decalin on the alkali-exchanged [Al]Beta-8 zeolites loaded with iridium.

Catalyst	$T_r /$ °C	$X_{Dec} /$ %	$S_{OCDs} /$ %	$Y_{OCDs, max.} /$ %	$(Y_{OCDs, max.} +$ $Y_{ROPs}) /$ %	$Y_{C_9} /$ %
3.4Ir/K _{0.66} ,H _{0.22} ,Na _{0.12} -[Al]Beta-8	295	85	37	31	53	23
3.4Ir/Rb _{0.56} ,H _{0.25} ,Na _{0.19} -[Al]Beta-8	294	83	34	28	53	23
3.5Ir/Cs _{0.62} ,H _{0.22} ,Na _{0.16} -[Al]Beta-8	370	84	15	12	33	37

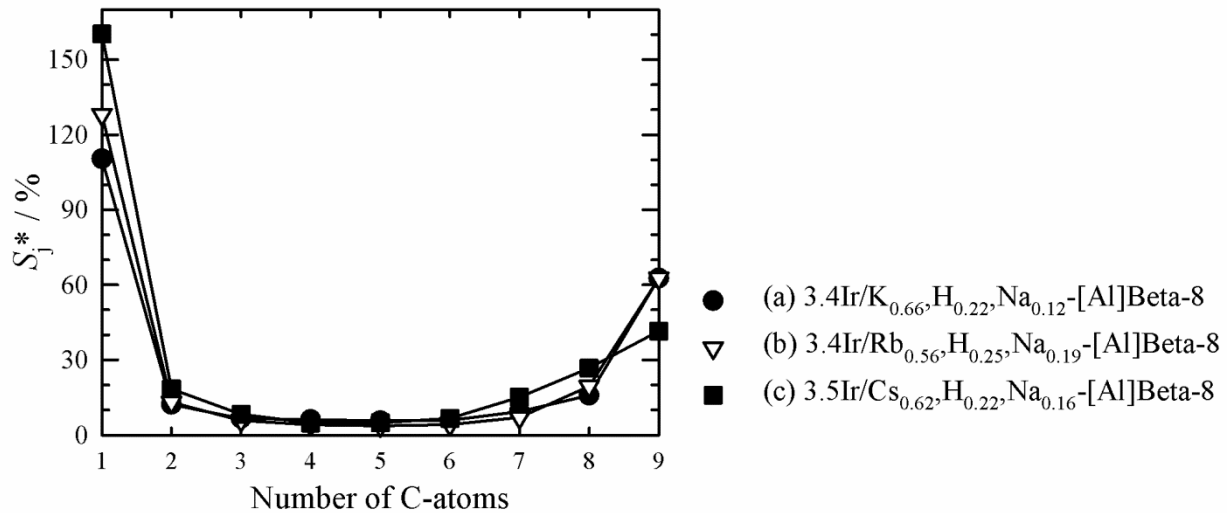


Figure 7.23: Carbon number distributions of the hydrocracked products obtained on alkali-exchanged [Al]Beta-14 zeolites loaded with iridium:

- (a): $T_r = 295 \text{ }^\circ\text{C}$; $X_{\text{Dec}} = 85 \text{ } \%$; $Y_{\text{C}_9-} = 23 \text{ } \%$; $\Sigma S_j^* = 235 \text{ } \%$.
 (b): $T_r = 294 \text{ }^\circ\text{C}$; $X_{\text{Dec}} = 83 \text{ } \%$; $Y_{\text{C}_9-} = 23 \text{ } \%$; $\Sigma S_j^* = 294 \text{ } \%$.
 (c): $T_r = 370 \text{ }^\circ\text{C}$; $X_{\text{Dec}} = 84 \text{ } \%$; $Y_{\text{C}_9-} = 37 \text{ } \%$; $\Sigma S_j^* = 287 \text{ } \%$.

Summing up, it can be stated that the variation of the strength of the Brønsted acid sites *via* alkali metal-exchange is a helpful tool for tailoring the properties of the zeolite catalysts. The assumption that a very low acid strength will lead to high yields of OCDs was not generally confirmed. It seems that there exists an optimal ratio between the strength of the Brønsted acid sites and the hydrogenolysis activity of the noble metal. If the strength of the Brønsted acid sites is too high, the paring reaction becomes prevailing which leads to the formation of high amounts of the undesired products iso-butane and methylcyclopentane. On the other hand, if the strength of the acid sides is too low, isomerization of decalin is nearly absent. Isomerization of decalin to naphthenes comprising at least one five-membered ring is vital for obtaining high yields of OCDs.

7.4 Variation of the Iridium Content

Since the performances of the iridium-containing Cs,H-[Al]Beta-14 catalysts concerning the yields of OCDs, ROPs and C₉- were exceptionally good, the content of iridium was varied on these catalysts between 1 and 5 wt.-% in order to investigate the influence of the iridium-loading on the ring-opening reaction of decalin.

In Figure 7.24 the conversions of decalin on the five Cs-Beta zeolites with varying iridium content are plotted in dependence of the reaction temperature. As expected the activities of

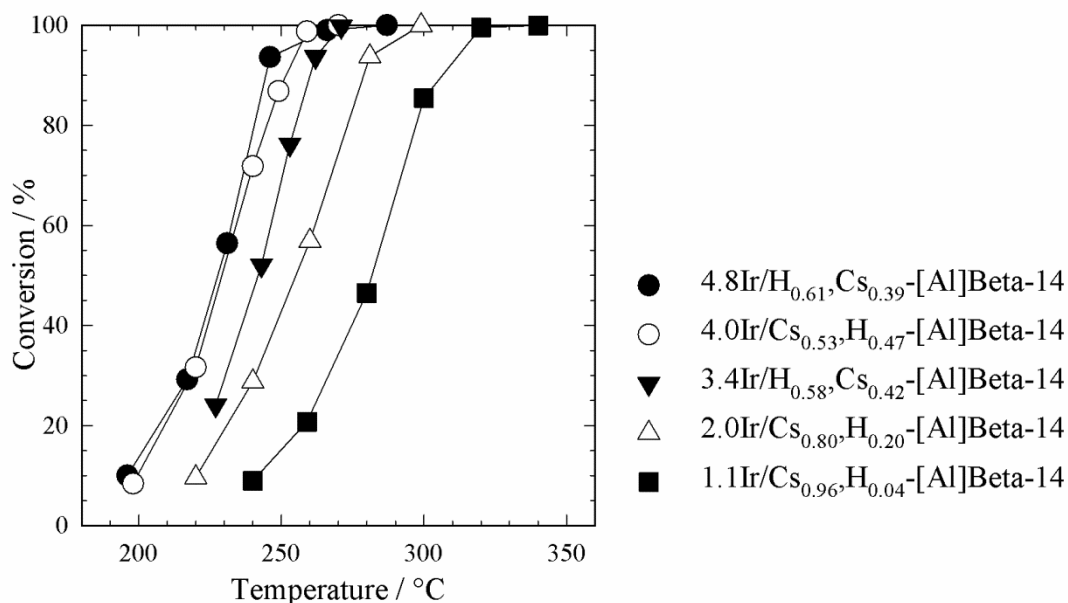


Figure 7.24: Decalin conversion on the five cesium-exchanged Beta zeolites with varying iridium contents, in dependence of the reaction temperature.

the catalysts increase with increasing iridium content. However, due to the higher metal loading not only higher amounts of active metal sites are present, but also more Brønsted acid sites are generated during the reduction of the noble metal. In addition, the strength of the generated acid sites is higher (see Figure 6.27, page 95), since the amount of cesium is reduced with increasing iridium content. Summing up, the activity differences stem from the varying noble metal content, the varying amount of acid sites, and the different acid site strengths.

In Figure 7.25 the conversions of decalin and selectivities of different groups of products on the five cesium-exchanged catalysts at different temperatures are depicted. A clear relationship between the iridium content and the behavior of the selectivities of the different product groups does not appear to exist. The selectivity of ring-opening products increases slightly at low conversions with decreasing iridium content from 4.8 to 4.0 wt.-%. However, a further reduction of the iridium content leads to decreasing amounts of ring-opening products. The same trend can be found for the maximum selectivities of OCDs. On the other hand, a reverse trend is evident for the selectivities of skeletal isomers. This finding will be discussed in more depth later in this Section.

Nevertheless, the strong dependence of the yield of OCDs on the iridium content shows how crucial the right balance between noble metal content, acid site concentration and acid site strength is to obtain high yields of OCDs.

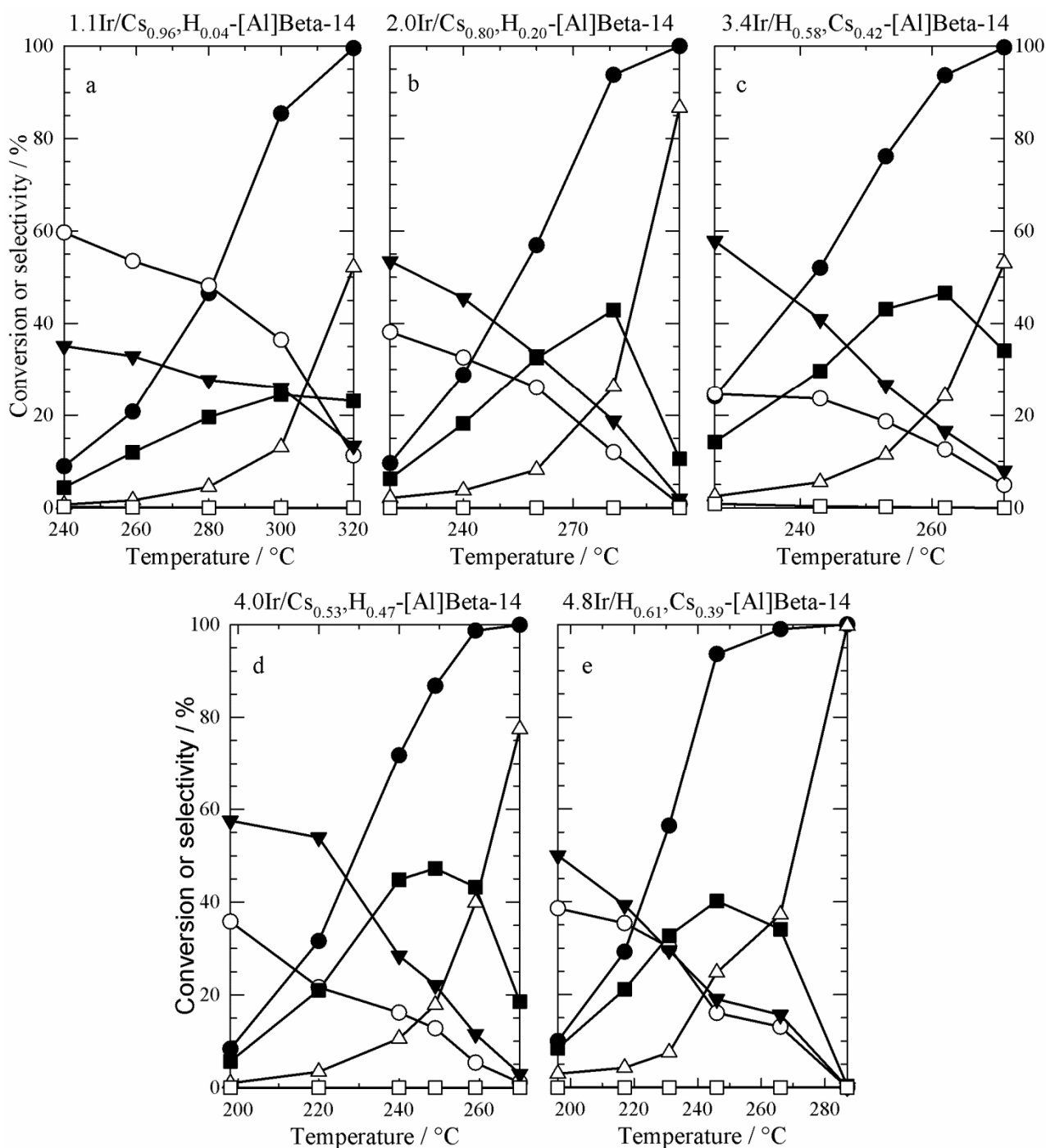


Figure 7.25: Conversion of decalin and selectivities of the different groups of products in dependence of the reaction temperature for the five Cs,H-[Al]Beta-14 catalysts with different iridium contents. (● X_{Dec} , ■ S_{OCDs} , ▼ S_{ROPs} , ○ $S_{sk-Isos}$, ▲ S_{C9-} , □ S_{DHPs}).

Table 7.10: Maximum yields and selectivities of OCDs, combined yields of ROPs and OCDs and yields of C₉- hydrocarbons at reaction conditions of maximal OCD yields in the hydroconversion of decalin on the five Cs,H-[Al]Beta-14 catalysts with different iridium contents.

Catalyst	$T_r /$ °C	$X_{Dec} /$ %	$S_{OCDs} /$ %	$Y_{OCDs, max.} /$ %	$(Y_{OCDs, max.} +$ $Y_{ROPs}) /$ %	$Y_{C_9-} /$ %
1.1Ir/Cs _{0.96} ,H _{0.04} -[Al]Beta-14	320	100	23	23	36	52
2.0Ir/Cs _{0.80} ,H _{0.20} -[Al]Beta-14	281	94	43	40	58	25
3.4Ir/H _{0.58} ,Cs _{0.42} -[Al]Beta-14	262	94	47	44	59	23
4.0Ir/Cs _{0.53} ,H _{0.47} -[Al]Beta-14	259	99	43	43	54	39
4.8Ir/H _{0.61} ,Cs _{0.39} -[Al]Beta-14	246	94	40	38	55	23

However, a comparison of the strength distribution of the Brønsted acid sites of 2.0Ir/Cs_{0.80},H_{0.20}-[Al]Beta-14 with other catalysts reveals that 3.4Ir/H_{0.58},Cs_{0.42}-[Al]Beta-14 and 3.1Ir/Na_{0.82},H_{0.18}-[Al]Beta-8 possess nearly identical strength distributions (see Figure 7.26a). Furthermore, the activity of the three catalysts is very similar, and in the case of 3.1Ir/Na_{0.82},H_{0.18}-[Al]Beta-8 and 2.0Ir/Cs_{0.80},H_{0.20}-[Al]Beta-14 it is nearly identical (Figure 7.26b). In addition, the selectivity patterns of these two catalysts are nearly identical (see Figure 7.12a and Figure 7.25b). Bearing in mind these findings, one can conclude that the alkali metal solely has an influence on the strength of the Brønsted acid sites and does not take part in the catalytic conversion of decalin. If that were the case, one would have observed differences in the catalytic behavior between the two catalysts.

Figure 7.27 depicts the carbon number distribution of the C₉- products observed on the Cs,H-[Al]Beta-14 zeolites with varying iridium content. As on the catalysts with different alkali metals, high amounts of C₁ and C₉ are formed, which unambiguously indicates a hydrogenolytic hydrocracking on the noble metal sites. However, in contrast to 3.3Ir/H_{0.74},Li_{0.26}-[Al]Beta-14 (see Figure 7.20a, page 125) none of the catalysts shows a purely M-shaped distribution curve. Only on 1.1Ir/Cs_{0.96},H_{0.04}-[Al]Beta-14 high amounts of C₄ and C₆ and relatively low amounts of C₅ are formed. The other three catalysts show a peculiarity, *viz.* similar values of S_j^* for C₄, C₅, and C₆ at a high level. This feature reminds, to some extent, the distribution curves found previously for hydrocracking of n-decane on bifunctional catalysts [105] and for hydrogenolysis of n-decane over platinum on non-acidic alumina [106]. It might hence be that the C₉- hydrocarbons are formed in part by some consecutive hydrocracking of open-chain decanes. Of course, however, hydrogenolysis on iridium must be the main mechanism for C₉- formation, as we conclude from the occurrence of C₁, C₂, C₈ and C₉.

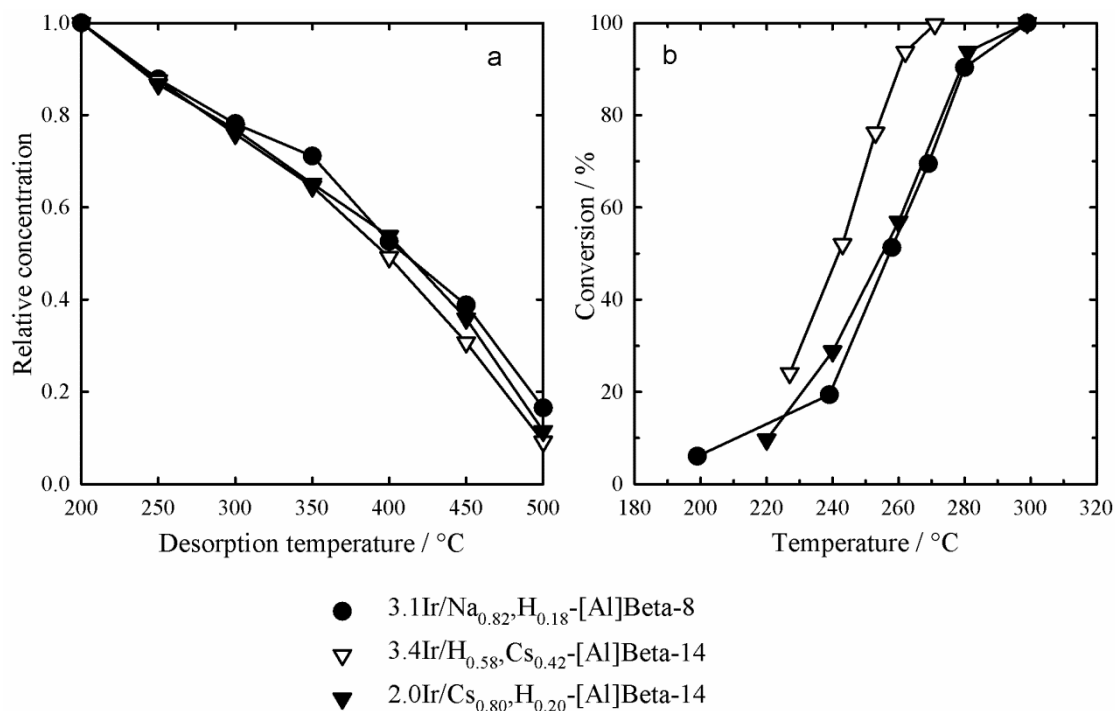


Figure 7.26: Relative pyridine concentrations adsorbed determined by FT-IR spectroscopy (a) and decalin conversion in dependence of the reaction temperature (b) on three cesium- or sodium-exchanged [Al]Beta zeolites loaded with iridium.

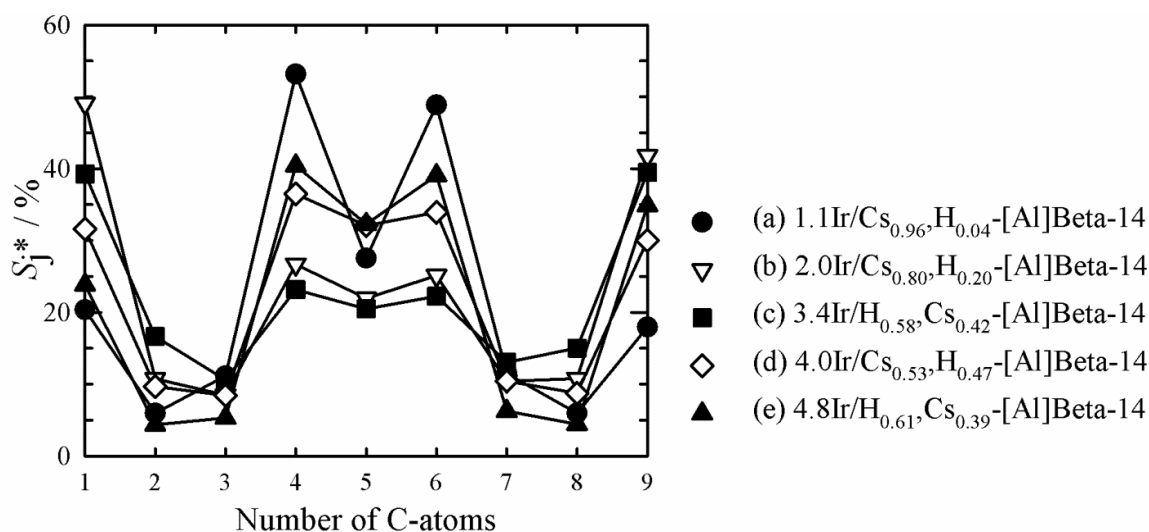


Figure 7.27: Carbon number distributions of the hydrocracked products obtained on the five Cs,H-[Al]Beta-14 catalysts with different iridium contents:

- (a): $T_r = 295 \text{ }^\circ\text{C}$; $X_{\text{Dec}} = 85 \%$; $Y_{\text{C}_9} = 23 \%$; $\Sigma S_j^* = 235 \%$.
- (b): $T_r = 294 \text{ }^\circ\text{C}$; $X_{\text{Dec}} = 83 \%$; $Y_{\text{C}_9} = 23 \%$; $\Sigma S_j^* = 294 \%$.
- (c): $T_r = 370 \text{ }^\circ\text{C}$; $X_{\text{Dec}} = 84 \%$; $Y_{\text{C}_9} = 37 \%$; $\Sigma S_j^* = 287 \%$.
- (d): $T_r = 370 \text{ }^\circ\text{C}$; $X_{\text{Dec}} = 84 \%$; $Y_{\text{C}_9} = 37 \%$; $\Sigma S_j^* = 287 \%$.
- (e): $T_r = 370 \text{ }^\circ\text{C}$; $X_{\text{Dec}} = 84 \%$; $Y_{\text{C}_9} = 37 \%$; $\Sigma S_j^* = 287 \%$.

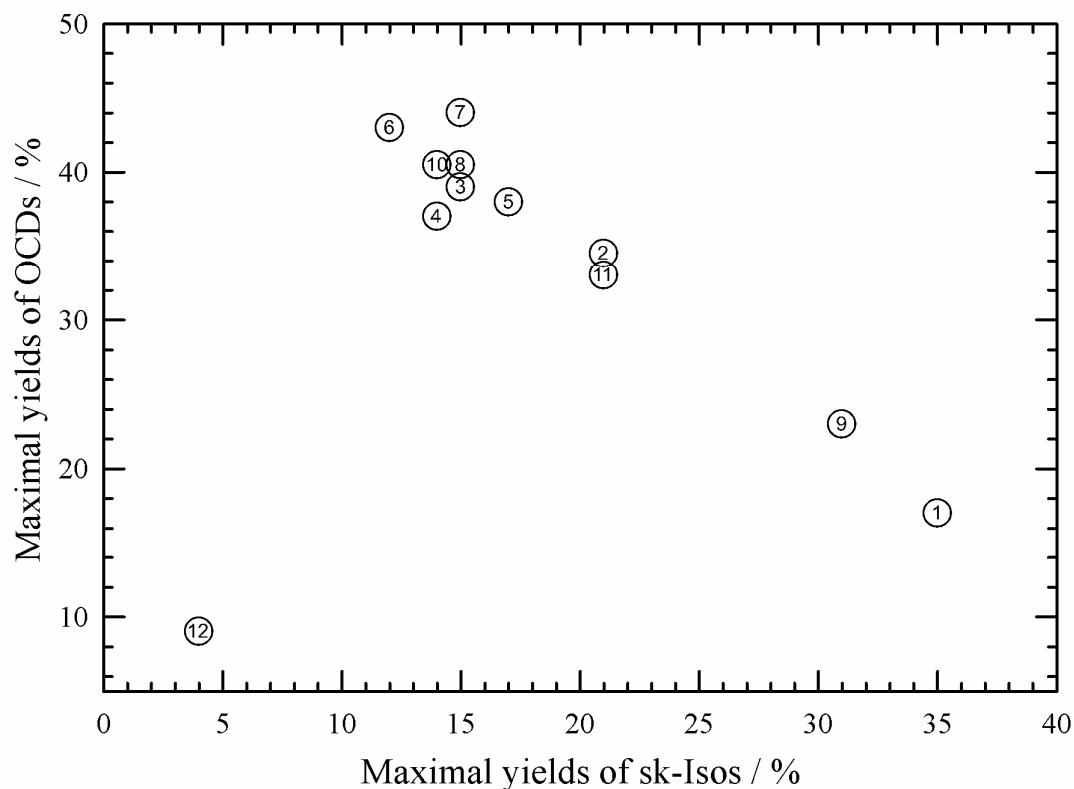


Figure 7.28: Maximal yields of OCDs versus maximal yields of skeletal isomers of some iridium-containing zeolites Beta. The numbers stand for the catalysts summarized in Table 7.11.

Table 7.11: Maximal yields of OCDs and sk-Isos and their corresponding reaction temperatures of some iridium-containing zeolite Beta catalysts.

Catalyst	$T_{Y_{\text{OCDs, max.}}} /$ °C	$Y_{\text{OCDs, max.}} /$ %	$T_{Y_{\text{sk-Isos, max.}}} /$ °C	$Y_{\text{sk-Isos, max.}} /$ %	
1	3.3Ir/H _{0.74} ,Li _{0.26} -[Al]Beta-14	246	17	246	35
2	3.0Ir/Na _{0.53} ,H _{0.47} -[Al]Beta-14	246	34	261	21
3	3.2Ir/H _{0.61} ,K _{0.39} -[Al]Beta-14	263	39	242	15
4	3.5Ir/Rb _{0.52} ,H _{0.48} -[Al]Beta-14	272	37	252	14
5	4.8Ir/H _{0.61} ,Cs _{0.39} -[Al]Beta-14	246	38	231	17
6	4.0Ir/Cs _{0.53} ,H _{0.47} -[Al]Beta-14	259	43	240	12
7	3.4Ir/H _{0.58} ,Cs _{0.42} -[Al]Beta-14	262	44	253	15
8	2.0Ir/Cs _{0.80} ,H _{0.20} -[Al]Beta-14	281	40	260	15
9	1.1Ir/Cs _{0.96} ,H _{0.04} -[Al]Beta-14	320	23	300	31
10	3.1Ir/Na _{0.82} ,H _{0.18} -[Al]Beta-8	280	40	269	14
11	3.4Ir/H _{0.56} ,Na _{0.44} -[Al]Beta-21	246	33	236	21
12	2.3Ir/H _{0.88} ,Na _{0.12} -[B]Beta-18	326	9	326	4

A comparison of the maximum yields of OCDs and skeletal isomers obtained on the iridium-containing Beta-supported catalysts (Figure 7.28) reveals a relationship between these two values. It can be seen from the Figure that the lowest yield of skeletal isomers corresponds to the highest yield of OCDs obtained on the Ir-Beta catalysts, with the exception of 2.3Ir/H_{0.88},Na_{0.12}-[B]Beta-18 (No. 12) which possesses very weak acid sites and behaves more like a non-acidic catalyst. Table 7.11 summarizes the maximal yields of OCDs and skeletal isomers obtained on these catalysts and the corresponding reaction temperatures.

For an explanation of this relationship one has to bear in mind that there are different reaction paths for the formation of ring-opening products (Figure 7.29). The assumption was made that, depending on the hydrogenolysis activity of the noble metal and the concentration and strength of the Brønsted acid sites, three different pathways are likely to exist. In the upper part of Figure 7.29 the direct ring opening of decalin on monofunctional iridium catalysts is shown. This direct formation of ROPs *via* endocyclic hydrogenolysis (for details see Figure 4.25, page 45), will be prevailing, if the hydrogenolysis activity of the noble metal is very high (typically iridium) and/or the strength of the acid sites is very low, *e.g.* on Ir/silica [85] or 2.3Ir/H_{0.88},Na_{0.12}-[B]Beta-18. However, compared to the formation of skeletal isomers by a so-called non-branching (or type A) isomerization *via* carbocations at the Brønsted acid sites, this reaction requires higher temperatures, typically *ca.* 250 to 350 °C [87, 88].

The reaction path in the middle of Figure 7.29 (highlighted by bold-faced arrows) is the desired one, since the mild isomerization of decalin leads to two-ring naphthenes with at least one five-membered ring which can easily be opened to ROPs by hydrogenolysis on iridium. For this reaction path to be followed, the right balance between the hydrogenolysis activity of the noble metal and the strength of the Brønsted acid sites has to be established. It is likely that such a balance is realized in HIPEROcs.

The reaction path depicted in the lower part of Figure 7.29 comprises one additional isomerization step which is induced by strongly acid sites and leads to highly branched isomers of decalin with a low amount of secondary-secondary C-C bonds. Since the hydrogenolytic cleavage of secondary-tertiary and tertiary-tertiary C-C bonds is much slower on iridium than the rupture of secondary-secondary C-C bonds (known as the selective mechanism [60]), the ring opening of highly branched isomers is slower compared to that of mildly branched ones. This, in turn, leads to higher selectivities of skeletal isomers and lower selectivities of ring-opening products and open-chain decanes. For this third reaction path, relatively strong Brønsted acid sites are required while the hydrogenolysis activity of the catalyst can be relatively low. Very likely, this is the case for 1.1Ir/Cs_{0.96},H_{0.04}-[Al]Beta-14: The hydrogenolysis activity of the catalyst is low due to the low amount of iridium. This leads to the formation of highly branched isomers *via* a second isomerization step,

comprising fewer secondary-secondary C-C bonds than mildly branched isomers. In the case of 4.8Ir/H_{0.61},Cs_{0.39}-[Al]Beta-14 and 3.3Ir/H_{0.74},Li_{0.26}-[Al]Beta-14 the activity of the Brønsted acid sites is too high, and again highly branched isomers are formed.

In addition, competing with the desired ring opening to form open-chain decanes are two very undesired reactions of ROPs (see Figure 7.29) which both lead directly to C₉-hydrocarbons: (i) One is the hydrogenolysis of exocyclic carbon-carbon bonds in the alkyl side chain(s) of the ROPs. It is evident from Figure 7.29 that, for selective ring opening of decalin, a hydrogenolysis component in the catalyst and reaction conditions are needed which favor as much as possible cleavage of endocyclic over that of exocyclic carbon-carbon bonds. (ii) The other one is the paring reaction leading to iso-butane and methylcyclopentane (see also Figure 4.17, page 34). As a matter of course, open-chain decanes can also undergo additional bond ruptures, hydrogenolytic or cationic, leading to C₉- products.

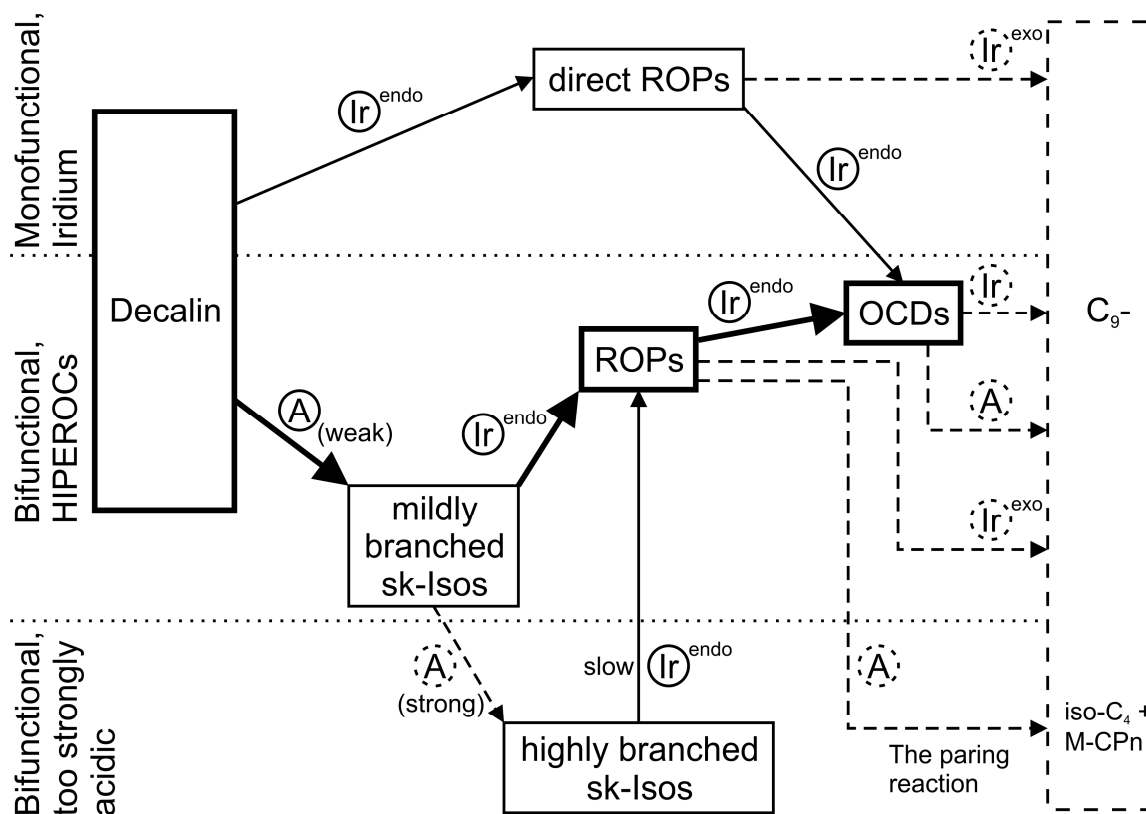


Figure 7.29: Proposed reaction scheme of the formation of OCDs from decalin on iridium-containing HIPEROCs. Arrows in bold face indicate the desired reaction path whereas the dashed arrows indicate undesired reactions. A stand for Brønsted-acid sites, *endo* and *exo* denote, respectively, hydrogenolysis of endocyclic and exocyclic carbon-carbon bonds.

7.5 Variation of the Hydrogen Pressure

In a recent publication [81], Kubička *et al.* reported that increasing the hydrogen partial pressure can have a beneficial effect on the yield of ring-opening products in the hydroconversion of decalin on an Ir/H-[Al]Beta catalyst. With this in mind, cis-decalin was hydroconverted at $p_{\text{H}_2} = 8.0$ MPa (instead of the standard hydrogen pressure of $p_{\text{H}_2} = 5.2$ MPa) on the best catalyst identified so far, *viz.* 4.0Ir/Cs_{0.53}H_{0.47}-[Al]Beta-14. The reaction temperature was varied, and all other experimental conditions were equal to those chosen as standard values (see Section 5.3, page 61).

The results are shown in Figure 7.30 in comparison with those obtained on the same catalyst at the standard hydrogen pressure of 5.2 MPa. It is seen that, upon increasing p_{H_2} to 8.0 MPa, the maximal selectivity of open-chain decanes is indeed higher, namely 50 instead of 47 %. Other beneficial effects of the elevated hydrogen pressure can be seen from Table 7.12: The combined yields of OCDs and ROPs are slightly higher (63 % instead of 60 %) and the yield of the undesired C₉- hydrocarbons at the maximal yield of OCDs is reduced from 39 to 34 %.

These findings are in-line with the results obtained by Weitkamp and Schulz [107] who investigated the influence of the hydrogen pressure on the hydroconversion of n-decane with a bifunctional Pt/Ca-Y catalyst. They found that the total conversion of n-decane is maximal at a hydrogen pressure of *ca.* 1.8 MPa and decreases with increasing hydrogen pressures up to $p_{\text{H}_2} = 9.7$ MPa. The selectivity of C₉- hydrocarbons passed through a maximum at $p_{\text{H}_2} = 2.0$ MPa and decreased sharply with further increasing pressure. In contrast to this the selectivity of iso-decanes passed through a distinct minimum at $p_{\text{H}_2} = 2.0$ MPa.

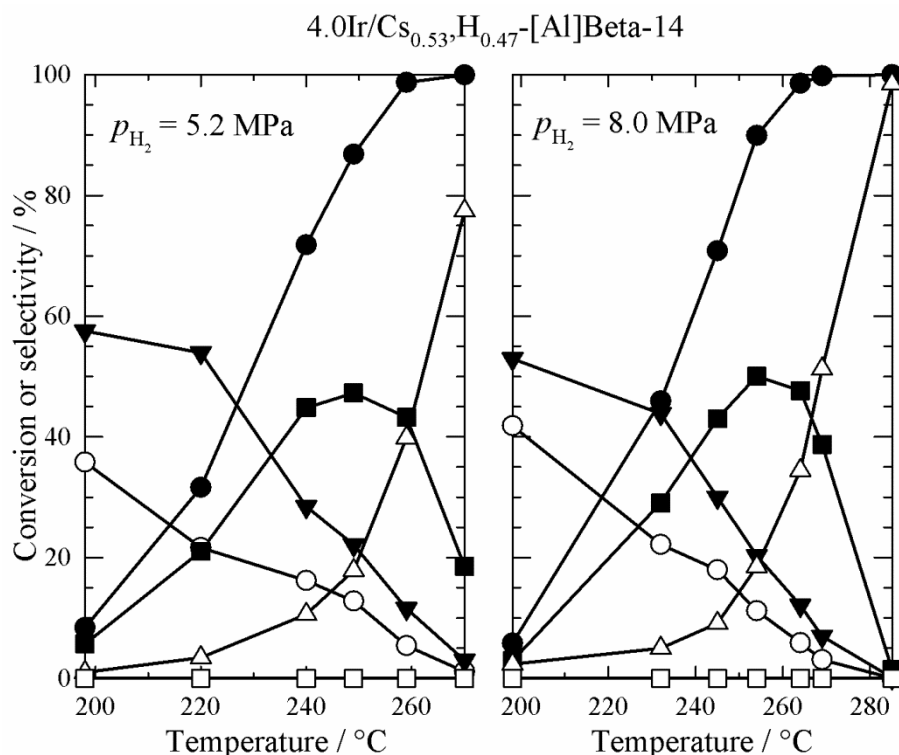


Figure 7.30: Conversion of decalin and selectivities of the different groups of products in dependence of the reaction temperature at a total pressure of 5.2 and 8.0 MPa on 4.0Ir/Cs_{0.53}H_{0.47}-[Al]Beta-14. (● X_{Dec} , ■ S_{OCDs} , ▼ S_{ROPs} , ○ $S_{sk-Isos}$, ▲ S_{C_9-} , □ S_{DHPs}).

Table 7.12: Maximum yields and selectivities of OCDs, combined yields of ROPs and OCDs and yields of C₉- hydrocarbons at reaction conditions of maximal OCD selectivities and yields in the hydroconversion of decalin at 5.2 and 8.0 MPa on 4.0Ir/Cs_{0.53}H_{0.47}-[Al]Beta-14.

Total pressure	$T_r /$ °C	$X_{Dec} /$ %	$S_{OCDs} /$ %	$Y_{OCDs} /$ %	$(Y_{OCDs} +$ $Y_{ROPs}) /$ %	$Y_{C_9-} /$ %
5.2 MPa	249	87	47	41	60	15
	259	99	43	43	54	39
8.0 MPa	254	90	50	45	63	17
	264	99	48	47	59	34

The lower amounts of C₉- products formed at $p_{H_2} = 8.0$ MPa are thus a possible reason for the higher amounts of OCDs: the consecutive hydrocracking of open-chain decanes is more and more unfavored with increasing hydrogen pressure, enabling higher amounts of OCDs.

A closer look at the selectivities of sk-Isos formed at $p_{H_2} = 5.2$ and 8.0 MPa on 4.0Ir/Cs_{0.53}H_{0.47}-[Al]Beta-14 reveals a slight increase of the selectivities at low conversions

upon increasing the hydrogen pressure. Bearing in mind Figure 7.29, page 137, the assumption can be made that 4.0Ir/Cs_{0.53},H_{0.47}-[Al]Beta-14 possesses a slightly too high hydrogenolysis activity which is reduced with increasing hydrogen pressure leading to higher amounts of OCDs. Another hint for this assumption are the very high maximum yields of OCDs obtained on catalyst 3.4Ir/H_{0.58},Cs_{0.42}-[Al]Beta-14 at $p_{H_2} = 5.2$ MPa ($Y_{OCDs, max.} = 44$ %, see Table 7.8, page 127) which possesses a lower amount of iridium and thus a lower hydrogenolytic activity.

Summing up it was possible, due to systematic modifications of the properties of the zeolites and reaction conditions, to increase the maximum yield of open-chain decanes in the catalytic hydroconversion of cis-decalin to 47 %.

7.6 Structural and Chemical Prerequisites for HIPEROCS

In this Section the necessary properties of a high-performance ring-opening catalyst (HIPEROCS) will be summarized. The influence of different zeolites loaded with platinum or iridium on the hydroconversion of cis-decalin was investigated in Section 7.2, pages 99 - 109. The most promising supports concerning the maximum yield of OCDs, regardless of the nature of the noble-metal, were zeolites with a three-dimensional 12-membered-ring pore system with a spaciousness index higher than 17, like zeolites Beta, EMC-2 or Y. A possible explanation for these findings are diffusional limitations in one-dimensional or 10-membered-ring pore systems (see Section 7.3.3, page 117). The diffusion limitations lead to longer residence times, and the longer the residence time of the hydrocarbons in the pores the greater the probability of secondary hydrocracking, leading to lower amounts of OCDs.

Another property that can be defined regardless of the nature of the noble metal is the concentration of the Brønsted acid sites. It is known from literature that a high strength and/or concentration of Brønsted acid sites favors the undesired paring reaction [65, 85, 86]. To avoid this reaction a low concentration of Brønsted acid sites is needed. Such low concentrations can be realized, as shown in this work, by their exclusive generation *via* the reduction of the noble metal (see Eq. (4.4), page 20).

A further discussion about the properties of HIPEROCS must involve the nature of the noble metal. In this work mainly platinum and iridium were investigated. These two noble metals possess very different properties, such as the hydrogenolysis activity, which is much higher for iridium than for platinum [55, 88], or the isomerization ability of platinum [56 - 58]. It has been already shown [25, 85, 86, 88] that a discussion of a possible reaction pathway from decalin to open-chain decanes and further on to C₉- products is much easier for iridium than for platinum, due to the inability of iridium to isomerize hydrocarbons in the absence of

Brønsted acid sites. Iridium thus enables one to investigate the formation of direct ROPs, direct OCDs, direct C₉ ROPs and direct OCNs in the hydrogenolytic hydrodecyclization of decalin on non-acidic supports (see Figure 4.25, page 45) [88].

The inability of iridium to promote skeletal isomerizations has an additional advantage: The isomerization activity of the catalyst depends only on the concentration and strength of the Brønsted acid sites and, as demonstrated in Section 7.3, these two properties can be tuned in a zeolite. This enabled a detailed investigation of the influence of the hydrogenolysis activity and the isomerization activity on the amounts of OCDs formed.

It could be shown that, in the case of iridium as the metal component, the isomerization of decalin at the Brønsted acid sites to five-membered-ring naphthenes or spiro[4.5]decane is an essential step for high yields of OCDs (see Section 7.4, page 130), which is in-line with the results obtained by other groups [72, 90]. Moreover, it was found that the balance between the two types of sites is very crucial: A too low acid strength, as in Na,H-[B]Beta-18 (Section 7.3.1, page 110), leads to low yields of OCDs due to the absence of easy-to-open five-membered-ring naphthenes, whereas a too high acid strength favors the formation of isobutane and methylcyclopentane *via* the paring reaction. Both extremes can easily be recognized from the different carbon number distributions of hydrocracked products: In the case of a too low acid strength, a hammock-type distribution curve results on iridium catalysts (see Figure 7.11, page 112), whereas an M-shaped curve, with maxima at C₄ and C₆ is obtained for the paring reaction (see Figure 7.13, page 115). Proposed reaction pathways for these two extremes and the desired pathway are schematically depicted in Figure 7.29 on page 137.

If the metal component in the ring-opening catalyst is platinum rather than iridium, the chemistry of ring opening is more complex, mainly because platinum is capable to isomerize decalin in the absence of acid sites. This makes it more difficult to find the right balance between the activity of the acid sites and the hydrogenolysis activity of the noble metal.

The answer to the question “what does a bifunctional catalyst make a HIPEROC” is hence not trivial and cannot be given with a few words. However, as this work has shown, factors that play a pivotal role include the pore size and pore dimensionality of the zeolite, the concentration and strength of its Brønsted acid sites, and the nature and loading of the noble metal. The proximity of both types of sites might play a role as well, but bearing in mind the work of Arribas *et al.* [73], all catalysts used in this work were prepared by introducing the noble metal *via* ion exchange, thereby minimizing the average distance between both types of sites.

8 References

- [1] EN 590:2009+A1:2010, "Automotive fuels. Diesel. Requirements and test methods".
- [2] J. Weitkamp, in: "Handbook of Heterogeneous Catalysis", 2nd Edn., G. Ertl, H. Knözinger, F. Schüth, J. Weitkamp (Eds.), Vol. 7, Wiley-VCH, Weinheim, 2008, p. 3133-3152.
- [3] D.S. Coombs, A. Alberti, T. Armbruster, G. Artioli, C. Colella, W. Galli, J.D. Grice, F. Liebau, J.A. Mandarino, H. Minato, E.H. Nickel, E. Passaglia, D.R. Peacor, S. Quartieri, R. Rinaldi, M. Ross, R.A. Sheppard, E. Tillmanns, G. Vezzalini, *Can. Mineral.* 35 (1997) 1571-1606.
- [4] <http://www.iza-structure.org> (Access on 13.02.2012)
- [5] W. Löwenstein, *Am. Mineralogist* 39 (1954) 92-96.
- [6] H.O. Pastore, S. Coluccia, L. Marchese, *Annu. Rev. Mater. Res.* 35 (2005) 351-395.
- [7] G. Sastre, D.W. Lewis, C.R.A. Catlow, *J. Phys. Chem.* 100 (1996) 6722-6730.
- [8] A. Corma, M. Moliner, Á. Cantín, M.J. Díaz-Cabañas, J.L. Jordá, D. Zhang, J. Sun, K. Jansson, S. Hovmöller, X. Zou, *Chem. Mater.* 20 (2008) 3218-3223.
- [9] P.A. Newell, L.V.C. Rees, *Zeolites*, 3 (1983) 22-27.
- [10] R.M. Barrer, H. Villiger, *Z. Kristallogr.* 128 (1969) 352-370.
- [11] J. Weitkamp, S. Ernst, R. Kumar, *Appl. Catal.* 27 (1986) 207-210.
- [12] Y. Traa, S. Sealy, J. Weitkamp, in: "Molecular Sieves-Science and Technology", H.G. Karge, J. Weitkamp (Eds.), Vol. 5, Springer, Berlin, Heidelberg, 2007, p. 103-154.
- [13] A. Corma, H. Garcia, *Chem. Rev.* 102 (2002) 3837-3892.
- [14] T. Chen, A. Men, P. Sun, J. Zhou, Z. Yuan, A. Guo, J. Wang, D. Ding and H. Li, *Catal. Today* 30 (1996) 189-192.
- [15] G.H. Köhl, *J. Phys. Chem. Solids* 38 (1977) 1259-1263.
- [16] H.G. Karge, *Z. Phys. Chem.* 76 (1971) 133-153.
- [17] H.G. Karge, J. Ladebeck, Z. Sarbak, K. Hatada, *Zeolites* 2 (1982) 94-104.
- [18] H.G. Karge, K. Hatada, Y. Zhang, R. Fiedorow, *Zeolites* 3 (1983) 13-21.
- [19] G.H. Köhl, in: "Catalysis and Zeolites - Fundamentals and Applications", J. Weitkamp, L. Puppe (Eds.), Springer, Berlin, Heidelberg, New York, 1999, p. 81-197.
- [20] A.E. Hirschler, *J. Catal.* 2 (1963) 428-439.
- [21] P.E. Pickert, J.A. Rabo, E. Dempsey, V. Schomaker, in "Proceedings of the Third International Congress on Catalysis", W.M.H. Sachtler, G.C.A. Schuit, P. Zwietering (Eds.), Vol. 1, North-Holland Publishing Company, Amsterdam, 1965, p. 714-728.
- [22] B. Gil, in: "Zeolites: From Model Materials to Industrial Catalysts", J. Čejka, J. Pérez-Pariente, W.J. Roth (Eds.), Transworld Research Network, Kerala, 2008, p. 173-206.

- [23] R.T. Sanderson, in: "Chemical Bonds and Bond Energy", 2nd Edn., E.M. Loebl (Ed.), Physical Chemistry, Vol. 21, Academic Press, New York, 1976, 218 pp.
- [24] P.A. Jacobs, W.J. Mortier, J.B. Uytterhoeven, J. Inorg. Nuc. Chem. 40 (1978) 1919-1923.
- [25] S. Rabl, D. Santi, A. Haas, M. Ferrari, V. Calemma, G. Bellussi, J. Weitkamp, Microporous Mesoporous Mater. 146 (2011) 190-200.
- [26] E. O'Donoghue, D. Barthomeuf, Zeolites 6 (1986) 267-270.
- [27] Y.S. Chen, M. Guisnet, M. Kern, J.L. Lemberston, New J. Chem. 11 (1987) 623-626.
- [28] M. Tielen, M. Geelen, P.A. Jacobs, Acta Phys. Chem. 31 (1985) 1-18.
- [29] J. Houžvička, R. Klik, L. Kubelková, V. Ponec, Appl. Catal., A 150 (1997) 101-114.
- [30] C.T.W. Chu, C.D. Chang, J. Phys. Chem. 89 (1985) 1569-1571.
- [31] J. Weitkamp, H.K. Beyer, G. Borbely, V. Cortes-Corberan, S. Ernst, Chem. Ing. Techn. 58 (1986) 969-971.
- [32] R.C. Deka, N. Tajima, K. Hirao, J. Mol. Struct.: theochem 535 (2001) 31-38.
- [33] E.G. Derouane, F.G. Fripiat, J. Phys. Chem. 91 (1987) 145-148.
- [34] L.A. Pine, P.J. Maher, W.A. Wachter, J. Catal. 85 (1984) 466-476.
- [35] H. Knözinger, in: "Handbook of Heterogeneous Catalysis", 2nd Edn., G. Ertl, H. Knözinger, F. Schüth, J. Weitkamp (Eds.), Vol. 2, Wiley-VCH, Weinheim, 2008, p. 1135-1163.
- [36] H. Knözinger, in: "The Hydrogen Bond", P. Schuster, G. Zundel, C. Sandorfy (Eds.), Vol. 3, North-Holland, Amsterdam, 1976, p. 1265-1353.
- [37] L.M. Kustov, V.Y. Borovkov, V.B. Kazanskii, J. Catal. 72 (1981) 149-159.
- [38] H.G. Karge, M. Hunger, H.K. Beyer, in: "Catalysis and Zeolites - Fundamentals and Applications", J. Weitkamp, L. Puppe (Eds.), Springer, Berlin, Heidelberg, New York, 1999, p. 198-326.
- [39] D. Cook, Can. J. Chem. 39 (1961) 2009-2024.
- [40] E.P. Parry, J. Catal. 2 (1963) 371-379.
- [41] C.H. Kline, Jr., J. Turkevich, J. Chem. Phys. 12 (1944) 300-309.
- [42] T.R. Hughes, H.M. White, J. Phys. Chem. 71 (1967) 2112-2201.
- [43] J. Take, T. Yamaguchi, K. Miyamoto, H. Ohyama, M. Misono, in: "New Developments in Zeolite Science and Technology", Y. Murakami, A. Iijima, J.W. Ward (Eds.), Studies in Surface Science and Catalysis, Vol. 28, Elsevier, Amsterdam, 1986, p. 495-502.
- [44] J. Datka, J. Chem. Soc., Faraday Trans. I 76 (1980) 705-710.
- [45] C.A. Emeis, J. Catal. 141 (1993) 347-354.
- [46] S. Khabtou, T. Chevreau, J.C. Lavalley, Microporous Mater. 3 (1994) 133-148.
- [47] M. Guisnet, P. Ayrault, J. Datka, Pol. J. Chem. 71 (1997) 1455-1461.

- [48] A. Corma, V. González-Alfaro, A.V. Orchillés, *J. Catal.* 200 (2001) 34-44.
- [49] A. Corma, A. Martínez, V. Martínez-Soria, *J. Catal.* 200 (2001) 259-269.
- [50] A. Soualah, J.L. Lemberon, L. Pinard, M. Chater, P. Magnoux, K. Moljord, *Appl. Catal., A* 336 (2008) 23-28.
- [51] D. Kubička, N. Kumar, T. Venäläinen, H. Karhu, I. Kubičková, H. Österholm, D.Y. Murzin, *J. Phys. Chem. B* 110 (2006) 4937-4946.
- [52] Z. Musilová-Pavlačková, M. Kubů, A.W. Burton, S.I. Zones, M. Bejblová, J. Čejka, *Catal. Lett.* 131 (2009) 393-400.
- [53] K. Hedden, J. Weitkamp, *Chem. Ing. Tech.* 55 (1983) 907-914.
- [54] A. Haas, Ph.D. Thesis, University of Stuttgart, 2012.
- [55] J.H. Sinfelt, *Catal. Rev.* 3 (1969) 175-205.
- [56] G.C. Bond, in: "Metal-Catalyzed Reactions of Hydrocarbons", M.V. Twigg, M.S. Spencer (Eds.), *Fundamental and Applied Catalysis*, Springer, New York, 2005, 666 pp.
- [57] F. Garin, S. Aeiyaeh, P. Légaré, G. Maire, *J. Catal.* 77 (1982) 323-337.
- [58] P. Légaré, F. Garin, *J. Catal.* 214 (2003) 336-340.
- [59] F.G. Gault, in: "Advances in Catalysis", D.D. Eley, H. Pines, P.B. Weisz (Eds.), Vol. 30, Academic Press, New York, 1981, p. 1-95.
- [60] G. Maire, G. Plouidy, J.C. Prudhomme, F.G. Gault, *J. Catal.* 4 (1965) 556-569.
- [61] J. Weitkamp, M. Hunger, in: "Introduction to Zeolite Science and Practice", J. Čejka, H. van Bekkum, A. Corma, F. Schüth (Eds.), *Studies in Surface Science and Catalysis*, Vol. 168, Elsevier, Amsterdam, 2007, p. 787-835.
- [62] J. Weitkamp, P.A. Jacobs, J.A. Martens, *Appl. Catal.* 8 (1983) 123-141.
- [63] W.O. Haag, R.M. Dessau, in: "Proceedings of the 8th International Congress on Catalysis", Vol. 2, Verlag Chemie, Weinheim, DECHEMA, Frankfurt am Main, 1984, p. 305-316.
- [64] J. Weitkamp, H. Schulz, *J. Catal.* 29 (1973) 361-366.
- [65] R.F. Sullivan, C.J. Egan, G.E. Langlois, R.P. Sieg, *J. Am. Chem. Soc.* 83 (1961) 1156-1160.
- [66] D.M. Brouwer, H. Hogeveen, *Recl. Trav. Chim. Pays-Bas* 89 (1970) 211-224.
- [67] D. Kubička, N. Kumar, P. Maki-Arvela, M. Tiitta, V. Niemi, T. Salmi, D.Y. Murzin, *J. Catal.* 222 (2004) 65-79.
- [68] D. Kubička, N. Kumar, P. Maki-Arvela, M. Tiitta, V. Niemi, H. Karhu, T. Salmi, D.Y. Murzin, *J. Catal.* 227 (2004) 313-327.
- [69] D. Kubička, T. Salmi, M. Tiitta, D.Y. Murzin, *Fuel* 88 (2009) 366-373.
- [70] M. Santikunaporn, J.E. Herrera, S. Jongpatiwut, D.E. Resasco, W.E. Alvarez, E.L. Sughrue, *J. Catal.* 228 (2004) 100-113.

- [71] M.A. Arribas, A. Martínez, *Appl. Catal.*, A 230 (2002) 203-217.
- [72] G.B. McVicker, M. Daage, M.S. Touvelle, C.W. Hudson, D.P. Klein, W.C. Baird, Jr., B.R. Cook, J.G. Chen, S. Hantzer, D.E.W. Vaughan, E.S. Ellis, O.C. Feeley, *J. Catal.* 210 (2002) 137-148.
- [73] M.A. Arribas, P. Concepción, A. Martínez, *Appl. Catal.*, A 267 (2004) 111-119.
- [74] M.A. Arribas, A. Martínez, G. Sastre, in: "Impact of Zeolites and Other Porous Materials on the New Technologies at the Beginning of the New Millennium", R. Aiello, G. Giordano, F. Testa (Eds.), *Studies in Surface Science and Catalysis*, Vol. 142, Part B, Elsevier, Amsterdam, 2002, p. 1015-1022.
- [75] M.A. Arribas, A. Corma, M.J. Díaz-Cabañas, A. Martínez, *Appl. Catal.*, A 273 (2004) 277-286.
- [76] M.A. Arribas, J.J. Mahiques, A. Martínez, in: "Zeolites and Mesoporous Materials at the Dawn of the 21st Century", A. Galarneau, F. Di Renzo, F. Fajula, J. Viedrine (Eds.), *Studies in Surface Science and Catalysis*, Vol. 135, Elsevier, Amsterdam, 2001, p. 303-311.
- [77] H. Ma, X. Yang, G. Wen, G. Tian, L. Wang, Y. Xu, B. Wang, Z. Tian, L. Lin, *Catal. Lett.* 116 (2007) 149-154.
- [78] N. Kumar, A. Lazuen, D. Kubička, T. Heikkilä, V.-P. Lehto, H. Karhu, T. Salmi, D.Y. Murzin, in: "Scientific Bases for the Preparation of Heterogeneous Catalysts", E.M. Gaigneaux, M. Devillers, D.E. De Vos, S. Hermans, P.A. Jacobs, J.A. Mertens, P. Ruiz (Eds.), *Studies in Surface Science and Catalysis*, Vol. 162, Elsevier, Amsterdam, 2006, p. 401-408.
- [79] N. Kumar, D. Kubička, A.L. Garay, P. Mäki-Arvela, T. Heikkilä, T. Salmi, D.Y. Murzin, *Top. Catal.* 52 (2009) 380-386.
- [80] H. Vuori, R.J. Silvennoinen, M. Lindblad, H. Osterholm, A.O.I. Krause, *Catal. Lett.* 131 (2009) 7-15.
- [81] D. Kubička, M. Kangas, N. Kumar, M. Tiitta, M. Lindblad, D.Y. Murzin, *Top. Catal.* 53 (2010) 1438-1445.
- [82] R. Contreras, J. Ramírez, R. Cuevas-García, A. Gutiérrez-Alejandre, P. Castillo-Villalón, G. Macías, I. Puente-Lee, *Catal. Today* 148 (2009) 49-54.
- [83] K.C. Mouli, V. Sundaramurthy, A.K. Dalai, Z. Ring, *Appl. Catal.*, A 321 (2007) 17-26.
- [84] K.C. Mouli, V. Sundaramurthy, A.K. Dalai, *J. Mol. Catal.*, A 304 (2009) 77-84.
- [85] J. Weitkamp, S. Rabl, A. Haas, D. Santi, M. Ferrari, V. Calemme, (a) in: "The Future Role of Hydrogen in Petrochemistry and Energy Supply", S. Ernst, A. Lercher, J. Lichtscheidl, M. Marchionne, F. Nees, E. Santacesaria (Eds.), *DGMK Tagungsbericht*

- 2010-3, DGMK, Hamburg, 2010, S. 77-86. (b) OIL GAS Eur. Mag. 37 (2) (2011) 94-98.
- [86] S. Rabl, A. Haas, D. Santi, C. Flego, M. Ferrari, V. Calemma, J. Weitkamp, *Appl. Catal.*, A 400 (2011) 131-141.
- [87] R. Moraes, K. Thomas, S. Thomas, S. Van Donk, G. Grasso, J.-P. Gilson, M. Houalla, *J. Catal.* 286 (2012) 62-77.
- [88] A. Haas, S. Rabl, M. Ferrari, V. Calemma, J. Weitkamp, *Appl. Catal.*, A 425-426 (2012) 97-109.
- [89] S. Rabl, Ph.D. Thesis, University of Stuttgart, 2011.
- [90] G. Bellussi, A. Haas, S. Rabl, D. Santi, M. Ferrari, V. Calemma, J. Weitkamp, *Chin. J. Catal.* 33 (2012) 70-84.
- [91] A. Arnold, S. Steuernagel, M. Hunger, J. Weitkamp, *Microporous Mesoporous Mater.* 62 (2003) 97-106.
- [92] G. Majano, L. Delmotte, V. Valtchev, S. Mintova, *Chem. Mater.* 21 (2009) 4184-4191.
- [93] Y. Miyamoto, N. Katada, M. Niwa, *Microporous Mesoporous Mater.* 40 (2000) 271-281.
- [94] P.R.H.P. Rao, M. Matsukata, *Chem. Commun.* 6 (1996) 1441-1442.
- [95] M. Bandyopadhyay, R. Bandyopadhyay, S. Tawada, Y. Kubota, Y. Sugi, *Appl. Catal.*, A 225 (2002) 51-62.
- [96] J. Weitkamp, R. Schumacher, U. Weiss, *Chem.-Ing.-Tech.* 64 (1992) 1109-1112.
- [97] R.A. Dalla Batta, M. Boudart, in: "Proceedings of the 5th International Congress on Catalysis", J.W. Hightower (Ed.), Vol. 2, North-Holland Publishing Company, Amsterdam, 1973, p. 1329-1341.
- [98] G. Engelhardt, U. Lohse, E. Lippmaa, M. Tarmak, M. Mägi, *Z. Anorg. Allg. Chem.* 482 (1981) 49-64.
- [99] M.A. Camblor, A. Corma, S. Valencia, *Microporous Mesoporous Mater.* 25 (1998) 59-74.
- [100] C. Fild, D.F. Shantz, R.F. Lobo, H. Koller, *Phys. Chem. Chem. Phys.* 2 (2000) 3091-3098.
- [101] H. Koller, C. Fild, R.F. Lobo, *Microporous Mesoporous Mater.* 79 (2005) 215-224.
- [102] L.G. Christner, B.V. Liengme, W.K. Hall, *Trans. Faraday Soc.* 64 (1968) 1679-1692.
- [103] H. Hattori, T. Shiba, *J. Catal.* 12 (1968) 111-120.
- [104] S. Ernst, J. Weitkamp, in: "Proceedings of the International Symposium of Zeolite Catalysis", Siófok, Hungary, May 13 to 16, 1985, p. 457-466.
- [105] J. Weitkamp in: "Hydrocracking and Hydrotreating", J.W. Ward, S.A. Qader (Eds.), *Amer. Chem. Soc. Symp. Ser.*, Vol. 20, Washington, D.C., 1975, p. 1-27.

- [106] J. Weitkamp, in: "Actas do 9.º Simpósio Iberoamericano de Catálise – Proceedings of the 9th Iberoamerican Symposium on Catalysis", M.F. Portela (Ed.), Vol. 2, Technical University, Lisboa 1984, p. 1332-1341.
- [107] J. Weitkamp, H. Schulz, in: "Compendium 74/75: Vorträge der 24. Haupttagung der DGMK (vom 30. September bis 3. Oktober 1974 in Hamburg)", D. Klamann, F. Asinger, H. Boigk, H.-H. Oelert, W. Peters (Eds.), Vol. 1, Industrieverlag, Leinfelden, 1975, p. 355-366.

9 Appendices

9.1 Retention Times

Table 9.1: Retention times (t_{ret}) and products of the hydroconversion of cis-decalin, as of February 01, 2012. For the conditions of the gas chromatographic analyses see Section 5.4, Table 5.2, page 65.

$t_{\text{ret}} / \text{min}$	Product	$t_{\text{ret}} / \text{min}$	Product
11.95	methane	55.90	C ₈
12.30	ethane	56.95	1,2,4-trimethylcyclopentane
13.20	propane	57.10	C ₈
14.55	iso-butane	58.35	1,2,3-trimethylcyclopentane
15.70	n-butane	58.80	C ₈
16.25	neo-pentane	59.80	C ₈
19.60	2-methylbutane	60.60	2,3-dimethylhexane
21.55	n-pentane	60.95	3-ethyl-2-methylpentane
24.95	2,2-dimethylbutane	61.30	C ₈
28.30	cyclopentane	61.55	2-methylheptane
28.35	2,3-dimethylbutane	61.85	4-methylheptane
28.75	2-methylpentane	62.40	3,4-dimethylhexane
30.60	3-methylpentane	62.70	C ₈
32.90	n-hexane	63.00	3-methylheptane
36.55	2,2-dimethylpentane	63.25	3-ethylhexane
37.10	methylcyclopentane	63.70	C ₈
37.45	2,4-dimethylpentane	64.00	cis-1,3-dimethylcyclohexane
38.50	C ₇	64.35	1,4-dimethylcyclohexane
40.95	C ₇	65.10	C ₈
41.65	3,3-dimethylpentane	65.60	1,1-dimethylcyclohexane
42.50	cyclohexane	65.90	1-ethyl-3-methylcyclopentane
43.55	2-methylhexane	66.30	1-ethyl-3-methylcyclopentane
44.00	2,3-dimethylpentane	66.55	1-ethyl-2-methylcyclopentane
44.70	1,1-dimethylcyclopentane	66.65	C ₈
45.10	3-methylhexane	67.15	1-ethyl-1-methylcyclopentane
46.45	trans-1,3-dimethylcyclopentane	67.65	n-octane
46.90	cis-1,3-dimethylcyclopentane	67.80	trans-1,2-dimethylcyclohexane
47.45	cis-1,2-dimethylcyclopentane	68.60	1,2,3,4-tetramethylcyclopentane
47.60	C ₇	68.85	C ₈
49.25	n-heptane	69.05	1,4-dimethyl-cyclohexane
53.30	trans-1,2-dimethylcyclopentane	69.75	C ₈
53.50	methylcyclohexane	70.35	propylcyclopentane
53.90	1,1,3-trimethylcyclopentane	70.95	C ₉
55.15	2,5-dimethylhexane	71.20	2,3,5-trimethylhexane
55.45	2,4-dimethylhexane	71.40	C ₉
55.60	ethylcyclopentane	71.65	2,2-dimethylheptane
55.80	C ₈	72.20	C ₉

t_{ret} / min	Product	t_{ret} / min	Product
72.40	2,4-dimethylheptane	83.70	C ₉
72.80	C ₉	83.85	C ₉
73.05	4,4-dimethylheptane	84.30	C ₉
73.30	C ₉	84.50	C ₉
73.50	4-ethyl-2-methylhexane	84.75	1,2,3-trimethylcyclohexane
73.60	2,6-dimethylheptane	85.00	1,1,3,5-tetramethylcyclohexane
73.75	C ₉	85.25	1-ethyl-4-methylcyclohexane
74.00	C ₉	85.75	1,2,3,4,5-pentamethylcyclopentane
74.25	1,3,5-trimethylcyclohexane	86.15	C ₉
74.45	ethylcyclohexane	86.25	1,1,4,4-tetramethylcyclohexane
74.85	2,5-dimethylheptane	86.40	C ₉
75.05	3,5-dimethylheptane	86.65	1,1,3-trimethylcyclohexane
75.20	3,5-dimethylheptane	87.20	n-nonane
75.45	3,3-dimethylheptane	87.45	3,3,5-trimethylheptane
75.65	C ₉	87.75	3-ethyl-2-methylheptane
76.00	1,1,4-trimethylcyclohexane	87.90	C ₉
76.25	C ₉	88.20	sk-Iso
76.55	1,3-diethylcyclopentane	88.55	C ₉
77.20	3-ethyl-2-methylhexane	88.75	sk-Iso
77.40	C ₉	89.15	ROP
77.60	C ₉	89.35	1-ethyl-2-methylcyclohexane
77.75	C ₉	89.65	C ₉
78.10	C ₉	89.80	sk-Iso
78.40	3-ethyl-3-methylhexane	89.90	C ₉
78.85	2,3-dimethylheptane	90.15	OCD
79.15	3-ethyl-4-methylhexane	90.25	OCD
79.30	3,4-dimethylheptane	90.60	ROP
79.45	3,4-dimethylheptane	90.85	sk-Iso
79.65	4-ethylheptane	91.00	OCD
80.15	4-methyloctane	91.30	2,4-dimethyloctane
80.30	2-methyloctane	91.40	sk-Iso
80.60	C ₉	91.60	2,3-dimethyloctane
80.85	C ₉	91.80	2-isopropyl-1,3-dimethylcyclopentane
81.05	C ₉	91.95	sk-Iso
81.50	3-ethylheptane	92.10	4,4-dimethyloctane
81.70	3-methyloctane	92.25	sk-Iso
81.80	C ₉	92.40	sk-Iso
81.95	C ₉	92.65	3,5-dimethyloctane
82.10	C ₉	92.80	2,5-dimethyloctane
82.35	C ₉	93.10	3,5-dimethyloctane
82.60	2,4,6-trimethylheptane	93.30	1,2,4,5-tetramethylcyclohexane
82.95	ROP	93.40	1,5-dimethylbicyclo[3.2.1]octane
83.10	1,1,3,5-tetramethylcyclohexane	93.65	2,7-dimethyloctane
83.30	C ₉	93.85	1-ethyl-2-methylcyclohexane
83.55	C ₉	94.00	OCD

t_{ret} / min	Product	t_{ret} / min	Product
94.15	OCD	102.70	sk-Iso
94.25	OCD	102.85	3-methylnonane
94.40	sk-Iso	103.00	sk-Iso
94.75	2,6-dimethyloctane	103.15	sk-Iso
95.00	4-ethyl-4-methylheptane	103.45	sk-Iso
95.20	sk-Iso	103.70	sk-Iso
95.40	3,3-dimethyloctane	104.05	cis-1-methyl-4-(methylethyl)cyclohexane
95.50	sk-Iso	104.15	sk-Iso
95.65	sk-Iso	104.50	3,7,7-trimethylbicyclo[4.1.0]heptanes
95.80	sk-Iso	104.70	sk-Iso
96.00	3,6-dimethyloctane	104.95	sk-Iso
96.25	3,6-dimethyloctane	105.25	sk-Iso
96.40	ROP	105.45	sk-Iso
96.55	sk-Iso	105.55	sk-Iso
96.65	sk-Iso	105.85	sk-Iso
96.75	3-ethyl-2-methylheptane	106.05	sk-Iso
96.95	sk-Iso	106.30	1-methyl-3-propylcyclohexane
97.15	sk-Iso	106.50	sk-Iso
97.25	4-propylheptane	106.75	sk-Iso
97.35	sk-Iso	107.00	ROP
97.55	3,4-diethylhexane	107.15	tert-butylcyclohexane
97.60	sk-Iso	107.45	cis-perhydroindane
97.75	sk-Iso	107.85	sk-Iso
97.95	4,5-dimethyloctane	108.30	sk-Iso
98.25	sk-Iso	108.35	sk-Iso
98.55	3-ethyl-3-methylheptane	108.60	sk-Iso
98.75	1,2,3,5-tetramethylcyclohexane	108.90	sk-Iso
98.85	sk-Iso	109.05	1-methyl-3-(methylethyl)cyclohexane
99.15	sk-Iso	109.15	sk-Iso
99.30	sk-Iso	109.35	n-decane
99.50	4-ethyloctane	109.65	ROP
99.65	sk-Iso	109.80	1-methyl-2-propylcyclohexane
99.90	ROP	110.05	1-methyl-1-propylcyclohexane
100.10	3,3-diethylhexane	110.35	sk-Iso
100.45	5-methylnonane	110.55	sk-Iso
100.75	4-methylnonane	110.60	sk-Iso
100.90	ROP	110.75	ROP
101.15	2-methylnonane	111.00	sk-Iso
101.30	trans-1,4-diethylcyclohexane	111.35	ROP
101.55	cis-1,4-diethylcyclohexane	111.50	sk-Iso
101.65	sk-Iso	111.80	sk-Iso
101.90	1-ethyl-2,4-dimethylcyclohexane	112.05	trans-1,4-diethylcyclohexane
102.20	3-ethyloctane	112.20	sk-Iso
102.45	sk-Iso	112.40	sk-Iso
102.60	sk-Iso	112.55	sk-Iso

$t_{\text{ret}} / \text{min}$	Product	$t_{\text{ret}} / \text{min}$	Product
112.75	sk-Iso	125.25	sk-Iso
112.90	sk-Iso	125.50	sk-Iso
113.15	1,2-diethylcyclohexane	126.10	sk-Iso
113.25	sk-Iso	126.60	sk-Iso
113.40	sk-Iso	126.80	sk-Iso
113.60	sk-Iso	127.05	sk-Iso
113.90	sk-Iso	127.20	sk-Iso
114.20	sk-Iso	127.85	sk-Iso
114.40	sk-Iso	128.10	sk-Iso
114.65	sk-Iso	128.40	sk-Iso
114.85	sk-Iso	128.65	sk-Iso
115.35	1-methyl-2-propylcyclohexane	129.60	sk-Iso
115.60	sk-Iso	129.75	sk-Iso
115.80	1,2-diethylcyclohexane	130.15	bicyclopentyl
116.35	1-(methylpropyl)cyclohexane	130.95	sk-Iso
116.70	1,1-diethylcyclohexane	131.45	bicyclo[5.3.0]decane
117.00	sk-Iso	132.10	sk-Iso
117.20	sk-Iso	132.65	endo-2-methylbicyclo[3.3.1]nonane
117.50	sk-Iso	133.40	sk-Iso
117.80	butylcyclohexane	133.85	bicyclo(5.3.0)decane
117.95	sk-Iso	134.00	sk-Iso
118.10	sk-Iso	134.30	sk-Iso
118.45	pentylcyclopentane	134.70	sk-Iso
118.65	sk-Iso	135.30	cis-decalin
118.85	sk-Iso	136.10	sk-Iso
119.05	sk-Iso	136.60	sk-Iso
119.30	sk-Iso	137.25	sk-Iso
119.70	sk-Iso	137.35	sk-Iso
120.05	octahydro-5-methyl-1H-indene	138.65	decahydro-2-methylnaphthalene
120.50	sk-Iso	140.35	sk-Iso
120.80	sk-Iso	141.20	sk-Iso
121.00	sk-Iso	142.00	sk-Iso
121.25	sk-Iso	142.80	sk-Iso
121.50	sk-Iso	143.35	sk-Iso
121.90	sk-Iso	144.70	cyclodecane
122.20	sk-Iso	145.00	sk-Iso
122.70	sk-Iso	145.60	sk-Iso
122.95	sk-Iso	147.50	tetralin
123.00	sk-Iso	152.60	naphthalene
123.70	bicyclo[4.1.0]heptane		
123.85	sk-Iso		
124.20	trans-decalin		
124.60	spiro[4.5]decane		
124.75	sk-Iso		
124.90	sk-Iso		

9.2 Derivation of the Equations for the Calculations of Conversion, Yields and Selectivities

9.2.1 Nomenclature

Symbols

Symbol	Unit	Designation
A	- (or counts)	dimensionless peak area in the chromatogram
\bar{A}	- (or counts)	arithmetic mean of peak areas from various chromatograms
f	-	compound-specific FID correction factor
m	kg	mass
\dot{m}	$\text{kg} \cdot \text{s}^{-1}$	mass flux
M	$\text{kg} \cdot \text{mol}^{-1}$	molar mass
n	mol	molar amount
\dot{n}	$\text{mol} \cdot \text{s}^{-1}$	molar flux
p, q	-	carbon number of hydrocracked products
s	kg (or $\text{kg} \cdot \text{counts}^{-1}$)	reciprocal sensitivity of the FID
S	-	selectivity
S^*	-	modified selectivity defined in Eq. (9.34)
X	-	conversion
Y	-	yield
γ	-	stoichiometric factor

Indices

Bz	benzene
Dec	pseudo-reactant decalin
conv	converted
GSL	in the gas sampling loop
i	a reactant in the stoichiometric equation
in	entering the reactor
j	a product or group of products in the stoichiometric equation
out	leaving the reactor

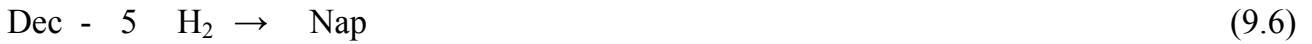
Abbreviations

Bz	benzene
C ₉ -	hydrocarbons with less than 10 carbon atoms (hydrocracked products)
C ₁₁ ⁺	hydrocarbons with more than 10 carbon atoms
Dec	pseudo-reactant decalin
Eq(s).	equation(s)
FID	flame ionization detector
GC	gas chromatograph(y)
GSL	gas sampling loop
Nap	naphthalene
OCD(s)	open-chain decane(s)
ROP(s)	ring-opening product(s)
sk-Iso(s)	skeletal isomer(s)
Ttr	tetralin

9.2.2 Conversion X_{Dec}

Fundamentals

In this work cis-decalin was used as a model hydrocarbon. It was converted in a flow reactor in the presence of a large excess of hydrogen at elevated pressure. Eqs. (9.1) to (9.6) give a simplified stoichiometry of the reactions which are possible at these conditions. Since trans-decalin is formed in a very fast isomerization reaction of cis-decalin, cis- and trans-decalin were lumped together to a pseudo-reactant decalin ($i = \text{Dec}$). It holds



where sk-Isos, ROPs, OCDs, C₉-, Ttr and Nap are, respectively, skeletal isomers with two naphthenic rings, ring-opening products with one remaining naphthenic ring, open-chain decanes, hydrocracked products with less than 10 carbon atoms and the dehydrogenated products (DHPs) tetralin and naphthalene. Hydrocarbons with more than 10 carbon atoms were not formed during the experiments.

In general, the conversion X in a flow reactor is defined by one of the following equations:

$$X_{\text{Dec}} = \frac{(\dot{n}_{\text{Dec}})_{\text{in}} - (\dot{n}_{\text{Dec}})_{\text{out}}}{(\dot{n}_{\text{Dec}})_{\text{in}}} \quad (9.7)$$

or

$$X_{\text{Dec}} = \frac{(\dot{m}_{\text{Dec}})_{\text{in}} - (\dot{m}_{\text{Dec}})_{\text{out}}}{(\dot{m}_{\text{Dec}})_{\text{in}}} \quad (9.8)$$

Where \dot{n} and \dot{m} are the molar flux and the mass flux, respectively.

Since, on-line gas chromatography with a gas sampling loop (GSL) was employed for the product analysis Eq. (9.8) is modified to Eq. (9.9) with absolute masses of the compounds inside the GSL:

$$X_{\text{Dec}} = \frac{(m_{\text{Dec}})_{\text{GSL at } X=0} - (m_{\text{Dec}})_{\text{GSL}}}{(m_{\text{Dec}})_{\text{GSL at } X=0}} \quad (9.9)$$

Where $(m_{\text{Dec}})_{\text{GSL}}$ is the mass of unconverted decalin in the gas sampling loop and $(m_{\text{Dec}})_{\text{GSL at } X=0}$ is a fictitious mass of decalin that would have been in the gas sampling loop, if no chemical transformation had occurred in the flow reactor, *i.e.*, at $X_{\text{Dec}} = 0$ %.

Calculation of $(m_{\text{Dec}})_{\text{GSL}}$

The mass of decalin in the GSL is proportional to the dimensionless peak area times the compound-specific FID correction factor f_{Dec} :

$$(m_{\text{Dec}})_{\text{GSL}} \sim f_{\text{Dec}} \cdot A_{\text{Dec}} \quad (9.10)$$

or with a proportionality factor s , the reciprocal sensitivity of the FID:

$$(m_{\text{Dec}})_{\text{GSL}} = s \cdot f_{\text{Dec}} \cdot A_{\text{Dec}} \quad (9.11)$$

However, as will be shown below the value for this proportionality factor is not really needed for the calculations of decalin conversion. The same equation can be used to calculate the masses of the products j in the gas sampling loop:

$$(m_j)_{\text{GSL}} = s \cdot f_j \cdot A_j \quad (9.12)$$

Usually the compound-specific FID correction factor f_i or f_j is referenced to benzene, *i.e.*, f_{Bz} is set to 1.000. This results in Eq. (9.13) for the calculation of f_{Dec} .

$$f_{\text{Dec}} = \frac{m_{\text{Dec}} - A_{\text{Bz}}}{m_{\text{Bz}} - A_{\text{Dec}}} \quad (9.13)$$

However, for this equation every single peak in the chromatogram must be assigned correct and each product j is need in pure form for a co-injection with benzene. This is not applicable for the experimental data generated in this work. Nevertheless, it is also possible to calculate the values for f_{Dec} and f_j , see Eqs. (9.14) and (9.15), respectively [1].

$$f_{\text{Dec}} = \frac{\frac{M_{\text{Dec}}}{M_{\text{C, Dec}}}}{\frac{M_{\text{Bz}}}{M_{\text{C, Bz}}}} = \frac{\frac{138 \text{ g}\cdot\text{mol}^{-1}}{120 \text{ g}\cdot\text{mol}^{-1}}}{\frac{78 \text{ g}\cdot\text{mol}^{-1}}{72 \text{ g}\cdot\text{mol}^{-1}}} = 1.062 \quad (9.14)$$

$$f_j = \frac{\frac{M_j}{M_{\text{C, j}}}}{\frac{M_{\text{Bz}}}{M_{\text{C, Bz}}}} = 1.083 \quad (9.15)$$

Where M_{Dec} , M_{Bz} , and M_j are, respectively, the molar masses of decalin, benzene and products j and $M_{\text{C, Dec}}$, $M_{\text{C, Bz}}$ and $M_{\text{C, j}}$ the molar masses of carbon in the respective hydrocarbon. Some FID correction factors of relevant hydrocarbons are summarized in Table 9.2.

Table 9.2: Compound-specific FID correction factors f of some relevant hydrocarbons, calculated by Eqs. (9.14) and (9.15).

Hydrocarbon	Formula	f
Methane	CH ₄	1.231
Ethane	C ₂ H ₆	1.154
Propane	C ₃ H ₈	1.129
Butanes	C ₄ H ₁₀	1.116
Pentanes	C ₅ H ₁₂	1.108
Hexanes	C ₆ H ₁₄	1.103
Methylcyclopentane	C ₆ H ₁₂	1.077
Open-chain decanes (OCDs)	C ₁₀ H ₂₂	1.093
Ring-opening products (ROPs)	C ₁₀ H ₂₀	1.077
Skeletal isomers of decalin (sk-Isos)	C ₁₀ H ₁₈	1.062
Decalin	C ₁₀ H ₁₈	1.062
Tetralin	C ₁₀ H ₁₂	1.016
Naphthalene	C ₁₀ H ₈	0.985

It follows that Eq. (9.11) can be re-written as

$$(m_{\text{Dec}})_{\text{GSL}} = s \cdot 1.062 \cdot A_{\text{Dec}} \quad (9.16)$$

Calculation of $(m_{Dec})_{GSL}$ at $X = 0$

To obtain $(m_{Dec})_{GSL}$ at $X = 0$ the following equation is used:

$$(m_{Dec})_{GSL \text{ at } X = 0} = (m_{Dec})_{GSL} + (m_{Dec})_{conv} \quad (9.17)$$

Where $(m_{Dec})_{GSL}$ and $(m_{Dec})_{conv}$ are, respectively, the mass of decalin in the GSL and the mass of decalin which was converted to other hydrocarbons. Since $(m_{Dec})_{GSL}$ can be directly measured, only $(m_{Dec})_{conv}$ has to be calculated. This is done by summation of the masses of decalin converted to the different product groups which can be calculated by the respective masses of products found in the gas sampling loop:

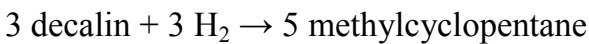
$$\text{- sk-Isos:} \quad (m_{Dec})_{conv} = s \cdot f_{sk-Isos} \cdot \sum_{sk-Isos} A_{sk-Isos} \quad (9.18)$$

$$\text{- ROPs:} \quad (m_{Dec})_{conv} = \frac{M_{Dec}}{M_{ROPs}} \cdot s \cdot f_{ROPs} \cdot \sum_{ROPs} A_{ROPs} \quad (9.19)$$

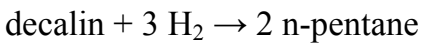
$$\text{- OCDs:} \quad (m_{Dec})_{conv} = \frac{M_{Dec}}{M_{OCDs}} \cdot s \cdot f_{OCDs} \cdot \sum_{OCDs} A_{OCDs} \quad (9.20)$$

$$\text{- } C_{9-}: \quad (m_{Dec})_{conv} = s \cdot \sum_{C_{9-}} \frac{|\gamma_{Dec}|}{\gamma_{C_{9-}}} \cdot \frac{M_{Dec}}{M_{C_{9-}}} \cdot f_{C_{9-}} \cdot A_{C_{9-}} \quad (9.21)$$

γ_{Dec} and $\gamma_{C_{9-}}$ are the stoichiometric factors in the equation leading from decalin to the respective hydrocracked products, *e.g.*,



$$\gamma_{Dec} = -3; \gamma_{M-CPn} = +5; \frac{|\gamma_{Dec}|}{\gamma_{M-CPn}} = +\frac{3}{5}$$



$$\gamma_{Dec} = -1; \gamma_{n-Pn} = +2; \frac{|\gamma_{Dec}|}{\gamma_{n-Pn}} = +\frac{1}{2}$$

Note that all stoichiometric factors are negative for all reactants *i* and positive for all products *j*.

A closer look at Eqs. (9.18) to (9.21) reveals that Eqs. (9.18) to (9.20) can be derived from Eq. (9.21): If j is hydrocarbon with 10 carbon atoms, the correction factor $|\gamma_{\text{Dec}}|/\gamma_j$ is unity, and Eqs. (9.20) or (9.19) result. If j is an isomer, the correction factor M_{Dec}/M_j is unity as well, and Eq. (9.18) result.

In general terms one can say that the mass of decalin converted is

$$(m_{\text{Dec}})_{\text{conv}} = s \cdot \sum_j \frac{|\gamma_{\text{Dec}}|}{\gamma_j} \cdot \frac{M_{\text{Dec}}}{M_j} \cdot f_j \cdot A_j \quad (9.22)$$

Substitution of Eqs. (9.11) and (9.22) into Eq. (9.17) and Eqs. (9.11) and (9.17) into Eq. (9.9) gives the conversion of decalin:

$$X_{\text{Dec}} = \frac{s \cdot \sum_j \frac{|\gamma_{\text{Dec}}|}{\gamma_j} \cdot \frac{M_{\text{Dec}}}{M_j} \cdot f_j \cdot A_j}{s \cdot f_{\text{Dec}} \cdot A_{\text{Dec}} + s \cdot \sum_j \frac{|\gamma_{\text{Dec}}|}{\gamma_j} \cdot \frac{M_{\text{Dec}}}{M_j} \cdot f_j \cdot A_j} \quad (9.23)$$

Note that s , the proportionality factor, appears in both the nominator and the denominator and can be canceled.

9.2.3 Yield Y_j

In a flow reactor the yield of a product or groups of products j is defined as:

$$Y_j = \frac{(\dot{n}_j)_{\text{out}} - (\dot{n}_j)_{\text{in}}}{(\dot{n}_i)_{\text{in}}} \cdot \frac{|\gamma_i|}{\gamma_j} \quad (9.24)$$

In this work $(\dot{n}_j)_{\text{in}}$ will generally be 0. As already discussed in Section 9.2.2, Eq. (9.24) can be re-written as

$$Y_j = \frac{(n_j)_{\text{GSL}}}{(n_{\text{Dec}})_{\text{GSL at } X=0}} \cdot \frac{|\gamma_{\text{Dec}}|}{\gamma_j} \quad (9.25)$$

or

$$Y_j = \frac{\frac{1}{M_j} \cdot (m_j)_{\text{GSL}}}{\frac{1}{M_{\text{Dec}}} \cdot (m_{\text{Dec}})_{\text{GSL at } X=0}} \cdot \frac{|\gamma_{\text{Dec}}|}{\gamma_j} \quad (9.26)$$

or

$$Y_j = \frac{(m_j)_{\text{GSL}}}{(m_{\text{Dec}})_{\text{GSL at } X=0}} \cdot \frac{|\gamma_{\text{Dec}}|}{\gamma_j} \cdot \frac{M_{\text{Dec}}}{M_j} \quad (9.27)$$

The calculation of $(m_{\text{Dec}})_{\text{GSL at } X=0}$ has already been discussed Section 9.2.2 and can be employed to Eq. (9.27) to give together with Eq. (9.12), Eq. (9.28):

$$Y_j = \frac{f_j \cdot A_j}{f_{\text{Dec}} \cdot A_{\text{Dec}} + \sum_j \frac{|\gamma_{\text{Dec}}|}{\gamma_j} \cdot \frac{M_{\text{Dec}}}{M_j} \cdot f_j \cdot A_j} \cdot \frac{|\gamma_{\text{Dec}}|}{\gamma_j} \cdot \frac{M_{\text{Dec}}}{M_j} \quad (9.28)$$

9.2.4 Selectivity S_j

The selectivity of a product or group of products j in a flow reactor is defined as:

$$S_j = \frac{(\dot{n}_j)_{\text{out}} - (\dot{n}_j)_{\text{in}}}{(\dot{n}_i)_{\text{in}} - (\dot{n}_i)_{\text{out}}} \cdot \frac{|\gamma_i|}{\gamma_j} \quad (9.29)$$

In this work $(\dot{n}_j)_{\text{in}}$ will generally be 0. As already discussed in Section 9.2.2, Eq. (9.24) can be re-written as

$$S_j = \frac{(n_j)_{\text{GSL}}}{(n_{\text{Dec}})_{\text{GSL at } X=0} - (n_{\text{Dec}})_{\text{GSL}}} \cdot \frac{|\gamma_{\text{Dec}}|}{\gamma_j} = \frac{(n_j)_{\text{GSL}}}{(n_{\text{Dec}})_{\text{conv}}} \cdot \frac{|\gamma_{\text{Dec}}|}{\gamma_j} \quad (9.30)$$

or

$$S_j = \frac{\frac{1}{M_j} \cdot (m_j)_{\text{GSL}}}{\frac{1}{M_{\text{Dec}}} \cdot (m_{\text{Dec}})_{\text{conv}}} \cdot \frac{|\gamma_{\text{Dec}}|}{\gamma_j} \quad (9.31)$$

or

$$S_j = \frac{(m_j)_{\text{GSL}}}{(m_{\text{Dec}})_{\text{conv}}} \cdot \frac{|\gamma_{\text{Dec}}|}{\gamma_j} \cdot \frac{M_{\text{Dec}}}{M_j} \quad (9.32)$$

Substituting Eqs. (9.12) and (9.22) into Eq. (9.32) gives:

$$S_j = \frac{f_j \cdot A_j}{\sum_j \frac{|\gamma_{Dec}|}{\gamma_j} \cdot \frac{M_{Dec}}{M_j} \cdot f_j \cdot A_j} \cdot \frac{|\gamma_{Dec}|}{\gamma_j} \cdot \frac{M_{Dec}}{M_j} \quad (9.33)$$

A summation over the selectivities of all products as defined in Eq. (9.33) will give 1.00 or 100 %.

9.2.5 Modified Selectivity S_j^*

For a detailed evaluation of the formation of hydrocracking products a modified selectivity S_j^* is introduced:

$$S_j^* = \frac{(\dot{n}_j)_{out}}{(\dot{n}_i)_{converted\ to\ C_9-}} \quad (9.34)$$

where j is a hydrocracked product. Re-writing the equations, due to the reasons mentioned in Section 9.2.2 gives:

$$S_j^* = \frac{(n_j)_{GSL}}{(n_{Dec})_{converted\ to\ C_9-}} \quad (9.35)$$

or

$$S_j^* = \frac{\frac{1}{M_j} \cdot (m_j)_{GSL}}{\frac{1}{M_{Dec}} \cdot (m_{Dec})_{converted\ to\ C_9-}} \quad (9.36)$$

or

$$S_j^* = \frac{(m_j)_{GSL}}{(m_{Dec})_{converted\ to\ C_9-}} \cdot \frac{M_{Dec}}{M_j} \quad (9.37)$$

Substituting Eqs. (9.12) and (9.22) into Eq. (9.37) and reducing s gives:

$$S_j^* = \frac{f_j \cdot A_j}{\sum_j \frac{|\gamma_{Dec}|}{\gamma_j} \cdot \frac{M_{Dec}}{M_j} \cdot f_j \cdot A_j} \cdot \frac{M_{Dec}}{M_j} \quad (9.38)$$

where j are only C₉-.

With this definition the sum of the modified selectivity $\sum_j S_j^*$ is 2.00 or 200 % for a pure primary hydrocracking and 10.00 or 1000 % for a severe hydrocracking of decalin all the way down to methane.

9.3 Pyridine Concentrations Determined by FT-IR Spectroscopy

Table 9.3: Pyridine concentrations at different desorption temperatures of some catalysts determined by FT-IR.

Catalyst	$T_{\text{des}} / ^\circ\text{C}$	$n_{\text{pyridine}} \cdot m_{\text{catalyst}}^{-1} / \mu\text{mol} \cdot \text{g}^{-1}$						
		200	250	300	350	400	450	500
5.3Pd/Na _{0.72} H _{0.28} -Y		725	716	652	661	599	580	356
4.9Rh/Na _{0.64} H _{0.36} -Y		572	547	456	363	249	111	0
3.5Re/Na _{0.97} H _{0.03} -Y		125	122	87	31	8	0	0
2.9Ir/Na _{0.90} H _{0.10} -mordenite		92	88	82	72	62	39	26
2.8Ir/K _{0.86} H _{0.14} -L		108	95	84	67	40	26	21
0.067Ir/SAPO-5		78	62	50	49	46	20	13
0.52Ir/H _{0.59} Na _{0.41} -ZSM-5		191	182	169	158	152	135	119
3.0Ir/Na _{0.80} H _{0.20} -EMC-2		158	154	137	116	98	71	38
3.0Ir/Na _{0.53} H _{0.47} -[Al]Beta-14		156	148	142	129	111	88	61
2.3Ir/H _{0.88} Na _{0.12} -[B]Beta-18		23	16	11	2	0	0	0
3.4Ir/H _{0.56} Na _{0.44} -[Al]Beta-21		194	190	179	166	149	135	96
3.1Ir/Na _{0.82} H _{0.18} -[Al]Beta-8		122	107	95	87	64	47	20
2.0Ir/Cs _{0.84} H _{0.16} -mordenite		67	67	67	61	47	32	19
2.9Ir/K _{0.68} Na _{0.21} H _{0.11} -L		130	125	123	99	70	42	20
2.0Ir/K _{0.65} Cs _{0.34} H _{0.01} -L		87	78	67	45	28	21	21
3.3Ir/H _{0.74} Li _{0.26} -[Al]Beta-14		189	188	185	173	158	141	108
3.6Ir/K _{0.55} H _{0.45} -[Al]Beta-14		170	160	145	128	103	76	44
3.5Ir/Rb _{0.52} H _{0.48} -[Al]Beta-14		121	109	93	82	66	48	25
3.4Ir/H _{0.58} Cs _{0.42} -[Al]Beta-14		129	113	98	83	64	40	12
3.4Ir/K _{0.66} H _{0.22} Na _{0.12} -[Al]Beta-8		287	245	212	165	97	41	2
3.4Ir/Rb _{0.56} H _{0.25} Na _{0.19} -[Al]Beta-8		243	220	185	134	69	11	2
3.5Ir/Cs _{0.62} H _{0.22} Na _{0.16} -[Al]Beta-8		73	59	45	31	8	0	0
2.8Pt/H _{0.74} Li _{0.26} -[Al]Beta-14		243	243	235	222	210	182	140
3.2Pt/H _{0.57} Na _{0.43} -[Al]Beta-14		243	241	231	218	197	174	131
2.8Pt/H _{0.55} K _{0.45} -[Al]Beta-14		175	169	156	135	114	88	63
2.8Pt/Rb _{0.58} H _{0.42} -[Al]Beta-14		226	215	203	182	157	130	95
2.9Pt/Cs _{0.51} H _{0.49} -[Al]Beta-14		203	186	172	158	134	111	78
1.1Ir/Cs _{0.96} H _{0.04} -[Al]Beta-14		82	70	60	54	42	23	0
2.0Ir/Cs _{0.80} H _{0.20} -[Al]Beta-14		116	101	89	76	63	42	13
4.0Ir/Cs _{0.53} H _{0.47} -[Al]Beta-14		172	154	147	135	119	97	77
4.8Ir/H _{0.61} Cs _{0.39} -[Al]Beta-14		244	239	239	219	204	181	109

9.4 References

- [1] E. Leibnitz, H.G. Struppe, "Handbuch der Gaschromatographie", 3rd Edn., Akademische Verlagsgesellschaft Geest & Portig, Leipzig, 1984, p. 422.